SATORU TAKAKURA

Characterization of a continuous polarization modulator using a half-wave plate for measurements of degree-scale cosmic microwave background with the POLARBEAR experiment

Characterization of a continuous polarization modulator using a half-wave plate for measurements of degree-scale cosmic microwave background with the POLARBEAR experiment

SATORU TAKAKURA

Department of Earth and Space Science
Osaka University

June 2017

Satoru Takakura: *Characterization of a continuous polarization modulator using a half-wave plate for measurements of degree-scale cosmic microwave background with the POLARBEAR experiment,* ©
June 2017

SUPERVISORS:
Kentaro Nagamine
Masashi Hazumi

LOCATION:
Machikaneyama 1 - 1, Toyonaka, Osaka, Japan

TIME FRAME:
June 2017

ABSTRACT

Measurements of the cosmic microwave background (CMB) B-mode signal on broad-angular scales provides unique information about cosmic inflation in the beginning of the Universe. In this thesis, we investigate such measurements using the POLARBEAR experiment. First, we search the lensing B-mode signal on the sub-degree scales from the first season of the observations, and report the detection with a significance of 4.7σ using only the CMB polarization data. Degree-scale observations, on the other hand, are difficult due to a low-frequency noise, the so-called $1/f$ noise. To solve the problem, we employ a novel technique of the polarization signal modulation using a continuously rotating half-wave plate (CRHWP). We construct a comprehensive model of a detector signal, including half-wave plate synchronous signals, detector non-linearities, beam imperfections, and all noise sources. We also perform test observations using a prototype CRHWP on the POLARBEAR telescope. We find a significant polarization leakage caused by detector non-linearities. However, a simple leakage subtraction method efficiently removes the leakage, and it enables observations from the multipole of $\ell \lesssim 40$ with sufficiently small instrumental errors due to the CRHWP. These results strongly support the feasibility of the measurements from large-angular scales to small-angular scales in future experiments.

要旨

インフレーションは、熱いビッグバン以前の宇宙最初期に加速膨張が起こったとする仮説であり、これまでの宇宙マイクロ波背景放射(CMB)などの精密観測により良く支持されている。しかし、インフレーション理論の最も重要な予言である原始重力波は未だ観測されていない。原始重力波ゆらぎと密度ゆらぎの大きさの比であるテンソル・スカラー比rはインフレーションのエネルギースケールと直接結びついており、実験室では到底到達できないような超高エネルギーにおける物理法則解明の手掛かりとなる。Bモードと呼ばれるCMBの偏光非等方性はrの値に制限を与えることができるユニークな観測対象である。そのためには2°程度の角度スケールの非等方性の観測が重要である。一方、CMBのBモード偏光は宇宙の大規模構造による重力レンズ効果によっても作られ、その信号は0.1°程度の角度スケールに現れる。rが0.01よりも小さい場合、重力レンズ効果起源Bモードも精密観測し、その影響を取り除く必要がある。

POLARBEARは、微弱なCMBのBモード信号観測のための超高感度超伝導検出器と、0.06°の角度分解能を持つ口径2.5 mの望遠鏡を用いた地上CMB観測実験である。2012年に観測を開始したのち、2年間にわたって小角度領域の観測を行い、重力レンズ効果起源Bモードの観測を達成した。これはCMBの偏光観測情報のみを用いて重力レンズ効果起源Bモードの存在を十分な有意性で検証した世界で初めての成果である。

しかし、原始重力波起源Bモード観測にはいくつかの重要な課題が残されている。そのうちの一つは、大気ゆらぎ、装置の温度変化、検出器の特性変化によって生じる低周波数ノイズ(1/fノイズ)である。その対策として、本研究では、これまでに提案されている連続回転半波長板を用いた偏光信号の変調による手法を採用した。まず、半波長板の角度に相関した信号、検出器の非線形性、ビームの非理想性、そして、全てのノイズ源を考慮した、包括的な検出器の信号のモデルを構築した。また、連続回転半波長板の試作機を開発し、POLARBEARを用いたテスト観測でその性能を評価した。その結果、かなりの無偏光信号から偏光信号への漏れ込みが検出器の非線形性により生じていることがわかったが、漏れ込みの除去を行うことで球面調和関数の次数$\ell \lesssim 40$までの観測を達成できることを示した。さらに、連続回転半波長板による装置由来の系統誤差の影響が十分小さいことも見積もった。これらの結果は大口径の地上CMB観測望遠鏡における連続回転半波長板の実証において初めての成果である。

連続的な偏光信号の変調技術を用いることで、将来のCMB観測実験は小角度スケールから大角度スケールにわたるCMB非等方性、特にBモードの角度パワースペクトルを、かつてない統計精度で、かつ、最小限の系統誤差で測定することができる。そして、テンソル・スカラー比rや、スカラーゆらぎのスペクトル指数n_sの制限を、$\sigma(r) < 0.001$、$\sigma(n_s) < 0.001$のレベルまで改善することが期待される。その結果、主要なインフレーションのモデルを選別することが可能となり、背後にある超高エネルギーの物理に光をあてることができるだろう。

ACKNOWLEDGMENTS

I would first like to give my great thanks to Prof. Masashi Hazumi for inviting me to this fantastic community and giving me so many unusual opportunities over the past four years. I would also like to thank Prof. Kentaro Nagamine for grateful advice on my research.

I am thankful to the POLARBEAR Collaboration, especially Principal Investigator Adrian T. Lee. I could not have done this doctoral work without the great instruments and all the effort of all the collaborators.

The development of the prototype CRHWP was supported by many colleagues: Prof. Tomotake Matsumura gave me many advisements for designing the rotator, Dr. Michael Myers provided the HWP, and Dr. Yuki Inoue, as well as Mr. Nolberto Oyarce, helped the installation onto the POLARBEAR.

Discussions with colleagues also gave me a lot of insights. Prof. Haruki Nishino introduced me all about the POLARBEAR data, and Dr. Chinone Yuji taught me the importance of statistics. Prof. Akito Kusaka gave me a lot of critical advice and sometimes corrected my misunderstandings. Complementary analysis by Mr. Neil Goeckner-Wald was also essential. I also thank Dr. Kaori Hattori, Dr. Davide Poletti, Mr. Frederic Matsuda, and Mr. Takuro Fujino for the productive collaborations.

The KEK CMB group have been both fruitful and a lot of fun to work with. Prof. Osamu Tajima has been a great leader of the GroundBIRD experiment. Prof. Masaya Hasegawa has an immense network and always brings news. Prof. Takayuki Tomaru had hundreds of ideas for instruments. Dr. Ryo Nagata kindly spent a lot of time for discussion with me. Dr. Kimihiro Kimura taught me the usage of GRASP. Dr. Hiroshi Yamaguchi supported the measurement of the HWP. I have enjoyed discussions with all the other students and postdocs, including Dr. Hideki Morii, Dr. Shugo Oguri, Dr. Yasuto Hori, Dr. Taketo Nagasaki, Dr. Junya Suzuki, Dr. Yuto Minami, Dr. Hiroki Watanabe, Dr. Jihoon Choi, Dr. Nozomu Tomita, Mr. Hikaru Ishitsuka, Mr. Yoshiki Akiba, Ms. Yuko Segawa, Ms. Sayuri Takatori, Mr. Takaho Hamada, and Mr. Daiki Tanabe. Special thanks to secretaries Mrs. Junko Yamada and Mrs. Keiko Imagawa. I would like to acknowledge Prof. Nobuhiko Katayama for funding.

I would also like to thank Professors Yutaka Fujita, Luca Baiotti, and Kengo Tomida for proofreading of this thesis, as well as encouraging me to graduate. I have also enjoyed the interaction with every student and postdoc in the Theoretical Astrophysics Group at Osaka University. I also thank secretaries Mrs. Yasuko Nishii and Mrs. Mariko Tokiwa.

It is also my pleasure to thank all the friends and teachers who have encouraged me to graduate.

This research was supported by Grant-in-Aid for JSPS Research Fellow.

Finally, I would like to thank my parents for their unconditional support.

CONTENTS

LIST OF FIGURES

LIST OF TABLES

ACRONYMS

2D two-dimensional
ABS Atacama B-Mode Search
AC alternating current
ADC analog-to-digital converter
AR anti-reflective
ARC anti-reflective coating
AZ azimuthal angle
BAO baryon acoustic oscillation
CDM cold dark matter
CES constant elevation scan, *Glossary:* CES
CfA Center for Astrophysics
CIB cosmic infrared background
CMB cosmic microwave background
COBE Cosmic Background Explorer
CRHWP continuously rotating half-wave plate
DC direct current
Dec declination
DMR Differential Microwave Radiometer
EL elevationn angle
EOS equation of state
FIR finite impulse response
FIRAS Far Infrared Absolute Spectrophotometer
FLRW Friedmann-Lemaître-Robertson-Walker
FOV field of view
FWHM full width at half maximum
GPS Global Positioning System
GRASP General Reflector antenna Analysis Software Package
GUT Grand Unified Theory
GW gravitational wave
***Herschel*-ATLAS** *Herschel*-Astrophysical Terahertz Large Area Survey
Herschel *Herschel* Space Observatory
HTT Huan Tran telescope
HWP half-wave plate
HWPSS HWP synchronous signal
I→P intensity to polarization, *Glossary:* **I→P**

IRAM Institut de Radioastronomie Millimétrique
IRIG Inter-Range Instrumentation Group
JSPS Japan Society for the Promotion of Science
KEK 高エネルギー加速器研究機構
ΛCDM Λ and cold dark matter
LSS large-scale structure
POLARBEAR POLARization of Background microwave Radiation
PSD power-spectrum density
PSM Planck Sky Model
PWV precipitable water vapor
QUIET Q/U Imaging ExperimenT
NEP noise equivalent power
NET noise equivalent temperature
NPT Network Time Protocol
RA right ascension
RJ Rayleigh-Jeans
RMS root-mean-square
RSJ resistively shunted junction
SPT South Pole Telescope
SQUID superconducting quantum interference device
TES transition-edge sensor
TF transfer function
TOD time-ordered data
WMAP Wilkinson Microwave Anisotropy Probe

GLOSSARIES

1/f noise A 1/f noise is a noise whose PSD depends on frequency as power law with negative index.
angular power-spectrum Power of the expansion coefficient (with spherical harmonics or 2D Fourier modes) of anisotropy map.
array An array is a set of all detectors.
detector minimum unit of device to measure signal
el-nod moving telescope up and down
observation one set of calibration data and scan data
Q↔U between Stokes Q polarization and U polarization
receiver vacuum chamber containing a array of detectors
scan one back-and-forth motion of telescope
sensitivity accuracy of detector or measurement
telescope a structure which move receiver in AZ and EL
Tau A the Crab nebula

1 INTRODUCTION

The measurement of the cosmic microwave background (CMB) anisotropy, especially the B-mode signal, is a powerful and unique probe of the inflation, which could be a missing piece of the Λ and cold dark matter (ΛCDM) model.

In this chapter, first, we describe the standard model of the cosmology, the so-called ΛCDM model, in section 1.1. Then, we introduce the inflation theory in section 1.2. In section 1.3, we explain the CMB anisotropy, especially its polarization signal. Finally, we characterize experiments observing the CMB polarization anisotropy in section 1.4.

1.1 STANDARD MODEL OF THE COSMOLOGY

Cosmology is a study revealing the history of the Universe, which is one of the most fundamental and fascinating subjects for us. At the beginning of the 20th century, the establishment of the general relativity (Einstein 1916), which describes the interaction between space-time and matter, made cosmology as one of the scientific topics. Then, along with the theoretical studies, development in technology enabled the observations of faint signals from space. By combining these theories and observations, the standard cosmological model was established.

Under the assumption of homogeneity and isotropy,[1] the space-time of the universe is described by Friedmann-Lemaître-Robertson-Walker (FLRW) metric:

$$ds^2 = -c^2dt^2 + a(t)^2\gamma_{ij}dx^i dx^j \quad \text{with} \quad \gamma_{ij} = \frac{\delta_{ij}}{1 + Kr^2/4}, \tag{1.1.1}$$

where (t, x^1, x^2, x^3) is time and coordinates in the comoving coordinate system, K is the curvature of the universe, $r^2 = \sum_{i=1}^{3}(x^i)^2$. The $a(t)$ is the scale factor, which relates the comoving coordinates to physical length. Here, the evolution of the FLRW metric is expressed by only the scale factor, $a(t)$. We set the current ($t = t_0$) value of scale factor as $a(t_0) \equiv 1$. To achieve a static universe, $a(t)$ must be constant.

The matter is described by energy density $\rho_X(t)$ and pressure $p_X(t)$ for each content, where X is a label of the content. All the contents can be classified by the equation of state parameter $w_X(t) \equiv \frac{p_X(t)}{\rho_X(t)}$: $w_X(t) = \frac{1}{3}$ for relativistic matter whose kinetic energy is larger than its stationary energy, and $w_X(t) = 0$ for non-relativistic matter whose kinetic energy is negligible compared to its stationary energy. From energy conservation, one can derive the evolution of energy density:

$$\rho_X(t) \propto a(t)^{-3[1+w_X(t)]} = \begin{cases} a(t)^{-4} & \text{for relativistic matter,} \\ a(t)^{-3} & \text{for non–relativistic matter.} \end{cases} \tag{1.1.2}$$

Therefore, the total energy density $\rho(t) \equiv \sum_X \rho_X(t)$ is dominated by contributions from relativistic (non-relativistic) matter when the universe is small (large).

1 These assumptions are verified by observations of e.g., the CMB and galaxy searches on a scale larger than $\sim$ 300–500 Mpc.

The evolution of the FLRW metric is then described by the first Friedmann equation:

$$H(t)^2 + \frac{Kc^2}{a(t)^2} - \frac{\Lambda c^2}{3} = \frac{8\pi G}{3c^2}\rho(t)\,, \tag{1.1.3}$$

where $H(t) \equiv \frac{1}{a(t)}\frac{da(t)}{dt}$ is the Hubble parameter, and Λ is the cosmological constant. The terms of curvature and cosmological constant can be treated as other contents of matter, whose energy densities are $\rho_K(t) \equiv -\frac{3c^4}{8\pi G}\frac{K}{a(t)^2}$ and $\rho_\Lambda(t) \equiv \frac{c^4}{8\pi G}\Lambda$ respectively, and can be moved to the right-hand side. By referencing to the current values, Eq. (1.1.3) can be reorganized as

$$H(t)^2 = H(t_0)^2\left[\frac{\Omega_r}{a(t)^4} + \frac{\Omega_m}{a(t)^3} + \frac{\Omega_K}{a(t)^2} + \Omega_\Lambda\right]. \tag{1.1.4}$$

Here, Ω_X is a fraction of current energy density to the critical energy density $\rho_c \equiv \frac{3c^2H(t_0)^2}{8\pi G}$, and contents of relativistic matter and that of non-relativistic matter are combined into Ω_r and Ω_m, respectively. The evolution of the universe can be obtained by solving Eq. (1.1.4),[2] if the cosmological parameters, the Hubble constant ($H_0 \equiv H(t_0)$), and density parameters (Ω_r, Ω_m, Ω_K, and Ω_Λ), are determined.

The first cosmological parameter determined by observation was the Hubble constant, H_0 (Hubble 1929). In 1929, Edwin Hubble observed neighboring galaxies and measured apparent radial velocities and distances using the brightest stars whose absolute luminosity can be predictable. He found that besides all the galaxies are receding from each other against gravity, distances and velocities have a linear correlation (Figure 1.1.1). The linear correlation can be excellently explained by the expansion of metric of the universe as its slope is equivalent to the Hubble constant, H_0. Because of systematic misestimation of distance, however, the original value of H_0 measured by Hubble was about eight times larger than the current measurement of $H_0 = 73.24 \pm 1.74\,\mathrm{km\,s^{-1}\,Mpc^{-1}}$ (Riess et al. 2016).

Next, the information of the density parameters for photons and baryons[3], Ω_r and Ω_b respectively, is obtained from studies of nucleosynthesis (Gamow 1948). The discovery of the expanding universe indicates the existence of very hot and relatively dense epoch in the past, the so-called *hot Big Bang Universe*. The universe was filled with a plasma of photons and baryons, namely electrons, protons, and neutrons. When the temperature is around $1\,\mathrm{MeV} \sim 10^{10}\,\mathrm{K}$, protons and neutrons efficiently interact with each other and build up nuclei with a larger mass number, which have lower potential energy. Because of expansion of the universe, however, the temperature and density rapidly decrease, and the nucleosynthesis ends before reaching equilibrium, which results in characteristic abundance distribution depending on the baryon density and duration of the event. Comparing the abundance with measurements and assuming the duration is comparable with the lifetime of the neutron, the density of baryons can be estimated. Since the density of photons is determined by the temperature, $10^{10}\,\mathrm{K}$, we can obtain baryon-to-photon number density ratio, $\eta \equiv \frac{n_b}{n_\gamma}$, which is currently determined as

$$5.8 \times 10^{-10} \leqslant \eta \leqslant 6.6 \times 10^{-10} \quad (95\%\ \mathrm{CL}) \quad , \tag{1.1.5}$$

from the abundance of D and ^{4}He (Cyburt et al. 2016).

2 In practice, a state of the content, relativistic or non-relativistic, can change as a function its energy density $\rho_X(t)$. In such a case, Eq. (1.1.4) cannot be used, and one needs to solve Eq. (1.1.3) directly considering the evolution of equation of state (EOS) parameter, $w_X(t)$, for each content.

3 We include electrons in baryons following a tradition.

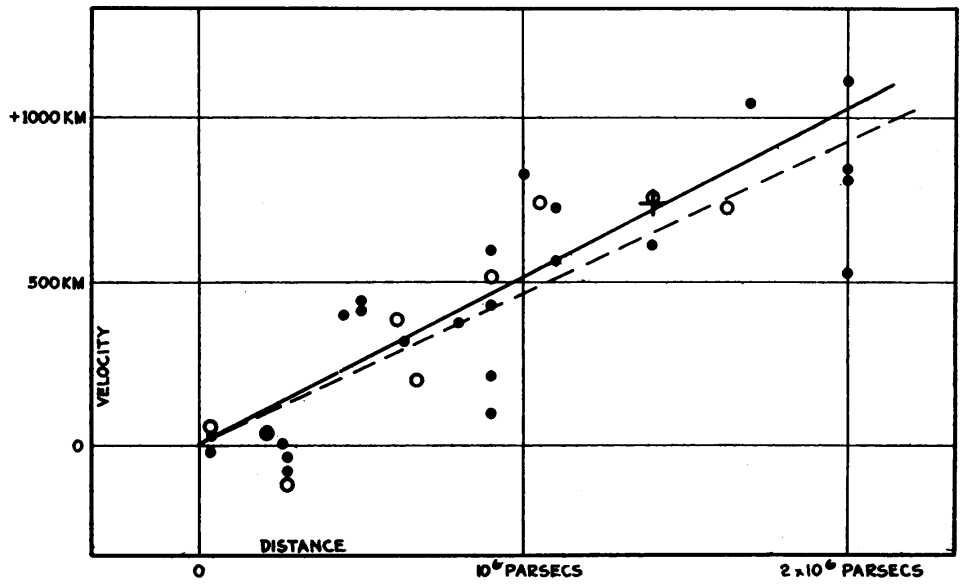

Figure 1.1.1: Discovery of the Hubble's law. The figure is from Hubble (1929).

Another result of the hot Big Bang Universe is the relic radiation. The photons in the plasma of early universe have an entirely thermal distribution because of frequent interaction with charged particles. The interaction between photons and charged particles continues until the so-called recombination, when the universe becomes neutral at a temperature of $\sim 3000\,\mathrm{K}$, where the number of ionization photons becomes not enough. After the recombination, the photons freely propagate through the space keeping the information at the recombination, i. e. direction and the Planck distribution, except that its temperature decreases inversely proportional to the scale factor as $T(t) \propto a(t)^{-1}$.

The relic radiation was discovered by Arno Penzias and Robert Wilson in 1965 (Penzias et al. 1965) at 4.080 GHz as an isotropic and unpolarized excess noise of $3.5 \pm 1.0\,\mathrm{K_{RJ}}$ in antenna temperature. Therefore, the relic radiation is called the cosmic microwave background (CMB). Following the discovery, many experiments measured the amplitudes of the CMB at different frequencies to obtain its spectrum, and Far Infrared Absolute Spectrophotometer (FIRAS) (Mather et al. 1994) on the Cosmic Background Explorer (COBE) (Boggess et al. 1992) satellite finally measured a complete blackbody spectrum with $T_{\mathrm{CMB}} = 2.725 \pm 0.001\,\mathrm{K}$ (Fixsen et al. 2002, and see also Figure 1.1.2). From this temperature, the density parameter of photons is determined as $\Omega_\gamma h^2 = 2.47 \times 10^{-5}$, and the density parameter of baryons can be constrained as $0.018 \leqslant \Omega_b h^2 \leqslant 0.027$ from Eq. (1.1.5), where $h \equiv H_0/(100\,\mathrm{km\,s^{-1}\,Mpc^{-1}})$ is the reduced Hubble constant.

In the actual universe, there are many kinds of structures, e.g. galaxy clusters, galaxies, and stars, which are considered to be generated from some initial density perturbations by gravitational instability (Rees et al. 1968). In particular, distribution of galaxies, so-called large-scale structure (LSS), stores information of the initial perturbations and evolution of the universe, thus allowing us to extract cosmological parameters. The existence of the LSS has been revealed by redshift surveys, e.g. Center for Astrophysics (CfA) (Davis et al. 1982) in the 1990s. On the other hand, the initial density perturbations, which must be observed as temperature anisotropies on the CMB, were found to be too small to create the LSS if matter

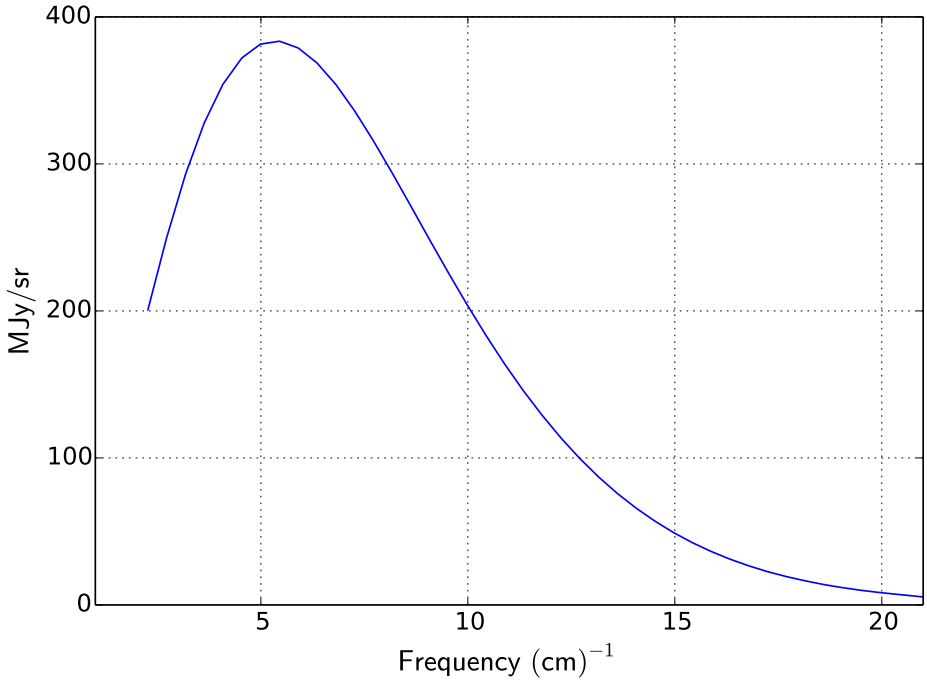

Figure 1.1.2: Measurement of the spectrum of the CMB with the FIRAS (Fixsen et al. 1996).

consists of baryons. To solve the problem, an additional content of matter, the so-called dark matter, was introduced into the cosmology. The dark matter is assumed to have no interaction or very weak interaction with normal matters and photons except gravitational interaction, and its existence was indicated by e.g. rotation curve of a galaxy (Rubin et al. 1980). It was found that, in particular, the cold dark matter (CDM), whose mass is sufficiently large to be non-relativistic during the hot Big Bang Universe, can produce sufficient growth of density perturbations, where the density parameter $\Omega_{\mathrm{CDM}} \sim 0.2$ is suggested (Davis et al. 1985).

Furthermore, improvements of galaxy surveys in the distance also revealed the existence of cosmological constant (or dark energy) in the 2000s. One of the important observations was a measurement of Hubble's law up to high-redshift ($z \sim 1$) using type-Ia supernovae (Riess et al. 1998; Perlmutter et al. 1999). As the Hubble parameter represents the velocity of cosmic expansion, the deceleration parameter of expansion can be defined as $q(t) \equiv -a(t)\left(\frac{d^2a(t)}{dt^2}\right)/\left(\frac{da(t)}{dt}\right)^2$, whose current value becomes $q_0 \equiv q(t_0) = \frac{\Omega_m}{2} - \Omega_\Lambda$. If $\Omega_\Lambda = 0$, the deceleration parameter must be positive, however, the measurement found that the q_0 is negative, i.e., the cosmic expansion is accelerating. The result thus indicated the existence of positive Ω_Λ.

Finally, the most powerful information was obtained from the measurements of anisotropies in the CMB (Figure 1.1.3). Differential Microwave Radiometer (DMR) on the COBE satellite first measured the CMB temperature anisotropy in the angular scale of $\geqslant 7^\circ$ and found that an angular power-spectrum of the anisotropy was consistent with scale-invariant spectrum with Gaussian statistics (Bennett et al. 1996). Furthermore, the Wilkinson Microwave Anisotropy Probe (WMAP) satellite measured the CMB anisotropies with the angular resolution of $\sim 0.2^\circ$, which enabled the measurement of structures from baryon acoustic oscillation (BAO) in $\sim 1^\circ$

scale. WMAP found that various features in the angular power-spectrum, such as amplitude or angular scale of peaks, can be excellently explained by the CDM theory, and determined cosmological parameters, such as density parameters: Ω_b, Ω_m, and Ω_K, with an unprecedented accuracy (Spergel et al. 2003).

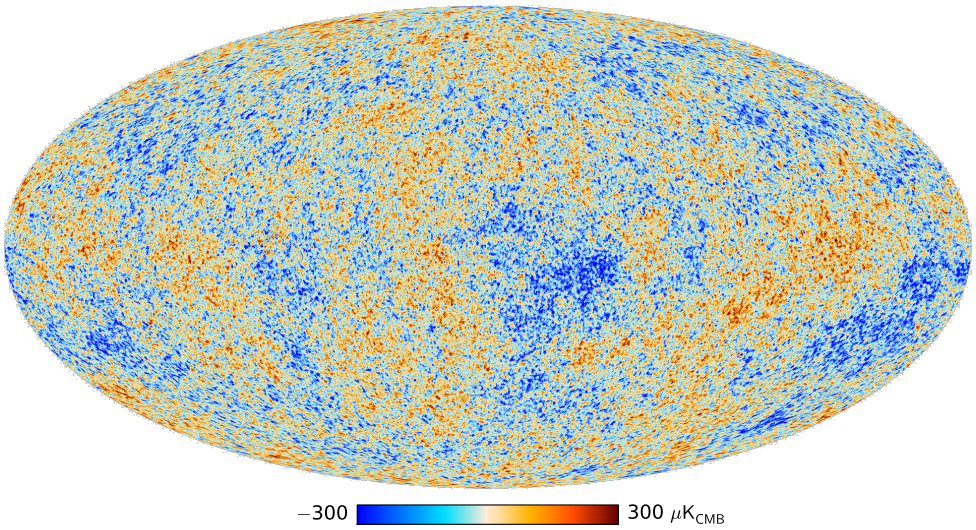

Figure 1.1.3: Measurement of the CMB anisotropy with the Planck satellite from Planck Collaboration (2016a).

The standard cosmological model, the so-called ΛCDM model, has been established eventually. Some features of the ΛCDM model are summarized as follows:

- the current universe consists of dark energy (69%), CDM (26%), and baryons (5%),[4]
- the curvature of the universe is zero,
- the initial density perturbation is adiabatic and has almost scale-invariant spectrum.

Current CMB observations and galaxy surveys have improved sensitivity and have measured higher order effects such as the anisotropy in CMB polarization and weak lensing effect from LSS, while the ΛCDM model still explains the measurements well.

1.2 INFLATION

Although the ΛCDM model explains the expansion history of the Universe and also the evolution of perturbations, such as CMB anisotropy and LSS, well, the ΛCDM model contains some unnatural conditions, which become significant when we consider the earliest epoch of the Universe. As described in the following sections, *inflation* is the most plausible scenario, which can explain the unnatural conditions.

1.2.1 *Unnaturalness in the ΛCDM model*

One of the most critical problems in the ΛCDM model is the origin of perturbations with scale-invariant spectrum. In the ΛCDM model, the initial condition of perturbations is introduced by hand, but there must be a physical process to produce the perturbations in the

4 Planck Collaboration et al. (2016c)

real Universe. The ΛCDM model cannot answer what the process is. Furthermore, there is a fundamental problem from causality, the so-called *horizon problem*. Since the propagation of information must not exceed the speed of light, the coherent scale of perturbations produced by the physical process must be smaller than the causal horizon at that time. In the universe dominated by relativistic particles, the causal horizon monotonically increases as $\frac{c}{H(t)} \propto a(t)^2$; thus there is a maximum coherent scale determined by the time when the process ends, and no perturbation beyond the scale can be produced. However, the CMB anisotropy discovered by DMR showed the existence of perturbation whose coherent scale was larger than the horizon even at the recombination, where all the physical process is well-understood at the energy scale (Bennett et al. 1996).

Another problem is the curvature of the universe, which has been measured to be consistent with flat geometry by e. g. WMAP. According to Eq. (1.1.4), as the universe expands, the impact of the curvature becomes significant compared to the energy densities of radiation and matter. If we translate the observational result, the effect of curvature is still sub-dominant, into the earliest epoch of the universe, the constraints on density parameter of curvature at that time, $\Omega_K(t) = \left(\frac{H(t_0)}{a(t)H(t)}\right)^2 \Omega_K(t_0) \sim a(t)\Omega_K(t_0)$, becomes tremendously severe. If the universe has begun from a quantum fluctuation in space-time, $|\Omega_K(t)| \sim 1$ is more natural instead. This mysterious fine tuning of curvature is called the *flatness problem*.

1.2.2 *Idea of inflation*

The most plausible idea to solve the horizon problem is the inflation theory; it asserts that the Universe experienced an exponential expansion at the earliest epoch of its history.

During the inflation, the universe expands as the de Sitter universe:

$$a(t) \propto e^{H_{inf} t}, \tag{1.2.1}$$

where H_{inf} is the Hubble parameter and supposed to be almost constant during inflation. The event horizon in the comoving distance shrinks as follows:

$$\frac{c}{a(t)H_{inf}} \propto e^{-H_{inf} t}. \tag{1.2.2}$$

The two points separated by a comoving distance λ are in causal contact initially for $\lambda < \frac{c}{a(t)H_{inf}}$, but they lose communication from $\lambda > \frac{c}{a(t)H_{inf}}$ until they enter the horizon again in normal FLRW universe following the inflation.

Besides, the inflation is driven by unknown energy, i. e. the inflaton which acts as a cosmological constant whose energy density is independent of the cosmic expansion. As the Universe expands during inflation, the energy density of the inflaton exceeds that of curvature, which depends on $a^{-2}(t)$; it makes the universe flat. Then the energy of the inflaton is released into other contents excepting curvature. This is called the reheating.

The inflation theory solves both horizon problem and flatness problem. However, the inflation theory has a big problem; we do not know what is the inflaton at all. As we discuss in section 9.2.3, the expected energy scale of inflation is about 10^{16} GeV, which is much greater than the current energy scale achievable in the laboratory and we cannot obtain any information from particle physics experiments. However, cosmological observations have potential to give us the information of inflation.

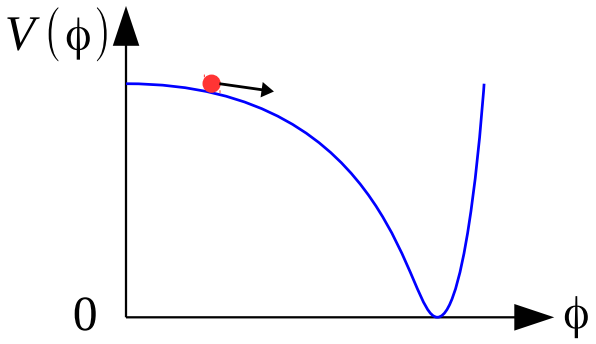

Figure 1.2.1: The illustration of a single-field slow-roll model. The blue curve shows the potential of the scalar field. The red point represents the position at a specific time, which is rolling down toward the black arrow.

1.2.3 *Single-field slow-roll model*

There are so many models of inflation, but here we review one of the most basic models, i. e. the so-called single-field slow-roll model.

In the single-field slow-roll model, we assume that the inflaton is a scalar field expressed by $\phi(t, x^i)$ with a potential energy density $V(\phi)$ as illustrated in Figure 1.2.1. In the homogeneous and isotropic universe, the energy density and pressure of the scalar field, $\rho_\phi(t)$ and $p_\phi(t)$, are obtained as

$$\begin{cases} \rho_\phi(t) = \dfrac{1}{2\hbar c^3}\dot{\phi}^2(t) + V(\phi(t)) \quad , \\ p_\phi(t) = \dfrac{1}{2\hbar c^3}\dot{\phi}^2(t) - V(\phi(t)) \quad , \end{cases} \tag{1.2.3}$$

where $\dot{\phi}(t) \equiv \frac{d\phi(t)}{dt}$. If the total energy density of the universe is dominated by the scalar field, the expansion of the universe, Eq. (1.1.3), is determined as

$$H^2(t) = \frac{1}{3M_{Pl}^2c^4}\left[\frac{1}{2}\dot{\phi}^2(t) + \hbar c^3 V(\phi(t))\right] \quad , \tag{1.2.4}$$

where $M_{Pl} \equiv \left(\frac{\hbar c}{8\pi G}\right)^{1/2} = 2.435 \times 10^{18}\,\mathrm{GeV}/c^2$ is the reduced Planck mass. The scalar field also evolves as the equation of motion,

$$\ddot{\phi}(t) + 3H(t)\dot{\phi}(t) + \hbar c^3 V'(\phi(t)) = 0 \quad , \tag{1.2.5}$$

where $\ddot{\phi}(t) \equiv \frac{d^2\phi(t)}{dt^2}$ and $V'(\phi) = \frac{dV(\phi)}{d\phi}$.

In Eq. (1.2.4), if the variation of the scalar field is sufficiently slow, i. e. $\dot{\phi}(t) \sim 0$, the universe continues the exponential expansion at the rate of

$$H_{inf}(t) \approx \left(\frac{\hbar V(\phi(t))}{3M_{Pl}^2 c}\right)^{1/2} \quad ; \tag{1.2.6}$$

thus the inflation occurs. Note that, however, the Hubble parameter $H_{inf}(t)$ gradually changes due to the evolution of $\phi(t)$. The rate of the variation of the Hubble parameter can be calculated as

$$-\frac{\dot{H}(t)}{H^2(t)} \approx \frac{M_{Pl}^2c^4}{2}\left(\frac{V'(\phi(t))}{V(\phi(t))}\right)^2 \equiv \epsilon_V(t) \quad , \tag{1.2.7}$$

where $\dot{H}(t) \equiv \frac{dH(t)}{dt}$. The dimensionless parameter, $\epsilon_V(t)$ is called the first slow-roll parameter. We can also define the second slow-roll parameter as

$$\eta_V(t) \equiv M_{Pl}^2 c^4 \frac{V''(\phi(t))}{V(\phi(t))} \quad , \tag{1.2.8}$$

where $V''(\phi) = \frac{d^2V(\phi)}{d\phi^2}$. The approximations in Eqs. (1.2.6) and (1.2.7) require $|\epsilon_V(t)| \ll 1$ and $|\eta_V(t)| \ll 1$, which are called the slow-roll conditions. The inflation ends when one of the slow-roll conditions breaks.

A problem of the single-field slow-roll model is that we have hundreds of candidates for the scalar field (see e.g. Martin et al. 2014); thus we need to identify the actual one. Since each of the models has a different shape of the potential $V(\phi)$, precise measurements of the slow-roll parameters: ϵ_V and η_V, could give us some hints to select the models.

1.2.4 *Quantum fluctuation*

One of the most important features of the inflation model is the generation of the scale-free fluctuation from quantum fluctuation.

During the inflation, the physical length of the event horizon $\lambda_{phy}(t) = \frac{c}{H_{inf}}$ stays constant. On the other hand, the comoving length of the event horizon $\lambda_{com}(t) = \frac{c}{a(t)H_{inf}}$ shrinks rapidly as $a(t)$ increases exponentially. Therefore, the fluctuation with its wavelength of $\lambda_\star$ freezes at $t_\star$ when the event horizon becomes comparable, i. e. $\lambda_\star = \lambda_{com}(t_\star)$. Let us consider a small time period from $t = t_\star$ to $t = t_\star + \Delta t$. The fluctuations with the wave number from $k_\star$ to $k_\star + \Delta k$ exit the horizon during this period, where $k_\star = \frac{2\pi}{\lambda_\star}$ and $\Delta k = H_{inf} k_\star \Delta t$. Here, the energy of these fluctuations would come from the virtual energy ΔE that arises from the quantum theory. From the uncertainty principle, the virtual energy is obtained as

$$\Delta E = \frac{2\pi\hbar}{\Delta t} \quad . \tag{1.2.9}$$

On the other hand, the quantum theory also asserts that any type of fluctuation must be a quantum particle. Assuming the mass of the particle is negligible, the energy of the particle is expressed by its physical wave number as

$$\Delta E = \frac{2\pi\hbar c}{a(t_\star)\lambda_\star} = 2\pi\hbar H_{inf} \quad . \tag{1.2.10}$$

By comparing these two equations, we obtain a constraint for the period as $\Delta t = \frac{1}{H_{inf}}$, which is the same as the timescale of exponential expansion. The energy density spectrum[5] $\Delta(k)$ is obtained as

$$\Delta(k_\star) = \frac{\Delta E}{\lambda_{phy}^3} \frac{k_\star}{\Delta k} = \frac{2\pi\hbar}{c^3} H_{inf}^4 \quad . \tag{1.2.12}$$

Next, we consider specific types of fluctuations. In the adiabatic case, we can decompose the fluctuations into only three types: scalar, vector, and tensor. The amplitudes of fluctuations

5 The energy density spectrum is the logarithmic derivative of the total energy density of the fluctuation ρ with respect to the wave number as

$$\rho = \int \frac{dk}{k} \Delta(k) \quad . \tag{1.2.11}$$

longer than the horizon stay constant as the universe expands for the scalar and tensor type, but decays for the vector type. Therefore, we ignore the vector type perturbation here.

The energy density of the scalar type fluctuation is dominated by the kinetic term of the scalar field,

$$\frac{1}{\hbar c^3}\langle \delta\dot{\phi}(\vec{k})\delta\dot{\phi}(\vec{k}')\rangle = \frac{2\pi^2}{k^3}\Delta(k)\delta(\vec{k}-\vec{k}') \quad , \tag{1.2.13}$$

where $\delta\dot{\phi}(\vec{k})$ is the three-dimensional Fourier transform of the velocity of the scalar field fluctuation, $\vec{k}$ or $\vec{k}'$ is the wave number vector, and the angle bracket represents the ensemble average. Since the velocity of the scalar field is only available during the inflation, however, it is more convenient to convert the amplitude as the space-time property such as comoving curvature. The comoving curvature fluctuation, $\mathcal{R}$ is connected with the scalar field as

$$\mathcal{R}(k_\star) \approx \frac{H_{\rm inf}}{\dot{\phi}}\delta\phi(k_\star) \approx \frac{2\pi}{\dot{\phi}}\delta\dot{\phi}(k_\star) \quad , \tag{1.2.14}$$

at the horizon exiting, $t = t_\star$, assuming the sound speed of the fluctuation is same with that of light. The power spectrum of the comoving curvature fluctuation, $\mathcal{R}$, is obtained as

$$\Delta_{\mathcal{R}}(k_\star) = \left(\frac{2\pi}{\dot{\phi}}\right)^2 2\hbar c^3\Delta(k_\star) = \frac{4\pi^3\hbar^2}{M_{\rm Pl}^2c^4}\frac{H_{\rm inf}^2(t_\star)}{\epsilon_V(t_\star)} \quad . \tag{1.2.15}$$

The energy density of the tensor type fluctuation is directly expressed by a derivative of the transverse-traceless component of the metric h, i. e. the energy density of the gravitational wave, as

$$\frac{c^2}{32\pi G}\langle \dot{h}(\vec{k})\dot{h}(\vec{k}')\rangle = \frac{2\pi^2}{k^3}\Delta(k)\delta(\vec{k}-\vec{k}')\,. \tag{1.2.16}$$

What stays constant outside of the horizon is h. Therefore, the power spectrum of h is also useful, which is obtained as

$$\Delta_h(k_\star) = \left(\frac{2\pi}{H_{\rm inf}}\right)^2 \frac{32\pi G}{c^2}\Delta(k_\star) = \frac{32\pi^3\hbar^2}{M_{\rm Pl}^2c^4}H_{\rm inf}^2(t_\star) \quad . \tag{1.2.17}$$

The power spectra of those scalar- and tensor-type fluctuations give us some information about the inflation. The ratio of the amplitude of the power spectrum for the tensor type to that for the scalar type is called the tensor-to-scalar ratio and defined as

$$r(k_\star) \equiv \frac{2\Delta_h(k_\star)}{\Delta_{\mathcal{R}}(k_\star)} = 16\epsilon_V(t_\star) \quad . \tag{1.2.18}$$

Here, the factor 2 on $\Delta_h(k_\star)$ comes from the two polarizations in the tensor-type fluctuation. The gradual variation of the amplitude as a function of the wave number, i. e. the tilt of the spectrum, is also useful. The spectral indices of the scalar- and tensor-type fluctuations are usually defined as

$$n_s(k_\star) - 1 \equiv \frac{d\ln\Delta_{\mathcal{R}}(k)}{d\ln k} = 2\eta_V(t_\star) - 6\epsilon_V(t_\star) \quad , \tag{1.2.19}$$

$$n_t(k_\star) \equiv \frac{d\ln\Delta_h(k)}{d\ln k} = -2\epsilon_V(t_\star) \quad . \tag{1.2.20}$$

From measurements of these parameters for a specific wave number $k_\star$, we can obtain the slow-roll parameters at the time $t_\star$ and determine the shape of the inflaton potential $V(\phi)$.

1.3 COSMIC MICROWAVE BACKGROUND

CMB is one of the most powerful probes for observational cosmology as described in section 1.1: the black body spectrum is a concrete evidence of thermal history in the Big-Bang Universe, and the temperature anisotropy determines contents of the universe and shows the existence of super-horizon correlations. Also, there are other types of information in the CMB, e. g. polarization and spectral distortions. Here we focus on the linear polarization signal in CMB anisotropy and describe its importance as a unique probe of inflation.

1.3.1 *Stokes parameters*

We begin with polarization states of a plane wave propagating toward $+z$ direction. Since an electromagnetic wave is a transverse wave, we can take two orthogonal polarization bases; we take $\vec{e}_1 = \vec{e}_x$ and $\vec{e}_2 = \vec{e}_y$ here. The electric field of the plane wave at $z = 0$ can be expressed as

$$\vec{E}(t) = E_x(t)\vec{e}_x + E_y(t)\vec{e}_y \quad , \tag{1.3.1}$$

where $E_x(t)$ and $E_y(t)$ are the electric fields for x- and y-polarization. In the case of an ideal monochromatic wave, the electric field can be completely defined by one frequency, ν, and two complex amplitudes, (E_x, E_y), as

$$E_x(t) = \frac{1}{2}E_x \exp(i2\pi\nu t) + \frac{1}{2}E_x^* \exp(-i2\pi\nu t) \quad \text{and} \quad E_y(t) = \frac{1}{2}E_y \exp(i2\pi\nu t) + \frac{1}{2}E_y^* \exp(-i2\pi\nu t) \quad , \tag{1.3.2}$$

where the asterisk denotes the complex conjugate. The (E_x, E_y) is called the Jones vector. Alternatively, the Jones vector can be transformed into four real values, (I, Q, U, V), as

$$\begin{cases} I &= |E_x|^2 + |E_y|^2 \\ Q &= |E_x|^2 - |E_y|^2 \\ U &= E_x^* E_y + E_x E_y^* \\ V &= \frac{1}{i}(E_x^* E_y - E_x E_y^*) \end{cases} . \tag{1.3.3}$$

These parameters are called the Stokes parameters, and a set of them is called the Stokes vector (Stokes 1852). To describe the polarization state of the plane wave, Stokes parameters are more useful than the Jones vector as illustrated in Figure 1.3.1: Stokes I represents the total intensity, Q and U represent the amplitude and angle of linear polarization, and V represents the amplitude of circular polarization. Note that Stokes parameters satisfy a relation, $I^2 = Q^2 + U^2 + V^2$, in this ideal monochromatic case, and the phase information has been dropped.

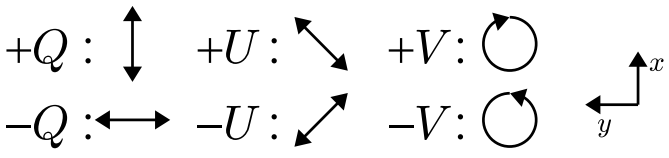

Figure 1.3.1: Illustration of Stokes parameters

However, an electromagnetic wave from an astronomical source cannot be ideally monochromatic (or coherent), because the size of an emission region is much larger than the wavelength

usually. For that reason, the Jones vector or the Stokes parameters must have a gradual time variation, but such time variation is still faster than the time-scales we are interested in. Meaningful values are the time-averaged Stokes parameters:

$$\begin{cases} I &= \langle |E_x|^2 + |E_y|^2 \rangle \\ Q &= \langle |E_x|^2 - |E_y|^2 \rangle \\ U &= \langle E_x^* E_y + E_x E_y^* \rangle \\ V &= \frac{1}{i} \langle E_x^* E_y - E_x E_y^* \rangle \end{cases} , \tag{1.3.4}$$

where the angle bracket denotes the time average. Note that Stokes parameters except I can be canceled among positive and negative values. Thus the relation between the Stokes parameters changes as $I^2 \geqslant Q^2 + U^2 + V^2$. An unpolarized signal can be expressed by a Stokes vector like $(I, 0, 0, 0)$.

Generalized expression from the monochromatic plane wave to multi-directional waves can be obtained by considering a flux of each Stokes parameter through an infinitesimal solid angle, $d\Omega$, with an infinitesimal frequency band, $d\nu$ as $\vec{S}(\vec{n}, \nu) d\Omega d\nu$, where $\vec{n}$ is a unit vector of the propagation direction. An important note is that the Stokes $Q(\vec{n}, \nu)$ and $U(\vec{n}, \nu)$ are dependent on the base $(\vec{e}_1, \vec{e}_2)(\vec{n})$. When we rotate the base to

$$(\vec{e}_1', \vec{e}_2')(\vec{n}) = (\vec{e}_1, \vec{e}_2)(\vec{n}) \begin{pmatrix} \cos\psi & \sin\psi \\ -\sin\psi & \cos\psi \end{pmatrix} ,$$

the Stokes parameters under the new base become

$$\begin{aligned} Q'(\vec{n}, \nu) &= Q(\vec{n}, \nu) \cos 2\psi - U(\vec{n}, \nu) \sin 2\psi \\ U'(\vec{n}, \nu) &= Q(\vec{n}, \nu) \sin 2\psi + U(\vec{n}, \nu) \cos 2\psi \end{aligned} . \tag{1.3.5}$$

In other words, complex sums, $P^{\pm}(\vec{n}, \nu) \equiv (Q \pm iU)(\vec{n}, \nu)$ are the spin-± 2 fields.

1.3.2 *Thomson Scattering*

Thomson scattering is the most prominent process at the final epoch before the recombination, and it is also the main process to create the polarization of the CMB (Rees 1968). Thomson scattering is caused by the dipole emission from ionized particles (mainly electrons) shaken by incident electromagnetic waves; the electric field of output wave is

$$\vec{E}_{out}(t, r, \vec{n}) = \frac{e^2}{4\pi\epsilon_0 c^2 m_e r} \vec{n} \times (\vec{n} \times \vec{E}_{in}(t - r/c)) , \tag{1.3.6}$$

where r is the distance from the scatterer, $\vec{n}$ is the direction of output wave, m_e is the electron mass, and $\vec{E}_{in}(t)$ is the incident electric field. The outer products in Eq. (1.3.6) show the anisotropy of Thomson scattering: the output wave is mainly emitted toward a direction orthogonal to the incident electric field ($\vec{n} \perp \vec{E}_{in}$), and in that case, the output electric field is parallel to the incident electric field ($\vec{E}_{out} \parallel \vec{E}_{in}$). Then we can easily find that a quadrupole anisotropy in surrounding radiation creates a linearly polarized radiation as shown in Figure 1.3.2. Therefore, the important points are how the quadrupole anisotropy is created and what kind of properties it has.

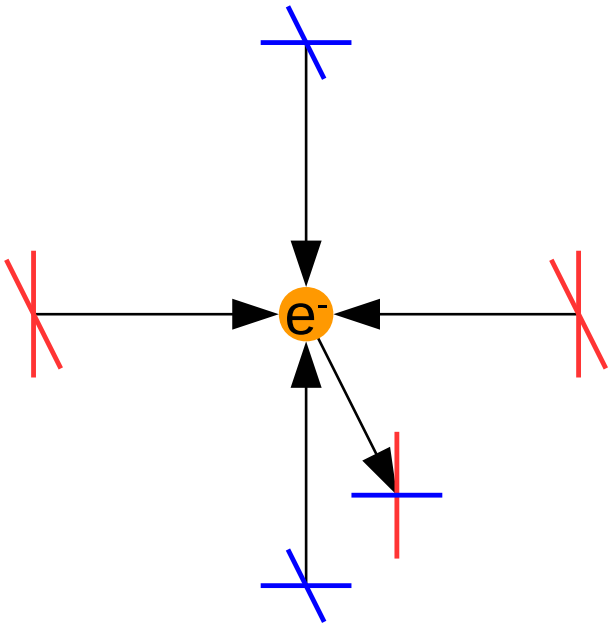

Figure 1.3.2: Illustration of creation of linear polarization from a quadrupole anisotropy via Thomson scattering by an electron.

1.3.3 *E-mode and B-mode*

The polarization signal in CMB anisotropy is observed as a projection onto the celestial sphere. Before digging into the mechanism to create the quadrupole anisotropy, here we explain the decomposition of polarization pattern. For simplicity, we consider partial sky observation and adopt the flat-sky approximation (see e. g. Hu 2000), in which the CMB anisotropy is expressed by the two-dimensional distribution as a function of $\vec{x} = (\theta\cos\phi, \theta\sin\phi)$, where $(\sin\theta\cos\phi, \sin\theta\sin\phi, \cos\phi) \equiv \vec{n}$, and z-axis is taken toward the center of the patch.

Although the CMB anisotropy generated by the initial perturbation from the inflation is random, its statistical information can be extracted from the averaged power of two-dimensional Fourier modes, i. e. angular power spectrum. As any two-dimensional (2D) vector field can be decomposed into a divergent component and a rotational component, the distribution of linear polarization expressed by $Q(\vec{x})$ and $U(\vec{x})$ is decomposed into two modes independent of each other. Due to the spin-2 nature of linear polarization, the decomposition is expressed by second order derivative of two scalar fields, so-called E- and B-modes, as

$$\begin{aligned} Q(\vec{x}) + iU(\vec{x}) &= (\eth_x + i\eth_y)^2(E(\vec{x}) + iB(\vec{x})) \\ &= (\eth_x^2 - \eth_y^2)E(\vec{x}) - 2\eth_x\eth_y B(\vec{x}) + i[2\eth_x\eth_y E(\vec{x}) + (\eth_x^2 - \eth_y^2)B(\vec{x})] \quad . \end{aligned} \tag{1.3.7}$$

Here $\eth_\bullet$ is a differential operator acting on a scalar function $f(\vec{x})$ as $\eth_\bullet f(\vec{x}) = \int \frac{d\vec{\ell}}{2\pi} f(\vec{\ell}) \frac{\ell_\bullet}{\ell} e^{i\vec{\ell}\cdot\vec{x}}$ for $\bullet = \{x, y\}$, where $f(\vec{\ell})$ is the Fourier transform of $f(\vec{x})$ and $\ell \equiv |\vec{\ell}|$. Angular power spectra of E- and B-modes, C_ℓ^{EE} and C_ℓ^{BB}, are then obtained as

$$\langle E^*(\vec{\ell}')E(\vec{\ell})\rangle = C_\ell^{EE}\delta(\vec{\ell} - \vec{\ell}') \quad \text{and} \quad \langle B^*(\vec{\ell}')B(\vec{\ell})\rangle = C_\ell^{BB}\delta(\vec{\ell} - \vec{\ell}') \quad , \tag{1.3.8}$$

where $E(\vec{\ell})$ and $B(\vec{\ell})$ are the Fourier transforms of $E(\vec{x})$ and $B(\vec{x})$, the angle brackets denote the ensemble average, and $\delta(\vec{\ell} - \vec{\ell}')$ is the delta function.

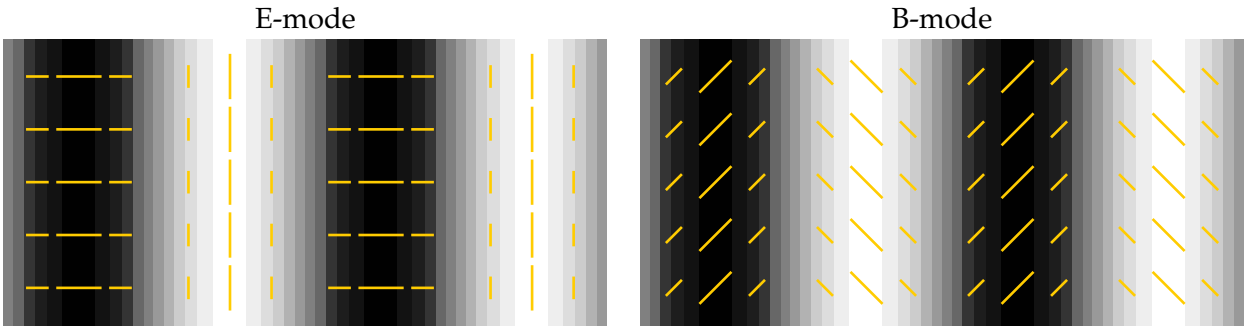

Figure 1.3.3: Illustrations of the E-mode and B-mode. The yellow lines represent the amplitudes and angles of the polarization signals. The grayscale shows the Stokes Q polarization for the E-mode or the Stokes U polarization for the B-mode.

Schematics of E-mode and B-mode for the case of a single Fourier mode with $\vec{\ell} = (\ell_x, 0)$ are shown in Figure 1.3.3, where $E(\vec{x})$ or $B(\vec{x})$ field is shown as grayscale and the polarization patterns are shown by yellow lines, whose angle and length represent polarization angle and amplitude, respectively. Note that the parity of polarization pattern is even for the E-mode and odd for the B-mode.

1.3.4 *CMB polarization from initial perturbations*

Now we consider the mechanisms to create the quadrupole anisotropy and CMB polarization from the initial perturbations from the inflation and derive an important property of CMB polarization that the scalar-type perturbation creates only the E-mode polarization but the tensor one creates both the E- and B-modes.

The smallness of initial perturbations observed by the CMB anisotropy as $\sim 10^{-5}$ ensures us to treat the problem as linear perturbations, in which the perturbations can be considered as the superposition of plane waves. Here we pick up one of the plane waves with a wave-number vector of $\vec{k}$.

The scalar-type perturbation is intrinsically a sound wave in the photon-baryon fluid in the early universe; thus there are compressing and expanding regions. In compressing regions, the energy of photons entering the region increases due to Doppler effect along a direction parallel to $\vec{k}$, but does not change for the other directions. Then, linear polarization perpendicular to the propagation direction, $\vec{k}$, is created. In expanding regions, on the other hand, the energy of photons decreases along a direction parallel to $\vec{k}$, and resulting polarization is parallel to $\vec{k}$. Since the polarization pattern has even parity in both the cases, the scalar-type perturbation creates only the E-mode as illustrated in Figure 1.3.4. By comparing with Figure 1.3.3, we can also find that the E-mode is derivative of the density or velocity distribution.

The tensor-type perturbation is equivalent to a gravitational wave (GW), which is a transverse wave of distortions in space-time. The GW creates quadrupole relative velocity between neighborhoods on the transverse plane. Photons moving in space receive the Doppler effect, which produces quadrupole red- and blue-shift anisotropy and resulting linear polarization. The GW has two polarizations, so-called $+$-polarization and $\times$-polarization, and the latter polarization can create B-mode as illustrated in Figure 1.3.5, where the $\times$-polarization GW

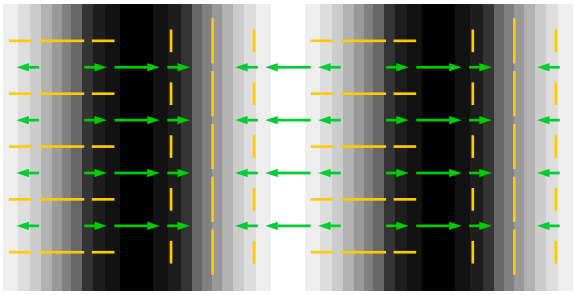

Figure 1.3.4: E-mode polarization generation from scalar-type perturbation propagating rightward. The density of photon-baryon fluid is shown as background gradation, the velocity of the fluid is shown as green arrows, and polarization is shown as yellow lines.

interacting with the last scattering surface with a slant incidence angle is shown. The spatial relations among the propagation direction, the polarization of the GW, and the slant incidence break parity symmetry, thus the parity-odd B-mode is generated.

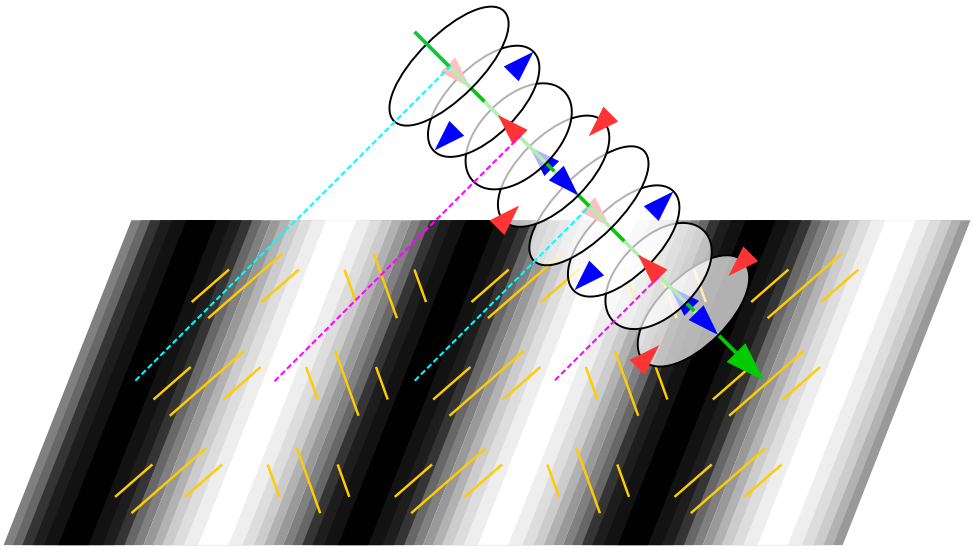

Figure 1.3.5: B-mode polarization generation from a GW. The GW is propagating toward the green arrow. The spacial distortion due to the GW is shown as the series of ellipses. The red or blue arrowheads represent the relative velocity due to the spacial distortion, which causes the blue-shift or red-shift. The last scattering surface is shown as the parallelogram, and the gradation represents the phase of the spacial distortion on the surface. The polarization patterns projected on the surface are shown as yellow lines.

Although the signals from the scalar-type perturbation are more prominent than those from the tensor for many cases, e. g. temperature and E-mode anisotropies in the CMB (see Figure 1.3.6), the absence of the B-mode generation from the scalar perturbation makes the B-mode as a unique and powerful probe of the tensor-type perturbation.

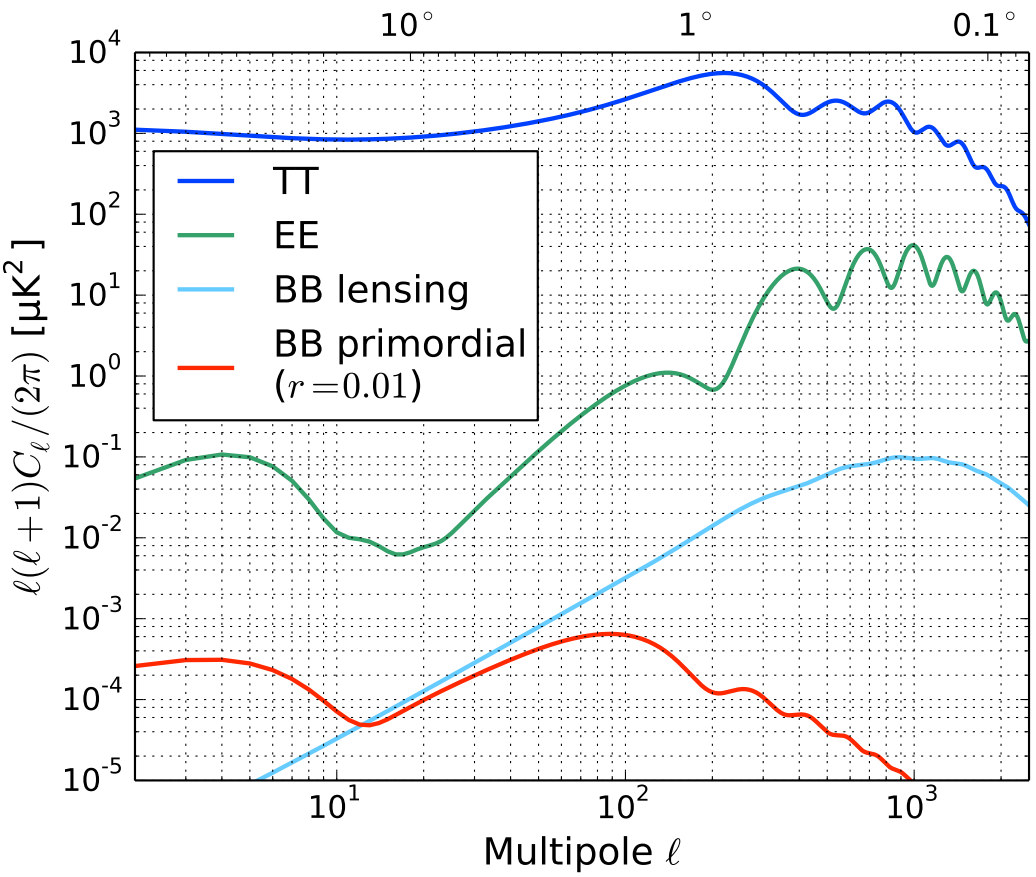

Figure 1.3.6: Angular power-spectra of the CMB anisotropies calculated from the ΛCDM model. The blue, green, cyan, and red curves correspond to the temperature, E-mode, lensing B-mode, and primordial B-mode, respectively. Here, the Cosmic Linear Anisotropy Solving System (CLASS) (Blas et al. 2011) is used for the calculation.

1.3.5 *Gravitational lensing*

The scalar-type perturbation does not create the B-mode originally as described in the last section; however, gravitational lensing effect of LSS distorts the path of the CMB photon during propagation to us. As shown in Figure 1.3.7, the signal that originally comes from the $\vec{n}$ direction is projected to a different direction, $\vec{n}'$ by

$$\vec{n}' = \vec{n} + \vec{d}(\vec{n}) \quad . \tag{1.3.9}$$

Here, the displacement vector is obtained by an integral of the gravitational potential gradient as

$$\vec{d}(\vec{n}) = -\frac{2}{c^2}\int_0^{r_{rec}} dr\, \frac{r_{rec}-r}{r_{rec}} \nabla_\perp \Phi(r\vec{n}; t) \quad , \tag{1.3.10}$$

where r_{rec} is the comoving distance of the last scattering surface at the recombination, $\nabla_\perp$ is a gradient tangential to $\vec{n}$, and $\Phi(r\vec{n}; t)$ is the gravitational potential at the position $r\vec{n}$ when the light passed. For later convenience, we can define a so-called lensing potential $\phi(\vec{n})$ as

$$\vec{d}(\vec{n}) = \nabla\phi(\vec{n}) \quad , \tag{1.3.11}$$

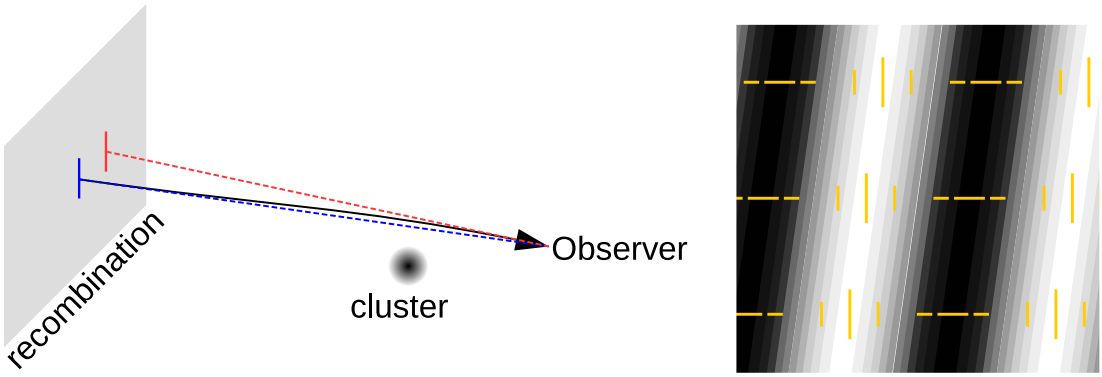

Figure 1.3.7: The left figure illustrates the gravitational lensing effect. Here, the propagation path of the CMB photon from the last scattering surface (the black arrow) is distorted by the cluster, which remaps the position of the signal from blue to red. If the remapping breaks the alignment between the polarization directions (the yellow lines) and patterns (the gradation) in the E-mode anisotropy, the B-mode is created as shown in the right figure.

and also second order distortion parameters

$$\begin{cases} \kappa(\vec{n}) = \dfrac{1}{2}\Delta\phi(\vec{n}) \quad , \\ \gamma_1(\vec{n}) = \dfrac{1}{2}(\partial_x^2 - \partial_y^2)\phi(\vec{n}) \quad , \\ \gamma_2(\vec{n}) = \partial_x\partial_y\phi(\vec{n}) \quad , \end{cases} \tag{1.3.12}$$

where $\kappa(\vec{n})$ is called *convergence*, and $\gamma_1(\vec{n})$ and $\gamma_2(\vec{n})$ are called *shears*. Note that the convergence is related to the density distribution of LSS like the Poisson equation.

The right panel of Figure 1.3.7 illustrates how the gravitational lensing creates the B-mode from the E-mode. Here the E-mode-like vertical and horizontal polarization patterns are shown as yellow lines. Note that the angle of polarization is the same as the original distribution as shown in Figure 1.3.3, but their positions are changed, where the upper part is shifted rightward while the lower part is shifted leftward. Then, the direction of polarization pattern wave changes from horizontal as shown by the black-and-white gradation. As a result, the B-mode component emerges for the new polarization pattern wave.

Because of this mechanism, the scalar-type perturbation also creates a B-mode, so-called lensing B-mode, as contamination from the E-mode. The angular power-spectrum of this lensing B-mode signal is also shown in Figure 1.3.6, which has a peak at a sub-degree scale ($\ell \sim 1000$), compared to the primordial B-mode from the tensor-type perturbation which has a peak at a degree scale ($\ell \sim 100$). The amplitude of the power spectrum of the lensing B-mode is well constrained from observations of temperature and E-mode anisotropies in the CMB though there are some uncertainties from e. g. the reionization history and neutrino masses. On the other hand, there is no clue for the amplitude of the primordial B-mode except the upper limits. If the tensor-to-scalar ratio, r, is less than ~ 0.01, the primordial B-mode

is completely covered by the lensing B-mode,[6] and we need to remove the lensing B-mode to measure the primordial B-mode. The method is called *delensing*.

1.4 CMB EXPERIMENTS

As described in the previous sections, the CMB is one of the most powerful probes in cosmology. Information of the CMB can be expressed by its spectrum and anisotropy. The former is also important to understand the history of the early universe, however, here, we focus on the CMB anisotropy.[7] Because of polarization states of the CMB radiation as described in section 1.3.1, CMB anisotropy still contains three types of information. Anisotropy in the unpolarized component is represented as temperature anisotropy, and anisotropy in the linear polarization component is decomposed into E-mode and B-mode as described in section 1.3.3. Note that amplitude of anisotropy is orders of magnitude different among these three types of information (see Figure 1.3.6). The small amplitude of the B-mode anisotropy makes its measurement difficult regarding both the statistical sensitivity and the systematic error due to instrumental contamination of the other anisotropies.

In this section, we introduce basics of CMB observation and calculate the statistical uncertainty for angular power spectrum measurements. Then, we consider non-idealities in instruments and find how the systematic error from temperature and E-mode anisotropies pollute the B-mode.

1.4.1 *Instruments for CMB observation*

To observe the CMB anisotropy, we point a telescope at specific direction; the telescope collects the photons from the direction and transfers the energy into a detector, which converts the power into an electrical signal to be stored. Because of the existence of many photons other than CMB, we additionally need a band-pass filter defining an observing frequency band where the CMB becomes dominant. Therefore, a CMB experiment could be characterized by the three properties: the size of the telescope, the sensitivity of the detector, and the observing frequency band(s).

First, we consider the observing frequency band. Because the black-body spectrum has broad continuous shape, the frequency band should be as wide as possible to minimize the Poisson noise of the CMB photons. For ground-based CMB experiments, however, there are strong atmospheric absorption/emission lines at 60 and 119 GHz by O_2 molecules and 183 GHz by H_2O molecules as shown in Figure 1.4.1. To avoid these lines, ground-based CMB experiments need to use several windows: below 50 GHz, 70-110 GHz, 130-170 GHz, and above 200 GHz.[8] Balloon-borne experiments have fewer constraints from the atmospheric absorption/emission, and satellite experiments can arbitrarily choose the observing frequency band.

Other obstacles for CMB observations are signals from Galactic astrophysical sources, so-called Galactic foregrounds, which are categorized by emission mechanisms, namely syn-

6 In the largest angular scales ($\ell \lesssim 10$), the primordial B-mode could surpass the lensing B-mode even with $r \sim 0.01$. However, observing the signal with ground-based experiments would be difficult because of the limitation of observable sky area.

7 Thus, we assume the spectrum is the black body spectrum with a small variation in its temperature for each direction and polarization.

8 However, the continuum absorption and emission by H_2O molecules rapidly degrade the sensitivity.

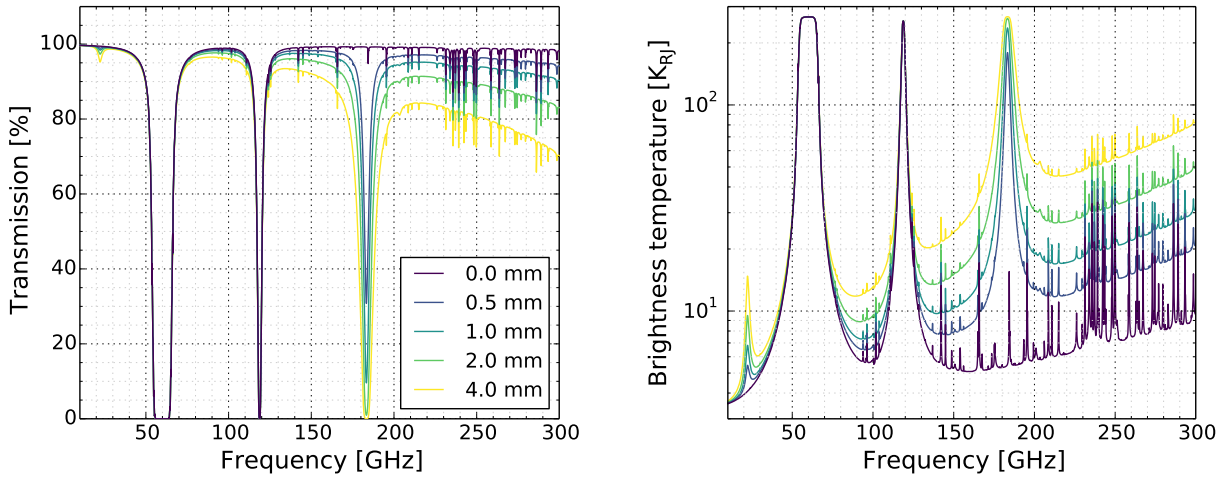

Figure 1.4.1: Spectra of transmission and brightness temperature of zenith angle at Chile for conditions of precipitable water vapor (PWV) = 0.0, 0.5, 1.0, 2.0, and 4.0 mm.

chrotron, bremsstrahlung (free-free), thermal emission from dust, emission from spinning dust with an electric dipole moment, and CO rotational transition lines (115, 230, and 345 GHz). Each foreground component has a different emission spectrum, and among those synchrotron emission and thermal emission from dust are expected to be polarized, thus contaminants for polarization measurements. Figure 1.4.2 shows root-mean-square (RMS)($= \sqrt{\sum (2\ell+1) C_\ell}$) of angular anisotropies of those foregrounds for unpolarized (temperature) signal and polarized signal as a function of microwave frequency, compared to those of CMB anisotropy. We find that the CMB temperature anisotropy is prominent only around 80 GHz.[9] The CMB polarization anisotropy is covered by both the synchrotron and thermal dust emission, but the RMS of foregrounds also takes minimum around 80 GHz. For that reason, observing with $\sim$ 80 GHz band is efficient for CMB measurements. However, lower and higher frequency observations are also necessary for foreground removal using the difference in frequency dependence between CMB and foregrounds. Note that it might be possible to minimize the necessity of foreground removal by observing a clean sky region where foregrounds are small.

When the observing frequency is determined, the telescope size is also determined by a required resolution for targeting signal. Because of diffraction, a telescope inevitably observes the sky convolved with a beam pattern, whose full width at half maximum (FWHM) is obtained as $\theta_{\mathrm{FWHM}} \sim \frac{\lambda}{D}$ for a diffraction-limited optical system, where λ is the wavelength of observing microwave and D is the aperture diameter of the telescope. Since structures with angular scale smaller than the θ_{FWHM} blur, we lose sensitivity to the signal exponentially. For primordial B-mode measurements (see Figure 1.3.6), the important multipole range is $\ell \lesssim 100$, which requires $\theta_{\mathrm{FWHM}} \lesssim \frac{180^\circ}{100} = 1.8^\circ$ and $D \geqslant 12$ cm for 80 GHz. For lensing B-mode measurements, we need to probe up to multipole $\ell \sim 1000$, which corresponds to 0.18°, thus the required aperture diameter is $D \geqslant 1.2$ m.

9 Note that this is for temperature anisotropy. The total flux is completely dominated by the CMB.

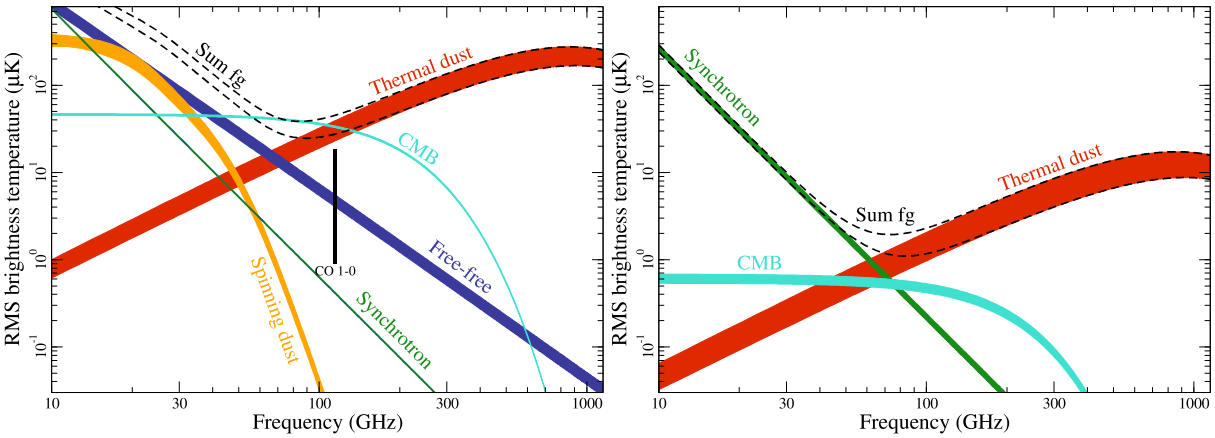

Figure 1.4.2: Spectra of foregrounds from Planck Collaboration (2016a).

High-sensitivity (or low-noise) detectors are another important feature of the experiment. A single-polarization-sensitive detector measures half of energy flux into the telescope from the sky, which can be expressed as

$$P_{\rm opt}(\vec{n}) \approx \frac{1}{2} \cdot \eta \cdot I(\vec{n}) \cdot A \cdot \Omega \cdot \Delta\nu \quad , \tag{1.4.1}$$

where η is the total efficiency including both from optical and microwave circuit, $I(\vec{n})$ is the intensity from the sky, A is the area of the telescope aperture, Ω is the solid angle of the beam, and $\Delta\nu$ is the bandwidth. Expressing the intensity in terms of brightness temperature as $I(\vec{n}) \equiv \frac{2\nu^2 k_B T_{\rm RJ}(\vec{n})}{c^2}$ and assuming the diffraction-limited optics as $A\Omega \sim \lambda^2$, we can simplify the equation as

$$P_{\rm opt}(\vec{n}) \approx \eta\Delta\nu \cdot k_B T_{\rm RJ}(\vec{n}) \quad , \tag{1.4.2}$$

where k_B is the Boltzmann constant. If we know the coefficient, $k_B\eta\Delta\nu$, by a specific absolute responsivity calibration, we can obtain the brightness temperature of the sky, $T_{\rm RJ}(\vec{n})$.[10]

Let us consider the noise of this measurement. A practical detector must have noise, thus measured samples $P_{\rm opt}^{(i)}(\vec{n})$, where i is an index of each sample, have a standard deviation of σ. The best estimation is obtained as an average of $P_{\rm opt}^{(i)}(\vec{n})$, whose uncertainty improves as $\sigma/\sqrt{N}$, i. e. as increasing the total number of samples N. Because N must be proportional to time, uncertainty in a unit time observation is a good measure of sensitivity. An instantaneous sensitivity in power, so-called noise equivalent power (NEP), is then defined as

$$\mathrm{NEP} = \sigma\sqrt{\Delta t} \quad , \tag{1.4.3}$$

where Δt is the sampling period. Using the conversion factor from power to brightness temperature, we can also define an instantaneous sensitivity in temperature, so-called noise equivalent temperature (NET). In practice, the NEP is obtained as a quadratic sum of contributions from several noise sources. Among those, shot noise of photons, so-called photon noise, gives us a fundamental limit of sensitivity. NEP of photon noise is obtained as (Richards 1994)

$$\mathrm{NEP}_\gamma^2 = 2h\nu P_{\rm opt} + \frac{2P_{\rm opt}^2}{\Delta\nu} \quad , \tag{1.4.4}$$

10 Conversion from brightness temperature to CMB temperature is well-defined using the temperature of the CMB which is precisely measured as 2.725 K by FIRAS.

where the first term comes from Poisson statistics, and the second term comes from bunching of photons. In terms of NET, we obtain

$$\mathrm{NET}_\gamma^2 = \frac{2h\nu T_{\mathrm{RJ}}}{\eta \Delta\nu k_{\mathrm{B}}} + \frac{2T_{\mathrm{RJ}}^2}{\Delta\nu} \quad . \tag{1.4.5}$$

For example, typical values for ground-based experiments, $\eta = 40\%$, $\nu = 150\,\mathrm{GHz}$, $\Delta\nu = 30\,\mathrm{GHz}$ and $T_{\mathrm{RJ}} = 33\,\mathrm{K_{RJ}}$,[11] yield $\mathrm{NET}_\gamma = 0.33\,\mathrm{mK_{RJ}}\sqrt{\mathrm{s}}$. State-of-the-art detector technology[12] has enabled a single detector to achieve this photon-noise-limited sensitivity. Therefore, to improve the total sensitivity of the experiment, we need to increase the number of detectors with a larger focal plane. A measurement with N_{det} detectors is equivalent to N_{det} times measurements with a single detector. Thus the total array sensitivity scales as $\propto N_{\mathrm{det}}^{-1/2}$ of NET for a single detector if the noise is uncorrelated among detectors.

1.4.2 *Observation and statistical uncertainties*

Next, we consider observation strategy of a CMB experiment. We first introduce scan strategy, then calculate map depth, and finally estimate uncertainty in the angular power-spectrum measurements.

In the previous section, we considered a stationary observation at the same orientation $\vec{n}$. For anisotropy measurements, however, we are interested in the variation between different sky directions, which can be obtained by rapidly comparing a value for a direction $\vec{n}$ with that for another direction $\vec{n}'$ using the same detector. If we continuously move the telescope in one direction (scan), we can perform the comparison between neighboring directions continuously. Then, the 2D anisotropy is traced into a one-dimensional time-ordered data (TOD), i.e., a signal from a structure with an angular scale of θ appears at a frequency of $\frac{\nu}{\theta}$ when the scan velocity is ν. The scan direction is usually chosen as azimuthal direction for keeping the loading from the atmosphere as stable as possible. We also limit the scanning azimuth range and move the telescope back and forth with turnarounds between them. With this azimuthal scan, a detector can only observe a line on the sky; however, thanks to the diurnal sky rotation, the position of the line on the sky moves gradually along the right ascension (RA) direction, and the detector can finally observe a certain region of the sky.

The solid angle of the observation region (patch size hereafter) is one of the most important parameters, which is directly related to science outcomes of the CMB experiment. First, the largest observable angular scale is constrained by the patch size. The relation between the lowest multipole ℓ_{min} and the diameter of the patch θ is naïvely expressed as $\ell_{\mathrm{min}} \sim \frac{2\pi}{\theta}$, thus, for example, θ must be larger than 9° to measure $\ell_{\mathrm{min}} \sim 40$. Next, the number of observable modes, which are the Fourier modes with the same norm $|\vec{\ell}|$ but the different direction, is proportional to the patch size. Since we can observe only one realization of CMB anisotropy in the real universe, we inevitably have Poisson noise in the estimation of angular power-spectrum, which is the so-called cosmic variance or sample variance. If the statistical uncertainty becomes below this sample variance, we need to increase the number of modes to reduce the sample variance. Finally, the uncertainty of the anisotropy map per unit solid angle, so-called

11 Loading contribution from the sky (atmosphere and CMB) is $12\,\mathrm{K_{RJ}}$, and that from the instrument is $21\,\mathrm{K_{RJ}}$.
12 E. g. transition-edge sensor (TES) bolometers. See Appendix A.1.

map depth, is proportional to the square root of the patch size. Assuming that the region is scanned uniformly, the map depth for temperature anisotropy is obtained as

$$w_T^{-1/2} = \mathrm{NET}\sqrt{\frac{4\pi f_{sky}}{t_{obs}}} \quad , \tag{1.4.6}$$

where NET is the instantaneous array sensitivity, t_{obs} is the total observation time, and $4\pi f_{sky}$ is the patch size. The map depth for polarization (Q or U) anisotropy map, $w_P^{-1/2}$, is usually $\sqrt{2}$ times larger than that for temperature. A better map depth becomes necessary in some analysis: e. g. map-based foreground removal, de-lensing, etc.

The angular power-spectrum is estimated from the two-dimensional Fourier transform of the observed anisotropy map as described in section 1.3.3. However, there is uncertainty in the angular power-spectrum due to the noise in the map and the sample variance described above. The statistical uncertainty per single Fourier mode, N_ℓ, can be expressed by square of the map depth $w^{-1/2}$ as

$$N_\ell = w^{-1} \cdot e^{\ell(\ell+1)\sigma_b^2} \quad , \tag{1.4.7}$$

where the exponential term represents the degradation of sensitivity due to resolution assuming a Gaussian beam with $\sigma_b = \theta_{FWHM}/\sqrt{8\ln 2}$. For the uncertainty of angular power-spectrum, we can improve the uncertainty by averaging among Fourier modes as

$$\Delta C_\ell = \sqrt{\frac{2}{(2\ell+1)f_{sky}}}(C_\ell + N_\ell) \quad , \tag{1.4.8}$$

where $(2\ell+1)f_{sky}$ is the approximate number of modes for the multipole ℓ, and the C_ℓ term in the bracket represents the sample variance. Note that ΔC_ℓ has a minimum with respect to the f_{sky}, which is important to determine the observation strategy of the CMB experiment.

1.4.3 *Challenges in practical experiments*

In practice, there are many obstacles both inside and outside of the instruments, which could degrade the ideal performance expected in the previous section and cause bias in the measured angular power-spectrum. Such non-idealities can easily obscure the faint signal of B-mode anisotropy as shown in Figure 1.3.6. Hence controlling them is one of the biggest challenges for the CMB experiments.

In this section, we briefly introduce the obstacles and discuss the possible effects on the angular power-spectrum measurements. We explain instrumental effects first and then describe extraterrestrial effects.

1.4.3.1 *Instrumental imperfections*

As described in section 1.4.1, instruments of a CMB experiment can be characterized by the observing frequency band (bandpass), the beam pattern, the detector responsivity, and the detector noise. Additionally, the angle of the linear-polarization-sensitive detector becomes important for polarization measurements. Although we design the instruments to optimize the sensitivity, the properties could often vary from the design due to manufacturing accuracy. We can calibrate the actual properties somewhat in the laboratory or during the observation. However, uncertainties of the calibrations could be introduced into the uncertainty of the

angular power-spectrum. Besides some unchanging properties could cause systematic biases in the B-mode angular power-spectrum by contaminating signals with temperature and E-mode CMB anisotropies.

Low-frequency noise (1/f noise) In section 1.4.1, we implicitly considered a white noise which is uncorrelated in time. The fundamental noises, e. g. photon noise, naturally have this property and Gaussianity moreover. In practice, however, a timestream of data of a detector usually has a correlation in time due to gradual variations in environments surrounding the detector, e. g. the loading from the atmosphere and temperature of the instruments, which appears at low-frequencies, thus degrades the sensitivity for large-angular scales. In addition, signals correlated with scans, e. g. the pick up of the ground structure due to the primary-mirror spillover and that of Earth's magnetism, would create spurious large-angular structures in the map. The noise increase can be included in the noise power spectrum, N_ℓ, and usually modeled with a power-law spectrum as

$$N'_\ell = \left[1 + \left(\frac{\ell_{\rm knee}}{\ell}\right)^\alpha\right] N_\ell \quad , \tag{1.4.9}$$

where the knee multipole $\ell_{\rm knee}$ is the multipole where the contribution from the low-frequency noise becomes comparable with that from the white noise, and α is the index of the power law. The low-frequency noise is also called $1/f$ noise from the shape of this formula.

Responsivity The signal from the sky is eventually converted into an electrical signal or even a digital signal; thus we need to revert the transfer to obtain the original signal. Assuming linearity of the detector, this process can be done simply by multiplying a single coefficient, i.e., a responsivity. The responsivity can be calibrated by comparing the detector signal and a known amplitude of the signal from a reference calibrator, which can be any of an artificial thermal source, the atmospheric emission, a bright astrophysical source such as planets, or even the CMB temperature anisotropy).[13] If C_ℓ is not zero,[14] the uncertainty of the responsivity calibration causes the uncertainty for the angular power-spectrum as

$$\Delta C_\ell = 2\frac{\Delta g}{g} C_\ell \quad , \tag{1.4.10}$$

where $\frac{\Delta g}{g}$ is the fractional uncertainty of the responsivity, and the factor 2 comes from a square nature of the power spectrum.

Beam There are two types of imperfections related to the beam: one is the deviation from the Gaussian beam assumed in section 1.4.2, and the other is the leakage from the intensity (unpolarized) signal to polarization signals. The former causes the uncertainty similar to that from the responsivity calibration uncertainty, and the latter causes bias in the (E- and) B-mode angular power-spectrum by contaminating signals with temperature anisotropies.

The beam pattern can be calibrated by scanning around a bright point-like source such as planets, whose solid angle is sufficiently smaller than the beam. The beam pattern is intrinsically different for each detector at the different position on the focal plane due to the

13 Since each method has pros and cons, we usually combine these methods by splitting the responsivity calibration into several relative calibration steps and the final absolute calibration step.

14 This uncertainty does not affect a rejection of the null hypothesis, but reduces a detection significance of a non-zero C_ℓ.

aberration of the optical system. Besides, polarization asymmetry in optical elements could cause a difference of the beam pattern between orthogonal polarization-sensitive detector pair in the same position. Since each sky pixel is observed by many detectors, however, we usually consider an effective beam averaged among detectors. Additionally, if we observe the sky with various parallactic angles,[15] the effective beam can be azimuthally averaged. Then, we can obtain the beam spectrum, B_ℓ, from a two-dimensional Fourier transform of the effective beam, which corresponds to $e^{\ell(\ell+1)\sigma_b^2}$ for the Gaussian beam case. Since the beam spectrum is equivalent to the responsivity degradation as a function of the multipole, the uncertainty in the beam spectrum, ΔB_ℓ, causes the uncertainty for the angular power-spectrum as

$$\Delta C_\ell = \frac{\Delta B_\ell}{B_\ell} C_\ell \quad . \tag{1.4.11}$$

The above description is sufficient for the temperature anisotropy measurements, however, more detailed discussions are necessary for the polarization measurements. Here, let us consider a polarization measurement by taking a difference between an orthogonal single polarization sensitive detector pair at the same position. If the detectors have identical properties except polarization, we can measure a pure single linear polarization, Stokes Q or U, without any contamination from Stokes I. However, if there is a mismatch in any properties between the detectors, the intensity signal contaminates the polarization signal. We can categorize the mismatch by the beam pattern of the leakage as illustrated in Figure 1.4.3. The intensity to polarization leakage injects the variance in the CMB temperature anisotropy into polarization signals, which results in a positive bias in the polarization angular power-spectrums. Since convolution with each categorized pattern acts as a different derivative operation in the two-dimensional map, the resulting bias ΔC_ℓ has a different shape as shown in Figure 1.4.4. Note that this contamination can be somewhat mitigated by averaging among detectors with different leakage patterns, by changing the polarization angle as described below, by rotating the parallactic angle of the sky, and by subtracting the leaked intensity signal analytically.[16]

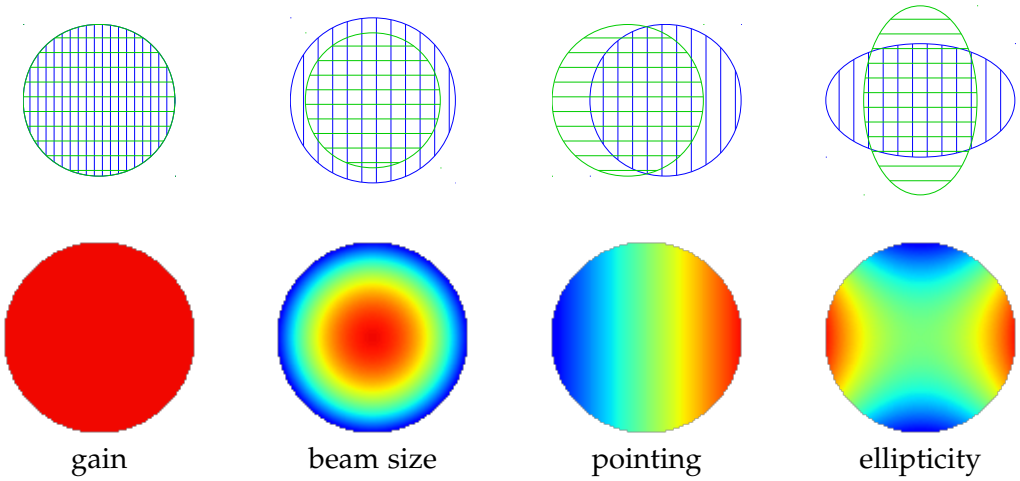

Figure 1.4.3: Differential beam systematics

15 It is not possible at the South Pole. There are some experiments which have a mechanism to rotate the entire telescope alternatively.

16 This method is called deprojection (BICEP2 Collaboration 2015).

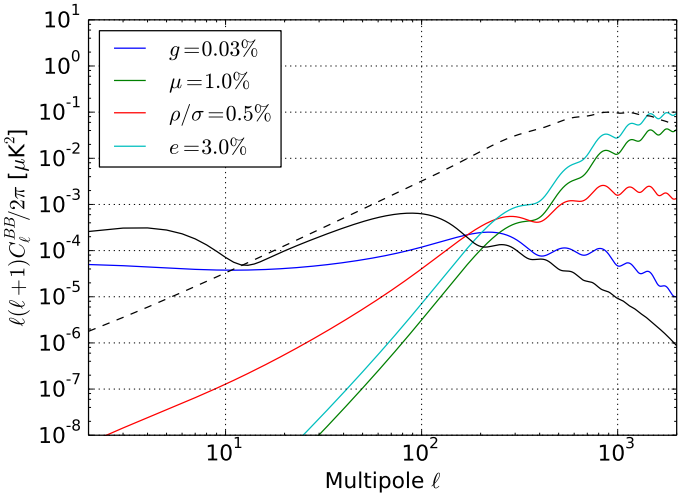

Figure 1.4.4: Possible bias in the angular power-spectrum of polarization anisotropy due to the intensity to polarization leakage. Parameters in legends are explained in Shimon et al. (2008).

Polarization angle Finally, we consider a polarization angle of a detector, which is the direction of linear polarization that the detector is sensitive to. The polarization angle is usually defined by an antenna of the detector or a wire grid above the focal plane. Additionally, to reduce some of the intensity to polarization leakage effect, some experiments have a mechanism to change the polarization angle by rotating the entire telescope or using a half-wave plate (see section 5.1). The polarization angle can be calibrated by observing a polarized source, e. g. Tau A (as known as the Crab nebula). Or, we can use CMB polarization to impose the condition of $C_\ell^{EB} = 0$, which is expected from parity conservation (Keating et al. 2013).[17] The error in the polarization angle by $\Delta\theta_{\rm det}$ contaminates the CMB E-mode angular power-spectrum into the B-mode as

$$\Delta C_\ell^{BB} = 4\Delta\theta_{\rm det}^2 C_\ell^{EE} \quad . \tag{1.4.12}$$

1.4.3.2 *Extraterrestrial contamination*

Any polarized foregrounds become contamination for the CMB polarization measurements. For the primordial B-mode measurements, even the lensing B-mode becomes an obstruction. Since these signals permanently exist, we need to remove them using specific analysis methods to mitigate their impacts.

Foregrounds We have both Galactic and extra-Galactic foregrounds: the Galactic one includes the synchrotron emission and the thermal dust emission as described in section 1.4.1, and the extra-Galactic one includes radio and dusty galaxies. Because of the distance to the source, each foreground has different angular power-spectrum as well as the emission spectrum difference shown in Figure 1.4.2. The Galactic foregrounds mainly contribute to the large-angular scale, and their angular power-spectrums are well modeled by power-law spectrum as $C_\ell \propto \ell^\alpha$ with $\alpha \sim -2.5$ (Planck Collaboration 2016b). Besides, both synchrotron and

17 With this method, however, we cannot use the average of C_ℓ^{EB} for cosmology.

thermal dust emissions have asymmetry between the E- and B-mode by $C_\ell^{BB}/C_\ell^{EE} \lesssim 0.5$. The extra-Galactic foregrounds are modeled by the randomly distributed Poisson component and the clustered component, whose angular power-spectrums have the multipole dependency with $\propto \ell^0$ and $\propto \ell^{-2.8}$, respectively (George et al. 2015).

The angular power-spectrums of the foregrounds cause positive bias in the angular power-spectrum measurements; thus we need to subtract their contributions to estimate the angular power-spectrum of the CMB anisotropy. A simple method is subtracting estimated foreground contributions, although the method could be affected by the systematic errors in the estimation due to lack of knowledge. Another method is the component separation using the measurements at different frequency bands. Let us assume a case that there is only one foreground component in addition to CMB and we have measurements with two frequencies denoted by A and B as

$$\begin{cases} C_\ell^{(A)} = C_\ell^{(CMB)} + C_\ell^{(FG)} + N_\ell^{(A)} \\ C_\ell^{(B)} = C_\ell^{(CMB)} + \alpha C_\ell^{(FG)} + N_\ell^{(B)} \end{cases}, \tag{1.4.13}$$

where $C_\ell^{(CMB)}$ and $C_\ell^{(FG)}$ are the angular power-spectrums for the CMB and foreground, respectively, α is the relative amplitude of the foreground between the frequencies, and N_ℓs represent noise of the measurements. From a linear combination of these measurements, we can remove the foreground contribution as

$$\frac{\alpha C_\ell^{(A)} - C_\ell^{(B)}}{\alpha - 1} = C_\ell^{(CMB)} + \frac{\alpha N_\ell^{(A)} + N_\ell^{(B)}}{|\alpha - 1|} \quad . \tag{1.4.14}$$

The second term represents the noise in the foreground subtracted angular power-spectrum, where we can find that improving both N_ℓs and also making α larger are important. We can consider more sophisticated methods, e. g. considering the variation of the α for each direction of the sky.

Lensing B-mode The lensing B-mode signal is one of the important targets of CMB polarization measurements, however, it also can be an obstacle to the primordial B-mode measurements. A simple method to remove the lensing B-mode is subtracting theoretical expectation as shown in Figure 1.3.6. But the sample variance of the lensing B-mode remains. Therefore, more dedicated methods, the so-called de-lensing, are proposed. In the de-lensing method, we estimate the lensing potential $\phi(\vec{n})$ and remap the observed lensed CMB anisotropy into the original unlensed positions. For estimation of the lensing potential $\phi(\vec{n})$, we can use the four-point correlation between E- and B-modes (Hu et al. 2002) or the cosmic infrared background (CIB) as a good tracer (Song et al. 2003).

2

INSTRUMENT OF THE POLARBEAR EXPERIMENT

This study is based on the data from the POLARization of Background microwave Radiation (POLARBEAR) experiment, which is one of the ground-based cosmic microwave background (CMB) experiments with a high-sensitivity polarimeter array. Here, we briefly describe the instruments of the POLARization of Background microwave Radiation (POLARBEAR) experiment.

2.1 SITE

Figure 2.1.1: Picture of the observation site of the POLARBEAR experiment. The telescope in the center is the Huan Tran telescope (HTT). There are four containers for operation and maintenance of the telescope.

The POLARBEAR experiment has a telescope, HTT, at the James Ax Observatory in Northern Chile on Cerro Toco at West longitude 67°47′10.40″, South latitude 22°57′29.03″, elevation 5,200 m. Figure 2.1.1 shows HTT and Mt. Cerro Toco.

The important property of the site is PWV, which represents the total amount of water in the air. Since water molecules absorb and emit the microwave we observe, that value is directly related to the optical heat loading into the detector, and high PWV degrades the sensitivity of the detector. The typical value of the PWV at the site is about 1.0 mm.

2.2 HUAN TRAN TELESCOPE

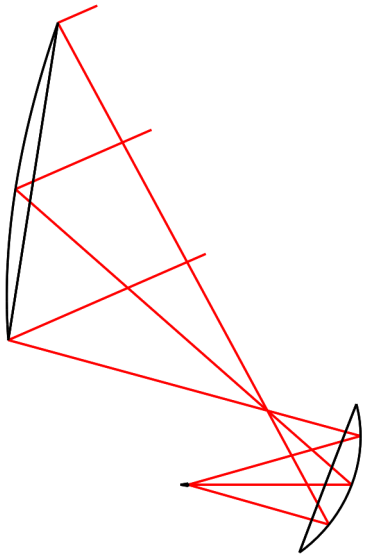

Figure 2.2.1: Optical design of HTT

The telescope of the POLARBEAR experiment, HTT has reflectors which construct an off-axis Gregorian configuration satisfying the Mizuguchi-Dragone condition (Tanaka et al. 1975; Mizugutch et al. 1976; Dragone 1978). If the condition is satisfied, the reflector system is equivalent to an on-axis single reflector system, and we can minimize the beam distortion and cross-polarization mixing (see also section B.1.2).

The primary mirror is an off-axis paraboloid with 2.2 m focal length made of a precise monolithic mirror whose diameter is 2.5 m on the projected plane along boresight. Also, we have outer panels to reflect the side-lobe to the sky. The secondary mirror is an ellipsoid with the diameter of 1.5 m in the cut plane, which covers footprints of a 19 cm focal plane. The FWHM of the beam is 3.5′ at 150 GHz.

The maximum scan speed is 4°/s.

2.3 POLARBEAR RECEIVER

The POLARBEAR receiver is installed in the HTT. Figure 2.3.1 shows components in the POLARBEAR receiver.

The pulse tube cooler and the three-stage helium sorption fridge provide 250 mK base temperature for the focal plane. The sorption fridge needs recharging, which limits our observation time. The holding time is about 36 hours.

On the focal plane, there are 637 dual-polarization pixels. Each pixel has a dual-polarization antenna and a contacting dielectric lenslet that couples optical radiation from free space to superconducting microstrip waveguides. The power is transmitted through the band-pass filter that defines our observation band centered at 148 GHz with 26% fractional integrated bandwidth and deposited on a transition-edge sensor (TES) bolometer (see section A.1 for more de-

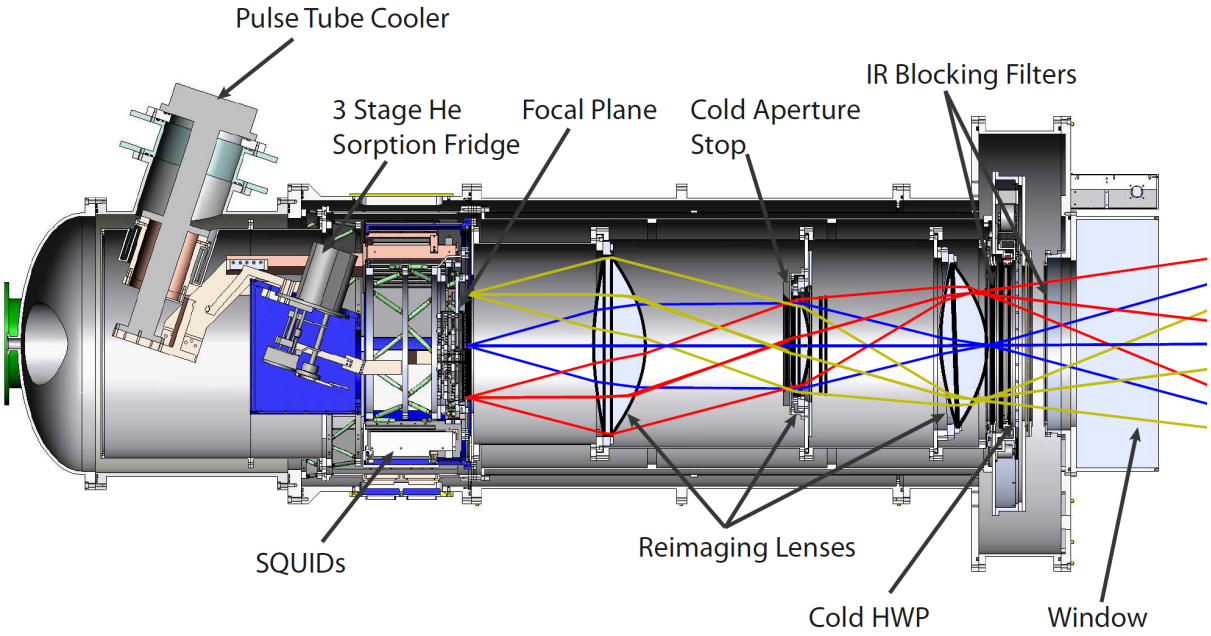

Figure 2.3.1: Design of the POLARBEAR receiver (from Kermish 2012).

tails). The power changes the current through the TES bolometer, and we read the change after amplification using a superconducting quantum interference device (SQUID). The sensitivity of the detector expressed by NET is about 550 $\mu K_{CMB}\sqrt{s}$ for each detector and 23 $\mu K_{CMB}\sqrt{s}$ for the whole detector array.

In the optical side, we have three reimaging lenses that reimage the focus of HTT onto a flat, tele-centric focal plane. A cold aperture stop defines the aperture and prevents detectors from seeing any stray lights. Infrared radiation blocking filters are necessary to absorb infrared power and to keep the receiver cooled.

The window has to endure the air pressure to keep the vacuum in the receiver. Also, since the window is 300 K, it has to be transparent enough. Zoteforms Plastazote HD30 is used for the 30 cm-diameter window in the POLARBEAR experiment.

The cold half-wave plate (HWP) (Figure 2.3.2) is an optical material which rotates the polarization angle of the detector and mitigates the systematic uncertainty. It was fixed during observations and stepped in angle by 11.25° between observations.

The total loading power from the receiver is 29 K_{RJ} in Rayleigh–Jeans temperature.

2.4 CALIBRATOR

We have a thermal source calibrator behind the secondary mirror. It emits unpolarized signals from a thermal source regulated at 700°C chopped at frequencies from 4Hz to 44Hz and illuminates detectors through a light pipe penetrating the secondary mirror. This calibrator is operated before and after observations. We use the data to select detectors that have the optical response. We also calibrate the responsivity and time constant of the detector.

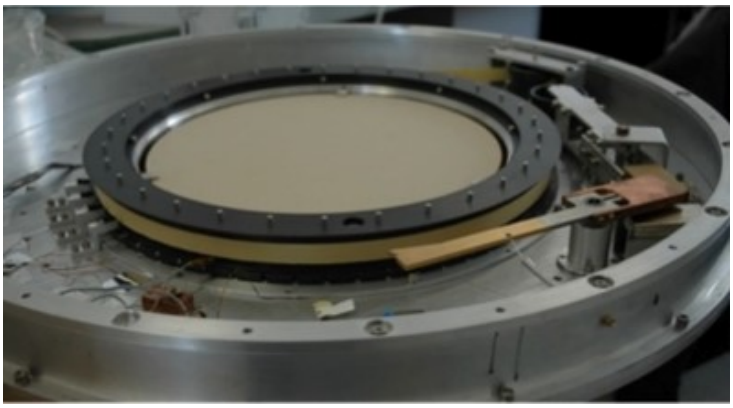

Figure 2.3.2: Picture of the cold HWP in the POLARBEAR receiver. The beige plate in the center is the HWP with the anti-reflective coating (ARC). The HWP is mounted on the rotation mechanism driven by the Kevlar belt. The angle of the rotator is stepped by the ratchet mechanism.

3

LENSING B-MODE MEASUREMENTS

In this chapter, we describe measurements of the lensing B-mode signal using data from the initial season of the POLARBEAR experiment. The POLARBEAR experiment started observation in January 2012 and started regular scientific observations in June 2012 after commissioning. Since the CMB B-mode had not been detected yet, the POLARBEAR experiment initially chose an observation strategy focusing on the detection of the CMB B-mode signal, i. e. observing small f_{sky} regions to minimize the map depth $w_T^{-1/2}$ of Eq. (1.4.6) as fast as possible. This observation strategy also enables us to choose clean regions from the foregrounds, although we can probe only the small-angular-scale anisotropy, i. e. the lensing B-mode signal (see discussion in section 1.4.2). Note that the detection of the lensing B-mode signal is an essential milestone for further precise measurements that have potential to constrain e. g. the sum of the neutrino masses (Abazajian et al. 2015).

Note that there is a potential problem, the so-called "observer bias" (Klein et al. 2005), in a measurement aiming at the first detection of a very faint signal like the B-mode. Such a measurement inevitably requires probing regions that have never been measured. Although we try to estimate possible contamination from available information, we may find an unknown or missing effect that is not expected and could mislead us, especially if we have own preconceptions, such as theoretical predictions. To prevent the human bias as much as possible, we have adopted the so-called blind analysis, i. e. we never view the science results until we fix all the analysis methods and validate that any possible contamination is well below the expected statistical uncertainty. In this analysis, we have masked the probes for the detection of the lensing B-mode, namely the angular power-spectrum of the B-mode and off-diagonal correlations, $\langle X(\vec{\ell}')Y(\vec{\ell})\rangle_{\vec{\ell}\neq\vec{\ell}'}$ for $X, Y \in \{T, E, B\}$, while other information of CMB is used for calibrations.

First, we describe three methods to detect the lensing B-mode signal in section 3.1. The description about the observation is available in section 3.2. From section 3.3 to section 3.5, we perform the low-level analyses, namely the calibration, the data selection, and the map-making. We estimate systematic uncertainties in section 3.6 to validate the data set and the analysis pipeline. Finally, in section 3.7, we describe the high-level analyses corresponding to the three methods described above and present the results.

3.1 METHODS FOR MEASURING THE LENSING B-MODE

As introduced in section 1.3.5, the lensing B-mode signal is a secondary product from the primordial E-mode anisotropy, which originated from the scalar-type perturbation. Distortion of the E-mode due to the gravitational lensing is described by the displacement vector $\vec{d}(\vec{n}) = \nabla\phi(\vec{n})$ as

$$\begin{aligned}[Q + iU]^{(\mathrm{lens})}(\vec{x}) &= [Q + iU]^{(\mathrm{prim})}(\vec{x} + \nabla\phi(\vec{x})) \\ &\approx [Q + iU]^{(\mathrm{prim})}(\vec{x}) + \nabla[Q + iU]^{(\mathrm{prim})}(\vec{x}) \cdot \nabla\phi(\vec{x}) \quad , \end{aligned} \tag{3.1.1}$$

where we adopt the flat-sky approximation, and $[Q+iU]^{(\mathrm{prim})}(\vec{x})$ and $[Q+iU]^{(\mathrm{lens})}(\vec{x})$ are the primordial and lensed CMB polarization anisotropy. From the first line to the second, we performed the Taylor expansion up to the linear order assuming the displacement is small. The 2D Fourier transform of Eq. (3.1.1) yields

$$B^{(\mathrm{lens})}(\vec{\ell}) \approx -\int \frac{d\vec{\ell}'}{(2\pi)^2}[\vec{\ell}'\cdot(\vec{\ell}-\vec{\ell}')]\sin(2\varphi_{\ell'\ell})\,E^{(\mathrm{prim})}(\vec{\ell}')\phi(\vec{\ell}-\vec{\ell}') \quad , \tag{3.1.2}$$

where $\varphi_{\ell'\ell}$ is the angle between $\vec{\ell}'$ and $\vec{\ell}$. Eq. (3.1.2) means that a Fourier mode of a lensing B-mode with a wave number vector $\vec{\ell}$ has a correlation with Fourier modes of E-mode and lensing potential with different wave numbers $\vec{\ell}'$ and $\vec{L}=\vec{\ell}-\vec{\ell}'$. The correlation among the B-mode, E-mode and lensing potential provides us with several approaches to measure the lensing B-mode signal other than the angular power-spectrum of the B-mode.

3.1.1 *Using angular power spectrum*

The first method to measure the B-mode is measuring the angular power-spectrum of the B-mode polarization. Since the lensing B-mode signal is expected to have the most prominent contribution at sub-degree angular scales ($\ell \sim 1000$), the detection of nonzero B-mode angular power-spectrum can be directly interpreted as the measurement of the lensing B-mode signal, if all the uncertainties and errors described in section 1.4.3 are under control.

3.1.2 *Using lensing potential reconstructed from CMB*

Another method is measuring the correlation between the E-mode and B-mode via the lensing potential. Because of Gaussianity of the primordial CMB anisotropy, i. e. $\langle E^{(\mathrm{prim})}(\vec{\ell})E^{(\mathrm{prim})}(\vec{\ell}')\rangle = C_\ell^{EE\,(\mathrm{prim})}\delta(\vec{\ell}+\vec{\ell}')$, we can statistically solve the Eq. (3.1.2) by collecting many correlations between E- and B-modes, $E(\vec{\ell}')B(\vec{\ell})$, keeping $\vec{\ell}-\vec{\ell}'=\vec{L}$ constant as

$$\hat{\phi}(\vec{L}) \approx A_{EB}(L)\int \frac{d\vec{\ell}'}{(2\pi)^2}\frac{C_{\ell'}^{EE\,(\mathrm{prim})}}{\hat{C}_{\ell'}^{EE}\hat{C}_\ell^{BB}}(\vec{L}\cdot\vec{\ell}')\sin(2\varphi_{\ell'\ell})\,\hat{E}(\vec{\ell}')\hat{B}(\vec{\ell}) \quad , \tag{3.1.3}$$

where $\hat{E}(\vec{\ell}')$ and $\hat{B}(\vec{\ell})$ are measured E- and B-modes in the Fourier domain, $\hat{C}_{\ell'}^{EE}$ and $\hat{C}_\ell^{BB}$ are angular power-spectrum for the measured E- and B-modes including noise, $C_{\ell'}^{EE\,(\mathrm{lens})}$ is the theoretical lensed E-mode angular power-spectrum, and $A_{EB}(L)$ is a normalization factor as

$$A_{EB}(L) = \left[\int \frac{d\vec{\ell}'}{(2\pi)^2}\frac{1}{\hat{C}_{\ell'}^{EE}\hat{C}_\ell^{BB}}\left\{C_{\ell'}^{EE\,(\mathrm{prim})}(\vec{L}\cdot\vec{\ell}')\sin(2\varphi_{\ell'\ell})\right\}^2\right]^{-1} \quad . \tag{3.1.4}$$

Measurements of the angular power-spectrum of this reconstructed lensing potential $\hat{\phi}(\vec{L})$ or the displacement vector $\hat{\vec{d}}(\vec{L})=\vec{L}\hat{\phi}(\vec{L})$ can confirm the existence of the B-mode, and can also prove that the origin of the B-mode is the gravitational lensing.

Note that this method is equivalent to a measurement of the four-point function of the CMB polarization anisotropy. Besides, this method requires only the CMB polarization data.

3.1.3 *Using CIB as a tracer of lensing potential*

Since the gravitational lensing is caused by the LSS between the CMB and us, we can also estimate the lensing potential using information other than CMB. Probing correlations between the lensing potential reconstructed from the CMB polarization and that estimated from the external tracer, is another way to measure the lensing B-mode.

The cosmic infrared background (CIB) is one of the tracers of the lensing potential, which is an integral of emissions from unresolved galaxies around redshift $z \sim 2$, where the LSS contributions to the gravitational lensing mainly come from. Note that, however, the CIB traces the density distribution, which is a second order derivative of the gravitational potential as described by Poisson's equation. To be correlated with the CIB directly, therefore, the convergence $\kappa(\vec{n})$ is appropriate, because it is also the second order derivative of the lensing potential (see section 1.3.5).

3.2 SMALL PATCH OBSERVATION

We observed three 8 $\deg^2$ patches. They are chosen considering

- availability through a day,
- clearness from the foreground contamination,
- overlap with the other experiments.

Information of each patch is listed in Table 3.2.1, and its position is also shown in Figure 3.2.1.

Table 3.2.1: The three POLARBEAR patches.

Patch	RA	Dec	Effective Area	Overlap
RA4.5	$4^h40^m12^s$	$-45°$	7.0 $\deg^2$	QUIET
RA12	$11^h53^m0^s$	$-0°30'$	8.7 $\deg^2$	*Herschel*-ATLAS, QUIET
RA23	$23^h1^m48^s$	$-32°48'$	8.8 $\deg^2$	*Herschel*-ATLAS

We observed each patch with a set of constant elevation scans (CESs) in which we scan a certain azimuth range corresponding to 3° in the sky back and forth with constant elevation and constant scan speed, 0.75°/s, on the sky. We started observations every day when any patch rose above 30° in elevation and followed the sky rotation by changing the scanning azimuth range and elevation every 15 minutes. We optimized the operation point of the detector every one hour since the optical loading changes in different elevation. Before and after the optimization, we did two kinds of quick calibrations. One is the thermal source calibration that determines the responsivity and time constant of the detector. The other is called elevation nod calibration in which we scan the sky in the elevation ("nodding") by 2° and measure the signal from atmosphere thickness variation to calibrate the responsivity and PWV.

We stepped the cold HWP every 1-2 days in the first five months. In the next three months, we occasionally stepped it. After February 2013, we stopped it.

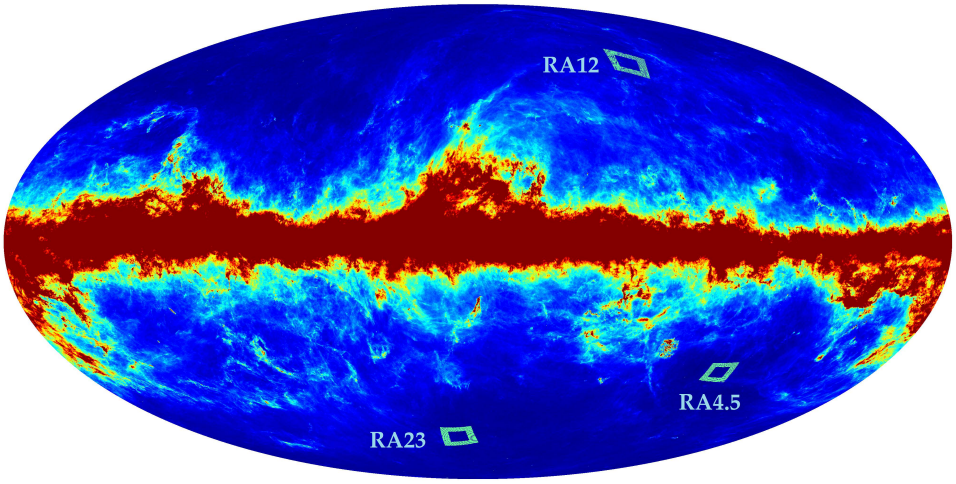

Figure 3.2.1: Positions of the three POLARBEAR patches compared to the distribution of the Galactic thermal dust emission obtained from the Planck satellite (from Figure 1, The POLARBEAR Collaboration: P. A. R. Ade et al. 2014, reproduced by permission of the AAS).

3.3 CALIBRATION

The first step of the analysis is the calibration analysis in which we characterize the instrument properties: the pointing, the beam spectrum, the responsivity and the polarization. Uncertainties in all these calibrations are evaluated in section 3.6.1, and none are found to produce significant contaminant signals on the detected signals.

3.3.1 *Pointing*

The pointing is information of direction that a detector is pointing. We model the pointing for each detector with two steps: the boresight pointing calibration and the pointing offset calibration.

The boresight is the position where the center detector is pointing. The boresight pointing is modeled by a five-parameter pointing model (Ulich 1981), which converts the encoded azimuth and elevation to the true values. We use parameters: IA, the azimuth encoder zero offset, IE, the elevation encoder zero offset, CA, the collimation error of the electromagnetic axis, AN, the azimuth axis offset/misalignment (north-south) and AW, the azimuth offset/misalignment (east-west). In the pointing calibration observations, we observe bright sources. We fit the difference between the measured positions and those in the catalog over the whole azimuth and elevation range. The standard deviation of residuals is 25″.

The pointing offset of each detector from the boresight is obtained from the Saturn and Jupiter observations. We fit the timestream of each detector with an elliptical Gaussian function with six parameters: the amplitude, the azimuthal offset, the elevational offset, the FWHM of the major axis, the FWHM of the minor axis, and the angle of the major axis. We average the azimuthal offset and the elevational offset from all the observations with weighting by fitting uncertainties. The standard deviation of residuals is 8″. The differential pointing offset between the two detectors in a pixel is arcsecond-level. The impact from the differential point-

ing offset is a negligible contaminant on the B-mode angular power-spectrum estimation in section 3.6.1.

3.3.2 *Beam spectrum*

Because of the finite angular resolution, we have an exponential degradation of the sensitivity to large multipole ℓ. The angular response spectrum is the beam spectrum.

A single map for each Jupiter observation is created by averaging all the detectors weighting by their sensitivities. We obtain a beam spectrum as the average of the 2-dimensional Fourier transformation of each single map azimuthally averaged every $\Delta\ell \approx 80$ bin. The resulting beam spectrum B_ℓ and its uncertainty in each multipole ℓ bin from observations of Jupiter are shown in Figure 3.3.1.

The point sources in our CMB patches, however, are larger than the expected size from the Jupiter observation. We consider that comes from the uncertainty of the pointing model. Therefore, the beam blurring is evaluated for each patch and included in the beam spectrum. The results are shown in Table 3.3.1. The patch-specific beam functions are displayed in Figure 3.3.1.

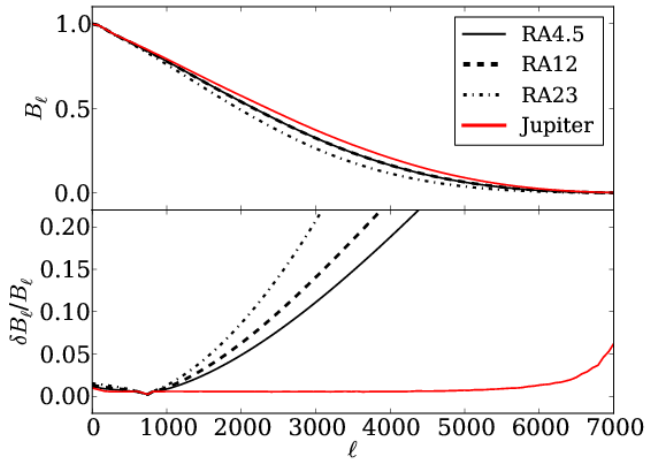

Figure 3.3.1: Beam spectrum for POLARBEAR observing fields (from Figure 2, The POLARBEAR Collaboration: P. A. R. Ade et al. 2014, reproduced by permission of the AAS). Top: Beam profiles measured from Jupiter (red) and from fitting point sources with a Gaussian-smoothed Jupiter beam (black). Bottom: Beam uncertainties given as one-sigma uncertainties normalized by the beam profile.

The beam uncertainty increases the uncertainty of our absolute gain calibration (see section 3.3.3) by a factor of 1.5, from 2.8% to 4.1%. The patch specific beam blurring only decreases our sensitivity in the highest ℓ-range of our reported band.

3.3.3 *Responsivity*

The responsivity, which is also called the gain, is a factor of the conversion from the recorded digital value to the CMB temperature unit. We used the thermal source calibrator (see sec-

Table 3.3.1: Pointing error for POLARBEAR observing fields (from Table 2, The POLARBEAR Collaboration: P. A. R. Ade et al. 2014, reproduced by permission of the AAS).

Field	RMS pointing error [″]
RA23	64.5 ± 20.9
RA12	26.7 ± 18.2
RA4.5	31.5 ± 15.3

tion 2.4), which produces the regulated amplitude signal. First, we obtained a model of the thermal source signal amplitude for the entire season for each detector by comparing to the integral power of the Saturn map. The model accounted for the effects of the polarization of the thermal source and the non-ideality of the cold HWP described in section 2.3. Then we calibrated the responsivity of each detector for each CMB observation using the nearest thermal source calibration data. Finally, we determined a single scale factor so that the CMB temperature power spectrum became consistent with that measured by WMAP-9 ΛCDM spectrum (Bennett et al. 2013).

3.3.4 *Polarization*

We also characterized the polarization angle. First, we calibrated the relative polarization angle for each pixel using the polarized astronomical source, Tau A. We obtained the polarization angle of each pixel by comparing the measured signal and the simulated signal obtained from the Tau A map observed by Institut de Radioastronomie Millimétrique (IRAM) 30 meter telescope at 90 GHz (Aumont et al. 2010). Then we determined our absolute angle so that the measured CMB EB cross spectrum, C_ℓ^{EB}, became null (Keating et al. 2013). Expected uncertainties are 0.43° for the absolute angle and 0.83° for the relative angle.

3.4 DATA SELECTION

In order to avoid the systematic error from the data with some unexpected problems, we applied data selection. Here, we categorize the data selection into four groups: each scan cut, each detector cut, each observation cut and each day cut.

The scan denotes the data selection for each throw of the telescope. We cut all the data during the time when the telescope is accelerating. We cut scans with a glitch caused by a cosmic ray hit.

In the each detector cut, we cut detectors,

- which do not show optical response during the thermal source calibration,
- which do not have calibration information, such as the pointing offset and the polarization angle,
- which have the large difference in the elliptical Gaussian fit parameters from the orthogonal detector,
- which have a large variation of the responsivity from the beginning to the ending of the observation, or
- which have unusual ground pick up.

In the each observation cut, we cut observations,

- which have a low yield,
- which were close to the Sun or the moon,
- which have high PWV,
- which have high scan-synchronous signals,
- which are in a particular elevation range where the telescope experiences a mechanical resonance,
- in which the telescope encoder was not functioning.

3.5 MAP MAKING AND PSEUDO-SPECTRUM ESTIMATION

We make the CMB anisotropy maps and estimate their angular spectra using the calibrations.

3.5.1 *Map making*

The detector timestreams are projected on the sky and combined into maps of the Stokes parameters I, Q and U.
The timestreams of two detectors in a pixel are processed as follows:

1. they are downsampled from 191 Hz to 31.8 Hz sampling to reduce the computational cost,
2. they are calibrated to the CMB temperature units,
3. they are low-pass filtered at 6.3 Hz to prevent the aliasing,
4. they are combined and transformed to the intensity and the polarization timestreams,
5. the intensity signal is filtered by the third-order polynomial function per stroke of constant elevation scan (CES),
6. the polarization signal is filtered by the first-order polynomial function per stroke of CES,
7. they are filtered by the ground filter which subtracts the constant signal on the ground.

The filtered timestreams are projected to the sky. The timestreams of all the pixels are combined into the Stokes I, Q and U maps weighting by the variance of the timestream from 1 Hz to 3 Hz corresponding from $\ell = 500$ to $\ell = 1500$. The maps from CES observations on the same day are combined into a daily map. Also, daily maps are combined into the season map. Figure 3.5.1 shows the season maps for Stokes parameter Q and U of the RA23 patch. They are apodized by the inverse of the variance of the map obtained from the white noise level of the detectors.

3.5.2 *Pseudo-spectrum estimation*

As described in section 1.3.3, we decompose the observed anisotropy into a superposition of Fourier modes with wave numbers of $\vec{\ell}$s. The calculation can be performed by the 2D Fourier transform for each of the temperature, E-mode and B-mode anisotropy as

$$\hat{T}_i(\vec{\ell}) = \int d\vec{n}\, W_i^T(\vec{n}) I_i(\vec{n}) e^{-i\vec{\ell}\cdot\vec{n}} \quad , \tag{3.5.1}$$

$$\hat{E}_i(\vec{\ell}) + i\hat{B}_i(\vec{\ell}) = \int d\vec{n}\, W_i^P(\vec{n}) [Q_i(\vec{n}) + iU_i(\vec{n})] e^{-2i\phi_\ell} e^{-i\vec{\ell}\cdot\vec{n}} \quad , \tag{3.5.2}$$

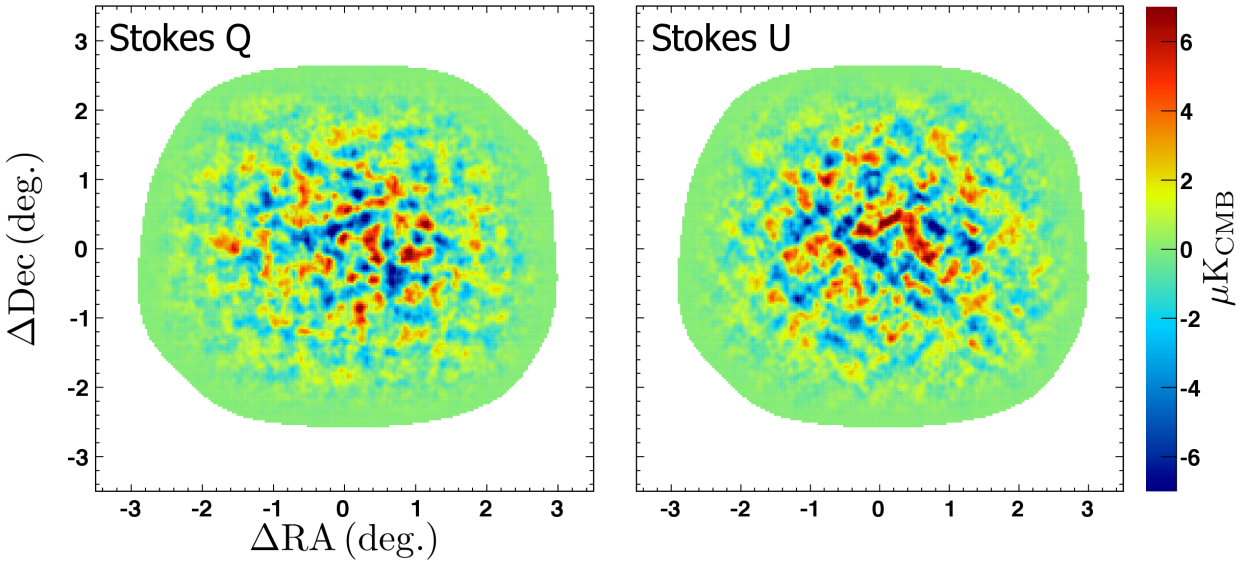

Figure 3.5.1: POLARBEAR CMB polarization maps of the RA23 patch (from Figure 6, The POLARBEAR Collaboration: P. A. R. Ade et al. 2014, reproduced by permission of the AAS). The left and right panels show the Stokes Q and U polarizations. The +- or ×-like patterns with sub-degree scales show the E-mode signal.

where the subscript i is the index of the daily map, $W_i^T(\vec{n})$ and $W_i^P(\vec{n})$ are the apodization window functions for the intensity and polarization maps, respectively, and ϕ_ℓ is the azimuth angle of $\vec{\ell}$. However, Eq. (3.5.2) mixes E-mode and B-mode owing to the gradient in the window function, $W_i^P(\vec{n})$. To minimize the mixing, we adopted the pure-estimator proposed by Smith (2006). Under the flat-sky approximation, the Fourier mode of the B-mode signal is estimated as

$$\begin{aligned}\hat{B}_i(\vec{\ell}) = &-\sin 2\phi_\ell \mathcal{F}[W_i^P Q](\vec{\ell}) + \cos 2\phi_\ell \mathcal{F}[W_i^P U](\vec{\ell}) \\ &- \frac{2i}{\ell}\left(\sin\phi_\ell \mathcal{F}\left[W_{i;x}^P Q + W_{i;y}^P U\right](\vec{\ell}) + \cos\phi_\ell \mathcal{F}\left[W_{i;y}^P Q - W_{i;x}^P U\right](\vec{\ell})\right) \\ &+ \frac{1}{\ell^2}\mathcal{F}\left[2W_{i;xy}^P Q + (W_{i;yy}^P - W_{i;xx}^P)U\right](\vec{\ell}) \quad ,\end{aligned} \tag{3.5.3}$$

where $\mathcal{F}$ is the Fourier transform operator as $\mathcal{F}[X](\vec{\ell}) = \int d\vec{n}\, X(\vec{n}) e^{-i\vec{\ell}\cdot\vec{n}}$, and the subscripts after the semicolon represent partial derivatives of the apodization window function. On the other hand, we do not apply the pure estimator for the E-mode because the mixing from B-mode to E-mode is negligible compared to the original E-mode signal. Note that the filters in the timestream processing and the apodization window function modify the original Fourier modes; thus the results are the pseudo-spectra.

3.6 DATA VALIDATION

All the systematic uncertainties from the modeled instrumental uncertainties are evaluated and confirmed to be sufficiently smaller than our statistical uncertainties. No contamination from unmodeled uncertainties is found in our null tests.

3.6.1 *Systematic error estimation*

Here we estimate the systematic error in the science products. We expect that the B-mode angular power-spectrum is more sensitive to the systematic error than the lensing potential reconstruction. Thus, we focus on the B-mode angular power-spectrum measurement and evaluate the impact of each systematic error regarding a single scaling factor A_{BB}, which is normalized by the theoretical expectation of the lensing B-mode signal from WMAP-9 ΛCDM model (Bennett et al. 2013). The results are summarized in Table 3.6.1.

Table 3.6.1: Summary of possible contributions to the amplitude A_{BB} from major sources of systematic uncertainty (from Table 9, The POLARBEAR Collaboration: P. A. R. Ade et al. 2014, reproduced by permission of the AAS).

Type	Source of systematics	Effect on A_{BB}
Systematic uncertainty:	Galactic dust	0.045
astrophysical foreground	Galactic synchrotron	0.001
	Radio galaxies	0.011
	Dusty galaxies	0.004
Systematic uncertainty:	Differential and boresight pointing	0.017
instrument	Instrument and relative polarization angle	0.014
	Pixel-pair relative gain: HWP-independent	0.002
	Pixel-pair relative gain: HWP-dependent	0.010
	Pixel-pair relative gain: drift	0.001
	Differential beam ellipticity	0.001
	Differential beam size	0.003
	Electrical crosstalk	0.002
Systematic uncertainty:	Scan synchronous template	0.002
analysis	E-to-B leakage subtraction	0.006 ± 0.037
	Total	0.119 ± 0.037
Multiplicative effect	Statistical variance and beam co-variance	± 0.041
	Polarization efficiency	± 0.036
	Transfer function	± 0.039
	Total	± 0.067

Foregrounds We consider contributions from polarized foreground emissions: the thermal emission from the Galactic dust, the Galactic synchrotron emission, the emission from Radio galaxies, and the emission from the dusty galaxies. The contribution from the Galactic dust is estimated by simulating the realistic scan with the template from the Planck Sky Model (PSM) software (Delabrouille et al. 2013) multiplying by a factor of two to be conservative. The contribution from the Galactic synchrotron emission is estimated by scaling the angular power-spectrum measured by QUIET (QUIET Collaboration 2012) at $\ell = 50$ and 95 GHz assuming

the frequency dependence of $\propto \nu^{-2.7}$ (Dunkley et al. 2009) and the multipole dependence of $\propto \ell^{-2.5}$ (La Porta et al. 2008). The contribution from the undetected radio galaxies is estimated by simulation assuming the distribution (de Zotti et al. 2005) and the polarization fraction (Sadler et al. 2006). The contribution from the dusty galaxies is estimated by scaling the angular power-spectrum of the intensity signal measured by SPT at $\ell = 3000$ and 153.8 GHz (Reichardt et al. 2012) assuming the polarization fraction of 1.54% (Seiffert et al. 2007).

Instrumental imperfections and calibration uncertainties The instrumental imperfections and the uncertainties of the calibrations could cause systematic bias in the B-mode angular power-spectrum measurement. We estimate their contributions using the Monte Carlo simulation method. We generate 100 realizations of the CMB anisotropy assuming the ΛCDM model with a null B-mode. We simulate realistic observations and analysis for the simulated sky considering instrumental imperfections and calibration uncertainties. Then, we estimate the impact of the instrumental systematic on the B-mode as the resulting B-mode angular power-spectrum. Major sources of the instrumental systematics are listed in Table 3.6.1. Note that the absolute gain uncertainty, the polarization efficiency uncertainty, and the beam spectrum uncertainty including the beam blurring due to the pointing uncertainty are treated below as another type of the instrumental uncertainty, i. e. the multiplicative effect. See The POLARBEAR Collaboration: P. A. R. Ade et al. (2014) for details of the each instrumental or calibration imperfection.

Uncertainties in analysis pipeline In addition to the instrumental imperfections, the filters used in the analysis pipeline could also cause a leakage from the E-mode to the B-mode. We estimate and subtract the leakage using the Monte Carlo simulations without the B-mode as described in section 3.7.1. We also perform the Monte Carlo simulations with both the E- and B-modes and find some bias after the leakage subtraction. The bias and the uncertainty are included in the systematic uncertainty.

Sequential applications of filters could also cause residuals and leakages. We investigate the impact of the scan synchronous signal on the resulting B-mode angular power-spectrum, which is estimated by simulating the realistic observations and analysis by scanning the simulated sky as well as the observed scan synchronous signals.

Multiplicative uncertainty The multiplicative effect is the uncertainty proportional to the non-zero signal. Note that we do not need to include the uncertainty to test the null hypothesis to the first order. We consider the uncertainties in the absolute gain calibration, the polarization efficiency estimation, and the transfer function estimation. The absolute calibration uncertainty is estimated as the combination of the sample variance in the temperature angular power-spectrum from the ΛCDM model (see section 3.3.3) and the uncertainty in the beam spectrum including the beam blurring due to the pointing uncertainty (see section 3.3.2). The polarization efficiency is estimated from the physical model of the cold HWP, and the uncertainty of the polarization efficiency is estimated from the Tau A observations. The uncertainty of the transfer function (see section 3.7.1) is estimated from the Monte Carlo simulations as the variance of the resulting B-mode angular power-spectrum.

3.7 SCIENCE ANALYSES AND RESULTS

In this section, we describe the science analyses based on all the three methods described in section 3.1 to measure the lensing B-mode signal using the pseudo-spectra of the observed CMB anisotropy obtained in the previous section. As we mention in this section, POLARBEAR confirmed the existence of the lensing B-mode by all these three methods described in section 3.1 for the first time. In particular, we reported the first direct evidence for polarization due to gravitational lensing based on purely CMB polarization information.

3.7.1 *B-mode angular power spectrum*

Here we estimate the binned modified angular power-spectrum $D_\ell \equiv \frac{\ell(\ell+1)}{2\pi} C_\ell$ of the B-mode signal using the pseudo-power spectrum method (Hivon et al. 2002).

The angular power-spectrum can be obtained by the auto-correlation for each Fourier mode as

$$\tilde{D}^{BB}_\ell = \left\langle \frac{\ell(\ell+1)}{2\pi} \langle\langle \tilde{B}^*_i(\vec{\ell}) \tilde{B}_j(\vec{\ell}) \rangle\rangle_{i\neq j} \right\rangle_{|\vec{\ell}|=\ell} \quad , \tag{3.7.1}$$

where $\tilde{B}_i(\vec{\ell})$ is the pseudo-spectrum of the observed B-mode from a day labeled as i, the asterisk denotes the complex conjugate, and the double and single angle brackets represent averaging among combinations of days and among Fourier modes with $|\vec{\ell}| = \ell$. Note that the total number of the daily maps is about an order of hundred, and removing the correlation with the same day minimizes the contributions from any random noise. However, the pseudo-angular power-spectrum $\tilde{D}^{BB}_\ell$ is affected by the filters and the window function that can be modeled as

$$\tilde{D}^{BB}_\ell = \sum_{\ell'} \begin{pmatrix} K^{E\to B}_{\ell\ell'} & K^{B\to B}_{\ell\ell'} \end{pmatrix} \begin{pmatrix} D^{EE}_{\ell'} \\ D^{BB}_{\ell'} \end{pmatrix} \quad , \tag{3.7.2}$$

where $D^{EE}_{\ell'}$ and $D^{BB}_{\ell'}$ are the true angular power-spectrums of E- and B-modes, and $K^{E\to B}_{\ell\ell'}$ and $K^{B\to B}_{\ell\ell'}$ represent the mixing and transfer of modes between E-mode and B-mode from multipole ℓ' to ℓ (Smith 2006).[1] We estimate the matrix $K_{\ell\ell'}$ by separating it into three effects as

$$\begin{pmatrix} K^{E\to B}_{\ell\ell'} & K^{B\to B}_{\ell\ell'} \end{pmatrix} = M^{B\to B}_{\ell\ell'} \begin{pmatrix} F^{E\to B}_{\ell'} & F^{B\to B}_{\ell'} \end{pmatrix} B^2_{\ell'} \quad , \tag{3.7.3}$$

where $M^{B\to B}_{\ell\ell'}$ is the mode mixing effect due to the window function, $B_{\ell'}$ is the beam spectrum, and $F_{\ell'}$ is the transfer function due to filtering. The mode mixing $M^{B\to B}_{\ell\ell'}$ is estimated analytically following Louis et al. (2013), and the beam spectrum $B_{\ell'}$ is estimated from the beam calibration. The transfer function is estimated using a Monte Carlo method: we create hundreds of random CMB maps with an input angular power-spectrum, simulate observations and analysis for each map without noise, and compare the output angular power-spectrum with the input. The leakage from the E-mode is subtracted using the measured E-mode angular power-spectrum as

$$\tilde{D}^{BB(\mathrm{sub})}_\ell = \tilde{D}^{BB}_\ell - \frac{F^{E\to B}_{\ell'}}{F^{E\to E}_{\ell'}} \tilde{D}^{EE}_\ell \quad . \tag{3.7.4}$$

1 In practice, the filters and window functions are not isotropic, and thus the mixing is not isotropic, although the scan strategy could improve the anisotropy. However, averaging among Fourier modes of isotropic CMB signal preserves robustness of this method.

Additionally, to improve the statistics for each point, the measured angular power-spectrums are averaged among multipoles from $\ell = 500$ to $\ell = 2100$, which are divided into four bins as

$$\tilde{D}_b^{BB} = \frac{1}{\Delta\ell_b} \sum_{\ell=\ell_b^{(min)}}^{\ell_b^{(max)}} \tilde{D}_\ell^{BB(sub)} \quad , \tag{3.7.5}$$

where the b is a label of a bin from $\ell_b^{(min)}$ to $\ell_b^{(max)}$, and the band width $\Delta\ell_b = \ell_b^{(max)} - \ell_b^{(min)}$ is 400. We also average the mixing matrix $K_{\ell\ell'}^{B\to B}$ into the same bins as $K_{bb'}^{B\to B}$. Finally we correct the mixing by multiplying an inverse matrix of the $K_{bb'}^{B\to B}$ and obtain the unbiased estimation of the angular power-spectrum of the sky as

$$\hat{D}_b^{BB} = \sum_{b'} (K^{B\to B})^{-1}_{bb'} \tilde{D}_{b'}^{BB} \quad . \tag{3.7.6}$$

Next, we estimate the uncertainty of the measured angular power-spectrum $\hat{D}_b$. The noise pseudo-power spectrum can be obtained by auto-correlation of each Fourier mode from the same map as

$$\frac{\ell(\ell+1)}{2\pi}\tilde{N}_\ell^{BB} = \left\langle \frac{\ell(\ell+1)}{2\pi} \langle\langle \tilde{B}_i^*(\vec{\ell})\tilde{B}_j(\vec{\ell})\rangle\rangle_{i=j} \right\rangle_{|\vec{\ell}|=\ell} - \left\langle \frac{\ell(\ell+1)}{2\pi} \langle\langle \tilde{B}_i^*(\vec{\ell})\tilde{B}_j(\vec{\ell})\rangle\rangle_{i\neq j} \right\rangle_{|\vec{\ell}|=\ell} \quad , \tag{3.7.7}$$

where the contribution from the signal is subtracted by the second term. We then obtain the unbiased binned noise power spectrum $\frac{\ell(\ell+1)}{2\pi}\hat{N}_b^{BB}$ by applying the same procedure which was used to obtain $\hat{D}_b^{BB}$. The statistical uncertainty is then estimated using the analytical formula (Eq. (1.4.8)) as

$$\Delta\hat{D}_b^{BB} = \sqrt{\frac{2}{\nu_b^{BB}}} \left(\hat{D}_b^{BB} + \frac{\ell(\ell+1)}{2\pi}\hat{N}_b^{BB} \right) \quad , \tag{3.7.8}$$

where ν_b^{BB} is the effective number of modes estimated as

$$\nu_b^{BB} = (2\ell_b^{(mean)} + 1)\Delta\ell_b f_{sky}^{(eff)} \quad . \tag{3.7.9}$$

Here the effective sky area $f_{sky}^{(eff)}$ is calculated as (Hivon et al. 2002)

$$f_{sky}^{(eff)} = \frac{1}{4\pi} \frac{\left[\int d\vec{n}\, W(\vec{n})^2\right]^2}{\int d\vec{n}\, W(\vec{n})^4} \quad , \tag{3.7.10}$$

where $W(\vec{n})$ is the weight function whose maximum is unity. This analytical uncertainty estimation is validated using the Monte Carlo simulation including both the CMB signals and the detector noise. The systematic uncertainties from both the instrumental imperfections and foregrounds are linearly superposed in addition to the statistical uncertainty.

The result of the binned modified angular power-spectrum of the B-mode signal is shown in Figure 3.7.1, and the central value and its uncertainty are tabulated in Table 3.7.1 for each ℓ bin. We fit the measured spectrum with the expectation from the WMAP-9 ΛCDM model (Bennett et al. 2013) with a single scaling factor A_{BB} and find

$$A_{BB} = 1.12 \pm 0.61(\text{stat})^{+0.04}_{-0.12}(\text{sys}) \pm 0.07(\text{multi}) \quad , \tag{3.7.11}$$

where (stat), (sys), and (multi) terms represent the statistical uncertainty, the systematic uncertainty independent of the signal, and the systematic uncertainty proportional to the signal, respectively. Assuming the non-existence of the signal, i. e. without the sample variance and the multiplicative uncertainty, the measurement rejects the no lensing B-mode hypothesis with a confidence of 97.2%.

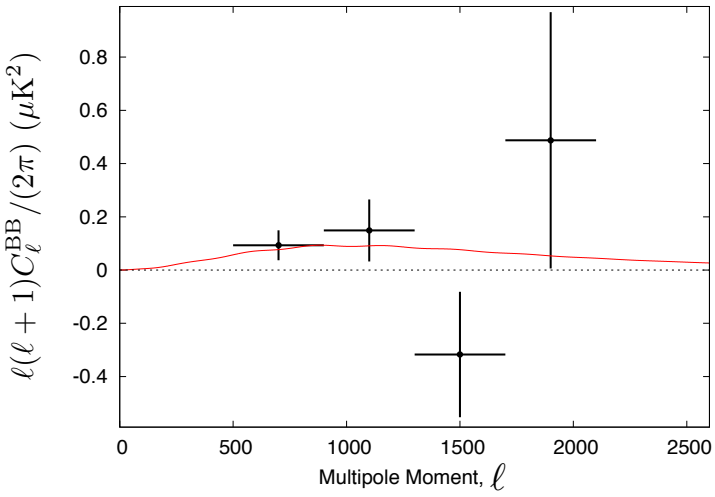

Figure 3.7.1: The result of the B-mode angular power-spectrum measurement (from Figure 12, The POLARBEAR Collaboration: P. A. R. Ade et al. 2014, reproduced by permission of the AAS). The black points are the measured binned B-mode power spectrum. The horizontal bar shows the range of binned multipoles and the vertical bar represents the 1-σ uncertainty. The red curve shows the expectation from the ΛCDM model.

Table 3.7.1: Band powers and their uncertainties (from Table 8, The POLARBEAR Collaboration: P. A. R. Ade et al. 2014, reproduced by permission of the AAS).

Central ℓ	$\ell(\ell+1)C_\ell^{BB}/2\pi$ [μK^2]	$\Delta\{\ell(\ell+1)C_\ell^{BB}/2\pi\}$ [μK^2]
700	0.093	0.056
1100	0.149	0.117
1500	−0.317	0.236
1900	0.487	0.482

3.7.2 *Gravitational lensing power spectrum from 4-point correlations*

Here we measure the power spectrum of the lensing deflection field reconstructed from the CMB polarization data. Again, we use the pseudo-power spectrum method (Hivon et al. 2002), thus estimate a biased pseudo-power spectrum first and correct the bias dividing by the transfer function estimated by the Monte Carlo simulation. For the reconstruction, we use EE estimator in addition to the EB estimator described in section 3.1.2 as (Hu et al. 2002)

$$\begin{cases} \tilde{d}_{EE}(\vec{L}) = L\dfrac{\sum_{\vec{\ell}} F_{EE}(\vec{\ell},\vec{\ell}')\langle\langle \tilde{E}_i(\vec{\ell}')\tilde{E}_j(\vec{\ell})\rangle\rangle_{i\neq j}}{\sum_{\vec{\ell}} F_{EE}^2(\vec{\ell},\vec{\ell}')(\hat{C}_{\ell'}^{EE}+\hat{N}_{\ell'}^{EE})(\hat{C}_{\ell}^{EE}+\hat{N}_{\ell}^{EE})} \\ \tilde{d}_{EB}(\vec{L}) = L\dfrac{\sum_{\vec{\ell}} F_{EB}(\vec{\ell},\vec{\ell}')\langle\langle \tilde{E}_i(\vec{\ell}')\tilde{B}_j(\vec{\ell})\rangle\rangle_{i\neq j}}{\sum_{\vec{\ell}} F_{EB}^2(\vec{\ell},\vec{\ell}')(\hat{C}_{\ell'}^{EE}+\hat{N}_{\ell'}^{EE})(\hat{C}_{\ell}^{BB}+\hat{N}_{\ell}^{BB})} \end{cases}, \tag{3.7.12}$$

where $F_{EE}(\vec{\ell},\vec{\ell}')$ and $F_{EB}(\vec{\ell},\vec{\ell}')$ are specific weight functions, $\hat{C}_\ell^{EE}+\hat{N}_\ell^{EE}$ and $\hat{C}_\ell^{BB}+\hat{N}_\ell^{BB}$ are the measured angular power-spectrum of the E- and B-modes including noise variance, respectively, and the summation among Fourier modes are performed within $|\vec{\ell}|, |\vec{\ell}'| \in \{500, 2700\}$

satisfying $\vec{\ell} + \vec{\ell}' = \vec{L}$. We can obtain the power spectrum of the lensing deflection field from auto- and cross-correlations of these two. Requiring at least one B-mode contribution, the possible combinations are $\langle EEEB \rangle$ and $\langle EBEB \rangle$. However, in the case of $\langle EBEB \rangle$, the correlation of noise causes a bias, the so-called Gaussian bias, which is much larger than the lensing signal. We estimate the Gaussian bias $N_L^{(0)}$ and also transfer functions T_L^{EEEB} and T_L^{EBEB} for filters using the Monte Carlo simulation, and correct their effects as

$$C_L^{dd} = \begin{cases} \dfrac{\langle \tilde{d}^*_{EE}(\vec{L}) \tilde{d}_{EB}(\vec{L}) \rangle_{|\vec{L}|=L}}{T_L^{EEEB}} & \text{for } \langle EEEB \rangle \quad , \\ \dfrac{\langle \tilde{d}^*_{EB}(\vec{L}) \tilde{d}_{EB}(\vec{L}) \rangle_{|\vec{L}|=L} - N_L^{(0)}}{T_L^{EBEB}} & \text{for } \langle EBEB \rangle \quad . \end{cases} \tag{3.7.13}$$

The uncertainty of the reconstructed lensing deflection field, N_L^{dd}, can be estimated analytically (Hu et al. 2002), and the covariance between $\langle EEEB \rangle$ and $\langle EBEB \rangle$ is estimated using the simulation.

The obtained lensing deflection power spectrum is shown in Figure 3.7.2. The rejection of the null hypothesis has a significance of $4.6\,\sigma$ statistically and $4.2\,\sigma$ when statistical and systematic errors are combined in quadrature.

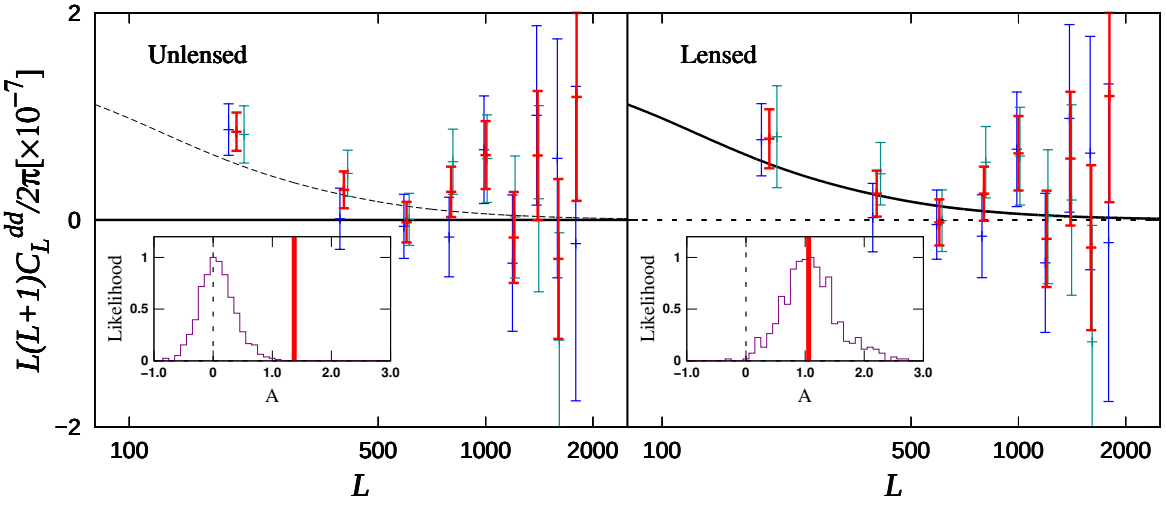

Figure 3.7.2: Polarization lensing power spectra co-added from the three patches and two estimators (from Ade et al. 2014b).

3.7.3 *Cross-correlation with cosmic infrared background*

Finally, we report our measurement of the power spectrum of cross correlation between the lensing convergence field reconstructed from the CMB polarization and the CIB observation data from *Herschel*-Astrophysical Terahertz Large Area Survey (*Herschel*-ATLAS) (Eales et al. 2010).

Similar to the method we explained in section 3.7.2, the pseudo-spectrum of the gravitational lensing convergence field κ can be estimated from the off-diagonal correlation of

$\langle \tilde{E}(\vec{\ell}')\tilde{B}(\vec{\ell})\rangle_{\vec{\ell}+\vec{\ell}'=\vec{L}}$. We correct the filtering effects using the transfer function estimated by the Monte Carlo simulation, where we correlate the reconstructed convergence $\tilde{\kappa}$ with the input κ assuming the CIB well traces the actual convergence field. Then we cross-correlate the convergence spectrum with CIB.

Obtained cross power spectrum is shown in Figure 3.7.3. The significance of the B-mode polarization is 2.3 σ.

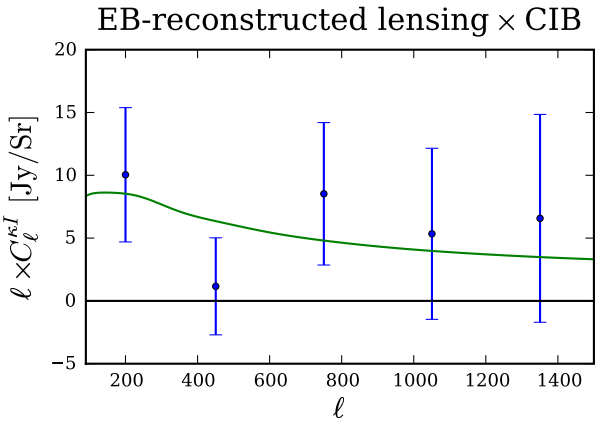

Figure 3.7.3: Cross power spectra of CMB polarization and CIB (from Ade et al. 2014a).

3.8 SUMMARY OF THE LENSING B-MODE MEASUREMENTS

We have investigated the lensing B-mode signal in the sub-degree-scale CMB polarization anisotropy, which had not been detected yet, from the observations of the three small (8 deg^2) patches using the POLARBEAR experiment. We have performed the three methods to probe the lensing B-mode signal, and find the signal in all the three methods, which is the first achievement among the CMB experiments. In particular, we report the first direct evidence for the B-mode signal based on purely CMB information by 4.7σ.

4

CURRENT STATUS AND CHALLENGES

In the previous chapter 3, we reported our first detection of the angular power-spectrum of the B-mode signal with the POLARBEAR experiment. After the publication of our result, some other CMB experiments:BICEP2/Keck Array (BICEP2 Collaboration 2014; BICEP2 and Keck Array Collaborations 2015; BICEP2/Keck Collaboration 2015; BICEP2 Collaboration 2016), SPTpol (Keisler et al. 2015), and ACTPol (Naess et al. 2014; Louis et al. 2016), have also reported their measurements of the B-mode angular power-spectrum, which are summarized in Figure 4.0.1.

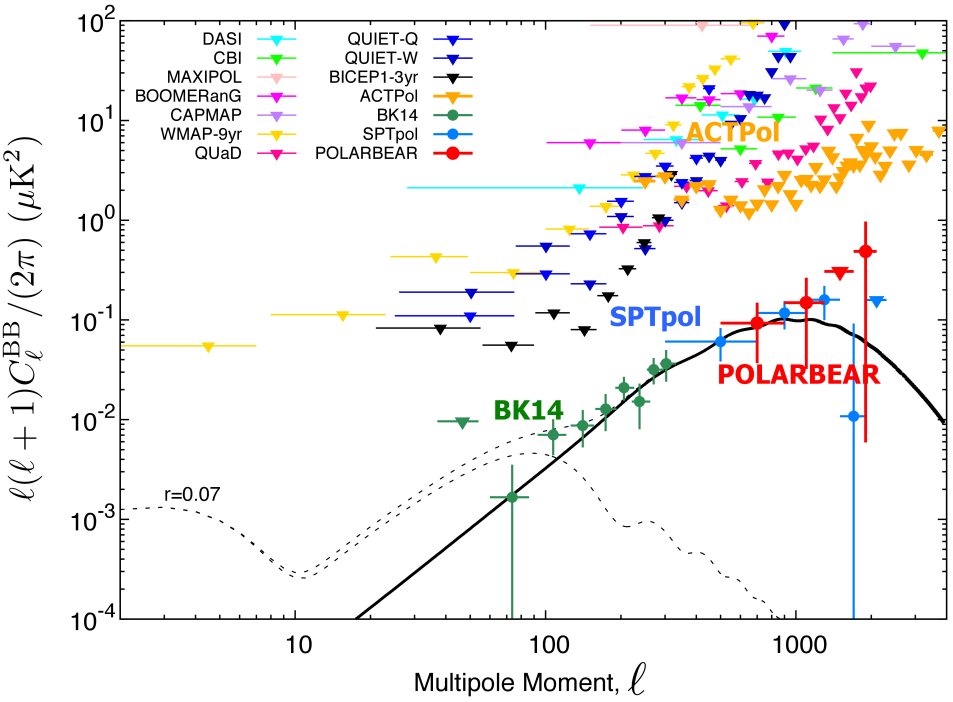

Figure 4.0.1: Measurements of the B-mode angular power-spectrum. Courtesy of Y. Chinone.

Following the current status, let us consider the directions of the future CMB experiments (especially ground-based experiments) focusing on the primordial B-mode detection. First of all, the simple but the most important point is improving the statistical uncertainty as much as possible by increasing the number of detectors and observing the larger sky area: e. g. if we can achieve NET $\sim 1\,\mu K\sqrt{s}$ with $\mathcal{O}(10^5)$ detectors, we can observe half of the sky with the map depth of $\sim 1\,\mu K\cdot$arcmin in three years (Abazajian et al. 2016). However, several challenges are standing in the way of the success:

FOREGROUNDS

As clarified in Planck Collaboration (2016d), the polarized diffused galactic foregrounds such as the synchrotron and thermal dust emissions have significant impacts on the B-mode polarization even in the high galactic latitude. To probe the primordial B-mode at

the level of $r \lesssim 0.01$, the foreground removal using observations with different frequency bands (see section 1.4.3.2) is necessary. However, the observations of foregrounds by the Planck satellite are not sensitive enough as shown by BICEP2 Collaboration (2016). Thus, the future CMB experiments must observe the foregrounds single-handedly. Several approaches have been performed to enable the multichroic observations: e. g. preparing a optics tube for each frequency band (e.g. BICEP2 Collaboration 2016) or using the multiband antenna.

LENSING B-MODE

Even if we successfully remove the foregrounds, the lensing B-mode could cover the primordial B-mode in the case of $r \lesssim 0.01$, and the sample variance of the lensing B-mode might limit the statistical uncertainty. We can remove the lensing B-mode by de-lensing (see section 1.4.3.2), and some demonstrations of de-lensing using CIB information have been reported (e.g. Larsen et al. 2016; Carron et al. 2017; Manzotti et al. 2017). To reconstruct the lensing potential with sufficient accuracy, however, we need measurements with large aperture telescopes which can resolve sub-degree angular scales.

LOW-FREQUENCY NOISE ($1/f$ NOISE)

The experiments with large aperture telescopes (POLARBEAR , SPTPOL, ACTPol, etc.) have potential to observe the degree scale anisotropy, $\ell \lesssim 100$. However, currently none of the experiments have reported the measurements of the angular scale as shown in Figure 4.0.1, even though they observed sufficient area of the sky. One impediment is the low-frequency noise, also called $1/f$ noise (see section 1.4.3.1), which degrades the sensitivity for large-angular scales. Besides, the $1/f$ noise might be non-Gaussian, and potentially causes instrumental systematic uncertainties which are difficult to estimate. Therefore, improvements and understanding of the $1/f$ noise are crucial for the large-aperture experiments to maximize their outcomes.

In the following chapters, we focus on improvements in the $1/f$ noise using polarization modulators (see e.g. Ade et al. 2009; Pisano et al. 2014). A continuously rotating half-wave plate is one of the most promising tools, which enables single polarization sensitive detectors to measure three of the Stokes parameters, I, Q and U, thereby avoiding the set of systematic errors and noises that can be introduced by mismatches in the properties of orthogonal detector pairs. We report the performance of a prototype continuously rotating half-wave plate implemented in the POLARBEAR experiment from the view points of the $1/f$ noise and the instrumental systematic uncertainties.

5 CONTINUOUSLY ROTATING HALF-WAVE PLATE

In this chapter, we construct a comprehensive model of the detector signal with a continuously rotating half-wave plate (CRHWP). First, we start the modeling with an ideal CRHWP in section 5.1. Next, in section 5.2, we consider non-idealities in the CRHWP. In addition, we incorporate non-idealities other than the CRHWP in section 5.3. Finally, we consider possible sources of the noise in section 5.4.

Before going into details of the CRHWP, let us quickly review the case without polarization modulation first, and introduce the concept of the polarization modulation in contrast:

CASE WITHOUT POLARIZATION MODULATION Suppose that we have an orthogonal detector pair, sensitive to x- and y-polarizations. Each polarization signal passes through many instruments and is recorded by each detector eventually as illustrated in Figure 5.0.1. Because each x- and y-polarization signal corresponds to Stokes $I + Q$ and $I - Q$, respectively, we obtain the Stokes Q polarization by taking difference between the two detectors. In practice, the detector pair inevitably have mismatch in properties, namely responsivity, time constant, bandpass, beam, etc.. Although some of them can be calibrated, the remaining mismatch could cause $1/f$ noise and instrumental systematic uncertainties.

CASE WITH POLARIZATION MODULATION A polarization modulator, usually placed somewhere in the optics, modulates the polarization signal, i. e. flip the sign of the polarization signal in time series as illustrated in Figure 5.0.2. The modulation enables a single detector to extract the polarization signal by taking difference in the time series, which results in a measurement free from any mismatch between the detector pair.

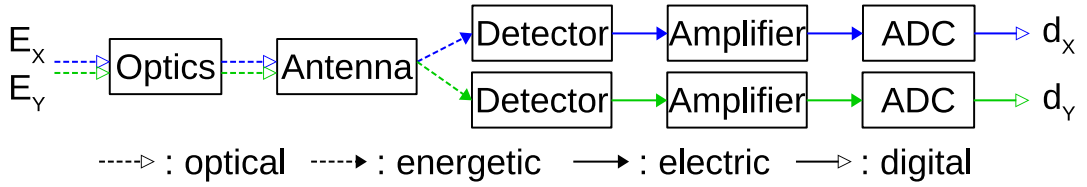

Figure 5.0.1: Schematic of the signal flow without the CRHWP. The forms of the signal are represented by the line styles, and the x- and y-components are shown by the blue and green colors. Note that each component goes through the different detector, amplifier, and analog-to-digital converter (ADC).

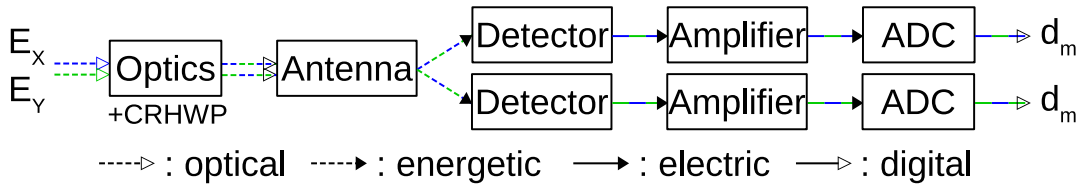

Figure 5.0.2: Schematic of the signal flow with the CRHWP. The forms and components of the signal are shown as the line styles and colors of the arrows. Here, the modulation between the x- and y-components is represented by the stripe.

5.1 POLARIZATION MODULATION USING IDEAL HALF-WAVE PLATE

5.1.1 *Half-wave plate*

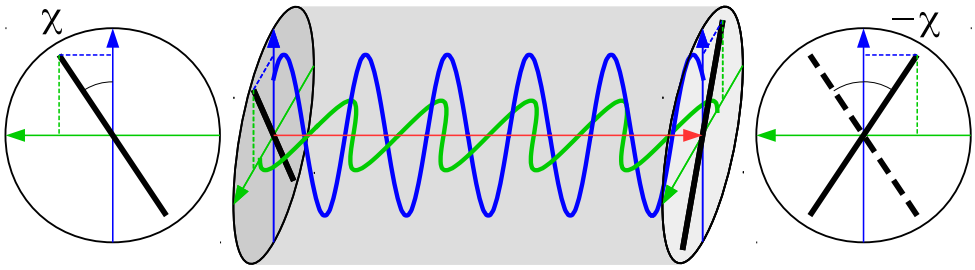

Figure 5.1.1: HWP

A HWP is an optical element made of birefringent material. The dielectric tensor of uniaxial birefringent material such as sapphire is expressed as

$$\epsilon_{ij} = \begin{pmatrix} \epsilon_e & 0 & 0 \\ 0 & \epsilon_o & 0 \\ 0 & 0 & \epsilon_o \end{pmatrix} \quad . \tag{5.1.1}$$

The electromagnetic wave whose phase normal vector is given as $\vec{s} = (s_x, s_y, s_z), s_x^2 + s_y^2 + s_z^2 = 1$ can be separated into two polarizations, ordinary wave, $\vec{E}_1$ and extraordinary wave,$\vec{E}_2$ as

$$\vec{E}_1 = E_1 \vec{e}_1 \quad , \qquad \vec{e}_1 \propto (0, s_z, -s_y) \quad , \tag{5.1.2}$$

$$\vec{E}_2 = E_2 \vec{e}_2 \quad , \qquad \vec{e}_2 \propto (1 - s_x^2, -s_x s_y, -s_x s_z) \quad . \tag{5.1.3}$$

Their phase velocities are

$$v_1 = v_o \quad , \tag{5.1.4}$$

$$v_2 = \sqrt{v_e^2 (1 - s_x^2) + v_o^2 s_x^2} \quad , \tag{5.1.5}$$

where

$$v_o = \frac{1}{\sqrt{\epsilon_o \mu}} \equiv \frac{c}{n_o} \quad , \tag{5.1.6}$$

$$v_e = \frac{1}{\sqrt{\epsilon_e \mu}} \equiv \frac{c}{n_e} \quad . \tag{5.1.7}$$

Here we have assumed isotropic permeability μ.

A HWP is made of this kind of birefringent material with a proper thickness. The thickness of a HWP is chosen so that the phase difference between ordinary wave and extraordinary wave which is propagating toward $\vec{s}_z = (0, 0, 1)$ with a wavelength λ becomes π after passing the plate. The ordinary wave and extra ordinary wave propagating this direction are easily given as $\vec{E}_1 = E_1 \vec{e}_y$ and $\vec{E}_2 = E_2 \vec{e}_x$ and their phase velocities become simple as $v_1 = v_o = c/n_o$ and $v_2 = v_e = c/n_e$, respectively. Then, we can obtain the thickness as

$$\Delta = \frac{\lambda}{2|n_e - n_o|} \quad . \tag{5.1.8}$$

The HWP flips a polarization angle of a linearly polarized light with respect to the birefringent axis. For example, the electric field of completely-linearly-polarized light is

$$\vec{E}(t,z) = E_0 \cos\theta e^{i(\omega t - 2\pi n_e z/\lambda)}\vec{e}_x + E_0 \sin\theta e^{i(\omega t - 2\pi n_o z/\lambda)}\vec{e}_y \quad , \tag{5.1.9}$$

where E_0 is an amplitude of electric field, θ is the polarization angle, and $\omega = 2\pi\lambda/c$ is the angular velocity of the light. At $z = 0$, the electric field of incoming light becomes

$$\vec{E}(t,0) = E_0(\cos\theta\vec{e}_x + \sin\theta\vec{e}_y)e^{i\omega t} \quad , \tag{5.1.10}$$

which points θ (or $\theta + \pi$) in the x-y plane. On the other hand at $z = \Delta$, the electric field becomes

$$\begin{aligned}\vec{E}(t,d) &= E_0(\cos\theta\vec{e}_x - \sin\theta\vec{e}_y)e^{i\omega t}e^{-i\pi\frac{n_e}{|n_e-n_o|}} \\ &= E_0(\cos(-\theta)\vec{e}_x + \sin(-\theta)\vec{e}_y)e^{i\omega t}e^{-i\pi\frac{n_o}{|n_e-n_o|}} \quad ,\end{aligned} \tag{5.1.11}$$

which points $-\theta$ (or $-\theta + \pi$).

We introduce a *Mueller matrix* to make the effect of the HWP clearer. As we discussed in section 1.3.1, the polarization state of light is expressed by Stokes' parameters, $\vec{S} = (I, Q, U, V)^T$. Mueller matrix, M operates on the Stokes' parameters as a usual matrix like

$$\vec{S}_{out} = M\vec{S}_{in} \quad . \tag{5.1.12}$$

In a case of the ideal HWP, ignoring the common phase, the electric field of an outgoing wave is expressed by that of an incoming wave as

$$\begin{cases} E_1^{out} = E_1^{in} \quad , \\ E_2^{out} = -E_2^{in} \quad . \end{cases} \tag{5.1.13}$$

Inserting these relations into the definitions of Stokes' parameters Eq. (1.3.3), we obtain

$$M_{HWP}^{ideal} = \begin{pmatrix} 1 & 0 & 0 & 0 \\ 0 & 1 & 0 & 0 \\ 0 & 0 & -1 & 0 \\ 0 & 0 & 0 & -1 \end{pmatrix} \quad . \tag{5.1.14}$$

5.1.2 *Polarization modulation*

We can modulate polarization signals by rotating the HWP.

First, we recall that the coordinate system dependence of the Stokes' parameters Q and U. The Mueller matrix of coordinate rotation is

$$R(\theta) = \begin{pmatrix} 1 & 0 & 0 & 0 \\ 0 & \cos 2\theta & -\sin 2\theta & 0 \\ 0 & \sin 2\theta & \cos 2\theta & 0 \\ 0 & 0 & 0 & 1 \end{pmatrix} \quad . \tag{5.1.15}$$

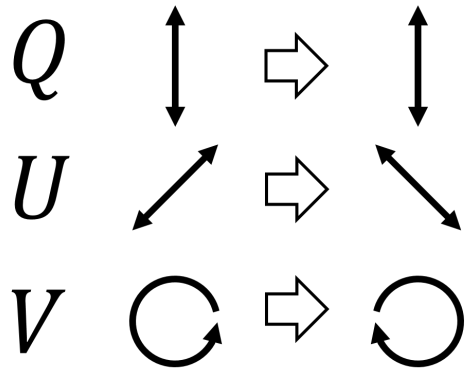

Figure 5.1.2: Effect of HWP for each Stokes' parameter

If the light passes a HWP whose birefringent axis has θ_{HWP} with respect to the coordinate system that describes the light, we can calculate the Stokes' parameters of outgoing light as

$$\vec{S}_{out} = R(-\theta_{HWP}) M_{HWP} R(\theta_{HWP}) \vec{S}_{in} \quad . \tag{5.1.16}$$

Here, we first move to HWP's coordinate system by $R(\theta_{HWP})$, then apply the HWP effect, M_{HWP} and finally go back to the original coordinate system by $R(-\theta_{HWP})$. In the case of the ideal HWP, we obtain

$$I_{out} = I_{in} \quad , \tag{5.1.17}$$
$$Q_{out} = Q_{in} \cos 4\theta_{HWP} + U_{in} \sin 4\theta_{HWP} \quad , \tag{5.1.18}$$
$$U_{out} = Q_{in} \sin 4\theta_{HWP} - U_{in} \cos 4\theta_{HWP} \quad , \tag{5.1.19}$$
$$V_{out} = -V_{in} \quad . \tag{5.1.20}$$

Here, Q and U rotate depending on the HWP angle, but I (and V) don't. Therefore, we can modulate only polarization signal by rotating the HWP.

Furthermore, we consider detecting the light by a polarization sensitive detector. The polarization sensitive detector measures $\vec{E}$. The measured signal is

$$d = D_{det} R(\theta_{det}) \vec{S}_{out} = D_{det} R(\theta_{det}) R(-\theta_{HWP}) M_{HWP} R(\theta_{HWP}) \vec{S}_{in} \quad , \tag{5.1.21}$$

where D_{det} is a vector that represents a responsivity of the detector and $D_{det} = (1, 1, 0, 0)$ for an ideal detector which is sensitive to the electric field along the x-axis. θ_{det} is the angle between the coordinates for the light and for the detector. In the case of the ideal HWP, we have

$$\begin{aligned} d &= I_{in} + Q_{in} \cos(4\theta_{HWP} - 2\theta_{det}) + U_{in} \sin(4\theta_{HWP} - 2\theta_{det}) \\ &= I_{in} + \frac{1}{2}(Q_{in} + iU_{in}) e^{-4i\theta_{HWP} + 2i\theta_{det}} + \frac{1}{2}(Q_{in} - iU_{in}) e^{4i\theta_{HWP} - 2i\theta_{det}} \quad . \end{aligned} \tag{5.1.22}$$

Now we continuously rotate the HWP as

$$\theta_{HWP}(t) = \omega_{rot} t, \tag{5.1.23}$$

where $\omega_{\rm rot}$ is the angular velocity of the continuous rotation and t is time. Then, Fourier transform of the detector signal is

$$d(\Omega) = I_{\rm in}(\Omega) + \frac{1}{2}(Q_{\rm in} + iU_{\rm in})(\Omega + 4\omega_{\rm rot})e^{2i\theta_{\rm det}} + \frac{1}{2}(Q_{\rm in} - iU_{\rm in})(\Omega - 4\omega_{\rm rot})e^{-2i\theta_{\rm det}} \quad . \tag{5.1.24}$$

Here we see that the polarization signals $(Q_{\rm in} + iU_{\rm in})(\Omega')$ appear around a frequency up-converted at $|\Omega' - 4\omega_{\rm rot}| \sim 4\omega_{\rm rot}$. That is, we can rescue the polarization signal from low-frequency to $1/f$ noise-free high-frequency.

5.1.3 *Demodulation*

We reconstruct the signal $\vec{S}_{\rm in} = (I_{\rm in}, Q_{\rm in}, U_{\rm in})^T$ by demodulating the data measured by the detector.

To obtain the intensity signal $I_{\rm in}$, we only have to apply the low-pass filter, $\mathcal{F}^{\rm LPF}$ as

$$d_0(t) = I_{\rm obs}(t) \equiv \mathcal{F}^{\rm LPF}[d(t)] \approx I_{\rm in}(t), \tag{5.1.25}$$

where $I_{\rm obs}$ is the observed intensity signal. For the polarization signal, we apply a band-pass filter, $\mathcal{F}^{\rm BPF}$ around the modulation frequency and demodulate using angles of the HWP and the detector as

$$d_4(t) = Q_{\rm obs}(t) + iU_{\rm obs}(t) \equiv \mathcal{F}^{\rm BPF}[d(t)] \times 2e^{4i\theta_{\rm HWP} - 2i\theta_{\rm det}} \approx Q_{\rm in}(t) + iU_{\rm in}(t), \tag{5.1.26}$$

where $Q_{\rm obs}(t)$ and $U_{\rm obs}(t)$ are observed polarization signals. Note that we obtain both polarization information $Q_{\rm in}(t)$ and $U_{\rm in}(t)$ from a single detector.

5.2 PRACTICAL MODEL OF OPTICAL SIGNAL

As we saw in Eq. (5.1.22), the ideal HWP only rotates the incoming polarization signal and doesn't create additional terms or mixing between I and Q or I and U. Practically, however, we have to consider non-idealities of the HWP, other optical elements in the telescope and the detector.

The most prominent signals from a practical observation using CRHWP are signals correlated with the angle of the HWP, and those are called HWP synchronous signals (HWPSSs). Hereafter, we Fourier expand the HWP synchronous signals (HWPSSs) as

$$\mathcal{P}_{\rm HWPSS}(t) = \sum_{n=1} {\rm Re}[A_n(t)e^{-in\theta_{\rm HWP}(t)}], \tag{5.2.1}$$

and look at the signals at different n. The main reasons are

- $n = 2$
  non-ideality of the HWP
- $n = 4$
  non-ideality of the optics between the sky and the HWP
- Other
  anti-reflective (AR) coating non-uniformity

  Hereafter, we look at each component.

5.2.1 *Non-ideality of the HWP*

Practically, the outgoing electric field changes from Eq. (5.1.13) as

$$E_1^{\rm out} = -E_1^{\rm in}\rho_1(\nu)e^{-i\Delta\phi(\nu)}, \tag{5.2.2}$$
$$E_2^{\rm out} = E_2^{\rm in}\rho_2(\nu)e^{i\Delta\phi(\nu)}, \tag{5.2.3}$$

where $\rho_1(\nu)$ and $\rho_2(\nu)$ are the amplitude transmissivities for the polarizations along the ordinary axis and the extra-ordinary axis of the HWP and $\Delta\phi(\nu)$ is the phase difference between the two polarizations. Note that they are dependent on the light frequency ν. Substituting these into the definition of the Stokes parameters Eq. (1.3.4), we have

$$M_{\rm HWP}^{\rm general}(\nu) = \begin{pmatrix} a_T(\nu) & b_T(\nu) & 0 & 0 \\ b_T(\nu) & a_T(\nu) & 0 & 0 \\ 0 & 0 & -c_T(\nu) & s_T(\nu) \\ 0 & 0 & -s_T(\nu) & -c_T(\nu) \end{pmatrix}, \tag{5.2.4}$$

where

$$\begin{aligned} a_T(\nu) &= (\rho_1^2(\nu)+\rho_2^2(\nu))/2, \qquad b_T(\nu) = (\rho_1^2(\nu)-\rho_2^2(\nu))/2, \\ c_T(\nu) &= \rho_1(\nu)\rho_2(\nu)\cos\Delta\phi(\nu), \quad s_T(\nu) = \rho_1(\nu)\rho_2(\nu)\sin\Delta\phi(\nu). \end{aligned} \tag{5.2.5}$$

Here, $a_T(\nu)$ is transmittance of the HWP, $b_T(\nu)$ represents the transmittance difference in each birefringent axis and $c_T(\nu)$ is related to the polarization efficiency of the HWP.

Besides, if the HWP is absorptive, it emits the polarized light from the fluctuation-dissipation theorem (Callen et al. 1951). The Stokes vector from the HWP is given as

$$\vec{S}_{\rm HWP}(\nu) = (1-a_A(\nu), -b_A(\nu), 0, 0)I_{\rm HWP}(\nu), \tag{5.2.6}$$

where $1-a_A(\nu)$ is absorptance and $b_A(\nu)$ is its anisotropy. The $I_{\rm HWP}(\nu)$ is blackbody radiation at the temperature of the HWP.

Including these effects, the signal into the detector becomes

$$\begin{aligned} \mathcal{P}_{\rm opt} =& \langle a_T\rangle I_{\rm in} + \langle 1-a_A\rangle I_{\rm HWP} \\ &+ {\rm Re}\left[\frac{\langle a_T - c_T\rangle}{2}(Q_{\rm in}-iU_{\rm in})e^{2i\theta_{\rm det}}\right] \\ &+ {\rm Re}\left[\langle b_T\rangle (Q_{\rm in}+iU_{\rm in})e^{-2i\theta_{\rm HWP}}\right] \\ &+ {\rm Re}\left[\left(\langle b_T\rangle I_{\rm in} - \langle b_A\rangle I_{\rm HWP} - i\langle s_T\rangle V_{\rm in}\right)e^{-2i\theta_{\rm HWP}+2i\theta_{\rm det}}\right] \\ &+ {\rm Re}\left[\frac{\langle a_T + c_T\rangle}{2}(Q_{\rm in}+iU_{\rm in})e^{-4i\theta_{\rm HWP}+2i\theta_{\rm det}}\right], \end{aligned} \tag{5.2.7}$$

where each coefficient with angle brackets represents averaged values across the frequency band, $f_{\rm det}(\nu)$, weighted by the source spectrum following it, i. e. (Bryan et al. 2010a)

$$\langle a_T\rangle = \frac{\int d\nu\, a_T(\nu)I_{\rm in}(\nu)f_{\rm det}(\nu)}{\int d\nu\, I_{\rm in}(\nu)f_{\rm det}(\nu)}, \quad \text{etc.} \tag{5.2.8}$$

The Eq. (5.2.7) shows that we have five types of signals: the unmodulated unpolarized signal, the unmodulated polaried signal, the unpolarized signal modulated by $2\theta_{\rm HWP}$, the polarized

signal modulated by $2\theta_{\rm HWP}$, and the polarized signal modulated by $4\theta_{\rm HWP}$. If we focus on the main signals only, the equation of the signal is simplified to

$$\mathcal{P}_{\rm opt} = \mathcal{T}\left(I_{\rm in} + {\rm Re}\left[\varepsilon(Q_{\rm in} + iU_{\rm in})e^{-4i\theta_{\rm HWP}+2i\theta_{\rm det}}\right]\right) \tag{5.2.9}$$

where we have introduced the transmission of the HWP, $\mathcal{T}$, and the polarization efficiency, ε, as

$$\begin{cases} \mathcal{T} = \langle a_T \rangle, \\ \varepsilon = \dfrac{\langle a_T + c_T \rangle}{2\langle a_T \rangle}. \end{cases} \tag{5.2.10}$$

5.2.2 *Non-ideality of the primary mirror*

Here we look at the non-ideality of the optical elements on the sky side of the HWP. As we find in section 6.1.1, we put the HWP at the prime focus in the POLARBEAR experiment. In this case, we only have a primary mirror between the HWP and the sky. Therefore, we focus on that situation.

At first, for simplicity, we consider a flat mirror made of a perfect conductor. Its Mueller matrix is the same with that of the ideal HWP as

$$M_{\rm mirror}^{\rm ideal} = \begin{pmatrix} 1 & 0 & 0 & 0 \\ 0 & 1 & 0 & 0 \\ 0 & 0 & -1 & 0 \\ 0 & 0 & 0 & -1 \end{pmatrix}. \tag{5.2.11}$$

Next we consider finite conductivity of the mirror. In that case, the electric field soaks into the mirror a little and causes absorption or phase retardance. Then, the Mueller matrix changes from the ideal case but is the same with the case of non-ideal HWP as

$$M_{\rm mirror}^{\rm general} = \begin{pmatrix} a_P(\nu) & b_P(\nu) & 0 & 0 \\ b_P(\nu) & a_P(\nu) & 0 & 0 \\ 0 & 0 & -c_P(\nu) & s_P(\nu) \\ 0 & 0 & -s_P(\nu) & -c_P(\nu) \end{pmatrix}. \tag{5.2.12}$$

In addition, the mirror also emits the thermal radiation. Because of the absence of the refraction in the mirror reflection, the emissivity and its asymmetry can be obtained as $1 - a_P(\nu)$ and $b_P(\nu)$.

The signal into the detector becomes

$$\begin{aligned} \mathcal{P}_{\rm opt} =& \langle a_P \rangle I_{\rm in} + \langle 1 - a_P \rangle I_{\rm mirror} + {\rm Re}\left[\langle b_P \rangle (Q_{\rm in} + iU_{\rm in})\right] \\ &+ {\rm Re}\left[\left(\frac{\langle a_P + c_P \rangle}{2}(Q_{\rm in} + iU_{\rm in}) + \frac{\langle a_P - c_P \rangle}{2}(Q_{\rm in} - iU_{\rm in})\right.\right. \\ &\left.\left. + \langle b_P \rangle I_{\rm in} - \langle b_P \rangle I_{\rm mirror} - i\langle s_P \rangle V_{\rm in}\right) e^{-4i\theta_{\rm HWP}+2i\theta_{\rm det}}\right]. \end{aligned} \tag{5.2.13}$$

In this case, we have many terms modulated in the same way as the polarization signal, $Q_{\rm in} + iU_{\rm in}$. Especially, the $\langle b_P \rangle I_{\rm in}$ term represents the leakage of the intensity signal into the polarization signal, which could cause the instrumental systematic uncertainties.

5.2.3 *Non-uniformity of the HWP*

Both surfaces of the HWP are coated by AR coating. If they have non-uniformity of their thickness or air gap, the transmission of that position varies. It appears as HWP synchronous signals.

For example, if the detector receives a signal only at $\theta_{\rm spot}$, we can express the signal as

$$\mathcal{P}_{\rm opt} = 2\pi A_{\rm spot}\delta(\theta_{\rm HWP} - \theta_{\rm spot}), \tag{5.2.14}$$

where $A_{\rm spot}$ is the amplitude of the signal from the spot and δ is the δ function. At the zeroth order, we expect they are constant as $A^{(0)}_{\rm spot}$. At the first-order, we expect they are proportional to the incoming power as

$$A_{\rm spot} = \lambda_{\rm spot} I^{\rm in} + A^{(0)}_{\rm spot}, \tag{5.2.15}$$

where $\lambda_{\rm spot}$ is a proportional factor. Fourier transformation of this signal yields

$$\mathcal{P}_{\rm opt} = \sum_{n=1} {\rm Re}\left[A_{\rm spot} e^{-in(\theta_{\rm HWP}-\theta_{\rm spot})}\right], \tag{5.2.16}$$

which appears in all the modes.

Distortion of the rotator or reflection by the rotator possibly makes the $n = 1$ HWPSS and more higher order signals.

5.2.4 *Imperfections of the beam*

In the previous sections, we have implicitly assumed that the beam is stable, i. e. the incoming Stokes parameters, $(I_{\rm in}, Q_{\rm in}, U_{\rm in}, V_{\rm in})$, do not depend on the HWP angle.

In practice, however, the HWP might change the beam pattern, which results in additional origins of the leakages in the HWPSSs. Especially, the leakages into the $n = 4$ HWPSS are equivalent to the intensity to polarization (I→P) leakage (as shown in Figure 5.2.1) and **Q↔U** mixing. For example, if the intensity beam is dependent on the HWP angle as $\mathcal{B}(\vec{n}; \theta_{\rm HWP})$, the incoming intensity signal is modulated as

$$I_{\rm in}(\vec{n}; \theta_{\rm HWP}) = \int d\vec{n}'\, \mathcal{B}(\vec{n}'; \theta_{\rm HWP}) I_{\rm sky}(\vec{n} - \vec{n}') \quad , \tag{5.2.17}$$

where $I_{\rm sky}(\vec{n})$ is the intensity anisotropy in the sky. This HWP angle dependence can also be decomposed into harmonics as

$$I_{\rm in}(\vec{n}; \theta_{\rm HWP}) = \sum_{n=0} {\rm Re}\left[[\mathcal{B}_n \star I_{\rm sky}](\vec{n}) e^{-in\theta_{\rm HWP}}\right] \quad , \tag{5.2.18}$$

where the star denotes the spacial convolution, and the $\mathcal{B}_n(\vec{n})$ is the averaged beam transferred into the n-th harmonic which is given by

$$\mathcal{B}_n(\vec{n}) \equiv \int \frac{d\theta_{\rm HWP}}{\pi} \mathcal{B}(\vec{n}; \theta_{\rm HWP}) e^{in\theta_{\rm HWP}} \quad . \tag{5.2.19}$$

Here, $\mathcal{B}_4(\vec{n})$ is in the I→P leakage beam, which can be used to estimate the instrumental systematic bias in the CMB polarization angular power-spectrum measurements.

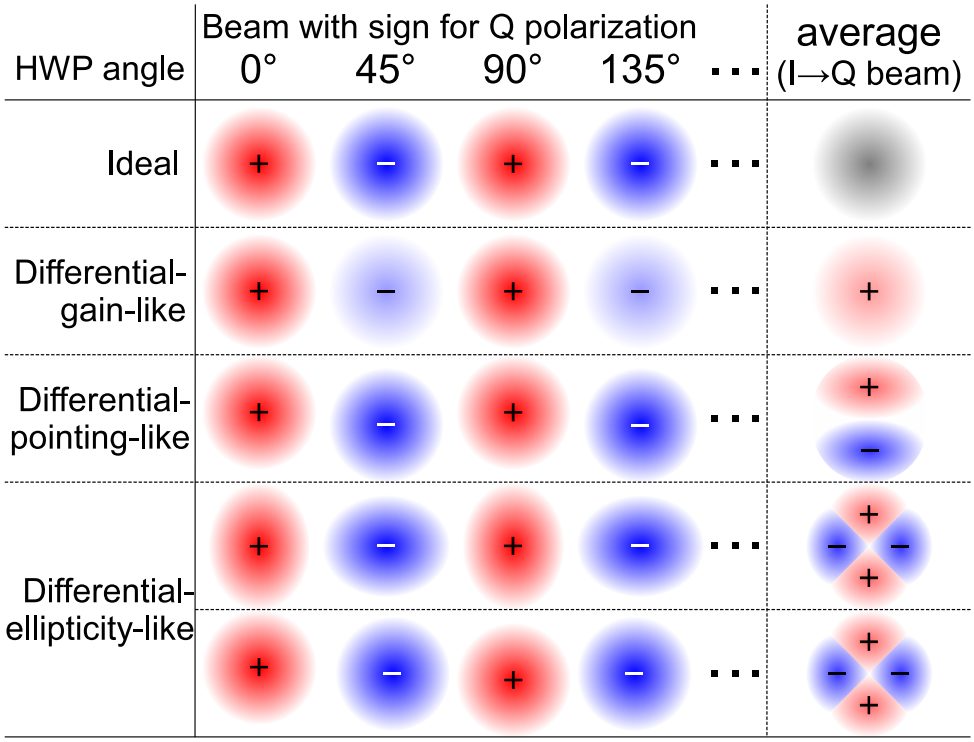

Figure 5.2.1: Beam patterns of the I→P leakage due to beam pattern variations as a function of HWP angle.

In general, we could have these kinds of beam imperfections for all Stokes parameters, I, Q, U, and V. Note that the beam variation should be originated in the instruments, and it would be useful to define the Q and U beams in the instrumental coordinates. In that case, the sky signal needs to be appropriately rotated when we take the convolution, since the Q and U polarization are dependent on the coordinate system. Besides, we also need to rotate the sky pattern, if we have a parallactic angle.

5.2.5 *Summary of optical non-ideality*

The optical signal into the detector is modeled as

$$\begin{aligned} \mathcal{P}_{\rm opt} =& \mathcal{T}\Big(I_{\rm in} + {\rm Re}\big[\varepsilon(Q_{\rm in} + iU_{\rm in})e^{-4i\theta_{\rm HWP}+2i\theta_{\rm det}}\big]\Big) \\ &+ \sum_{n=1} {\rm Re}\big[(A_n^{(0)} + \lambda_n^{\rm opt} I_{\rm in})e^{-in\theta_{\rm HWP}}\big] \\ &+ \sum_{n=0} {\rm Re}\big[[\mathcal{B}_n \star S_{\rm sky}](\vec{n})e^{-in\theta_{\rm HWP}}\big] \end{aligned} \tag{5.2.20}$$

where $\mathcal{T}$ (or ε) is the transmission (or polarization efficiency) through the entire optical system, $A_n^{(0)}$ is the HWPSS and $\lambda_n^{\rm opt}$ is the leakage coefficient from the intensity signal projected into each harmonic, and the last line includes all mixing terms from polarization signals.

5.3 EFFECTS FROM RESPONSE OF THE DETECTOR

In practice, a detector does not record the exact incoming power at time t, $\mathcal{P}^{\rm opt}(t)$, but records a value convolved with a response function, $G(t)$ as

$$d(t) = \int_0^\infty dt'\, G(t')\mathcal{P}^{\rm opt}(t-t') \quad . \tag{5.3.1}$$

A simple model of the response function of the detector is

$$G(t) \approx \begin{cases} g\dfrac{e^{-t/\tau}}{\tau} & (t>0) \\ 0 & (t<0) \end{cases} , \tag{5.3.2}$$

where g is the responsivity of the detector, and τ is the time constant. For the signal that varies slowly compared to the time constant, we can approximate the detector response as

$$d(t) \approx g\,\mathcal{P}^{\rm opt}(t-\tau) \quad . \tag{5.3.3}$$

Both the responsivity and the time constant affect the detector signals using CRHWP as we will see in the following sections. The time constant could shift the polarization angle, and the non-linear behavior causes additional I→P leakage.

5.3.1 *Time constant of the detector*

The time constant affects the angle of the HWP. Here we just focus on the time constant effect and assume that the others are ideal. The detector signal is retarded as

$$d(t) = I_{\rm in} + {\rm Re}\left[(Q_{\rm in}+iU_{\rm in})e^{-4i\theta_{\rm HWP}(t-\tau)+2i\theta_{\rm det}}\right] \tag{5.3.4}$$

where

$$\theta_{\rm HWP}(t) = \omega_{\rm rot}t. \tag{5.3.5}$$

If we demodulate this data $d(t)$ following section 5.1.3 with $\theta_{\rm HWP}(t)$, we obtain

$$Q'_{\rm obs} + iU'_{\rm obs} = (Q_{\rm in}+iU_{\rm in})e^{4i\omega_{\rm rot}\tau}, \tag{5.3.6}$$

which means that we wrongly measure the angle of $Q_{\rm in}+iU_{\rm in}$ by the amount of $4\omega_{\rm rot}\tau$.

5.3.2 *The detector non-linearity*

In practice, the responsivity and time constant of the detector are not constant, and have temporal variations. There can be several origins of the variations, e. g. temperature variations of the detector, dynamic range of the detector, etc. Here, we focus on the non-linearity of the detector, i. e. one of the classes of the responsivity and time constant variations that is dependent on the incoming signal: e. g. the response of the TES bolometer, the gain of the SQUID, the non-uniformity of ADC, etc. are included. We consider a small signal, and expand the dependence with Taylor series as

$$g(\mathcal{P}(t)) = g^{(0)}_{|\langle\mathcal{P}\rangle} + g^{(1)}_{|\langle\mathcal{P}\rangle}\Delta\mathcal{P}(t) + \cdots , \tag{5.3.7}$$

$$\tau(\mathcal{P}(t)) = \tau^{(0)}_{|\langle\mathcal{P}\rangle} + \tau^{(1)}_{|\langle\mathcal{P}\rangle}\Delta\mathcal{P}(t) + \cdots , \tag{5.3.8}$$

where $\langle\mathcal{P}\rangle$ is an arbitrary origin of the Taylor expansion, and $\Delta\mathcal{P}(t) \equiv \mathcal{P}(t) - \langle\mathcal{P}\rangle$ is a deviation.

We can obtain full expression of the detector signal by inserting Eq. (5.3.7) and Eq. (5.3.8) into Eq. (5.3.3). Here, however, let us consider the simplified case to look at the I→P leakage due to the non-linearity. Fist, let us assume that there are the responsivity variation, which is caused by only the intensity signal, and the optical signal including only the $n = 4$ HWPSS. In such a situation, the detector signal becomes

$$\begin{aligned} d(t) &= \left(g^{(0)}_{|\langle\mathcal{P}\rangle} + g^{(1)}_{|\langle\mathcal{P}\rangle} I_{in}(t)\right) \mathrm{Re}\left(A^{(0)}_4 e^{-4i\theta_{HWP}(t)}\right) \\ &= g^{(0)}_{|\langle\mathcal{P}\rangle} \mathrm{Re}\left(\left[A^{(0)}_4 + \frac{g^{(1)}_{|\langle\mathcal{P}\rangle}}{g^{(0)}_{|\langle\mathcal{P}\rangle}} A^{(0)}_4 I_{in}(t)\right] e^{-4i\theta_{HWP}(t)}\right) \quad . \end{aligned} \tag{5.3.9}$$

Here, the second line shows that we have an additional leakage from the intensity signal into the $n = 4$ HWPSS, whose leakage coefficient is effectively given by

$$\lambda^{nl}_4 = \frac{g^{(1)}_{|\langle\mathcal{P}\rangle}}{g^{(0)}_{|\langle\mathcal{P}\rangle}} A^{(0)}_4 \quad . \tag{5.3.10}$$

Note that both the intensity signal and the original HWPSS are included in the optical signal. We can take another opposite combination, i. e. the responsivity variation caused by the HWPSS also modulates the intensity signal in the optical signal. Therefore, the leakage effect becomes twice as large as Eq. (5.3.10):

$$\lambda^{nl}_4 = 2\frac{g^{(1)}_{|\langle\mathcal{P}\rangle}}{g^{(0)}_{|\langle\mathcal{P}\rangle}} A^{(0)}_4 \quad . \tag{5.3.11}$$

By considering the similar case for the time constant variation, we also find that the non-linearity of the time constant also causes the I→P leakage, whose coefficient becomes

$$\lambda^{nl}_4 = i\omega_{rot}\tau^{(1)}_{|\langle\mathcal{P}\rangle} A^{(0)}_4 \quad . \tag{5.3.12}$$

5.4 NOISE MODEL

In this section, we describe the noise of the data using the CRHWP. After a brief description about the white noise, we mainly discuss the possible sources that potentially contribute to the $1/f$ noise.

5.4.1 *White noise*

At first, we look at the ideal detector with white noise. In this case, the detector sees the noise additionally to the signal as

$$d(t) = I_{in}(t) + \mathrm{Re}\left[\left(Q_{in}(t) + iU_{in}(t)\right) e^{-4i\theta_{HWP}(t) + 2i\theta_{det}}\right] + \delta\mathcal{N}(t), \tag{5.4.1}$$

where $\delta\mathcal{N}(t)$ is the white noise, i. e. the power-spectrum density (PSD), $\mathcal{S}^{\mathcal{N}}(\omega)$, defined as $\langle\delta\mathcal{N}(\omega)\delta\mathcal{N}(\omega')^*\rangle = \mathcal{S}^{\mathcal{N}}(\omega)\delta(\omega - \omega')$, is frequency-independent. Note that the PSD is related to the NET as

$$\mathrm{NET} = \sqrt{\mathcal{S}^{\mathcal{N}}/2}. \tag{5.4.2}$$

If we demodulate the signal following section 5.1.3, we can obtain the observed signals in Fourier domain as

$$\begin{aligned} I_{obs}(\Omega) &= I_{in}(\Omega) + \delta\mathcal{N}(\Omega), \\ Q_{obs}(\Omega) &= Q_{in}(\Omega) + \mathrm{Re}(2\delta\mathcal{N}(\Omega - 4\omega_{rot})) \\ &= Q_{in}(\Omega) + \delta\mathcal{N}(\Omega - 4\omega_{rot}) + \delta\mathcal{N}(-\Omega + 4\omega_{rot}), \\ U_{obs}(\Omega) &= U_{in}(\Omega) + \mathrm{Im}(2\delta\mathcal{N}(\Omega - 4\omega_{rot})) \\ &= U_{in}(\Omega) - i(\delta\mathcal{N}(\Omega - 4\omega_{rot}) - \delta\mathcal{N}(-\Omega + 4\omega_{rot})), \end{aligned} \tag{5.4.3}$$

where the frequency Ω takes values within a specific cutoff frequency, ω_{cutoff}, of the low-pass or the band-pass filters used for the demodulation. By counting the number of $\delta\mathcal{N}$ terms, we find that the white-noise PSDs for the polarization signals are twice as large as that for the intensity signal:

$$\mathcal{S}_Q^{\mathcal{N}} = \mathcal{S}_U^{\mathcal{N}} = 2\mathcal{S}_I^{\mathcal{N}} = 2\mathcal{S}^{\mathcal{N}} \quad , \tag{5.4.4}$$

where $\mathcal{S}_X^{\mathcal{N}}$ is the white noise PSD of the signal X.

In addition, we need to consider a situation with thousands of detectors in a single receiver system as discussed in section 2.3 or chapter 4. If we consider the averaged timestream among N_{det} detectors, the white noise of the averaged timestream naïvely becomes

$$\delta\mathcal{N}^{(array)}(t) = \frac{1}{N_{det}} \sum_i \delta\mathcal{N}^{(i)}(t) \quad . \tag{5.4.5}$$

Because the origins of the white noise might be fundamentally microscopic fluctuations, the different detectors are less likely to have correlations, i. e. $\langle \delta\mathcal{N}^{(i)}(t)\delta\mathcal{N}^{(j)}(t)\rangle = 0$ for detectors labeled i and j ($i \neq j$). Therefore, the white-noise PSD of the averaged timestream improves by N_{det} times as

$$\mathcal{S}^{\mathcal{N}(array)} = \frac{\mathcal{S}^{\mathcal{N}}}{N_{det}} \quad , \tag{5.4.6}$$

where all the detectors are assumed to have the same property.

5.4.2 *Atmospheric noise*

The main component of the $1/f$ noise is the atmospheric fluctuation, especially for ground-based CMB experiments. Since the atmosphere is in a state of turbulence, the distributions of the density, temperature, or humidity, have spatially logarithmic spectra, and their time evolution can also be described by the temporally logarithmic spectra (Lay et al. 2000). The detectors scan the logarithmic distributions, which result in a logarithmic noise, i. e. $1/f$ noise. Fortunately, the atmospheric fluctuation is unpolarized to good approximation (Hanany et al. 2003). However, if we have clouds in the sky, ice grains in the clouds might contaminate polarized signals (Pietranera et al. 2007).

The atmospheric noise can be included in the incoming Stokes parameters as

$$\begin{aligned} I_{in}(t) &= I_{sky}(t) + \delta I_{atm}(t) \quad , \\ Q_{in}(t) &= Q_{sky}(t) + \delta Q_{atm}(t) \quad , \\ U_{in}(t) &= U_{sky}(t) + \delta U_{atm}(t) \quad , \end{aligned} \tag{5.4.7}$$

where the subscriptions, $_{sky}$ and $_{atm}$, denote signals from the space, and from the atmosphere. The unpolarized atmospheric noise, $\delta I_{atm}(t)$, is the dominant source of the $1/f$ noise in the

intensity signal for ground-based CMB experiments. Besides, if we have the I→P leakage due to the optics (see e. g. section 5.2.2) or the detector non-linearity (see section 5.3.2), the unpolarized atmospheric noise also contaminates the polarization signal. The polarized components, $\delta Q_{atm}(t)$ and $\delta U_{atm}(t)$, are expected to be small, but also problematic, because they cannot be suppressed even with the polarization modulation using the CRHWP.

Since the atmospheric fluctuation have spatial correlation, different detectors see the same low frequency noise at the same time. Therefore, in the averaged timestream $d^{(array)}(t)$, PSD of the atmospheric noise does not follow the N_{det} times improvement as we saw in the white noise case (see Eq. (5.4.6)). The number of independent modes, which depends on frequency, can be estimated as

$$N_{DOF}(\omega) = \begin{cases} 1 & \text{for} \quad \omega < \omega_{FOV} \\ \left(\frac{\omega}{\omega_{FOV}}\right)^2 & \text{for} \quad \omega_{FOV} < \omega < \omega_{beam} \\ N_{det} & \text{for} \quad \omega > \omega_{beam} \end{cases} . \tag{5.4.8}$$

where ω_{FOV} and ω_{beam} are the frequencies which are the inverse of the time for the telescope to scan the angle corresponding to the field of view (FOV) and the beam size, respectively. The contributions of the atmospheric noise in the PSD of the averaged timestream result in

$$\mathcal{S}^{I_{atm}(array)}(\omega) = \frac{\mathcal{S}^{I_{atm}}(\omega)}{N_{DOF}(\omega)} , \tag{5.4.9}$$

where $\mathcal{S}^{I_{atm}}(\omega)$ is the PSD of the unpolarized atmospheric noise for a single detector. Note that $N_{DOF} = 1$ for a signal whose angular scale is larger than the FOV, thus the PSD for the averaged timestream is identical to that for the single detector. Therefore, suppressing the atmospheric noise below the white noise is more challenging for a large-angular-scale measurement with a large number of detectors.

5.4.3 *Variation of the HWPSSs*

Another source of $1/f$ noise is variation of the HWPSSs, $A_n(t)$, in Eq. (5.2.1). Although the main origin of the variation is the leakage from the intensity signal, $\lambda_n^{opt} I_{in}(t)$, the temperature variations of the optical elements, e. g. the HWP and the primary mirror, also change the HWPSSs. For example, in Eq. (5.2.13), there is a term, $\langle b_P \rangle I_{mirror}$, in the $n = 4$ HWPSS. Here, I_{mirror} is equivalent to the temperature of the mirror and $\langle b_P \rangle$ also has a dependence on the temperature. Therefore, the mirror temperature variation, $\delta I_{mirror}(t)$, causes the $n = 4$ HWPSS variation, $\delta A_4(t)$, which results in the noise of the polarization signal.

Note that this HWPSS variation noise might be correlated among detectors, thus no mitigation might work in the averaged timestream, $d^{(array)}(t)$. It is obvious for the case of the primary mirror for example, because all the detectors see the single primary mirror.

5.4.4 *Unmodulated instrumental noise*

In the previous section, we discussed the temperature variations of the optical elements on the sky-side of the CRHWP or the HWP itself. Thermal emissions from the optical elements in the detector-side of the HWP, on the other hand, are not modulated by the CRHWP. The effect of the focal plane temperature variation is also one of the most prominent sources of

unmodulated signals, although it is not an optical signal. We wrap up these contributions as an instrumental noise, $\delta\mathcal{P}_{\rm inst}(t)$.

Because of the polarization modulation using the CRHWP, the unmodulated instrumental noise does not contaminate the polarization signal directly. However, if the detector has the non-linearity as described in section 5.3.2, the instrumental noise couples with the HWPSS, and could leak into the polarization signal. Note that, this instrumental noise mainly contaminates the intensity signal, and the ratio of the leakage into the polarization to that into the intensity is the same as $\lambda_n^{\rm nl}$s in section 5.3.2, because of the same origin.

5.4.5 *CRHWP angle error*

In the observations using the CRHWP, the angle of the CRHWP is a critical information to reconstruct the original signal. Errors in the angle data become a noise in the reconstructed signal. Suppose that we use a wrong angle information $\theta'_{\rm HWP}(t)$, which is different from the true angle $\theta_{\rm HWP}(t)$ by

$$\theta'_{\rm HWP}(t) = \theta_{\rm HWP}(t) + \theta_0 + \delta\theta(t) \quad , \tag{5.4.10}$$

where θ_0 is a stable offset and $\delta\theta(t)$ is the other temporal error. Then, we can find that the angle offset affects the polarization angle of observed signal as

$$Q'_{\rm obs} + iU'_{\rm obs} = (Q_{\rm in} + iU_{\rm in})e^{4i\theta_0} \quad , \tag{5.4.11}$$

and the angle error becomes additional noise for each HWPSS as

$$A_n(t) = A_n^{(0)} + inA_n^{(0)}\delta\theta(t) \quad . \tag{5.4.12}$$

The former angle offset can be one of the sources of the absolute polarization angle error, thus needs to be calibrated. The latter angle error is important to reduce the noise in the imaginary part.

One of the origins of the angle error is the resolution of the encoder. However, if we have a precise timing information of the encoder pulse, we can interpolate the angle at a timing of the detector sample with a precision better than the angle resolution. Thus, the synchronization between the detector timestream and the encoder timestream becomes important. If time stamps of the two timestreams have a deviation by $\delta t(t)$, the angle of the CRHWP is estimated with an error by $\delta\theta(t) = \omega_{\rm rot}\delta t(t)$.

On the other hand, the physical fluctuation of the rotation speed is not problematic as far as it is measured precisely as we discussed above. This is because we can subtract the HWPSSs using the measured angle.

5.5 SUMMARY OF DETECTOR SIGNAL MODEL

We model the signal from a detector, $d(t)$, as follows. Here, we assume a bolometer as the detector, which measures a variation of incoming power, $\Delta\mathcal{P}(t)$, as

$$d(t) \approx g(t)\Delta\mathcal{P}(t - \tau(t)) + \delta\mathcal{N}(t) \quad , \tag{5.5.1}$$

where $\delta\mathcal{N}(t)$ is white noise, and the responsivity and time constant are modeled as

$$g(t) \approx g^{(0)}_{|\langle\mathcal{P}\rangle} + g^{(1)}_{|\langle\mathcal{P}\rangle}\Delta\mathcal{P}(t) + \delta g(t) \tag{5.5.2}$$

$$\tau(t) \approx \tau^{(0)}_{|\langle\mathcal{P}\rangle} + \tau^{(1)}_{|\langle\mathcal{P}\rangle}\Delta\mathcal{P}(t) \quad , \tag{5.5.3}$$

respectively. Here, the first coefficients represent long-timescale variations parameterized by the bias power $\langle \mathcal{P} \rangle$, which can be corrected by calibration, and the others are short-timescale variations, namely the detector non-linearity and other responsivity variations, which cannot be calibrated. We consider four components that contribute to the incoming power variation as

$$\Delta\mathcal{P}(t) = \Delta\mathcal{P}_{\rm in}(t) + \mathcal{P}_{\rm HWPSS}(t) + \delta\mathcal{P}_{\rm beam}(\vec{n}(t)) + \delta\mathcal{P}_{\rm inst}(t) \quad . \tag{5.5.4}$$

Each term in Eq. (5.5.4) is described as follows:

$\Delta\mathcal{P}_{\rm in}(t)$: The first term is variation of the incoming optical signal which includes the target signals as

$$\Delta\mathcal{P}_{\rm in}(t) = \eta\,\mathcal{T}\left(\Delta I_{\rm in}(t) + \varepsilon {\rm Re}\left([Q_{\rm in}(t) + iU_{\rm in}(t)]e^{-2i\theta_{\rm pa}(t) - 4i\theta(t) + 2i\theta_{\rm det}}\right)\right) \quad , \tag{5.5.5}$$

where $I_{\rm in}(t)$, $Q_{\rm in}(t)$, and $U_{\rm in}(t)$ are the Stokes parameters, ε is the overall polarization efficiency, $\mathcal{T}$ is the transmission of the CRHWP, and $\eta\mathcal{T}$ is the overall conversion factor from temperature to power. The angles, $\theta_{\rm pa}(t)$, $\theta(t)$, and $\theta_{\rm det}$, are the parallactic angle, the CRHWP angle, and the detector angle, respectively.

$\mathcal{P}_{\rm HWPSS}(t)$: The second term is an optical signal synchronous to the CRHWP angle, which can be decomposed into harmonics of $\theta(t)$ as

$$\mathcal{P}_{\rm HWPSS} = \eta \sum_{n=1} {\rm Re}\left([A^{(0)}_{n|\langle I_{\rm in}\rangle} + \lambda^{(\rm opt)}_n \Delta I_{\rm in}(t) + \delta A_n(t)]e^{-in\theta(t)}\right) \quad . \tag{5.5.6}$$

We model the coefficient of each harmonic with a stable term, $A^{(0)}_{n|\langle I_{\rm in}\rangle}$, an optical leakage term proportional to the intensity variation, $\lambda^{(\rm opt)}_n \Delta I_{\rm in}(t)$, and a variation due to other reasons, $\delta A_n(t)$. Besides, we consider the polarization of the stable term and the optical leakage coefficient as

$$A^{(0)}_{n|\langle I_{\rm in}\rangle} = I^{(0)}_{n|\langle I_{\rm in}\rangle} + P^{(0)}_{n|\langle I_{\rm in}\rangle} e^{2i\theta_{\rm det}} \quad , \tag{5.5.7}$$

$$\lambda^{(\rm opt)}_n = \lambda^{(I)}_n + \lambda^{(P)}_n e^{2i\theta_{\rm det}} \quad , \tag{5.5.8}$$

where $I^{(0)}_{n|\langle I_{\rm in}\rangle}$ and $\lambda^{(I)}_n$ are those for unpolarized component and $P^{(0)}_{n|\langle I_{\rm in}\rangle}$ and $\lambda^{(P)}_n$ are those for polarized component which change amplitudes depending on the detector angle of $\theta_{\rm det}$. Note that all of these are complex numbers.

$\delta\mathcal{P}_{\rm beam}(\vec{n}(t))$: The third term represents higher order I→P leakage and/or Q↔U mixing effects due to the beam imperfections. Note that the lowest monopolar I→P leakage from the intensity signal has been already implemented as $\lambda^{(\rm opt)}_n$. Again, we decompose the effects into the harmonics of the CRHWP angle as

$$\delta\mathcal{P}_{\rm beam}(\vec{n}) = \eta \sum_{n=0} {\rm Re}\left(e^{-in\theta(t)} \textstyle\sum_j [\mathcal{B}^{(j)}_n \star \vec{S}^{(\rm ant)}_{\rm sky}](\vec{n})\right) \quad , \tag{5.5.9}$$

where $\mathcal{B}^{(j)}_n(\vec{n})$ is the pattern of a beam imperfection labeled by j, $\vec{S}^{(\rm ant)}_{\rm sky}(\vec{n})$ is the Stokes parameters in the coordinates with respect to the antenna, and the star denotes a spacial convolution.

$\delta\mathcal{P}_{\rm inst}(t)$: The last term represents any variations of the incoming power due to instrumental origins, e. g. the temperature variations of the focal plane, and the optical elements.

Furthermore, we extract the signal for each harmonic using demodulation method as

$$d_n(t) = \begin{cases} \mathcal{F}^{\mathrm{LPF}}[d(t)] & \text{for } n = 0 \quad , \\ \mathcal{F}_n^{\mathrm{BPF}}[d(t)]2e^{in\theta'(t)-2i\theta_{\mathrm{det}}} & \text{for } n > 0 \quad . \end{cases} \tag{5.5.10}$$

Note that, instead of $\theta(t)$, we use the measured angle, $\theta'(t) = \theta(t) + \theta_0 + \delta\theta(t)$, which could includes an offset θ_0 and an error $\delta\theta(t)$. By inserting the modeled detector signal, we obtain the explicit form of each harmonic, $n = \{0, 2, 4\}$ for example, as

$$d_0(t) \approx g^{(0)}_{|\langle\mathcal{P}\rangle}\,\eta\left[\mathcal{T}\Delta I_{\mathrm{in}}(t) + \textstyle\sum_j[\mathcal{B}_0^{(j)} \star \vec{S}^{(\mathrm{ant})}_{\mathrm{sky}}](\vec{n}(t))\right] + g^{(0)}_{|\langle\mathcal{P}\rangle}\delta\mathcal{P}_{\mathrm{inst}}(t) + \delta\mathcal{N}_0(t) \quad , \tag{5.5.11}$$

$$\begin{aligned} d_2(t) \approx g^{(0)}_{|\langle\mathcal{P}\rangle}\,\eta\, e^{2i\theta_0+2i\omega_{\mathrm{rot}}\tau^{(0)}_{|\langle\mathcal{P}\rangle}}\Big[&A'^{(0)}_{2|\langle I_{\mathrm{in}}\rangle} + \lambda'_2\Delta I_{\mathrm{in}}(t) + A'^{(0)}_{2|\langle I_{\mathrm{in}}\rangle}[\delta g'(t) + 2i\delta\theta(t)] + \lambda'^{(\mathrm{nl})}_2\frac{\delta\mathcal{P}_{\mathrm{inst}}(t)}{\eta} \\ &+ \delta A'_2(t) + \textstyle\sum_j[\mathcal{B}'^{(j)}_2 \star \vec{S}^{(\mathrm{ant})}_{\mathrm{sky}}](\vec{n}(t))\Big] + \delta\mathcal{N}_2(t) \quad , \end{aligned} \tag{5.5.12}$$

$$\begin{aligned} d_4(t) \approx g^{(0)}_{|\langle\mathcal{P}\rangle}\,\eta\, e^{4i\theta_0+4i\omega_{\mathrm{rot}}\tau^{(0)}_{|\langle\mathcal{P}\rangle}}\Big[&\mathcal{T}\varepsilon[Q_{\mathrm{in}}(t) + iU_{\mathrm{in}}(t)]e^{-2i\theta_{\mathrm{pa}}(t)} + A'^{(0)}_{4|\langle I_{\mathrm{in}}\rangle} + \lambda'_4\Delta I_{\mathrm{in}}(t) \\ &+ A'^{(0)}_{4|\langle I_{\mathrm{in}}\rangle}[\delta g'(t) + 4i\delta\theta(t)] + \lambda'^{(\mathrm{nl})}_4\frac{\delta\mathcal{P}_{\mathrm{inst}}(t)}{\eta} + \delta A'_4(t) \\ &+ \textstyle\sum_j[\mathcal{B}'^{(j)}_4 \star \vec{S}^{(\mathrm{ant})}_{\mathrm{sky}}](\vec{n}(t))\Big] + \delta\mathcal{N}_4(t) \quad , \end{aligned} \tag{5.5.13}$$

where ω_{rot} is the rotation speed of the CRHWP. The leakge coefficient is modified as

$$\lambda'_n \equiv \lambda'^{(\mathrm{opt})}_n + \lambda'^{(\mathrm{nl})}_n \tag{5.5.14}$$

$$\lambda'^{(\mathrm{opt})}_n = \lambda^{(\mathrm{I})}_n e^{-2i\theta_{\mathrm{det}}} + \lambda^{(\mathrm{P})}_n \tag{5.5.15}$$

$$\lambda'^{(\mathrm{nl})}_n = 2g_1 A'^{(0)}_{n|\langle I_{\mathrm{in}}\rangle} + in\omega_{\mathrm{rot}}\tau_1 A'^{(0)}_{n|\langle I_{\mathrm{in}}\rangle} \tag{5.5.16}$$

with the detector non-linearity, $g_1 = \eta\mathcal{T}g^{(1)}_{|\langle\mathcal{P}\rangle}/g^{(0)}_{|\langle\mathcal{P}\rangle}$ and $\tau_1 = \eta\mathcal{T}\tau^{(1)}_{|\langle\mathcal{P}\rangle}$. The relative variation $\delta g'(t) = \delta g(t)/g^{(0)}_{|\langle\mathcal{P}\rangle}$ is the one for the gain, and the other prime marks represent the detector angle correction effects, i. e. $A'^{(0)}_{n|\langle I_{\mathrm{in}}\rangle} = A^{(0)}_{n|\langle I_{\mathrm{in}}\rangle}e^{-2i\theta_{\mathrm{det}}}$, etc. The white noise $\delta\mathcal{N}(t)$ is spread into the terms $\delta\mathcal{N}_n(t)$, where $\delta\mathcal{N}_n(t)$ is complex for $n \leqslant 1$, and the variance of each of the real part and imaginary part is twice as large as the variance of $\delta\mathcal{N}_0(t)$. Note that we also consider the aliasing effects.

We utilize this comprehensive model to interpret the practical signals as described in the following chapters.

6 A PROTOTYPE CRHWP FOR THE POLARBEAR EXPERIMENT

As described in the previous chapter 5, the polarization modulation using a CRHWP is one of the most promising techniques to improve the low frequency noise (1/f noise) and systematic errors due to the instrumental imperfections. To test the prospects, we have developed a prototype CRHWP, and taken test observation data using the POLARBEAR in February 2014. In the following sections, we describe the details of the prototype CRHWP in section 6.1, as well as the operation of the CRHWP in the test observations in section 6.2.

6.1 DEVELOPMENT OF A PROTOTYPE CRHWP

Before going into the practical details of the prototype CRHWP, let us summarize guiding principles in designing the prototype CRHWP as follows:

- Position
  As described in section 5.2.2, any optical elements on the sky side of the CRHWP may cause the I→P leakage. Thus, the best position of the CRHWP is the first element of the optics. In the case of large aperture telescopes, however, it is impossible due to the maximum size of the HWP. Even though we inevitably suffer from the I→P leakage, the CRHWP should be placed in sky side in the optics chain as much as possible to minimize the I→P leakage.
- Temperature
  As described in section 5.2.1, the loss in the HWP or its ARC causes additional loading on the detector, and degrades the sensitivity limited by the photon noise (see section 1.4.1). If the additional loading is intolerant, we need to reduce the loading by cooling the CRHWP to cryogenic temperature.
- Material and size
  The material of the HWP must have the birefringent property. Larger index difference between ordinary axis and extra-ordinary axis and lower loss are desirable to reduce the optical loading into the detector. Besides, available maximum size and its cost are also important factors.
- Rotation mechanism
  The rotator is required to rotate at sufficient speed to up-convert all the science frequency bands beyond the knee frequency of the 1/f noise. Stability of the rotation speed is not necessary as far as its angle is precisely encoded, but desired. The vibration must not create additional noise. Robustness tolerable to the long-term observation is necessary.
- Angle encoding
  Encoding the angle of the HWP is the most important point for the experiment using CRHWP since the angle error could cause additional noise as described in section 5.4.5.

As described below, the position of the CRHWP is determined to be the prime focus because of availability of a HWP, and accessibility. Since all components are in ambient temperature, we can easily operate the rotator and the encoder.

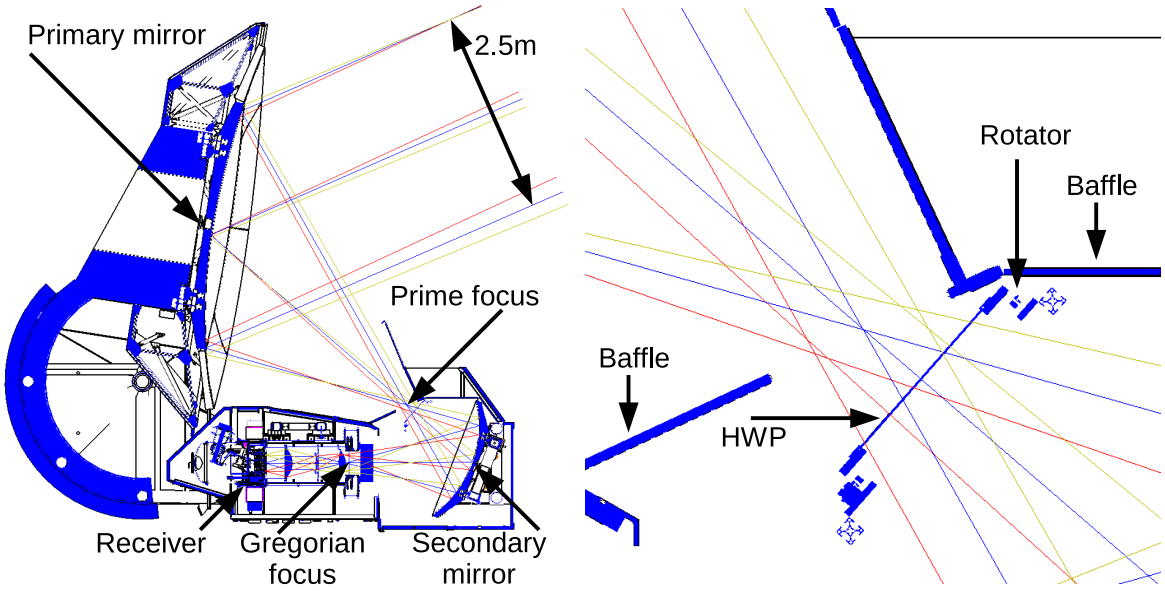

Figure 6.1.1: Position of the HWP in HTT

6.1.1 *Position and temperature*

Because of the limitation of available HWP size, the CRHWP need to be placed around a focus of the optics. The HTT employs an off-axis Gregorian optical system, and provides two focuses: the prime focus and the Gregorian focus (see Figure 6.1.1). The Gregorian focus is better to put the CRHWP at from the view point of the instrumental cross-polarization (see Appendix B), although it is inside of the cryogenic receiver, and thus difficult to access. On the other hand, since the prime focus is outside of the receiver, we can easily install and uninstall the prototype CRHWP. In practice, because of interference with the prime-focus baffle, the prototype CRHWP was installed at a position 11 cm behind the prime focus as shown in right panel of Figure 6.1.1. We can also see the proximity of the CRHWP rim and the ray for outer detectors, which might cause diffraction and truncation.

The CRHWP is therefore operated at the ambient temperature. For the single frequency band observation at 150 GHz, we can achieve sufficient transmission with a single layer ARC, and thus we have a minimal effect of loss in the ARC. The expected additional loading from the CRHWP is about 1 K, which is acceptable at this stage.

In the case of the configuration shown in Figure 6.1.1, the optical element between the CRHWP and the sky is the aluminum primary mirror (Tran et al. 2008). The instrumental polarization due to reflection by a metal surface is calculated as (Barkats et al. 2005)

$$A^{(0)}_{4|\langle I_{in}\rangle} = -\lambda_4^{opt}[T_{mirror} - \langle I_{in}\rangle] \sim 60\,\mathrm{mK}\,, \tag{6.1.1}$$

where $T_{mirror} \sim 300\,\mathrm{K}$ is the temperature of the primary mirror and $\langle I_{in}\rangle \sim 15\,\mathrm{K}$ is the total intensity from the sky. The I→P leakage coefficient of $n = 4$ is expressed as (Barkats et al. 2005)

$$\lambda_4^{opt} = -\varepsilon\sqrt{4\pi\epsilon_0\nu\rho}\,[\sec\chi - \cos\chi] \sim -0.02\%\,, \tag{6.1.2}$$

where ν is the frequency of the incoming radiation, ρ is the resistivity of the metal and χ is the incident angle.[1] Here, the polarization modulation efficiency, ε is applied since this signal is polarized. The expected values are estimated with $\varepsilon = 1$, $\nu = 148\,\mathrm{GHz}$ (The POLARBEAR Collaboration: P. A. R. Ade et al. 2014), $\rho = 2.417 \times 10^{-8}\,\Omega\cdot\mathrm{m}$ (Desai et al. 1984) for aluminum, and $\chi = 32.5°$ which measured from Figure 6.1.1. Note that both $A^{(0)}_{4|\langle I_{in}\rangle}$ and λ_4^{opt} are complex values, whose arguments represent the polarization angles. In the off-axis optical systems as shown in Figure 6.1.1, these polarization angles are aligned to the optical plane and are almost uniform across the focal plane.

6.1.2 *Half-wave plate*

The HWP was built in U. C. Berkeley by M.J. Myers.

The HWP is made from a 28 cm diameter 3.1 mm thick single sapphire plate, which is coated for anti-reflection on both surfaces by a 0.23 mm thick layer of Rogers RT/duroid 6002 material. Figure 6.1.2 shows the HWP.

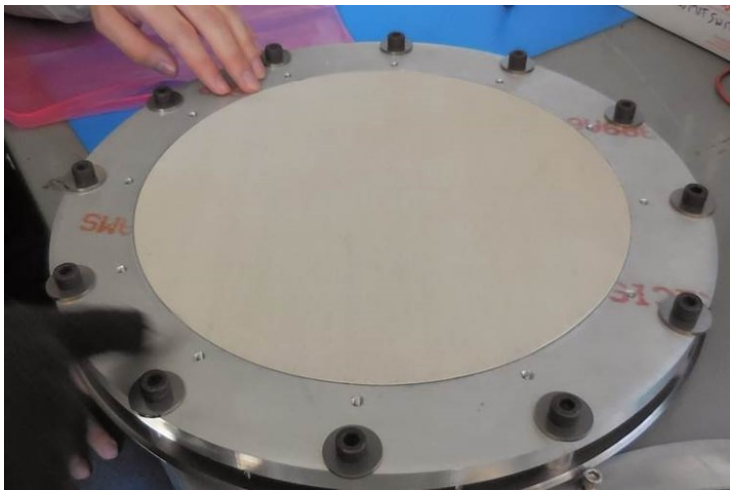

Figure 6.1.2: The HWP mounted on the rotator.

We measured the performance of the HWP in the laboratory using the optical test bench in KEK. We input the perfectly linear polarized light passing through the HWP in various angles and measured the transmission power in the same polarization direction. Assuming the Mueller matrix of the HWP as in Eq. (5.2.4), we can model the measured data as

$$d = \frac{3a_T - c_T}{4} + b\cos 2\theta_{HWP} + (a_T + c_T)\cos 4\theta_{HWP}. \tag{6.1.3}$$

We fit the data with this model and determined the parameters at each frequency. Figure 6.1.3 shows the results, and fitted parameters are listed in Table 6.1.1. By averaging these data multiplying the detector band function, we obtain the coefficient of the leakage from the intensity signal to $n = 2$ HWPSS as

$$\lambda_2 = b_T/a_T = 0.3\%, \tag{6.1.4}$$

and the polarization efficiency of the HWP as

$$\varepsilon = (1 + c_T/a_T)/2 = 98.5\%. \tag{6.1.5}$$

1 We ignore curvature of the mirror here.

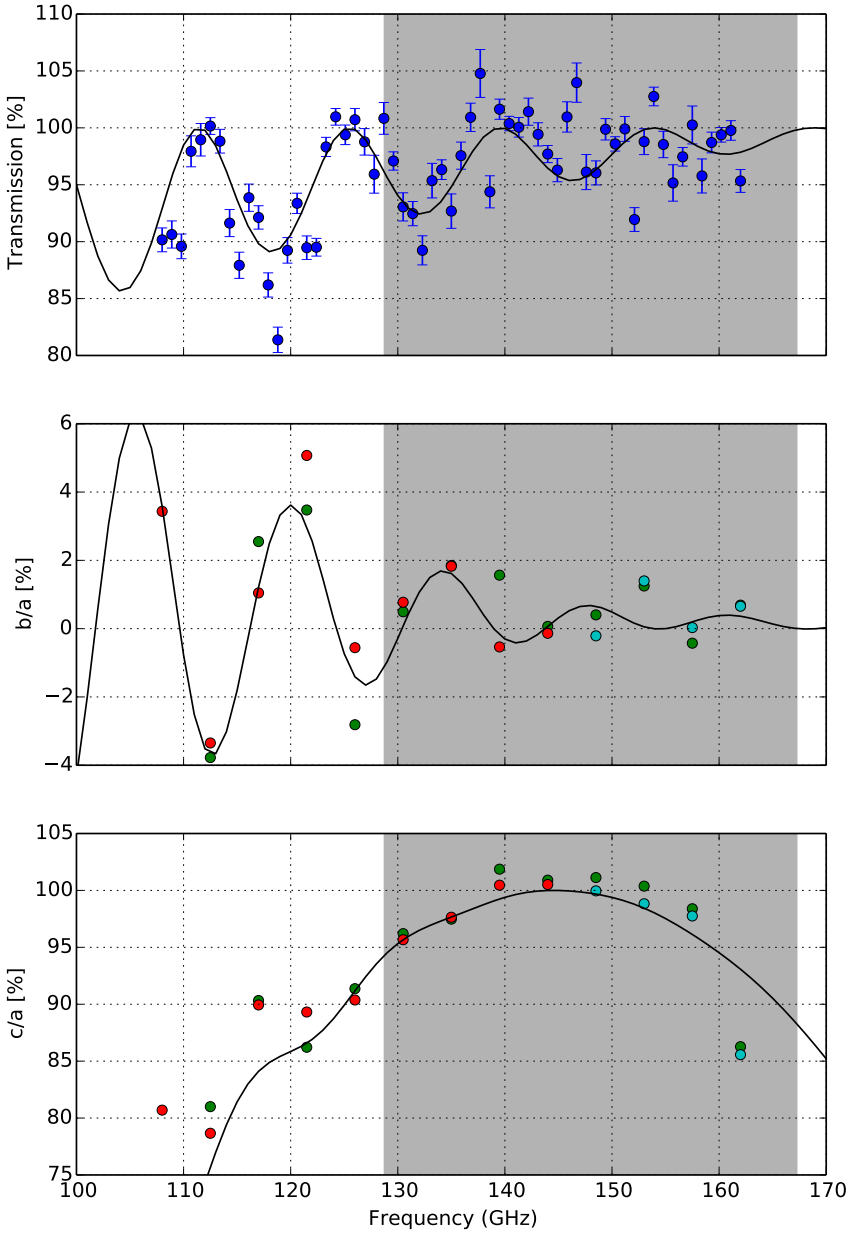

Figure 6.1.3: Optical measurement results of the HWP in the laboratory. The top panel shows the transmission for the extra-ordinary axis. The middle panel shows the ratio b/a in Eq. (5.2.4), which represents the leakage factor from the intensity signal to $n = 2$ HWPSS. The bottom panel shows the ratio c/a in Eq. (5.2.4), which represents the polarization efficiency. The points show the measured data, and the different colors represent the different measurement runs. The black curves show the fits. The shaded frequency range is the band-pass of the detector.

These are satisfactory for the CMB polarization observations.

Table 6.1.1: Parameters of the HWP

parameter	value	fit
Index of Duroid	1.71	fixed
Index of sapphire for ordinary axis	3.056	fixed
Index of sapphire for extra-ordinary axis	3.393	fixed
Thickness of AR	0.23 mm	fitted
Thickness of HWP	3.08 mm	fitted

6.1.3 *Rotator*

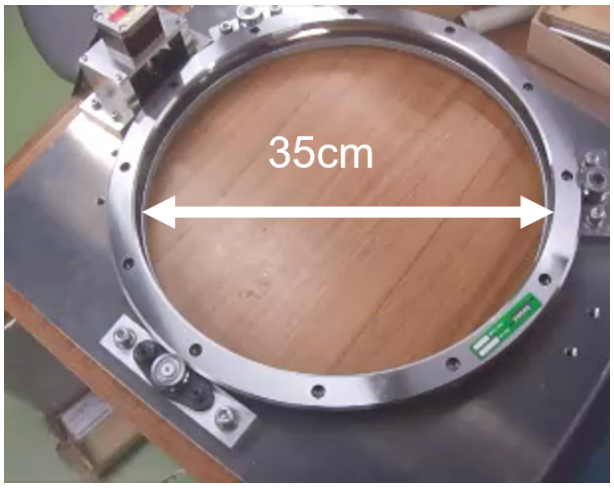

Figure 6.1.4: The rotator.

The rotator was designed in KEK by S.Takakura.

A rotator of the CRHWP consists of a 364.8 mm diameter HepcoMotion double edge ring slide with 456 gear teeth. The rotator is supported by three small bearings. A stepper motor drives the rotator via a pinion gear with 76 teeth, and the maximum rotation speed of the rotator is 2 Hz. There is a backlash between the rotator and the pinion gear by about 0.1 mm, which corresponds to an uncertainty of angle by 0.1°. We will find the effect of the backlash in section 7.2.2.

6.1.4 *Encoder*

The angle of the CRHWP is measured by counting the pulse signal from an encoder. We use an encoder connected to the motor, whose resolution corresponds to 0.03° of the CRHWP angle. The encoder has an index pulse, which appears once every rotation. Because the counter sometimes mistakes counting due to electrical noise or forgets the current position due to power down, we use the index pulse to reset the counter. Because of the 6 : 1 gear ratio

between the rotator and the pinion gear, however, we have six index signals per single rotation of the rotator, which results in uncertainty of the angle offset by multiples of 60°. We use the HWPSS in the detector signal to determine the offset for each observation.

In addition, the synchronization between the encoder timestream and the detector timestream is a critical matter of the CRHWP. Here we describe the details of the data taking and synchronization in the readout system of the POLARBEAR as summarized in Figure 6.1.5.

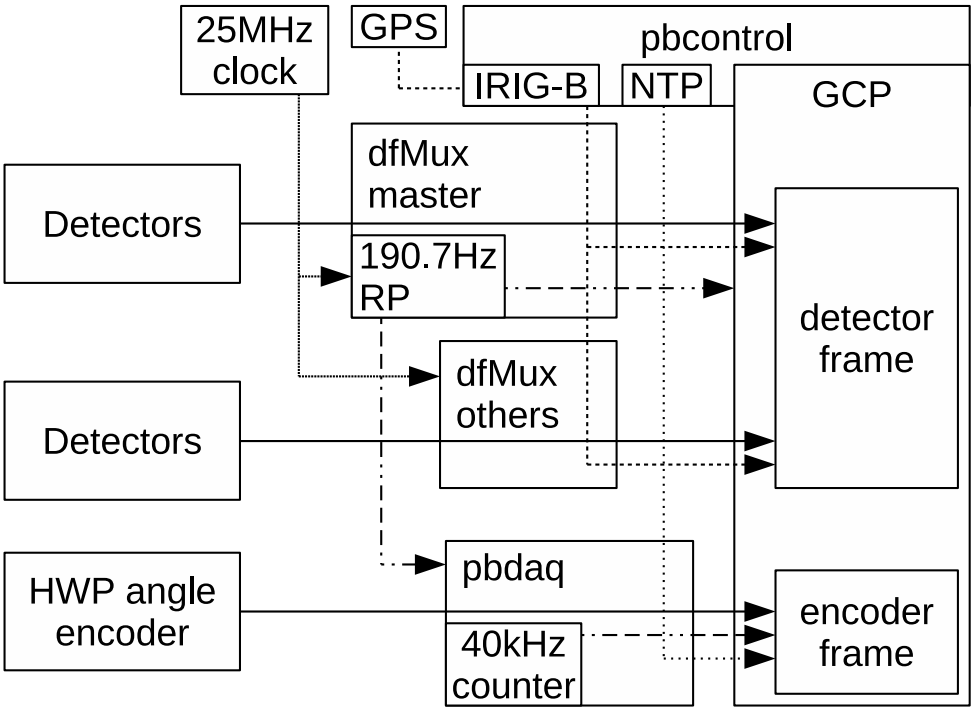

Figure 6.1.5: Schematic of the synchronization network. *DfMux* modules, which demodulate multiplexed detector signals, have a common external 25 MHz clock. They sample the demodulated signals at 190.73 Hz. They also read the IRIG-B signal from Global Positioning System (GPS) and append a time stamp to detector signals. As synchronized with the 190.73 Hz sampling, each of *dfMux* module generates a trigger pulse called RP. One of RP signals is distributed to *PBDAQ* and *GCP*. *PBDAQ* has its own clock and is monitoring signals at 40 kHz. When the edge of RP signal is detected, it samples data appending time stamp from Network Time Protocol (NPT) and value of the counter. *GCP* aggregates those data from *dfMux* and *PBDAQ* and packages them but into different frames.

Signals of detectors are collected by *dfMux* modules. All the *dfMux* modules are synchronized by an external 25 MHz clock. Each *dfMux* module downsamples the clock by a factor of 2^{17} and samples data every 5.2 ms. They also read the IRIG-B signal from GPS, and put time stamp for each sample. The detector timestream is passed to the *GCP* module, and packed into the detector frame.

On the other hand, the encoder signal is monitored and counted by a *PBDAQ* module at 40 kHz. The *PBDAQ* module also monitors a trigger signal from the *dfMux* module. When the trigger signal arrives, the *PBDAQ* sends the value of the counter to the *GCP* module with a time stamp synchronized with the NPT module. In addition, index of the sample, i. e. a counter which regularly counting up at 40 kHz, is also appended. Since the time stamp from NTP has

unacceptable jitter, we use the internal counter information to synchronize timestreams as described in section 7.2.1.

6.2 TEST OBSERVATIONS WITH THE CRHWP

The CRHWP was temporarily installed to the HTT in February 2014 as shown in Figure 6.2.1.

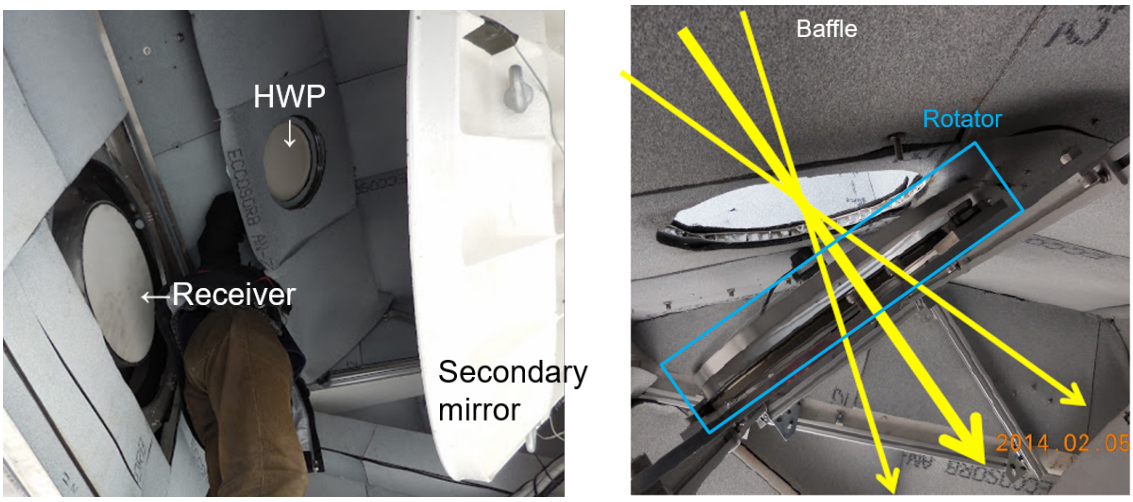

Figure 6.2.1: Deployment of the CRHWP

In this study, we use eight observations taken through the night on February 14th, 2014, six of which were CMB observations, one of which was a Tau A observation and one of which was a Jupiter observation. The data were taken at several different azimuths and elevations following the sky rotation. Each observation included a one-hour set of scans and two types of calibrations before and after the scan set.

The CMB data were acquired with CESs, in which we scanned the sky back and forth in azimuth at a constant elevation to keep the atmospheric loading on the detector as stable as possible, and to distinguish the sky signal from the ground pickup. The scan velocity was kept at 0.3°/s on the sky except during turnarounds. The scan width was 15° on the sky and the CRHWP was operating at 2.0 Hz.

The Tau A and Jupiter observations were used to calibrate the absolute angle and transmission of the CRHWP, respectively. Tau A, also known as the Crab nebula, is linearly polarized and it was also used to calibrate the relative polarization angle of the detectors in the analysis of previous science observations (The POLARBEAR Collaboration: P. A. R. Ade et al. 2014). Jupiter, which is one of the brightest sources in our band, was also regularly observed to determine the beam shape. Tau A and Jupiter were observed with raster scans, in which the elevation is kept constant across one stroke and is stepped by 2′ between strokes. The scan velocity was kept at 0.2°/s on the sky and the CRHWP was rotated at 2.0 Hz.

In the first calibration method, we used a device called the stimulator to identify optically-responsive detectors and to calibrate the properties of the detectors. The stimulator is placed at the back side of the secondary mirror and injects a chopped optical signal from a thermal source, which is kept at 700 °C, through a small hole on the secondary mirror. The chopper frequencies are changed in six steps from 4 Hz to 44 Hz. From the frequency dependence of

the amplitudes seen in the detector, we calibrated the responsivity and the time constant of each detector. The rotation of the HWP was stopped during the stimulator calibration.

For the other calibration method, called the elevation nod (el-nod), we moved the telescope up and down by 2° in elevation. This injects an intensity signal due to the thickness variation of the atmosphere. The CRHWP was rotated at 2.0 Hz during the el-nod calibration.

These calibrations were done sequentially; each calibration set before a scan set started from the stimulator followed by the el-nod. The order was reversed in the calibration after the scan set.

7

EVALUATIONS OF THE CONTINUOUSLY ROTATING HALF-WAVE PLATE

In this chapter, we evaluate the performance of the CRHWP using the data from the test observation described in section 6.2. Here, we investigate the following properties:

- the loading from the CRHWP in section 7.1,
- the angle reconstruction of the CRHWP in section 7.2,
- the instrumental beam characterization with the CRHWP in section 7.3,
- the HWP synchronous signal (HWPSS) and intensity to polarization (I→P) leakage in section 7.4,
- and the low frequency noise ($1/f$ noise) performance in section 7.5.

We also propose an simple and powerful method to subtract the I→P leakage in section 7.5.1.

Note that the impacts of these CRHWP performances on the B-mode angular power-spectrum measurement are discussed in chapter 8.

7.1 LOADING FROM THE CRHWP

Since the CRHWP system is an additional component in the optical system of the POLARBEAR experiment, it might increase the optical loading into detectors. The possible origins of the loading are the emission from the HWP due to the absorption in sapphire and ARC, and the truncation of the beam. The impact from the former is expected to be uniform across the detectors, while that from the latter would affect the peripheral detectors more. Note that the position of the CRHWP is placed at the position $\sim$ 11 cm behind the prime focus, thus we might have larger truncation than the optimal position.

We can estimate the loading from the CRHWP using the operation power of the detector, $\mathcal{P}_{\rm bias}$. In a quasi-steady state, the operation power balances with the other contributions as

$$-\mathcal{P}_{\rm bias} = \mathcal{P}_{\rm sky} + \mathcal{P}_{\rm load} - \mathcal{P}_{\rm bath} \quad , \tag{7.1.1}$$

where $\mathcal{P}_{\rm sky}$, $\mathcal{P}_{\rm load}$, and $\mathcal{P}_{\rm bath}$ are the loading from the sky, the loading from the instruments, and the heat release to the heat bath. The operation power is tuned before each observation to optimize the response of the detector. Assuming that the $\mathcal{P}_{\rm sky}$ and $\mathcal{P}_{\rm bath}$ do not change, we can obtain the variation of the instrumental loading from the variation of the operation power as $\mathcal{P}_{\rm CRHWP} = \Delta\mathcal{P}_{\rm load} = -\mathcal{P}_{\rm bias}$. In practice, both the $\mathcal{P}_{\rm sky}$ and $\mathcal{P}_{\rm bath}$ are not stable. Especially, the $\mathcal{P}_{\rm bath}$ dramatically changes depending on the bath temperature. Therefore, we cut the data within several hours from the end of the fridge cycle, where the base temperature is not stable enough. The loading from the sky also varies depending on the weather and the observing elevation. Such a variation could be a source of uncertainty of the CRHWP loading measurement.

To estimate the average operating power with the CRHWP, we use the data set from the last two days of the test observation, when the weather seems stable. For the estimation of that without the CRHWP, we use the data set from the three days following the test observation, expecting that the weather and the performance of the fridges are similar. We also calculate

the uncertainties of the estimated operating power from the standard deviation of the samples divided by square-root of the number of samples.

The estimated loading from the CRHWP system is shown in Figure 7.1.1 for each detector as a function of the position of the detector on the focal plane. We find clear increase of the loading for the peripheral detectors, especially in the upper-left part. To clarify such radial profile, we fit the distribution with a one-dimensional function of the radius from a specific center:

$$\mathcal{P}_{\mathrm{CRHWP}}(r) = \mathcal{P}_0 + \mathcal{P}_{300\mathrm{K}}\mathrm{erfc}\left[\sigma_{\mathrm{cut}} - \frac{r}{r_{1\sigma}}\right] \tag{7.1.2}$$

$$\text{with} \qquad r = \sqrt{(x - x_0)^2 + (y - y_0)^2} \quad , \tag{7.1.3}$$

where the first parameter $\mathcal{P}_0$ represents the uniform component and the second term represents the truncation effect. The detail of each parameter is available in Table 7.1.1. The radial profile is also shown in Figure 7.1.1 with the fitting curve, whose parameters are listed in Table 7.1.1. Note that a constant conversion factor $\eta = 0.18\,\mathrm{K_{RJ}/pW}$ is assumed to convert the electrical power to the Rayleigh-Jeans (RJ) temperature.

The overall trend of the observed radial profile well agrees with the model. Thus, the loading increase at the outer detectors could be due to the truncation of the beam. For the outermost pixels, the loading from the HWP is estimated as $\sim 30\,\mathrm{K_{RJ}}$, which corresponds to the truncation by 10%. For the uniform component, the loading is estimated as $\sim 6.7\,\mathrm{K_{RJ}}$, which corresponds to ~2% of the loss. The value is several times larger than the expected value of $\sim$ 0.3%. The discrepancy might come from the imperfection of the fitting model, which assumes one dimensional slice. In practice, however, the beam is truncated by a circular rim of the HWP. Therefore, the center pixel might have more contribution from the truncation than fitting model. On the other hand, the contribution from the HWP loss would decrease.

The additional loading from the CRHWP system may increase the detector noise, especially the photon noise (see section 1.4.1). If the optical loading increases from $33\,\mathrm{K_{RJ}}$ to $40\,\mathrm{K_{RJ}}$, the photon noise increases by $\Delta(\mathrm{NET}_\gamma^2) \sim (0.2\,\mathrm{mK}\sqrt{\mathrm{s}})^2$, which is negligible for our detector sensitivity.

Table 7.1.1: Parameters for the loading profile fitting.

Description	Parameter	Value	Fitting
Uniform component of the loading	$\mathcal{P}_0$	1.2 pW	(fit)
Loading from black body at room temperature	$\mathcal{P}_{300\mathrm{K}}$	54 pW	(fix)
Truncation position for center pixel	σ_{cut}	2.7	(fit)
Size of the beam	$r_{1\sigma}$	7.7 cm	(fit)
Position of the CRHWP center	x_0	0.1 cm	(fit)
	y_0	−1.4 cm	(fit)

7.2 SYNCHRONIZATION AND ROTATION STABILITY

Here, we describe the synchronization, the CRHWP angle decoding, and the rotation stability of the CRHWP. The details of the demodulation method are also described here.

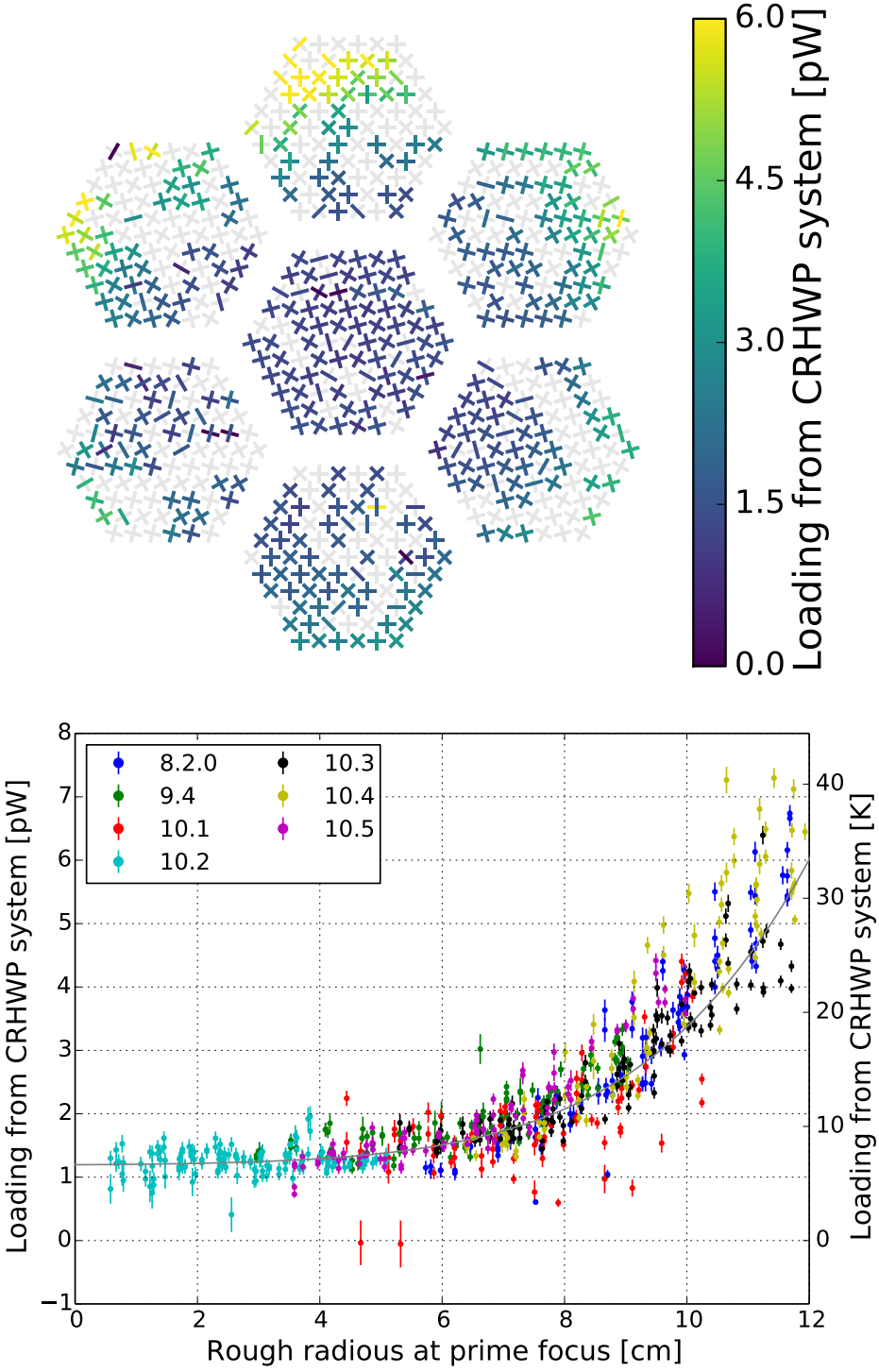

Figure 7.1.1: Loading from the CRHWP system. The upper figure shows the focal-plane distribution of the loading. Each rectangle represents each of the detectors. The lower figure shows the radial profile of the loading.

7.2.1 *Synchronization between the detector and the encoder*

As described in section 6.1.4, we use different modules, namely *dfMux* and *PBDAQ*, to record the detector timestream and the CRHWP angle. For further analyses, e. g. the demodulation of the detector timestream, the synchronization between the two modules is necessary.

In the data-taking stage, both the modules monitor a common trigger signal, and sample data almost at the same time, or a constant timing offset at least, which is less problematic. In the analysis stage, however, a serious problem described below has come up.

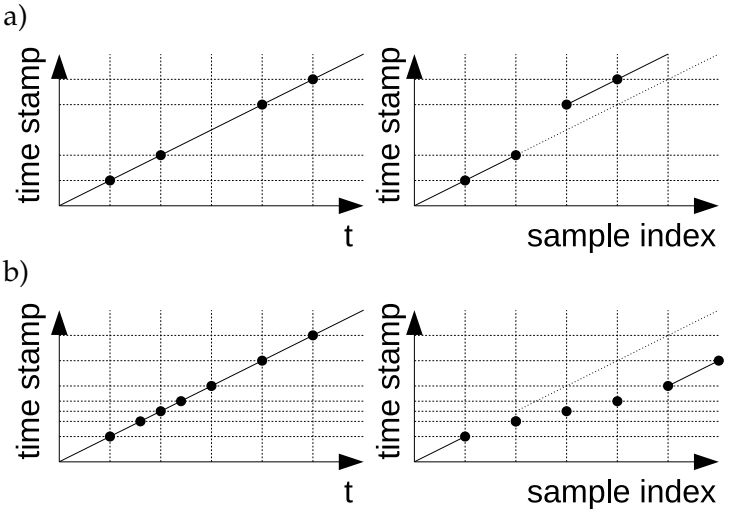

Figure 7.2.1: Illustrations of wrong samplings. The x-axis of left figures and that of right figures are actual time and sample index, respectively. The case of a missing sample is shown in the upper figures, a). In this case, the third sample is missing, which results in the delay of the time stamps of the following samples compared to the original value (dashed line). The lower figures, b), shows the case of a fake trigger event. In this case, additional sampling between the second and third has happened. Then the time stamps of the following samples move forward.

The origin of the problem is the issues in the sampling, namely the missing sample problem and the fake trigger problem. As illustrated in Figure 7.2.1, both the problems shift the TOD of each module independently. Then, if we read samples of the TODs one-by-one from both the modules, a problematic sample make the TODs misaligned. Besides, the time-stamp of the *PBDAQ* module is not synchronized with that of the *dfMux* module and has found to have a considerable variation by ~ 1 s (see Figure 7.2.3), which is too large to align samples with an accuracy better than the sampling period of 5 ms. On the other hand, the time stamp of the *dfMux* module is synchronized with the GPS module, and has a better stability. The *PBDAQ* module also has an counter counting up every $\sim 25\,\mu$s, which is defined by the internal clock frequency of the *PBDAQ* module, and less affected by the software problem. Although the counter does not has chronological information, it can be used to detect the sampling problems described above.

The method to correct the sampling problems is illustrated in Figure 7.2.2. We detect the problematic samples using the time-stamp difference between neighboring samples, remove the sample if necessary, and fill the missing samples by interpolating the data linearly. The lower panel of Figure 7.2.3 shows comparison of the time stamps between the *dfMux* module

and the *PBDAQ* module after the sampling correction. For the *PBDAQ* module, the internal counter information is scaled to the chronological information assuming the constant counting period. If there is any remaining problematic sample, we find a jump by the sampling period, i. e. 5 ms. Here, however, we do not see such a jump, which means that all the sampling problems are corrected. The gradual drift is caused by the variation of the clock frequency of the *PBDAQ* module.

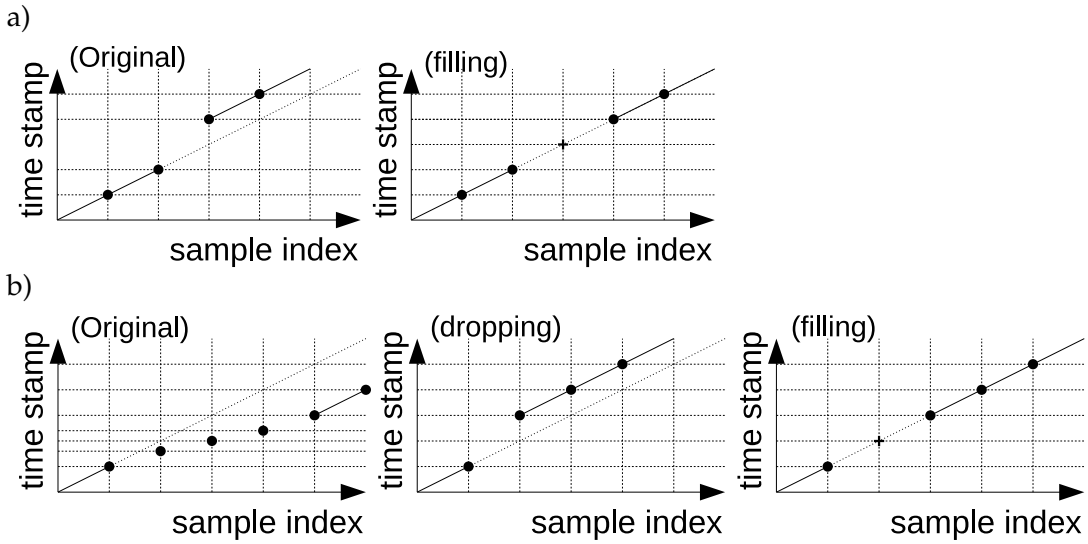

Figure 7.2.2: Illustrations of steps to correct wrong samplings, which are shown from left to right. In the case of a missing sample, a), first we esitimate the number of missing samples (which is one here), and fill the missing samples, which is shown as the point marked with +. In the case of a fake trigger event, b), first we drop the suspicious samples which have abnormal interval to neighboring samples. Then we fill dropped samples in the same manner with the former case.

Furthermore, we can fix the constant offset between the two timestreams using the small time stamp deviation less than 5 ms, which can be seen as several spikes in Figure 7.2.3. Such a small time stamp deviation is caused by the sampling phase change, which happens at the beginning of each observation when we synchronize the *dfMux* module. Figure 7.2.4 shows an example of the resetting event. A few second before the reset, the *dfMux* module stops sampling but still continues to generate the trigger signal until ~ 50 ms before the reset. After the synchronization, the *dfMux* module restarts the sampling and the trigger signal generation. Since the *PBDAQ* continues sampling at the timing of the trigger signal, we can align the two timestreams by matching the restarted samples.

Following the processes described above, we can successfully synchronize the detector timestream and the encoder timestream. Note that this synchronization is critical for the polarization angle calibration. As described in section 5.4.5, the time offset between the detector and the encoder becomes an error of the CRHWP angle, which changes the polarization angle and also causes noise.

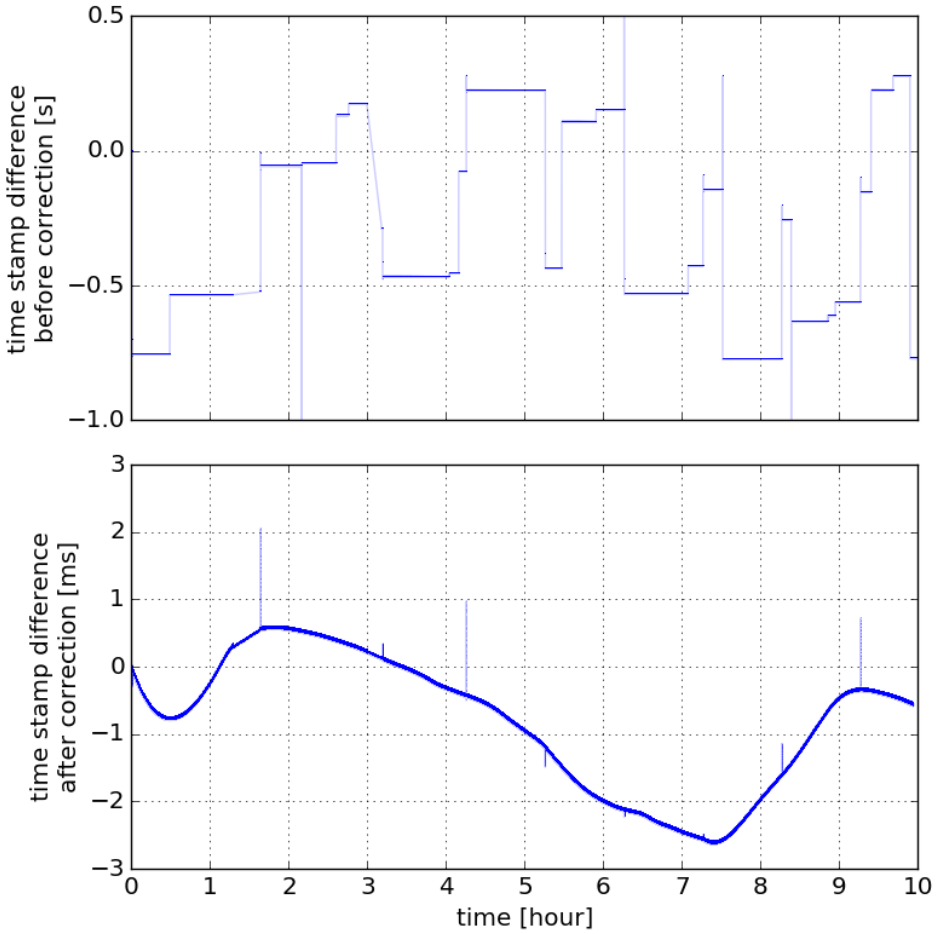

Figure 7.2.3: These figures show the difference between the time stamp of detector and that of encoder as a function of time before the correction (upper) and after the correction (lower). Before the correction, there are many jumps, which are caused by the missing samples in both the detector and encoder data, or fake trigger in encoder data. The amplitude of jump naively represents the number of wrong samples. After the wrong sampling correction, there are no jumps larger than the interval of 5 ms, which means that there is no misalignment between the detector and encoder. A gradual drift comes from frequency jitter of the clock on *PBDAQ*, The thickness of the curve is 25 µs, which is the resolution of 40 kHz counter on *PBDAQ*. Some small spikes are caused by resetting of the RP pulse which happen at the beginning of each observation (see Figure 7.2.4).

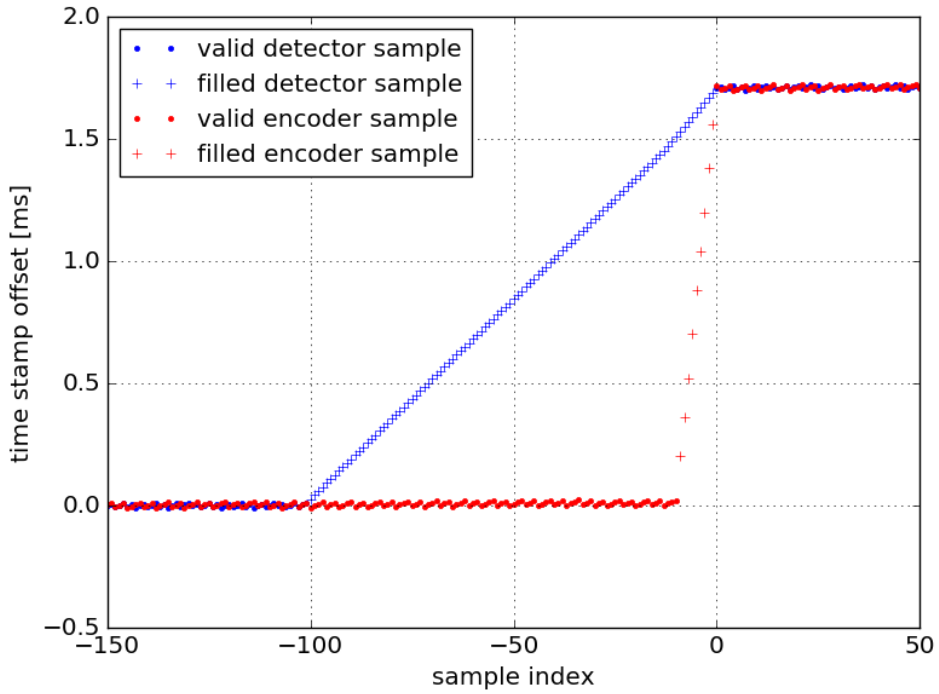

Figure 7.2.4: An example of an RP signal resetting event. It shows the time stamp of detector or encoder data as offset from the uniform sampling, which is expected to stay around zero with small fluctuation due to time stamp resolution. However, we can find a step of ~ 1.7 ms in this example, which is not a multiple of the sampling interval, 5.24 ms. This event could be due to resetting of the RP pulse, which stopped at $x = -10$ and restarted at $x = 0$, here, as shown in the encoder samples. The detector samples started to be missing at $x = -100$ before the RP pulse stops, which was probably because the *dfMux* board was preparing for the resetting. Since the timing of the restarted RP pulse should be the same between the detector and encoder samples, we can determine the offset between the two.

7.2.2 *The angle decoding of the CRHWP*

Next, we describe the method to decode the angle of the CRHWP. The encoder signal consists of two incremental signals and one index signal at the origin of the angle. The *PBDAQ* module counts up the incremental signals, which is reset to zero by the index signal. We can obtain the CRHWP angle by scaling the counter information into radian. However, the counter sometimes miscounts an accidental electrical noise, which needs to be removed. Besides, the timestreams sometimes have missing samples (see section 7.2.1), which need to be interpolated correctly. After such corrections, we obtain the raw CRHWP angle timestream.

However, each sample of the raw angle data has an uncertainty of $\sim 0.1°$ as shown in Figure 7.2.5, which is consistent with the expectation due to the backlash of the gears (see section 6.1.3).[1] Since the rotation of the rotator has substantial amount of inertia compared to that of the pinion gear or the motor, the actual rotation of the rotator should be stable than the encoded angle. Thus, we fit the raw angle timestream with polynomials as a function of time, and interpolate the angle using the time stamp.[2] Figure 7.2.5 also shows the interpolated angle data as a green line, which are used in the following analyses. Note that Figure 7.2.5 shows a deviation of the angle from that of the constant speed rotation with constant sampling frequency, i. e. the jitter of the sampling frequency affects the plot. Without the effect, the rotation is more stable as shown as the yellow line in Figure 7.2.5.

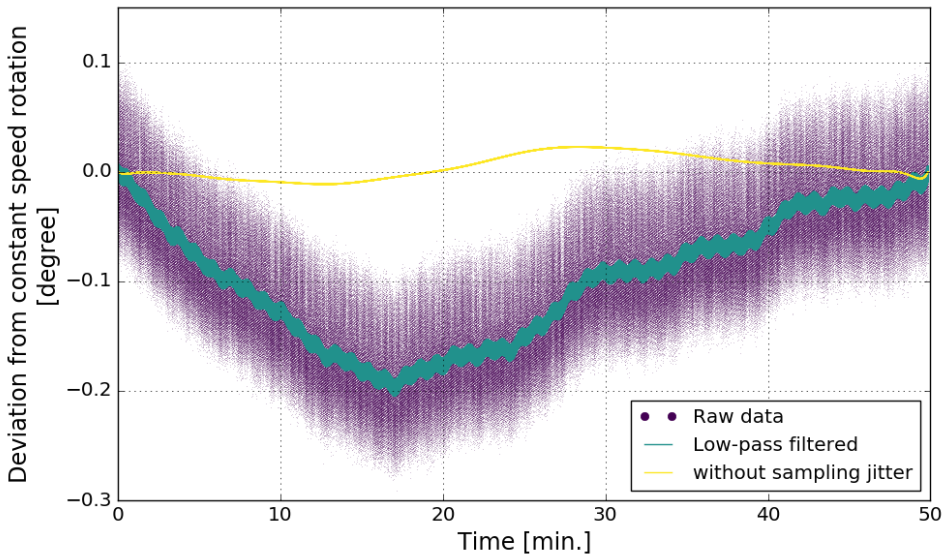

Figure 7.2.5: An example of the CRHWP-angle TOD as a deviation from a constant speed rotation. The purple points show each sample of raw encoded angle. The blue line shows the low-pass filtered data, which are used in the following analyses. The yellow line shows the same low-pass filtered data without the effect of the sampling non-uniformity.

In addition, Figure 7.2.6 shows the PSDs of the angle timestreams explained above. We can find that the interpolation improves the PSD by more than two orders of magnitudes. Without this interpolation, the noise due to the angle error dominates the noise in the de-

1 The resolution of the encoder is 0.03°.

2 The resolution of the time stamp is $\sim 10\,\mu s$, which corresponds to 0.007° at the rotation speed of $\omega_{rot}/(2\pi) = 2.0\,Hz$.

modulated data, which means that the assumption of the stable rotation is reasonable. In the raw angle PSD, there are prominent spikes at 4 Hz and 8 Hz, which are higher harmonics of the rotation speed of $\omega_{\rm rot}/(2\pi) = 2.0$ Hz. They might be the actual fluctuation of the rotation which should not be removed by the interpolation. Removing the actual rotation could cause residuals in the HWPSS removal. However, such harmonics might be as stable as the rotation speed. Since the powers of the harmonics are orders of magnitudes smaller than that of the overall rotation by $\lesssim 10^{-7}$, their sidebands might also smaller than that of the overall rotation, which is shown as the yellow line, at the same level. Therefore, the contributions in the detector noise from the harmonics are negligible. Both the wide bump around 40 mHz and the spike at 16 mHz are not the actual rotation fluctuation. The former is caused by quantization noise of the encoder with a long period, and the latter is caused by the jitter of the clock frequency.

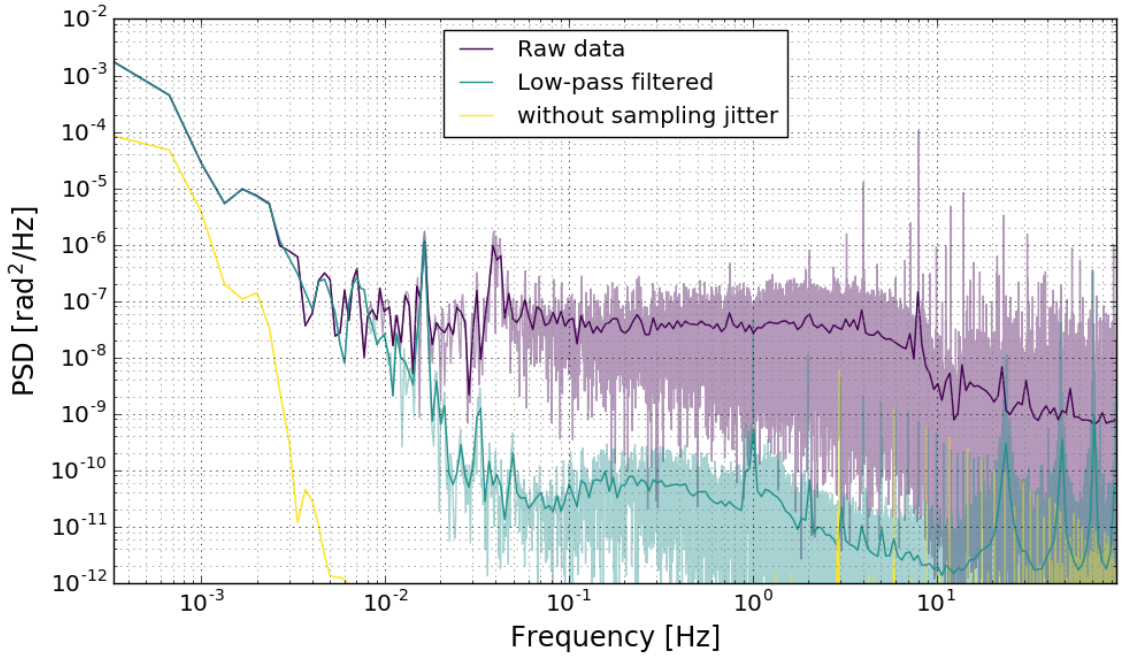

Figure 7.2.6: PSDs of Figure 7.2.5. The thin lines show raw spectra without binning, and the thick lines show logarithmically binned spectra.

7.2.3 *Demodulation*

We then extract intensity and polarization components from the calibrated data, $d'_m(t)$ using the demodulation method (Johnson et al. 2007; Kusaka et al. 2014) as described in section 5.1.3. The intensity component was obtained by applying a low-pass filter up to 3.8 Hz by convolving finite impulse response (FIR) window filters. To extract the polarization component, we first apply a band-pass filter around the modulation frequency with a ± 3.8 Hz band, then multiply the demodulation function by $2e^{4i\theta_{\rm enc}(t)}$, and apply a low-pass filter with the identical cut-off frequency. After the low-pass filtering, we downsample the timestreams by a factor of 24, down to 7.95 Hz. The 3.8 Hz band (corresponding to a maximum multipole ℓ of 4,560)

is selected as slightly less than twice of the frequency of the CRHWP rotation, 2.0 Hz, with 0.2 Hz margin to cut the sidebands of $n = 2$ HWPSS.

For the polarization component, there are three effects which need to be corrected. One is the time-constant of the detector, τ, which delays the phase of the modulated polarization signal by $\sim 9^\circ$ and also decreases the response to the signal by $\sim 1\%$. This effect is corrected from the polarization component by multiplying by the inverse of the effect, $(1 - i\omega_{mod}\tau)$, where τ is calibrated with the stimulator data. Another effect is the polarization angle rotation due to the detector angle, θ_{det}, and the origin of the encoder, θ_o, which is corrected by multiplying a factor, $e^{2i\theta_{det}+4i\theta_o}$, where θ_{det} is calibrated in the science observation (The POLARBEAR Collaboration: P. A. R. Ade et al. 2014) and θ_o is determined from the Tau A observation to keep its angle consistent. After the correction, the real part and imaginary part of the polarization signal become Stokes Q and U with respect to the global instrumental coordinates defined by (El, Az). The other is the polarization efficiency, ε, which will be considered in a future paper.

7.3 BEAM

In this section, we evaluate the performance of the beam in observations using the CRHWP. First, we evaluate the beam pattern for each pixel using the Jupiter observation data, and estimate the impact of the CRHWP on the beam size magnification and the transmission. We also calibrate the polarization angle using the Tau A observation data. Next, we calculate the average beam patterns and evaluate the I→P leakage using the Jupiter data, and **Q↔U** mixing using the Tau A data.

7.3.1 *Representative beam parameters for each detector*

Here, we evaluate the impact of the CRHWP on beam patterns for each detector by comparing the values from the observations with and without the CRHWP. We focus on the beam size magnification and the transmission. The former might be caused by the defocus of the beam due to the sapphire plate with high refractive index, or the truncation at the rim of the CRHWP. The latter is also caused by the transmission of the HWP or the truncation as discussed in section 7.1.

The beam patterns for each detector could have various fine structures due to diffraction and/or aberration. Here, however, we ignore such structures and fit the beam pattern with a single elliptical Gaussian pattern to extract the six representative parameters, namely the amplitude of the signal, angular offsets from the boresight, sizes of the beam in the long axis and short axis directions, and the rotation angle of the ellipse. For each detector, we fit the detector timestream with the elliptical Gaussian pattern using the boresight pointing information. The analysis procedure for the data using the CRHWP is almost common with that applied for the data without the CRHWP (The POLARBEAR Collaboration: P. A. R. Ade et al. 2014), except the HWPSS removal using the CRHWP angle information. The results of the fitting are shown in Figure 7.3.1.

The beam size is obtained from the diameters of the elliptical Gaussian as $\sigma = \sqrt{\sigma_1 \sigma_2}$, where σ_1 and σ_2 are the diameter of the long- and short-axes. We compute the beam size for each of the data from Jupiter observations with and without the CRHWP, and evaluate the beam size magnification as the ratio of the two. The results are shown in Figure 7.3.2. We find

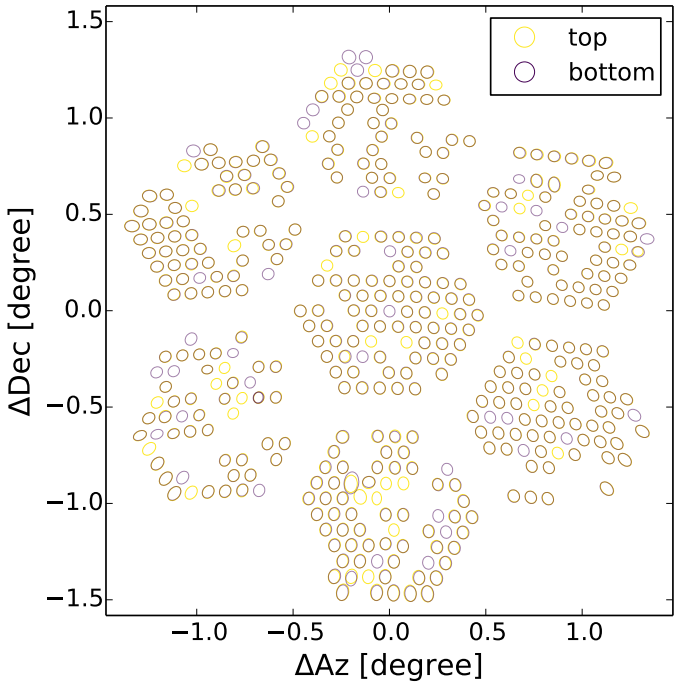

Figure 7.3.1: The beam shapes for the detectors modeled by elliptical Gaussian patterns. Each ellipse represents the position of the detector from the boresight, and the FWHM of the fitted elliptical Gaussian pattern. Each pixel consists of two orthogonal detectors sensitive to single polarizations, thus the two are addressed as a top detector and a bottom detector, and shown with different colors.

the beam size magnification is almost uniform among all the detectors, and the average value is 102%.

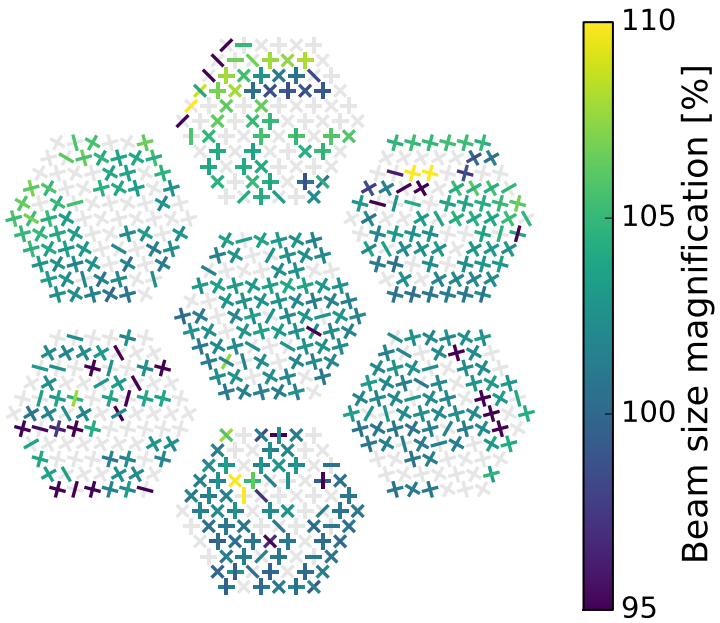

Figure 7.3.2: Distribution of the beam-size magnification due to the CRHWP system.

The transmission of the CRHWP, which corresponds to the parameter $\mathcal{T}$ in section 5.5, can be evaluated from the ratio of the total flux of the beam, which is proportional to $\tilde{A}\sigma_1\sigma_2$, where $\tilde{A}$ is the amplitude of the elliptical Gaussian beam calibrated by the thermal source. Note that the thermal source is placed at the position behind of the secondary mirror, thus the CRHWP at the prime focus does not affect the calibration signal. The results are shown in Figure 7.3.3. Here, we find that the peripheral detectors have lower transmission, which is similar to the feature found in the loading from the CRHWP (see section 7.1). Therefore, we again plot the transmission data as a function of the radius from the specific center as shown in Figure 7.3.3. The measured transmission is consistent with the expectation from the properties of the HWP obtained from the laboratory measurement (see section 6.1.2) and the truncation effect evaluated in section 7.1. In the following analyses, we correct this transmission using the average value for each wafer, which is listed in Table 7.3.1.

Next, we calibrate the polarization angle using the Tau A observation. Tau A is one of the brightest polarized sources. The polarization fraction of Tau A is $\sim 9\%$, and the polarization angle is measured as $\sim 150^\circ$ (Aumont et al. 2010). The detector measures the polarization signal with the instrumental absolute angle error. Using the measured Tau A angle as a reference, we calibrate the instrumental angle error. Note that the CRHWP introduces additional angle errors, θ_o, due to e. g. an offset between the birefringent axis and the origin of the encoder.

First, we analyze the detector timestream of the Tau A observation, and determine the instrumental polarization angle for each detector as follows: we fit the intensity timestream with the elliptical Gaussian pattern, and then we fit the (demodulated) polarization timestreams, $[Q_{obs} + iU_{obs}](t)$, again with the same elliptical Gaussian parameters except the amplitude, $\tilde{A}_{Q+iU}$, which results in the detector angle as $\theta_{TauA} + \theta_o = \frac{1}{2}\arctan[\tilde{A}_{Q+iU}]$. Next, we com-

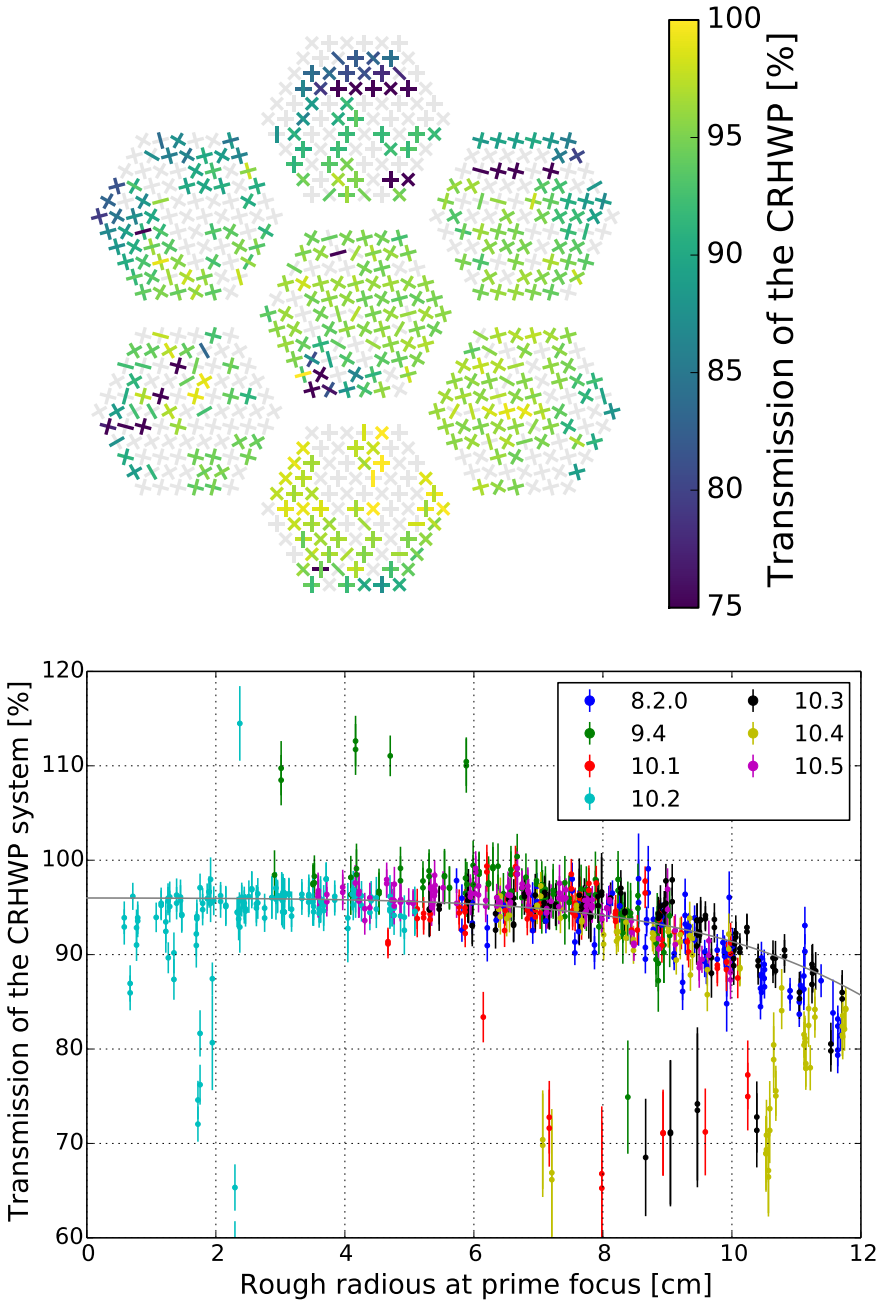

Figure 7.3.3: Distribution of the transmission of the CRHWP system.

Table 7.3.1: Estimated transmission of the CRHWP system for each device wafer.

Device wafer	Transmission (%)
8.2.0	91.2 ± 0.4
9.4	96.6 ± 0.2
10.1	93.9 ± 0.3
10.2	94.9 ± 0.2
10.3	93.2 ± 0.3
10.4	91.0 ± 0.5
10.5	95.3 ± 0.2
all	93.6 ± 0.1

pare the polarization angles with those calibrated in the observations without the CRHWP, and estimate a single value of the absolute angle offset due to the CRHWP. Finally, we use the polarization angle from the observations without the CRHWP adding the estimated angle offset.

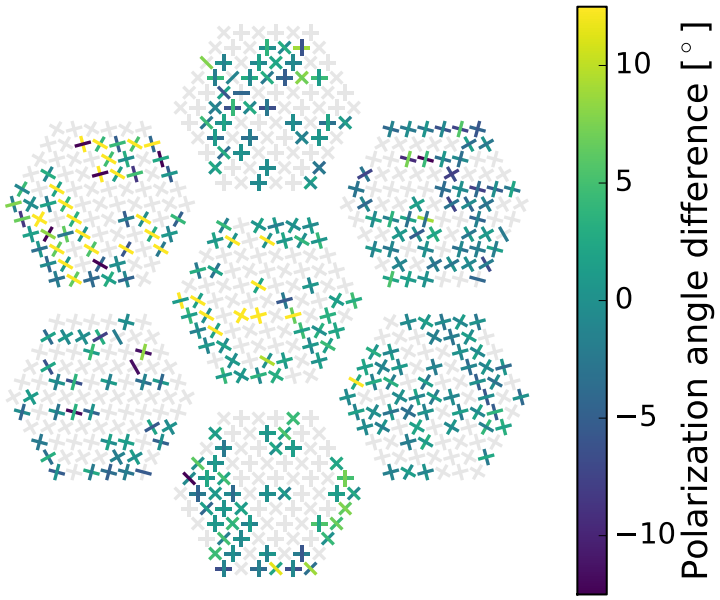

Figure 7.3.4: Polarization angle difference between the observations with and without the CRHWP.

7.3.2 *Average beam patterns*

We evaluate the intensity beam as well as the I→P leakage beam combining all the detector timestreams. The former can be used for the absolute responsivity calibration, and the beam profile estimation (Boettger 2014). Since the analysis is common with that for the data without

the CRHWP, we just show the result map, and skip the detail of the analysis here. On the other hand, the latter is a new feature of the CRHWP as described in chapter 5, and is necessary to estimate the instrumental systematic uncertainties due to the beam imperfections.

We can estimate the intensity beam from the Jupiter observation data, since the Jupiter is unpolarized to a good approximation. Using the beam offset information from section 7.3.1, we project the detector timestream into a map matching the position of Jupiter. We average the projected timestreams for each sky pixel with inverse-variance weighting. The result is shown in Figure 7.3.5. We can see a beautiful Gausian beam pattern.

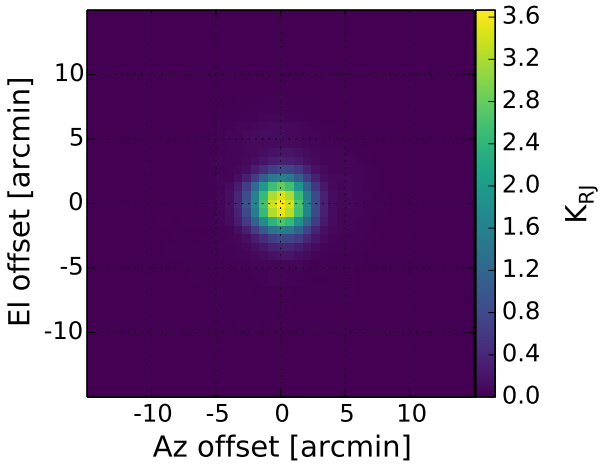

Figure 7.3.5: coadded Jupiter map

The I→P beam can be obtained from the polarization map of the Jupiter observation, assuming the absence of the intrinsic polarization. We again project the demodulated polarization timestream onto the sky, and take average among the detectors as is the case for the intensity.[3] The results are shown in Figure 7.3.6. Since the polarization signal consists of Stokes Q polarization and U polarization, we have the leakage beam for each polarization. Note that the polarization angle is calibrated using the Tau A observation as described in section 7.3.1, and the coordinates defining the Q and U are set to the instrumental coordinates instead of the sky coordinates. The most prominent feature in Figure 7.3.6 is the monopole pattern in the $I \to Q$ leakage beam. By comparing the signal amplitude between the intensity beam and the leakage beam, we can estimate the leakage coefficient as $\sim 0.5\%$. It can be caused by the I→P leakage from the primary mirror, and/or the detector non-linearity as described in chapter 5. We discuss this monopole leakage more in the later section.

Note that the I→P leakage beam evaluated above is the $n = 4$ case of the I→P beams, $\mathcal{B}^{I}_{n}(\vec{n})$, described in section 5.2.4. We can also evaluate the leakage beam for other harmonics by mapping the demodulated timestream of corresponding harmonics. Such a leakage beam into harmonics other than the $n = 4$ polarization signal could become important to evaluate the instrumental systematic errors due to the aliasing. Here, however, since the aliasing effect is expected to contribute in small-angular scale mainly, we assume that the effect is negligible at this stage.

3 Thanks to the CRHWP, we do not necessarily solve a matrix inversion, which is necessary for the case without the polarization modulation.

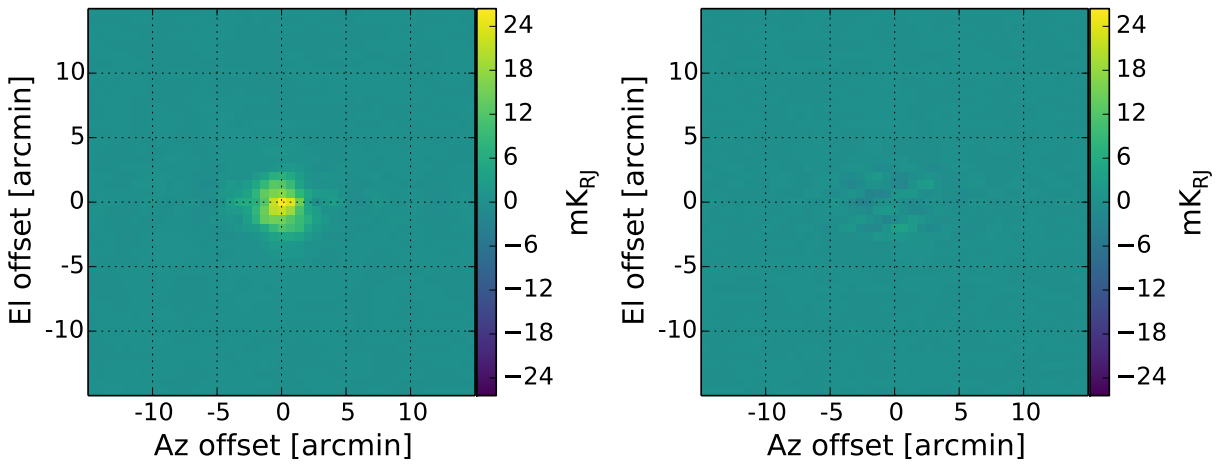

Figure 7.3.6: Polarization maps of Jupiter. The left and right panels shows the Stokes Q and U polarization signals with respect to the instrumental coordinates, respectively.

Next, we evaluate the beam patterns for the polarization signal using the averaged map of the Tau A observation data. The map-making procedure is common with that performed to make the Jupiter maps (Figure 7.3.5 and Figure 7.3.6). The Tau A intensity (I) map and polarized intensity ($P = \sqrt{Q^2 + U^2}$) map are shown in Figure 7.3.7.

We estimate the polarization efficiency, ε in chapter 5, from the Tau A maps. The average polarization fraction, $\langle P/I \rangle$, within the 5 arcmin radius from the center is calculated to be $6.3 \pm 0.5\%$, where the error is taken from the I→P leakage in the Jupiter data. By comparing the polarization fraction we observed with Aumont et al. 2010, the polarization efficiency is estimated as $\varepsilon = 86 \pm 11\%$.

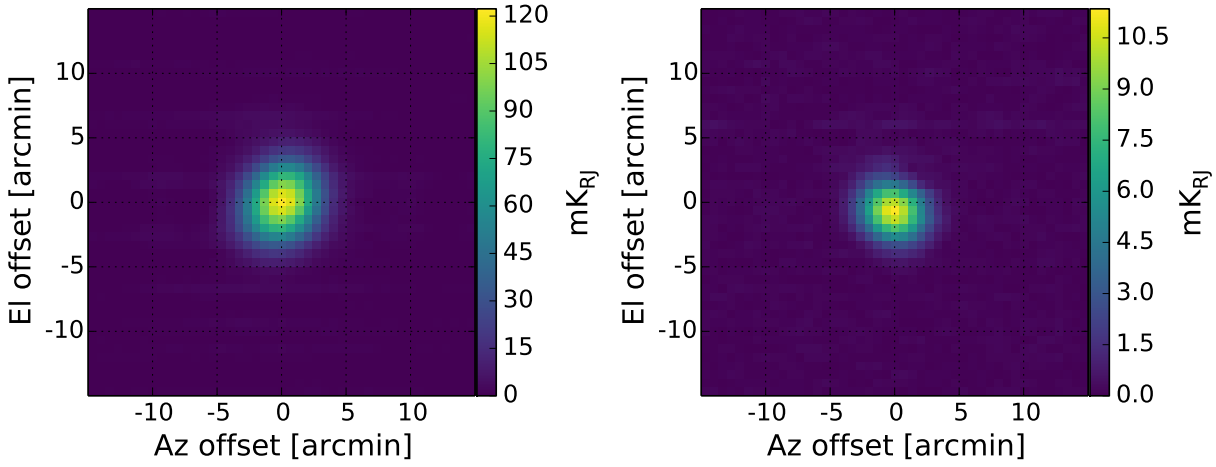

Figure 7.3.7: Intensity and polarization maps of Tau A observation. The left panel shows the intensity signal, and the right panel shows the amplitude of the polarization signal.

Finally, we evaluate the $Q \leftrightarrow U$ mixing beam, especially, the parity-conserving mode, i. e. the imaginary part of the $Q + iU \rightarrow Q + iU$ beam.[4] Basically, we can measure the $Q \leftrightarrow U$ mixing beam by observing the source contains only the Q component, and measuring the U component in the observed data. In practice, because of the parity-conservation, the source signal is not necessarily a purely Q signal, nor we do not need to know the polarization angle of the signal, as far as the signal is purely polarized. We rotate the polarization angle of the measured polarization signal $Q + iU$ by multiplying a rotation factor, $e^{i\xi}$, to make the direction of the prominent signal becomes real. Then, we can obtain the $Q \leftrightarrow U$ mixing beam as the imaginary part of the rotated beam. However, since Tau A is a diffused source compared to our beam size, the imaginary part of the rotated beam contains the intrinsic structure. To distinguish the instrumental beam effect and the intrinsic structure, we make beam maps for the device wafers located in different position on the focal plane, and measure the difference from the average beam among all the detectors.

Figure 7.3.8 shows the real part and the imaginary part of the all-detector-averaged polarization map of Tau A after the polarization angle rotation. The dipole structure in the imaginary part comes from the intrinsic polarization angle variation of Tau A. The $Q \leftrightarrow U$ mixing map after the intrinsic structure subtraction is shown in Figure 7.3.9, where the $Q \leftrightarrow U$ mixing map for the center wafer and that for one of the peripheral wafers are shown. The former has no significant structure around the center region, while the latter has a dipole pattern, which is consistent with the expectations (see Appendix B). Comparing the $Q \leftrightarrow U$ mixing signal with the amplitude of the original Q polarization, we can estimate the leakage coefficient of the dipole as $\sim 4\%$. In the following chapter, we evaluate the impact of this $Q \leftrightarrow U$ mixing on the instrumental systematic error of the B-mode angular power-spectrum measurements.

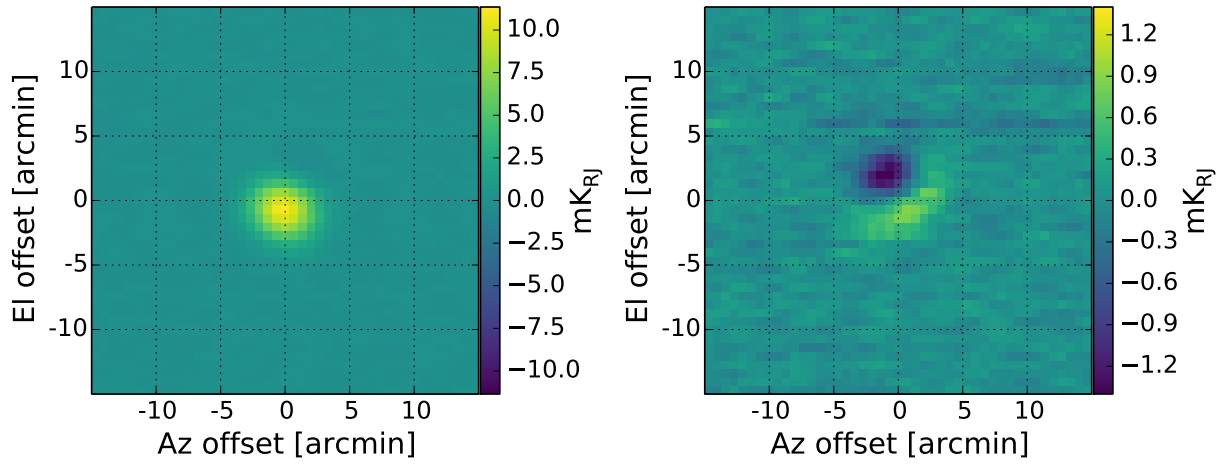

Figure 7.3.8: Polarization maps of Tau A averaged among all the detectors after the polarization angle rotation. The left panel is the Q-polarization map, which shows the main component of the linear polarization of Tau A. On the other hand, the right panel is the U-polarization map, which shows the small intrinsic structures reflecting the variation of the polarization angle.

4 We potentially have parity-violating modes as $Q + iU \rightarrow Q - iU$, however, their contributions are expected to be small.

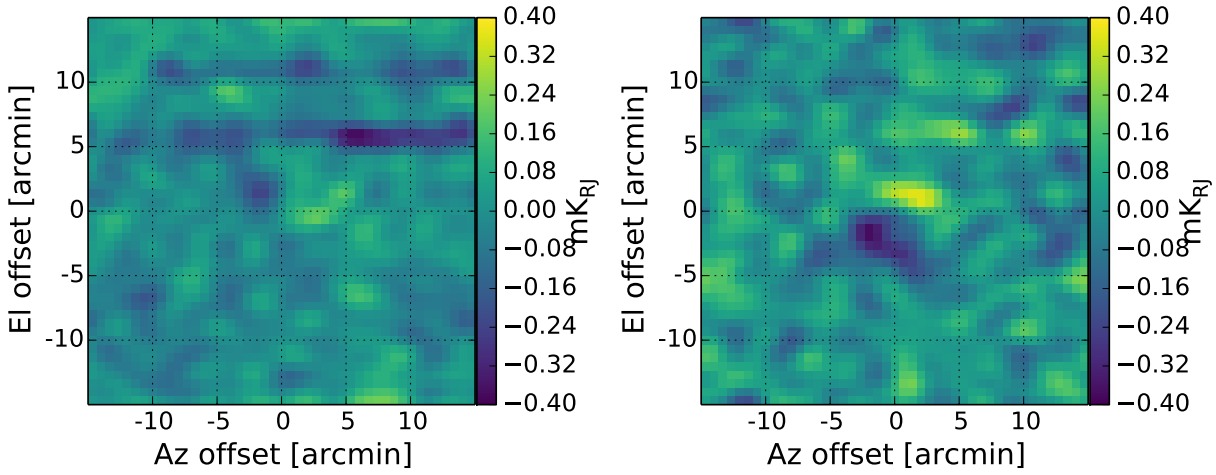

Figure 7.3.9: Examples of Q↔U mixing beam. The left panel and the right panel show the Q↔U mixing beam at the center on the focal plane (wafer-10.2) and the upper right on the focal plane (wafer-10.3), respectively. These maps are smoothed by convolution with a Gaussian of FWHM=1.75′.

7.4 HWPSS AND LEAKAGE

In this section, we evaluate the properties of the HWPSS, $A_n(t)$, introduced in chapter 5. Although we can consider all the harmonics of $n = \{1, 2, \cdots\}$, here, we focus on the $n = 4$ harmonic, which corresponds to the polarization signal. As described in section 5.5, we separate the time variation of the HWPSS into two time-scales as

$$A_4(t) = A^{(0)}_{4|\langle I_{in}\rangle} + \lambda_4^{opt} \Delta I_{in}(t) \quad , \tag{7.4.1}$$

where the first term is the average of the HWPSS during one observation, and the second term is the I→P leakage. We assume that the origins of the HWPSS variation other than I→P leakage, e. g. the temperature variation of the primary mirror, are negligible. Note that the former also changes observation-by-observation as a function of the average of the total intensity, $\langle I_{in}\rangle$. The purpose of this section is to measure the two parameters, $A^{(0)}_{4|\langle I_{in}\rangle}$ and λ_4^{opt}.

In practice, the detector signal is affected by the detector non-linearity as described in section 5.3.2. Then, the leakage coefficient is modified as Eqs. (5.5.14) and (5.5.16) as

$$\lambda_4' \equiv \lambda_4^{opt} + \lambda_4^{nl}, \tag{7.4.2}$$

where λ_4^{nl} is the additional leakage due to the detector non-linearity, which is obtained as

$$\lambda_4^{nl} = 2g_1 A^{(0)}_{4|\langle I_{in}\rangle} + i4\omega_{rot}\tau_1 A^{(0)}_{4|\langle I_{in}\rangle} \quad , \tag{7.4.3}$$

where the first term comes from the non-linearity of the detector responsivity, and the second term comes from the non-linearity of the detector time constant. Therefore, we need to separate λ_4^{opt} and λ_4^{nl}.

7.4.1 *Methods to measure leakage*

To distinguish the leakage from the optics and that from the non-linearity, we perform three methods :

METHOD A : Using the average of the instrumental polarization[5]

In this method, we use the amplitude of the instrumental polarization, which mainly comes from the polarized emission of the room temperature mirror.[6] As described in Eq. (5.2.13), the HWPSS from the primary mirror becomes

$$A^{(0)}_{4|\langle I_{in}\rangle} = \lambda_4^{opt}(\langle I_{in}\rangle - I_{mirror}) \tag{7.4.4}$$

Thus, we obtain the optical leakage

$$\lambda_4^{opt} = -\frac{\left\langle\!\left\langle A^{(0)}_{4|\langle I_{in}\rangle}\right\rangle\!\right\rangle}{\langle\!\langle I_{mirror} - \langle I_{in}\rangle\rangle\!\rangle}\,, \tag{7.4.5}$$

where the double angle bracket represents average among observations.[7] Here, the instrumental polarization, $A^{(0)}_{4|\langle I_{in}\rangle}$, is obtained from the average of the polarization signal. The intensity from the mirror is assumed to be the Rayleigh-Jeans emission with the temperature of the mirror, T_{mirror}, which is measured using a thermometer. The total intensity from the sky, $\langle I_{in}\rangle$, can be obtained from the el-nod observation or external precipitable water vapor information.

METHOD B : Using the variation of the instrumental polarization[8]

In this method, we use the variation of the instrumental polarization $A^{(0)}_{4|\langle I_{in}\rangle}$ correlated with the total intensity $\langle I_{in}\rangle$, which will vary depending on the observing elevation and/or weather.[9] Using the derivative of Eq. (7.4.4), we can obtain the optical leakage from the slope of the correlation as

$$\lambda_4^{opt} = \frac{\Delta A^{(0)}_{4|\langle I_{in}\rangle}}{\Delta\langle I_{in}\rangle}\,, \tag{7.4.6}$$

where Δ represents variation among observations e.g. $\Delta\langle I_{in}\rangle \equiv \langle I_{in}\rangle - \langle\!\langle \langle I_{in}\rangle\rangle\!\rangle$.

METHOD C : Using the leakage in the timestream[10]

In this method, we take the correlation between the intensity and polarization timestreams for each observation. Using the derivatives of Eq. (5.5.11) and Eq. (5.5.13), the slope of the correlation results in the total leakage as

$$\lambda'_4 = \frac{\delta d_4(t)}{\delta d_0(t)}\,, \tag{7.4.7}$$

where δ represents variation during each observation: e.g. $\delta d_4(t) \equiv d_4(t) - \langle d_4\rangle$. The total leakage, λ'_4, includes both the effects from optical and the detector non-linearity.

5 This method can be applied to optical systems in which all the optical elements between the CRHWP and the sky are reflective.

6 We assume that the contribution from the non-ideality of the HWP on $n = 4$ HWPSS, $A^{(0)}_{4|\langle I_{in}\rangle}$, is small compared to that from the instrumental polarization here.

7 One observation can be a CMB scan set or an el-nod calibration, but we use only el-nod here to combine with the total intensity measurement.

8 This method is performed in Essinger-Hileman et al. (2016).

9 We assume that T_{mirror} is stable compared to the variation of $\langle I_{in}\rangle$, here. This assumption is consistent with the measurement (see section 7.4.2.1). A possible effect from the T_{mirror} variation is discussed in section 5.4.3.

10 This method is performed in Johnson et al. (2007).

Note that we need many observations to obtain the leakage in the method A or B, while we do only one observation in C. In other words, the timescale is longer than the calibration period for the method A or B, while not for C. That is the reason why we see the effect from the non-linearity of the detector only in the method C.

7.4.2 *Results of the leakage measurements*

In this section, we describe the measurements of the I→P leakage in the POLARBEAR experiment. First, we perform the methods A and B using the el-nod data. Then, we perform the method C with the el-nod data and the CMB scan data.

7.4.2.1 *Methods A and B : $\lambda_4^{\rm opt}$ measurements using instrumental polarization*

To perform methods A and B described in section 7.4.1, we need the $n = 4$ HWPSS, $A^{(0)}_{4|\langle I_{\rm in}\rangle}$, the total intensity from the sky, $\langle I_{\rm in}\rangle$, and the temperature of the mirror, $T_{\rm mirror}$.

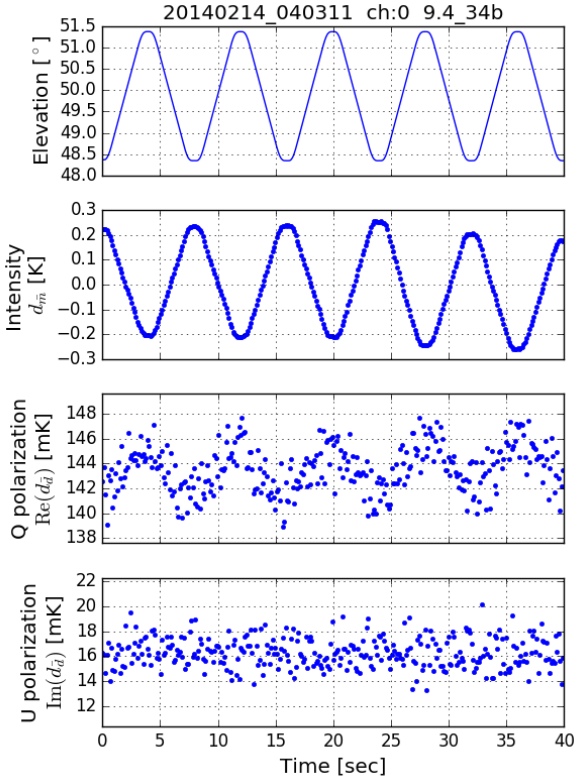

Figure 7.4.1: Example TOD from an el-nod observation. The top panel shows the observing elevation. The second panel shows the intensity signal. The third panel shows the real part of the polarization signal. The fourth panel shows the imaginary part of the polarization signal. The intensity signal depends on the thickness of the atmosphere along the line of sight combined with a small 1/f noise component. The real part of the polarization signal shows variation from I→P leakage above the white noise.

The former two can be obtained from the el-nod observation. Figure 7.4.1 shows example time-ordered data (TOD) in an el-nod observation. The $n = 4$ HWPSS, $A^{(0)}_{4|\langle I_{\rm in}\rangle}$, is obtained

as the mean value of the polarization timestream, $\langle d_4 \rangle$ (see Eq. (5.5.13)). The total intensity from the atmosphere, on the other hand, cannot be measured as the average of the intensity timestream, since the detector is only sensitive to the relative variation and there is larger uncertainty in the absolute value. Here, we model the total intensity from the sky as follows:

$$I_{in}(t) = I_0 + T_{atm} \frac{\csc \mathrm{EL}(t)}{\langle \csc \mathrm{EL} \rangle} , \tag{7.4.8}$$

where, I_0 is the contribution from the CMB, which is 1.6 K_{RJ} in the Rayleigh-Jeans temperature,[11] and the second term is the elevation-dependent intensity from the atmosphere, which is proportional to the cosecant of the elevation, $\mathrm{EL}(t)$. The average and fluctuation of the total intensity become

$$\langle I_{in} \rangle = I_0 + T_{atm} , \tag{7.4.9}$$

and

$$\delta I_{in}(t) \equiv I_{in}(t) - \langle I_{in} \rangle = T_{atm} \left[\frac{\csc \mathrm{EL}(t)}{\langle \csc \mathrm{EL} \rangle} - 1 \right] , \tag{7.4.10}$$

respectively. The average of the total intensity from the atmosphere, T_{atm}, can be obtained by fitting the correlation between the elevation, $\mathrm{EL}(t)$, and the intensity timestream, $d'_{\tilde{m}}(t) = \delta I_{in}(t)$, shown in Figure 7.4.1 with Eq. (7.4.10). Note that $A^{(0)}_{4|\langle I_{in} \rangle}$ and T_{atm} are obtained for each detector for each el-nod observation.

The T_{mirror} is measured by a 1-wire digital thermometer on the primary mirror. Since the observations were done in the night, the T_{mirror} was stable, which was 270.6 K with ± 0.3 K variation at a maximum.

The correlation between the real or imaginary part of the $n = 4$ HWPSS and the total intensity from the atmosphere is shown in Figure 7.4.2 for each device wafer. Here, each point represents the average value for all the detectors for each el-nod observation. Figure 7.4.2 also shows the best fit line of the correlation, whose amplitude is listed in Table 7.4.1 with the optical leakage λ_4^{opt} which is derived using the method A, and whose slope, which directly represents λ_4^{opt} in the method B, is listed in Table 7.4.2. The slopes of the real part show small negative correlation for all the device wafers from -0.04% to -0.12%. The slopes of the imaginary part are smaller than the slopes of the real part and have both positive and negative values.

Note that in the error bars in Figure 7.4.2 or uncertainties in Table 7.4.1, we considered five types of uncertainties[12] : uncertainty of the signal from each el-nod data, uncertainty in the responsivity from each stimulator calibration, uncertainty in the time-constant from stimulator calibration, statistical uncertainty in the absolute responsivity from previous science observation, and detector to detector variation. For fitting the slope, however, we can remove the latter two uncertainties. Since uncertainty in the absolute responsivity affects both $A^{(0)}_{4|\langle I_{in} \rangle}$ and T_{atm} by the same ratio, the slope does not change. Detector to detector variation can also be removed by subtracting the average for each detector, which also does not change the slope.

11 We used the bandpass measured in the laboratory using a Fourier transform spectrometer (Arnold et al. 2012).
12 The error bars and uncertainty values are the quadratic mean of the five uncertainties listed.

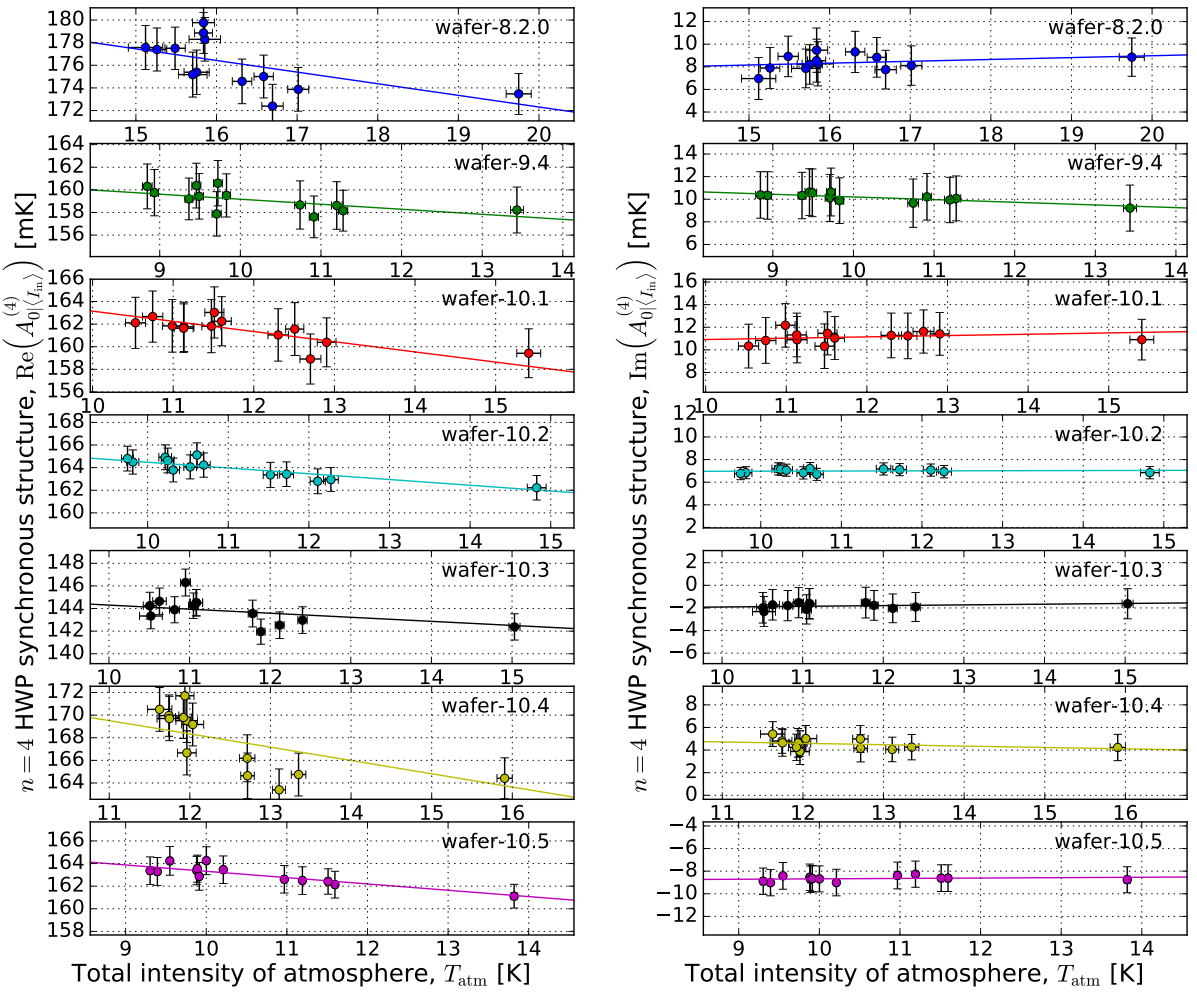

Figure 7.4.2: Correlation between the real (or imaginary) part of the HWPSS and the intensity from atmosphere is shown as left (or right) panel. Each point is obtained from each el-nod observation. It shows the average and one sigma error bar among all working detectors. The error bars show statistical uncertainties dominated by the detector to detector systematic variation, which is common among observations. The difference in T_{atm} among the device wafers is due to the difference in detector frequency bandpasses between wafers.

Table 7.4.1: The amplitude of the HWPSS obtained from the fit shown in Figure 7.4.2 and the optical leakage from the method A for each device wafer. The uncertainties include only statistical contributions. Note that we have larger systematic uncertainties due to the absolute responsivity calibration.

Device wafer (position on sky)	$\mathrm{Re}\left(\left\langle\left\langle A^{(0)}_{4\|\langle I_{in}\rangle}\right\rangle\right\rangle\right)$	$\mathrm{Im}\left(\left\langle\left\langle A^{(0)}_{4\|\langle I_{in}\rangle}\right\rangle\right\rangle\right)$	$\mathrm{Re}\left(\lambda_4^{opt}\right)$ (%)	$\mathrm{Im}\left(\lambda_4^{opt}\right)$ (%)
8.2.0 (upper left)	176.2 ± 0.5 mK	8.4 ± 0.5 mK	-0.0697 ± 0.0002	-0.0033 ± 0.0002
9.4 (bottom)	159.1 ± 0.5 mK	10.1 ± 0.6 mK	-0.0615 ± 0.0002	-0.0039 ± 0.0002
10.1 (lower left)	161.4 ± 0.6 mK	11.1 ± 0.5 mK	-0.0628 ± 0.0002	-0.0043 ± 0.0002
10.2 (center)	163.9 ± 0.3 mK	7.0 ± 0.1 mK	-0.0636 ± 0.0001	-0.0027 ± 0.0001
10.3 (upper right)	143.8 ± 0.3 mK	-1.8 ± 0.4 mK	-0.0558 ± 0.0001	0.0007 ± 0.0001
10.4 (top)	167.7 ± 0.5 mK	4.5 ± 0.3 mK	-0.0654 ± 0.0002	-0.0018 ± 0.0001
10.5 (lower right)	163.0 ± 0.3 mK	-8.7 ± 0.3 mK	-0.0631 ± 0.0001	0.0034 ± 0.0001

Table 7.4.2: The coefficient of the optical leakage obtained from the fit shown in Figure 7.4.2 for each device wafer.

Device wafer	$\mathrm{Re}\left(\lambda_4^{opt}\right)$ [%]	$\mathrm{Im}\left(\lambda_4^{opt}\right)$ [%]
8.2.0	-0.103 ± 0.008	0.016 ± 0.006
9.4	-0.044 ± 0.006	-0.024 ± 0.003
10.1	-0.090 ± 0.004	0.012 ± 0.007
10.2	-0.051 ± 0.005	0.001 ± 0.001
10.3	-0.036 ± 0.004	0.006 ± 0.002
10.4	-0.118 ± 0.010	-0.012 ± 0.004
10.5	-0.056 ± 0.003	0.004 ± 0.002

7.4.2.2 *Method C : λ_4 measurement using el-nod data*

Here, using method C described in section 7.4.1, we evaluate the total leakage, λ_4, which includes both the optical leakage and the leakage from the non-linearity of the detector. We use el-nod data in this section.

Here, we obtain the coefficient of the leakage as follows to remove the bias from the white noise of the detector. First, we calculate the covariance matrix among the intensity signal and one of the polarization signals. For the real part, for example, we obtain

$$\begin{aligned} \mathrm{Cov}^{(\mathrm{Re})} &\equiv \begin{pmatrix} \langle d'^2_{\bar{m}} \rangle & \langle d'_{\bar{m}} \mathrm{Re}(d'_{\bar{a}}) \rangle / \sqrt{2} \\ \langle d'_{\bar{m}} \mathrm{Re}(d'_{\bar{a}}) \rangle / \sqrt{2} & \langle \mathrm{Re}(d'_{\bar{a}})^2 \rangle / 2 \end{pmatrix} \\ &\approx \begin{pmatrix} V_I + N & \mathrm{Re}(\lambda_4) V_I / \sqrt{2} \\ \mathrm{Re}(\lambda_4) V_I / \sqrt{2} & \mathrm{Re}(\lambda_4)^2 V_I / 2 + N \end{pmatrix}, \end{aligned} \tag{7.4.11}$$

where $d'_{\bar{m}}(t)$ and $d'_{\bar{a}}(t)$ are the timestreams of an el-nod observation, $V_I \equiv \langle \delta I_{in}^2 \rangle$ is the variance of the intensity signal that mainly comes from the atmospheric fluctuation, and N is from the white noise of the detector. Note that the polarization timestream is divided by a factor of $\sqrt{2}$ so that the white-noise terms in the diagonal components are the same as N. Cross correlations of the white noise with other noise sources are assumed to be zero. The eigenvalues and eigenvectors of this covariance matrix are calculated as follows:

$$E_1^{(\mathrm{Re})} = [1 + \mathrm{Re}(\lambda_4)^2/2] V_I + N\,, \tag{7.4.12}$$

$$E_2^{(\mathrm{Re})} = N\,, \tag{7.4.13}$$

$$\vec{v_1}^{(\mathrm{Re})} \propto (1, \mathrm{Re}(\lambda_4)/\sqrt{2})^T\,, \tag{7.4.14}$$

$$\vec{v_2}^{(\mathrm{Re})} \propto (-\mathrm{Re}(\lambda_4)/\sqrt{2}, 1)^T\,, \tag{7.4.15}$$

where $E_1^{(\mathrm{Re})}$ and $E_2^{(\mathrm{Re})}$ are the eigenvalues and $\vec{v_1}^{(\mathrm{Re})}$ and $\vec{v_2}^{(\mathrm{Re})}$ are their eigenvectors. We obtain the leakage coefficient from the ratio of the components of $\vec{v_1}^{(\mathrm{Re})}$. Its uncertainty is estimated using the eigenvalues and the number of samples, n_{sample}, as $\sqrt{2}(E_1^{(\mathrm{Re})}/E_2^{(\mathrm{Re})})^{-1/2} n_{\mathrm{sample}}^{-1/2}$. With a similar calculation for the imaginary component, we obtain $\mathrm{Im}(\lambda_4)$, too.

Note that any additional component, such as a base temperature fluctuation and electrical noise, is not considered here, which might appear in the intensity-intensity component of the covariance matrix as $V_I + N + V_{\mathrm{other}}$. With this additional term, we would underestimate both the leakage and its uncertainty by a factor of $(1 + V_{\mathrm{other}}/V_I)^{-1}$, which may result in a residual $1/f$ noise (see section 7.5).

The measured total leakage, which is averaged among the observations and detectors for each device wafer, is shown in Figure 7.4.3. We find that the absolute values for both the real part and imaginary part of the total leakage are much larger than those for the optical leakage obtained in the previous section; the real (imaginary) part of the total leakage is about 0.3% (0.1%) for median and 0.8% (0.2%) for maximum.

7.4.2.3 *Method C : λ_4 measurement using CMB scan data*

In the previous section, the intensity timestream, $d'_{\bar{m}}(t)$, is obviously dominated by the variation of the total intensity from the atmosphere, $\delta I_{in}(t)$. In the case of the hour long CMB scan data, however, $d'_{\bar{m}}(t)$ is dominated by the $1/f$ noise, which should come from the intensity

fluctuation from the atmospheric turbulence, but may come from other sources. Here, we perform method C again but with the CMB scan data to check whether the leakage coefficient is consistent with that obtained from el-nod data.

Although the CMB scan is different from the el-nod (e.g., the data length is one hour for a CMB scan and 40 seconds for an el-nod), we can use exactly the same process explained in the previous section.

The total leakage measured from the CMB scan data is also shown in Figure 7.4.3, which shows a similar trend with that obtained from the el-nod data.

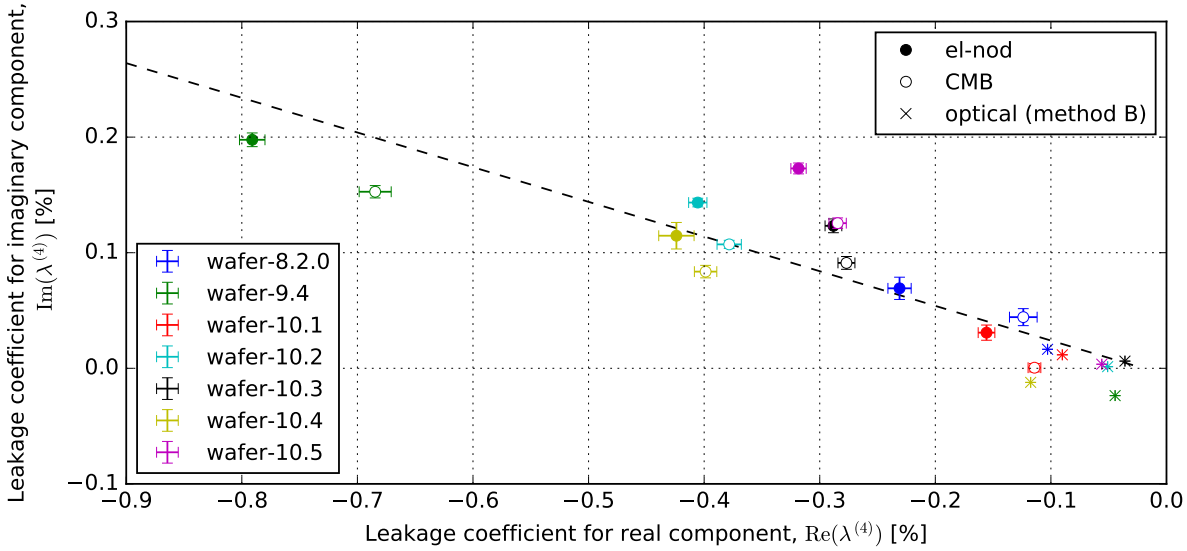

Figure 7.4.3: The total leakage coefficients from the el-nod and CMB scan data averaged among the detectors on each device wafer. Each error bar shows the 1σ uncertainty of the averaged value including the systematic uncertainty from detector-by-detector and observation-by-observation variation. The optical leakage coefficients are also plotted for comparison.

7.4.3 *Discussion on the measured I→P leakage*

As described in the introduction of section 7.4, there are two origins of the I→P leakage; one is the optical leakage and the other is the leakage due to detector non-linearities. In the previous section, we have shown the four types of measurements to shed light on the origin of the I→P leakage.

7.4.3.1 *The optical leakage*

The optical leakage, $\lambda_4^{\rm opt}$, measured using method B in Table 7.4.2 is found to be between -0.04% and -0.12%. The trend that the imaginary part of the optical leakage is closer to zero than the real part, agrees with the expectation. With method A in Table 7.4.1, we obtain -0.06% from all the device wafers, which is in agreement with the results from method B. The following properties seen in method A are also in agreement with the expectation: the $n = 4$ HWPSS, $A^{(4)}_{0|\langle I_{\rm in}\rangle}$, is polarized, and its polarization angle is aligned with the vertical direction of the telescope. Our naïve expectation of the optical leakage is $\lambda_4^{\rm opt} \sim -0.02\%$ from Eq. (6.1.2),

which is close to our measurements but is smaller. This can be attributed to the uncertainty in the property of the mirror material or the non-idealities of the HWP. Among the device wafers, we could have ±8% relative variation because of the difference in the incident angle χ by ±1°, and ±2% relative variation from bandpass center frequency difference by ±5 GHz, according to Eq. (6.1.2). Besides, the peripheral wafers might also have contributions from the diffraction at edge of the rotator and the non-uniformity of the ARC. However, we cannot find any clear feature of these effects in Table 7.4.1 due to systematic uncertainty in calibration.

In summary, the measured amplitude of the optical leakage is at a level of about 0.1% or less, and overall properties agree with the expectations.

7.4.3.2 *The I→P leakage from the detector non-linearity*

The amplitude of the total leakage, λ_4, measured by method C in section 7.4.2.2 and section 7.4.2.3, was found to be much larger than the optical leakage, λ_4^{opt}, measured by method A or B. Here we assume that the difference comes from the leakage due to the detector non-linearity, as described in section 5.3.2, and assess the effect more quantitatively.

The non-linearity of the detector can be estimated from the physical model of the detector. By expanding equations for the constant-voltage-biased TES bolometer (e.g. Irwin et al. 2005) up to second order perturbations, we obtain the non-linearity of the responsivity and time-constant as follows:

$$g_1 \approx -\frac{\eta}{2P_{\mathrm{elec}}}\frac{\mathcal{L}}{\mathcal{L}+1}\frac{\mathcal{L}+1+\omega_{\mathrm{mod}}^2\tau_0^2}{(\mathcal{L}+1)^2+\omega_{\mathrm{mod}}^2\tau_0^2}\mathcal{C}\,, \tag{7.4.16}$$

and

$$\tau_1 \approx \tau_0\frac{\eta}{P_{\mathrm{elec}}}\frac{\mathcal{L}^2}{\mathcal{L}+1}\frac{1}{(\mathcal{L}+1)^2+\omega_{\mathrm{mod}}^2\tau_0^2}\mathcal{C}\,, \tag{7.4.17}$$

where $\mathcal{L}$ is the effective loop gain, η is a conversion factor from kelvin to pico-watt and P_{elec} is the electrical power injected into the TES circuit, and $\tau_0 = (\mathcal{L}+1)\tau$ is the thermal time constant of the TES bolometer, and $\mathcal{C}$ is a factor related to the second order derivatives of the TES resistance model, $R(T, I)$. The design value of η is about 0.18 pW/K (Kermish 2012) but here we use 0.17 pW/K due to the transmission of the CRHWP. P_{elec} can be obtained from the data as about 10 pW. The thermal time-constant τ_0 is measured using several calibration data as about 10 ms. The loop gain is estimated from the time-constant and it is about two. The factor $\mathcal{C}$ is estimated from two popular models, the two-fluid model (Irwin et al. 1998) or the resistively shunted junction (RSJ) model (Kozorezov et al. 2011), as 0.83 or 2.1 at fractional resistance of 60%. Then, the non-linearity is estimated as −0.17%/K or −0.42%/K. Using the measured amplitude of the $n = 4$ HWPSS of 0.16 K, the leakage from the non-linearity is estimated as $2g_1 A^{(4)}_{0|\langle I_{\mathrm{in}}\rangle} = -0.05\%$ or −0.13%. The time-constant drift, τ_1, is estimated as 0.02 ms/K or 0.05 ms/K, which corresponds to the imaginary part of the leakage as $\omega_{\mathrm{mod}}\tau_1 A^{(4)}_{0|\langle I_{\mathrm{in}}\rangle} = 0.02\%$ or 0.04%.

The trend of the device wafer difference in Figure 7.4.3 agrees with the model. Detectors on device wafer 9.4 are operated at lower electrical power, about 5 pW, and show larger leakages. On the other hand, those on the device wafer 10.1 are operated at larger electrical power,

about 30 pW, and show smaller leakages From Eqs. (7.4.16), (7.4.17) and (7.4.3), the ratio of the leakage into the real and imaginary parts can be estimated as

$$\frac{\omega_{\rm mod}\tau_1 A^{(4)}_{0|\langle I_{\rm in}\rangle}}{2g_1 A^{(4)}_{0|\langle I_{\rm in}\rangle}} = -\frac{\mathcal{L}\omega_{\rm mod}\tau_0}{\mathcal{L}+1+\omega^2_{\rm mod}\tau_0^2} \sim -0.3\,, \tag{7.4.18}$$

which is in good agreement with the measurement shown in Figure 7.4.3.

All the results mentioned above follow the same trend as the model. Therefore, we suspect that the transition shape dependent factor, $\mathcal{C}$, is responsible for the difference in the absolute values between the measurements and expectation. The physical model of the TES transition is not yet fully understood, which is a source of uncertainties. Besides, our TES is alternating current (AC) biased (Dobbs et al. 2012), which might have different properties from direct current (DC) biased TES as pointed out in van der Kuur et al. (2011). If $\mathcal{C}$ is about 4, expectations of both real and imaginary parts of the total leakage are in good agreement with the measured values. The direct measurement of the TES parameters is needed for further investigation.

We have also investigated other origins of non-idealities, such as a load resistance, a stray inductance, and the SQUID amplifier, and found that the load resistance has the largest effect among these. The load resistance is the sum of a 0.03 Ω shunt resistance and a parasitic resistance in the TES circuit, and is estimated to be about 0.1 Ω or less compared to the operating TES resistance of 1.0 Ω. Including the load resistance into the model changes the responsivity and increases the leakage into the real part from −0.05% to −0.1%, but it does not change the leakage into the imaginary part, which is determined by the time-constant. Then, the imaginary-to-real ratio of the estimated leakage decreases from Eq. (7.4.18), which does not agree with the data in Figure 7.4.3.

7.4.3.3 *Comparison with other experiments*

Here we compare our measurements of the instrumental polarization and the I→P leakage with the MAXIPOL and ABS experiments, and summarize in Table 7.4.3.

Table 7.4.3: Comparison of instrumental polarization and I→P leakage

Experiment	Position of CRHWP	$\lvert A^{(0)}_{4\lvert\langle I_{\rm in}\rangle}\rvert$ (mK)	$\lvert\lambda_4^{\rm opt}\rvert$ method A	$\lvert\lambda_4^{\rm opt}\rvert$ method B	$\lvert\lambda_4\rvert$ method C
MAXIPOL[a]	After one warm mirror, one window, and two cold mirrors	33–600	———	———	$\lesssim$ 1%–5%
ABS[b]	First optical element	40	———	∼ 0.013%	< 0.07%,[c]
POLARBEAR (this work)	After the primary	∼ 160	∼ 0.06%	$\lesssim$ 0.12%	$\lesssim$ 0.9%

a Johnson et al. 2007
b Essinger-Hileman et al. 2016
c This is a conservative 2-σ upper limit for the average across the focal plane.

MAXIPOL (Johnson et al. 2007) has an optical system, which has a warm primary mirror, a polypropylene vacuum window, two cold mirrors and an aperture stop on the sky side of

the CRHWP. They found that $|A^{(4)}_{0|\langle I_{in}\rangle}|$ ranges from 33 mK to 600 mK and $|\lambda_4|$ from $\lesssim 1\%$ to 5% for each detector, which was measured by method C using Jupiter observations.

ABS (Essinger-Hileman et al. 2016) adopts an optical system in which the CRHWP is the first optical element. There is no instrumental polarization and therefore, $A^{(4)}_{0|\langle I_{in}\rangle}$ and λ_4^{opt} have only small contributions from non-uniformity of the HWP. They found $|A^{(4)}_{0|\langle I_{in}\rangle}| \sim 40$ mK and $|\lambda_4^{opt}| \sim 0.013\%$ for each detector, which was measured by method B. They also put an upper limit on the leakage from Jupiter observations as $|\lambda_4| < 0.07\%$, which corresponds to method C.

In spite of differences in the optical system, such as the number of mirrors and the position of the CRHWP, our measurements of $|\lambda_4^{opt}| \sim 0.06\%$ from method A or $|\lambda_4^{opt}| < 0.12\%$ from method B and $|\lambda_4| < 0.9\%$ from method C are similar with those measurements within an order of magnitude.

7.5 1/f NOISE PERFORMANCE

Here we evaluate the 1/f noise performance of the observation using the CRHWP both in the time domain and the map space.

Possible noise sources are discussed in section 5.4. Among the sources, the I→P leakage is found to have the significant contribution to the 1/f noise. To solve the problem, we perform a leakage subtraction as described below.

7.5.1 *Leakage subtraction*

As described in section 5.4.2, the atmospheric noise has the largest contribution to the 1/f noise in the intensity signal, and could also contaminate the polarization signal due to the I→P leakage. Let us focus on the effects. The detector timestream of the intensity signal can be expressed as

$$d_0(t) = \Delta I_{sky}(t) + \delta I_{atm}(t) + \delta \mathcal{N}_0(t) \quad , \tag{7.5.1}$$

where $\Delta I_{sky}(t)$ is the intensity signal from the sky, $\delta I_{atm}(t)$ is the unpolarized atmospheric noise, and $\delta\mathcal{N}_0(t)$ is the white noise of the detector. The detector timestream of the polarization signal also becomes as

$$d_4(t) = [Q_{sky}(t) + iU_{sky}(t)] + \lambda_4[\Delta I_{sky}(t) + \delta I_{atm}(t)] + \delta\mathcal{N}_4(t) \quad , \tag{7.5.2}$$

where $Q_{sky}(t)$ and $U_{sky}(t)$ are the polarization signals from the sky, and $\delta\mathcal{N}_4(t)$ is the white noise of the detector for the polarization timestream. Here, the term of $\lambda_4\delta I_{atm}(t)$ represents the contamination of the atmospheric 1/f noise. Note that the I→P leakage coefficient λ_4 includes both the optical leakage and the leakage due to the detector non-linearity as Eq. (5.5.14).

However, we can easily find that the 1/f noise due to the I→P leakage can be removed by subtracting the leakage component using the intensity timestream as

$$d_4^{sub}(t) \equiv d_4(t) - \lambda_4 d_0(t) = [Q_{sky}(t) + iU_{sky}(t)] + \delta\mathcal{N}_4(t) - \lambda_4\delta\mathcal{N}_0(t) \quad . \tag{7.5.3}$$

Here, the leakage-subtracted polarization timestream, $d_4^{sub}(t)$, does not contain the atmospheric noise, $\delta I_{atm}(t)$, as well as the intensity signal from the sky, $\Delta I_{sky}(t)$. The white noise increase due to the last term, $-\lambda_4\delta\mathcal{N}_0(t)$, is negligible because of $|\lambda_4| \ll 1$.

The leakage coefficient, λ_4, can be estimated by the correlation between the intensity and polarization timestreams as described in section 7.4.2.2. Therefore, this leakage subtraction is equivalent to the template subtraction using the own intensity timestream as a template.

7.5.2 1/f *noise in the time domain*

Here, we evaluate the 1/f noise in the time domain, i. e. we calculate the PSD of the detector timestream. In the PSD, we can magnify the 1/f noise in the lowest frequency range, or can identify characteristic noises in specific frequencies.

We analyze the six CMB observation data. The data length for each observation is about one hour; thus we can obtain the PSD down to the frequency of $\sim 1\,\mathrm{mHz}$.

A PSD of a specific timestream can be calculated by Fourier-transforming the timestream. In practice, the timestream could have a drift due to the 1/f noise whose period is longer than the data length. The Fourier transformation of the finite length of data intrinsically assumes the periodicity of the data. However, the drift makes a gap between the start and the end. Then, the Fourier transformation tries to reconstruct the jump as the superstition of many frequencies, which results in spurious signals. To prevent mixing of the lowest frequency power into the higher frequencies, we apply a second-order polynomial filter for the entire one-hour observation and apply a Hann window function, which ensures both the start and the end to match as zero (Blackman et al. 1958).

First, we calculate the PSD for each detector. Note that the polarization timestream consists of two polarization signals as the real and the imaginary parts. Thus, we can obtain the PSD for each polarization. We fit the PSDs with a 1/f noise spectrum formula:

$$S_X(f) = S_X^{1/f}\big|_{f_0} \left(\frac{f_0}{f}\right)^{\alpha} + S_X^{N} \quad , \tag{7.5.4}$$

where the subscript X is a label of the timestream, f_0 is an arbitrary pivot frequency, $S_X^{1/f}\big|_{f_0}$ is the PSD of the 1/f noise at the pivot frequency, α is the power law of the 1/f noise, and S_X^{N} is the PSD of the white noise. The frequency where the 1/f noise and the white noise become comparable, the so-called knee frequency, is defined as

$$f_X^{\mathrm{knee}} \equiv \left(\frac{S_X^{1/f}\big|_{f_0}}{S_X^{N}}\right)^{1/\alpha} f_0 \quad . \tag{7.5.5}$$

The cumulative distribution of the knee frequencies for both the cases with and without the leakage subtraction are shown in Figure 7.5.1. We find that most of the detectors have the 1/f knee frequency less than 3 mHz for both the real part and the imaginary part after the leakage subtraction. Note that the power law is fixed as $\alpha = 2$ because the 1/f noise is almost covered by the white noise.

However, we have to note that the 1/f noise could be correlated among detectors in contrast to the white noise as discussed in section 5.4. For the anisotropy whose angular size is larger than the FOV of the telescope, all the detectors see the signal at the same time. Thus, we need to consider the averaged timestream among detectors to evaluate the 1/f noise performance for the large-angular-scale signal, which could be worse than the 1/f noise performance

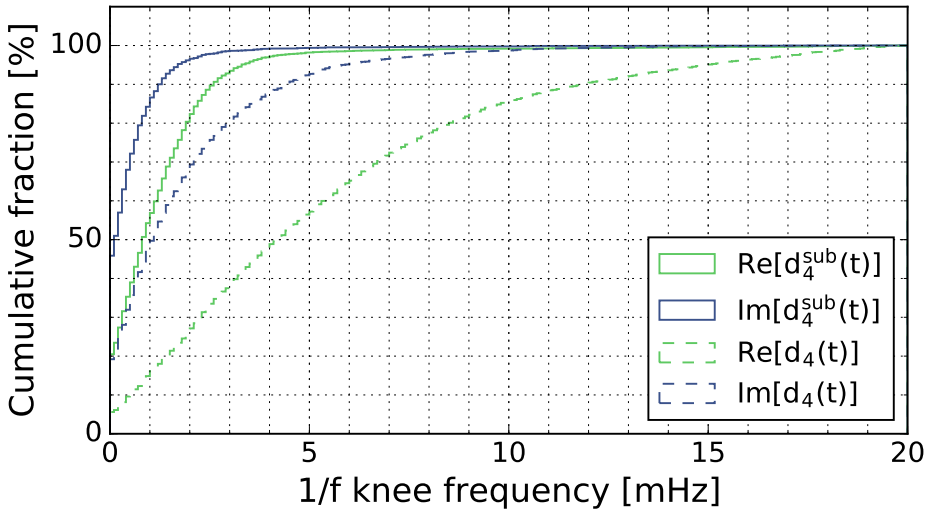

Figure 7.5.1: Cumulative distribution of the $1/f$ knee frequencies for single detectors. The solid lines and the dashed lines represent the cases with and without the leakage subtraction, respectively. The green lines and the blue lines correspond to the real part and the imaginary part of the polarization timestream. Since the leakage coefficient into the real part is larger than that into the imaginary part, the $1/f$ knee frequency of the real part is higher than the imaginary part.

of single detectors evaluated above. We calculate the averaged timestream with the weighting based on the white noise PSD as

$$d_4^{(\mathrm{array})}(t) = \left(\sum_i \frac{d_4^{(i)}(t)}{S_4^{\mathcal{N}(i)}} \right) \Bigg/ \left(\sum_i \frac{1}{S_4^{\mathcal{N}(i)}} \right) \quad , \tag{7.5.6}$$

where the superscript i represents the index of a detector, and the white noise PSD $S_4^{\mathcal{N}(i)}$ is the sum of the white noise PSDs for the real and the imaginary parts of the polarization signal.

Figure 7.5.2 shows the PSD of the averaged timestream for each polarization signal before and after the leakage subtraction, as well as the PSD of the averaged intensity timestream. The fitting curves with the $1/f$ noise spectrum are also plotted. We find that the $1/f$ noise in the polarization signal before the leakage subtraction has decreased more than an order of magnitude in the power after leakage subtraction. The knee frequency has also improved by about an order of magnitude. These results suggest that the $1/f$ noise of the intensity and polarization timesteams are dominated by the atmospheric intensity fluctuation and its leakage.

Note that the peaks in the polarized signal at the harmonics of the scan frequency, 0.01 Hz, are the scan synchronous signals, which come from the ground as observed by the far side-lobe of the telescope and could be somewhat polarized. We subtract such scan synchronous signals by applying the ground-template filtering in the map-making process (see section 3.5.1).

We can naïvely evaluate the $1/f$ noise in terms of multipoles by scaling the frequency using the scan velocity of $0.3°/s$. For the real part (or imaginary part), the knee frequency of the PSD after the leakage subtraction is $22\,(9)$ mHz, which corresponds to a multipole $\ell \simeq 26\,(11)$.

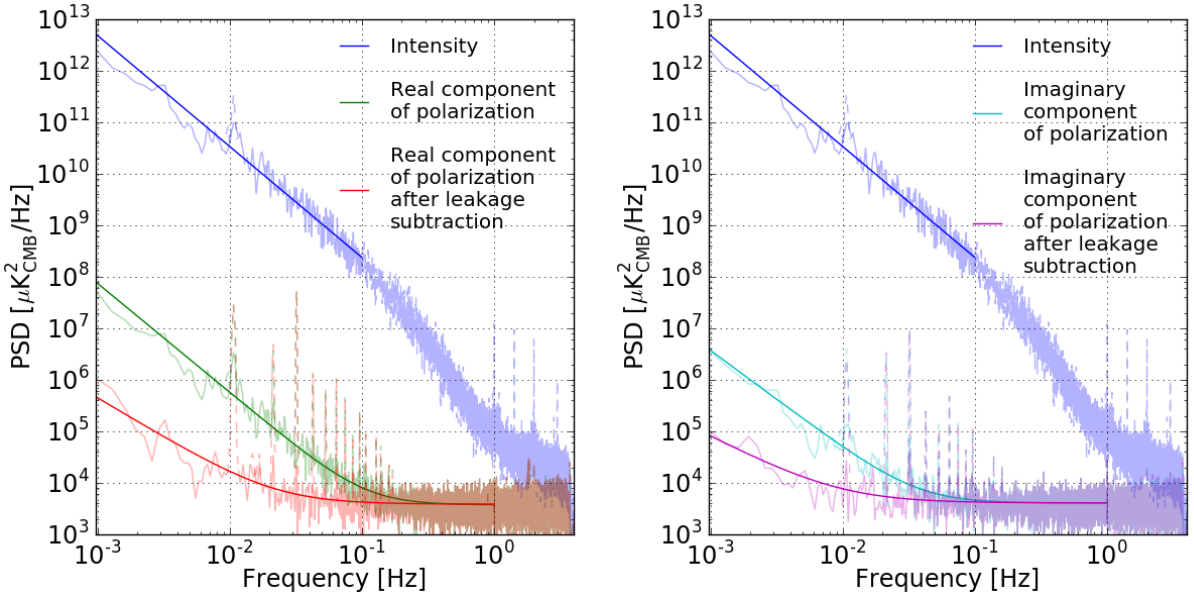

Figure 7.5.2: The PSDs of the coadded timestreams for all the detectors for the real part (left panel) and for the imaginary part (right panel). The blue line shows the intensity fluctuation and the green (cyan) and red (magenta) lines show the real (imaginary) part of the polarization signal before and after leakage subtraction, respectively. The spikes at the harmonics of 0.01 Hz are the scan synchronous signals.

However, the knee frequency depends on the white noise which could change every observation due to the observation condition. Assuming the typical array sensitivity, $\mathrm{NET}_{\mathrm{array}}$, of $23\,\mu\mathrm{K}\sqrt{\mathrm{s}}$ of POLARBEAR (The POLARBEAR Collaboration: P. A. R. Ade et al. 2014), the knee frequency becomes 32 (15) mHz, which corresponds to multipole $\ell \simeq 39\,(18)$. This naïve estimation indicates that the achieved 1/f noise performance is promising for the measurement of r, whose signal becomes significant at $\ell < 100$.

7.5.3 1/f *noise in the map space*

Next, we evaluate the 1/f noise performance in the map domain, i. e. we calculate the noise angular power-spectrum.

First, we create a map $X(\vec{n})$ for each signal $X \in \{Q, U\}$, where $\vec{n}$ is the direction in the sky. Since we can calculate both the polarization signals for each detector thanks to the CRHWP, we simply take an average of the timesteams among detectors for each polarization with weighting by the inverse of the white noise variance. Here, remember that the Stokes Q and U signals depend on the coordinate bases (see section 1.3.1). We stack the Q_{ant} and U_{ant} defined on the coordinate bases fixed on the instruments, $(\vec{e}_{\mathrm{EL}}, \vec{e}_{\mathrm{AZ}})$, instead of the Q_{sky} and U_{sky} defined on the sky coordinates, $(\vec{e}_{\mathrm{Dec}}, \vec{e}_{\mathrm{RA}})$.[13] This procedure is useful to separate the performance of the 1/f noise for Q_{ant} and U_{ant}: the Q_{ant} could have a larger contribution from the I→P leakage, while the U_{ant} could have the noise due to the CRHWP angle error.

13 Note that the polarization signal from the sky is averaged with different polarization angles and thus diminished.

In addition, we apply filters to reduce the contamination from the lowest frequency noise and the scan synchronous signal. we apply the following filters for each detector:

1. the second-order polynomial filter for the entire one-hour observation,
2. the leakage subtraction (see section 7.5.1),
3. the first-order polynomial filter for each half stroke, and
4. the scan synchronous signal filter with azimuth angle bins of $\Delta Az = 4.8'$.

Note that these filters, especially the latter two, subtract aiming signals, too. The effect needs to be corrected by estimating the transfer function (TF) as explained below.

The resulting maps are shown in Figure 7.5.3. The shape of the scanned region is con-

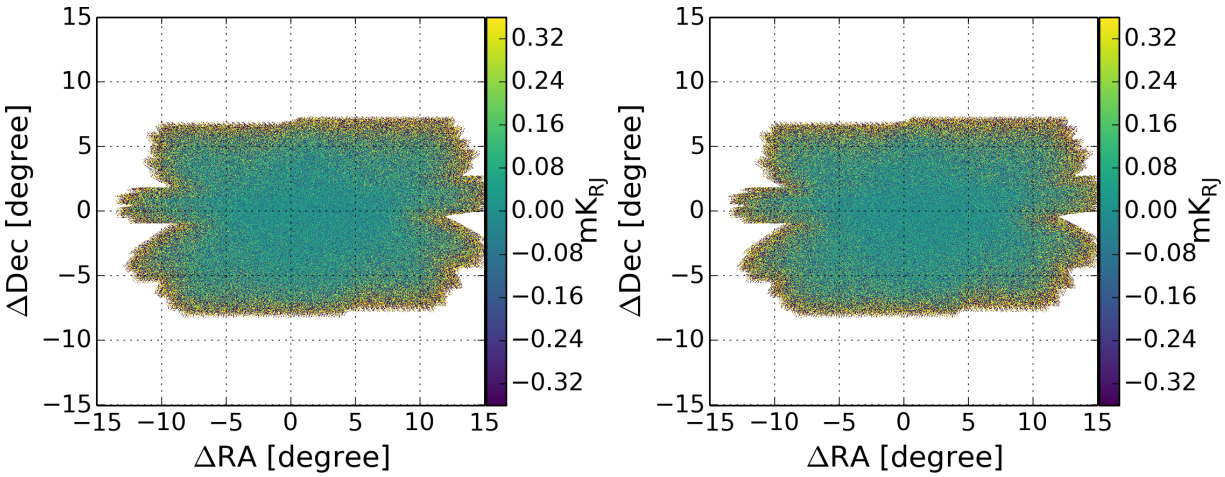

Figure 7.5.3: Maps from the CMB observation data. The left panel and the right panel show the Q_{ant} and U_{ant} polarization, respectively. Both the maps do not have any large-angular structures and look dominated by the white noise.

structed by a superposition of the six CMB observations; each of them scans a parallelogram region with a various oblique side that depends on the parallactic angle. Both the polarization signals, Q_{ant} and U_{ant}, do not have any large structure due to the 1/f noise and seem dominated by the white noise.

We can obtain the noise pseudo-angular power-spectrum from the 2D Fourier transformation of the map as[14]

$$(2\pi)^2 \hat{N}_X(\vec{\ell})\delta(\vec{\ell}) = \frac{\left|\int d\vec{n}\, W_P(\vec{n}) X(\vec{n}) e^{-i\vec{\ell}\cdot\vec{n}}\right|^2}{\int d\vec{n}\, W_P^2(\vec{n})} \quad , \tag{7.5.7}$$

where $\hat{N}_X(\vec{\ell})$ is the noise pseudo-angular power-spectrum of $X \in \{Q_{ant}, U_{ant}\}$, $\delta(\vec{\ell})$ is the delta function, and $W_P(\vec{n})$ is the apodization window function for the polarization signal that is the inverse square of the map depth normalized by its maximum (see section 1.4.2, as well as section 3.5.2). Note that the noise pseudo-angular power-spectrum is modified from the original noise angular power-spectrum due to the filters. Besides, the effects of the filters are anisotropic in $\vec{\ell}$ depending on the filter type and the scan direction. We estimate the filtering effects using the Monte Carlo simulation, where we simulate the realistic observation with the

14 We ignore the contribution from the sky signal, which is sufficiently smaller than the contribution of the noise.

Gaussian white noise, and calculate the noise pseudo-angular power-spectrum. Without the filtering, the noise angular power-spectrum of the white noise simulation is expected to be constant among all the Fourier modes. Thus, the decrease of the power in the pseudo-angular power-spectrum corresponds to the transfer function (TF). Figure 7.5.4 shows the 2D TF, $F(\vec{\ell})$, estimated from the 100 realizations.

Here, we find some features: clear vertical lines and a faint cross around the center. The vertical lines come from the scan synchronous signal filter, which removes the stripes in the RA direction resulting in the $\ell_{RA} = 0$ line. The other lines at $\ell_{RA} \sim \pm 900$ also caused by the scan synchronous signal filter. Because of the large azimuthal range of the scan, the one cycle of the back-and-forth motion takes $\sim 100\,s$. During the scan, the sky rotates by $\sim 0.4°$ which corresponds to $\ell_{RA} \sim \pm 900$. Such a sparse scan allows several independent trajectories to fill the gap. The additional freedom causes the filtered lines at $\ell_{RA} \sim \pm 900$.

On the other hand, the faint cross comes from the first order polynomial filter for each scan stroke. The filter mainly removes the modes orthogonal to the scan direction, as well as the lowest $|\vec{\ell}|$ modes of the scan direction. Since the scan direction is different for each observation, the efficiency of the filtering changes, i. e. a specific Fourier mode is completely removed for a CMB observation, but not for another observation. The average of the effect results in the faint cross feature.

Figure 7.5.4 also shows the radial profile of the TF, where the grayscale represents the histogram of the TF for multiple directions of the Fourier modes in the same radius, and the red or cyan line shows the average of the TF for Q_{ant} or U_{ant} as a function of the radius $|\ell|$. Here, two lines at $F(\ell) \sim 0\%$ and $F(\ell) \sim 20\%$ come from the vertical line in the 2D TF at $|\ell_{RA}| < 10$. We also find a small dip around $\ell \sim 900$, which also comes from the scan synchronous signal filter as described above. The decrease of the TF below $\ell < 100$ is caused by the polynomial filter for each scan stroke.

The pseudo-angular power-spectrum from the real observation is corrected by dividing by this 2D TF. In practice, however, the Fourier mode for which the TF is close to zero diverges after the division, and might unnecessarily worsen the evaluation of the noise angular power-spectrum. Therefore, we mask the modes with $F(\vec{\ell}) < 0.1$, i. e. the vertical lines shown in Figure 7.5.4 and $|\vec{\ell}| < 20$.

The Figure 7.5.5 and Figure 7.5.6 show the noise pseudo-angular power-spectrum before the TF correction for each polarization. In the 2D pseudo-angular power-spectrums, Figure 7.5.5, we find sporadic peaks, which are likely the random fluctuations with the exponential distribution. The typical size of the peak in the wave number space is determined by the map size as described in section 1.4.2. The radial profile, Figure 7.5.6, shows both the histogram of the pseudo-angular power-spectrum as the grayscale and their average as the red and cyan lines for Q_{ant} and U_{ant}, respectively. We cannot find any significant difference of the pseudo-angular power-spectrum between Q_{ant} and U_{ant} in the region of $\ell > 100$. In the region of $\ell < 100$, both of them are affected by the filters as shown in Figure 7.5.4, whereas the Q_{ant} polarization has larger power than the U_{ant} polarization. The difference suggests the larger contribution from the 1/f noise for the Q_{ant}.

The noise angular power-spectrum after the TF correction is shown in Figure 7.5.7 for each of the Q_{ant} and U_{ant} signals. Here, the absolute value is normalized by the average value above $\ell > 1000$, thus the normalized angular power-spectrum represents the factor of the noise increase due to the 1/f noise. Again each figure shows the histogram of the angular power-spectrum for each ℓ bin as the grayscale, as well as the average value as the red or cyan

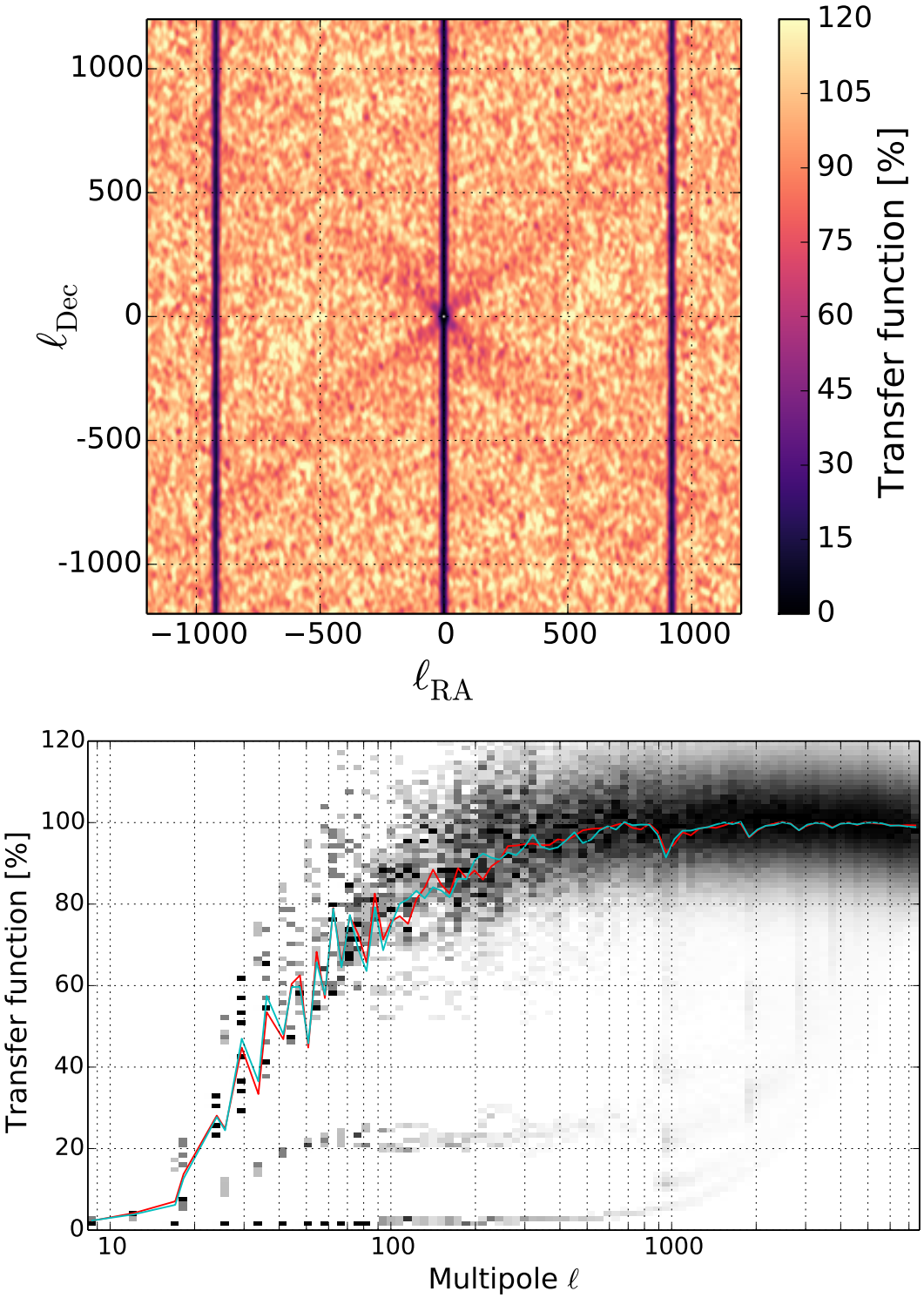

Figure 7.5.4: The one-dimensional TF. Beam effect is not included.

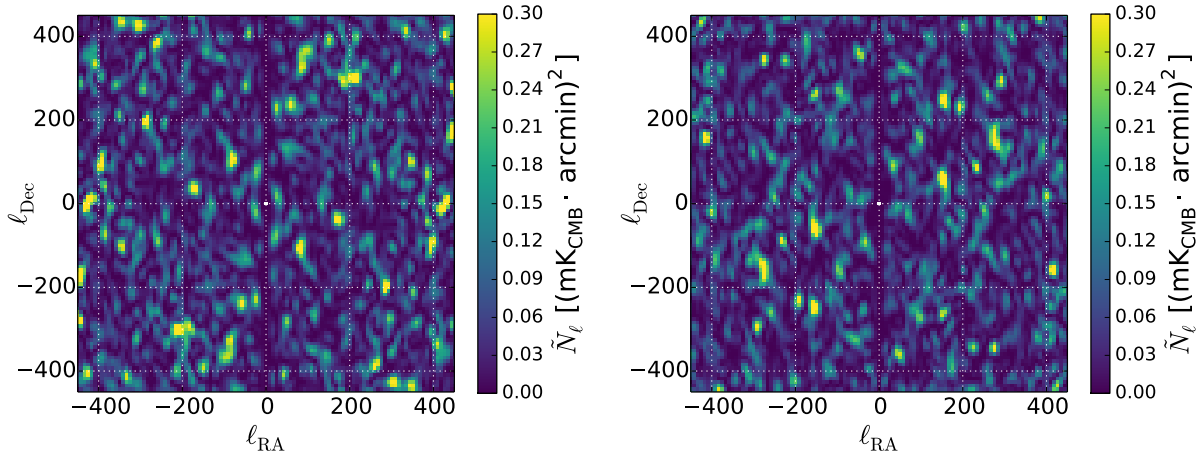

Figure 7.5.5: Two-dimensional distribution of the noise pseudo-angular power-spectrums as a function of the wave number $\vec{\ell}$. The left panel and the right panel show the distribution for the Q_{ant} polarization and U_{ant} polarization, respectively. Both figures likely show the random distribution from the white noise except the vertical line at $\ell_{\mathrm{RA}} = 0$, which is removed by the scan synchronous signal filter.

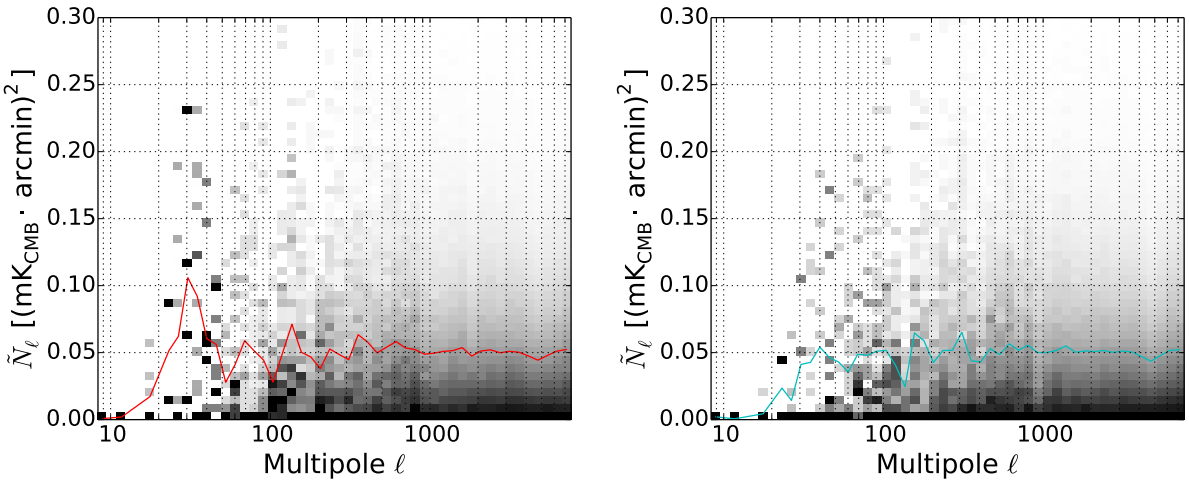

Figure 7.5.6: Radial profile of the noise pseudo-angular power-spectrums. The left panel and the right panel show the results for the Q_{ant} polarization and the U_{ant} polarization, respectively. Each figure shows the histogram for each ℓ bin as the grayscale, and the average values as the solid line.

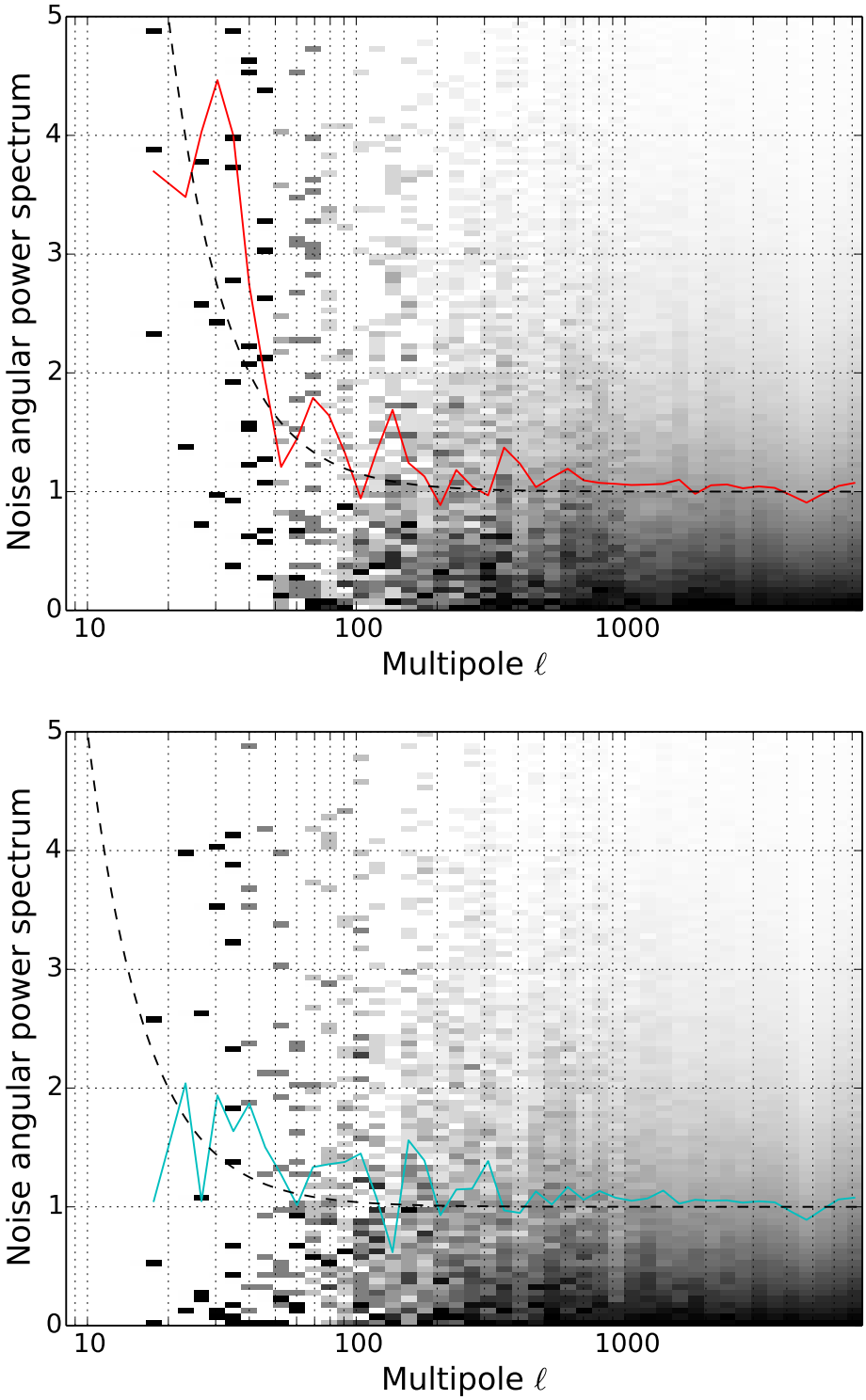

Figure 7.5.7: Radial profile of the normalized noise angular power-spectrums after the TF correction. The top panel and the bottom panel show the results for the Q_{ant} polarization and the U_{ant} polarization. The grayscale represents the distribution of the power of Fourier modes among multiple $\vec{\ell}$ directions for each ℓ bin, and the solid line shows the average. The 1/f noise spectrum is also shown as the dashed line for comparison.

line, for Q_{ant} or U_{ant}. The 1/f noise spectrum, $n_\ell = 1 + (\ell_{knee}/\ell)^\alpha$, is also shown as the dashed line, whose 1/f knee multipole is $\ell_{knee} = 40$ or $\ell_{knee} = 20$ for Q_{ant} or U_{ant}. We find that the spectrum of the noise increase factor roughly matches with the 1/f noise spectrum.

Note that the measurement of the angular power-spectrum below the multipole $\ell \lesssim 100$ is important for the measurement of the primordial B-mode signal as shown in Figure 1.3.6. The 1/f noise performance evaluated in this study is sufficient to probe the primordial B-mode signal for both the Q_{ant} and U_{ant} polarization.

7.6 SUMMARY OF THE CRHWP PERFORMANCE

We have evaluated the performance of the CRHWP, and the results are summarized in Table 7.6.1.

We find a somewhat large increase of the loading from the truncation of the beam by the CRHWP. It could be because the position of the CRHWP has an offset from the prime focus by ~ 11 cm as described in section 6.1.1. It is expected to be mitigated in the continuing science observation using a new CRHWP, which is placed at the prime focus.

The CRHWP angle error is critical for the noise performance of the modulated polarization signal, especially for the U_{ant} signal. We have successfully fixed the problems in the synchronization and the backlash and achieved a sufficient performance as evaluated in section 8.1.

The impact on the beam shape is not significant, and the transmission and the polarization efficiency roughly agree with the measurements in the laboratory (see section 6.1.2). The I→P leakage measured from the Jupiter observation is consistent with the other measurements described below. The Q↔U mixing is also investigated using the Tau A observation, and probably less than ~ 4%.

The properties of the $n = 4$ HWPSS, which corresponds to the polarization signal, are consistent with expectation, i. e. it is polarized and aligned to the Q_{ant} direction, excepting the amplitude, which is several times larger than the expectation from the primary mirror property. The optical leakge, λ_4^{opt} is measured to be $\lesssim 0.1$ using the variation of the amplitude of the $n = 4$ HWPSS , while the total leakage, which includes the effect due to the detector non-linearity as $\lambda_4 = \lambda_4^{opt} + \lambda_4^{nl}$, is measured from the correlation between the intensity timestream, $d_0(t)$, and the polarization timestream, $d_4(t)$, and found to be $\lesssim 0.9\%$. The results indicate that there is a considerable contribution from the detector non-linearity.

However, we have demonstrated that the I→P leakage can be removed using the simple subtraction method described in section 7.5.1. After the leakage subtraction, we find that the 1/f noise performance as the knee multipole $\ell_{knee} \lesssim 40$, which is sufficient for the measurement of the primordial B-mode signal.

Table 7.6.1: Summary of the performance of the CRHWP evaluated in chapter 7.

Description	Performance
Loading from the CRHWP	
for center pixel	1.2 pW (6.7 K_{RJ})
for edge pixel	6 pW (33 K_{RJ})
PSD of the CRHWP angle error, $\delta\theta_{HWP}(t)$	$\lesssim 10^{-10}$ rad^2/Hz
Beam size magnification	102%
Transmission of the CRHWP, $\mathcal{T}$	$93.6\% \pm 0.1\%$(stat.)
Polarization efficiency, ε	$86\% \pm 11\%$(sys.)
The I→P leakage from the planet observation	$\sim 0.5\%$
The Q↔U mixing beam (dipole mode)	$\lesssim 4\%$
The amplitude of the $n = 4$ HWPSS	
for the Q_{ant} component	~ 160 mK_{RJ}
for the U_{ant} component	$\lesssim 10$ mK_{RJ}
The optical I→P leakage for $n = 4$ HWPSS, λ_4^{opt}	
for the Q_{ant} component	$\lesssim 0.12\%$
for the U_{ant} component	$\lesssim 0.02\%$
The total I→P leakage for $n = 4$ HWPSS, $\lambda_4 = \lambda_4^{opt} + \lambda_4^{nl}$	
for the Q_{ant} component	$\lesssim 0.8\%$
for the U_{ant} component	$\lesssim 0.2\%$
The 1/f knee frequency per single detector	
for the Q_{ant} component	$\lesssim 3$ mHz
for the U_{ant} component	$\lesssim 1$ mHz
The 1/f knee frequency for the averaged timestream	
for the Q_{ant} component	~ 32 mHz
for the U_{ant} component	~ 15 mHz
The 1/f knee multipole	
for the Q_{ant} component	~ 40
for the U_{ant} component	~ 20

8

IMPACT OF THE CRHWP ON POWER SPECTRUM MEASUREMENTS

In chapter 7, we have evaluated the performance of the CRHWP from various points of view, namely the additional loading, the angle decoding accuracy, beam imperfections, I→P leakage, and 1/f noise performance. In this chapter, we discuss the impacts of these performances on the angular power-spectrum measurements, especially the B-mode angular power-spectrum measurements.

As introduced in section 1.4, we could have uncertainties and/or bias errors in an angular power-spectrum measurement. Here, we classify the uncertainties on the ΔC_ℓ into four components as

$$\Delta C_\ell = \Delta C_\ell^{SV} + \Delta C_\ell^{stat} + \Delta C_\ell^{multi} + \Delta C_\ell^{sys} \tag{8.0.1}$$

where ΔC_ℓ^{SV} is the systematic uncertainty from the sample variance, ΔC_ℓ^{stat} includes the statistical uncertainties which improve over time, ΔC_ℓ^{multi} represents the instrumental uncertainties related to the responsivity calibration, and ΔC_ℓ^{sys} is a possible bias due to contamination of any other signals. In the following sections: section 8.1, section 8.2, and section 8.3, we discuss the impact of the CRHWP on ΔC_ℓ^{stat}, ΔC_ℓ^{multi}, and ΔC_ℓ^{sys}, respectively.

Here we assume a large patch observation with the POLARBEAR experiment: the fractional sky area, f_{sky}, is 1.7%, and the total observation time, t_{obs}, is 2×10^7 s.

8.1 STATISTICAL UNCERTAINTIES

We start the discussion from the statistical uncertainties. As explained in section 1.4.2, they can be estimated as

$$\begin{cases} \Delta C_\ell^{stat} = \sqrt{\dfrac{2}{(2\ell+1) f_{sky}}} N_\ell \quad , \\ N_\ell = w^{-1} \cdot e^{\ell(\ell+1)\sigma_b^2} \quad , \\ w_P^{-1/2} = \mathrm{NEPol} \sqrt{\dfrac{4\pi f_{sky}}{t_{obs}}} \quad , \end{cases} \tag{8.1.1}$$

where N_ℓ is the noise angular power-spectrum, $w_P^{-1/2}$ is the map depth for single polarization mode, σ_b is the beam size, and NEPol is the instantaneous array sensitivity for single polarization signal. These parameters are related to the performance of the CRHWP.

The main component limiting the instantaneous sensitivity is the photon noise (see section 1.4), which is determined as

$$\mathrm{NEPol}_\gamma^2 = \frac{2}{\varepsilon^2} \left[\frac{2h\nu T_{RJ}}{\mathcal{T}\eta\Delta\nu k_B} + \frac{2T_{RJ}^2}{\Delta\nu} \right] \quad , \tag{8.1.2}$$

where effects of the CRHWP are the polarization efficiency, ε, and the transmission, $\mathcal{T}$, as well as the total loading, T_{RJ}, which is expressed as

$$T_{RJ} = T_{RJ}^{sky} + T_{RJ}^{CRHWP} + \frac{T_{RJ}^{inst}}{\mathcal{T}} \quad , \tag{8.1.3}$$

where T_{RJ}^{sky}, T_{RJ}^{CRHWP}, and T_{RJ}^{inst} are the loading from the sky, the CRHWP, and the other instruments, respectively, and the T_{RJ}^{inst} is assumed to come from the components between the CRHWP and the detectors. Using the evaluated parameters of $\varepsilon \sim 90\%$, $\mathcal{T} \sim 94\%$, and $T_{RJ}^{CRHWP} \sim 7\,K_{RJ}$, the $NEPol_\gamma$ is estimated to increase as $0.47\,mK_{RJ}\sqrt{s} \to 0.64\,mK_{RJ}\sqrt{s}$, where the other parameters are assumed to be typical values: $\eta = 40\%$, $\nu = 150\,GHz$, $\Delta\nu = 30\,GHz$, $T_{RJ}^{sky} = 12\,K_{RJ}$, and $T_{RJ}^{inst} = 21\,K_{RJ}$. If we scale the POLARBEAR array sensitivity, $NEPol_{array} = 23\sqrt{2}\,\mu K_{CMB}\sqrt{s}$, by the same ratio, we obtain $NEPol_{array} = 31\sqrt{2}\,\mu K_{CMB}\sqrt{s}$.

Another effect of the CRHWP on the instantaneous sensitivity is the CRHWP angle uncertainty (see section 5.4.5), whose contribution can be expressed as

$$(NEPol)^2 = \frac{1}{2}\left(4A^{(0)}_{4|\langle I_{in}\rangle}\right)^2 \mathcal{S}^{\theta_{HWP}}/2 \quad , \tag{8.1.4}$$

where $A^{(0)}_{4|\langle I_{in}\rangle}$ is the amplitude of the $n = 4$ HWPSS, $\mathcal{S}^{\theta_{HWP}}$ is the PSD of the CRHWP angle error, and the first factor of one half comes from the fact that only the imaginary part of the polarization signal suffers from the noise. The $n = 4$ HWPSS is measured as 160 mK in Table 7.4.1. The PSD of the angle error should come from the quantization noise of the time stamp as

$$\mathcal{S}^{\theta_{HWP}} = 2\frac{\omega_{rot}^2 \Delta t^2}{12\, f_{sample}} \approx 2(2.6\times 10^{-6}\,rad\sqrt{s})^2 \quad , \tag{8.1.5}$$

where $\omega_{rot} = 2\pi \cdot 2\,Hz$ is the rotation speed of the CRHWP, $\Delta t = 10\,\mu s$ is the resolution of the time stamp, and $f_{smaple} = 191\,Hz$ is the sampling frequency. Then, the noise increase due to the angle error is estimated as $(NEPol_{array})^2 = (1.2\,\mu K_{RJ}\sqrt{s})^2$. Note that this noise is correlated among all the detectors.

The other noise sources considered in section 5.4, namely the atmospheric noise, HWPSS variation, and the instrumental noise, could be the source of the low-frequency noise (1/f noise). Here, we implement the 1/f noise effect into the noise angular power-spectrum, N_ℓ, as

$$N_\ell = n(\ell)\cdot w^{-1}\cdot e^{\ell(\ell+1)\sigma_b^2} \quad , \tag{8.1.6}$$

$$n(\ell) = \left[1 + \left(\frac{\ell}{\ell_{knee}}\right)^{-\alpha}\right] \tag{8.1.7}$$

where $n(\ell)$ is the noise increase factor due to the low-frequency noise relative to the white noise contribution. The exponent α represents the rapidity of the 1/f noise increase at lower multipoles, and the ℓ_{knee} is the multipole of the equality between the white noise and 1/f noise. As shown in Figure 7.5.7, the measured noise increase factor is in good agreement with the 1/f noise spectrum with $\ell^Q_{knee} \approx 40$ for the instrumental Q polarization signal and $\ell^U_{knee} \approx 20$ for the instrumental U polarization signal. Both of the knee multipoles are sufficiently good to probe the primordial B-mode signal which appears at $\ell \lesssim 100$. Here, we combine the different 1/f noise performances of the two polarization signals by taking their average as

$$n(\ell) = \left[1 + \frac{1}{2}\left(\frac{\ell}{\ell^Q_{knee}}\right)^{-\alpha} + \frac{1}{2}\left(\frac{\ell}{\ell^U_{knee}}\right)^{-\alpha}\right] \quad , \tag{8.1.8}$$

where α is assumed to be 2.

We have also found that the beam size is magnified by 102%, which could increase the beam term, $e^{\ell(\ell+1)\sigma_b^2}$. Since the fraction of the noise increase, $2\ell(\ell+1)\sigma_b\Delta\sigma_b$, rapidly decreases at multipoles smaller than that of the beam size, $\ell_b = 1/\sigma_b \sim 2300$ for the beam with 3.5 arcmin FWHM, the effect is negligible for the degree scale measurements at $\ell \lesssim 100$.

Figure 8.1.1 shows the expected statistical uncertainties for B-mode angular power-spectrum measurement.

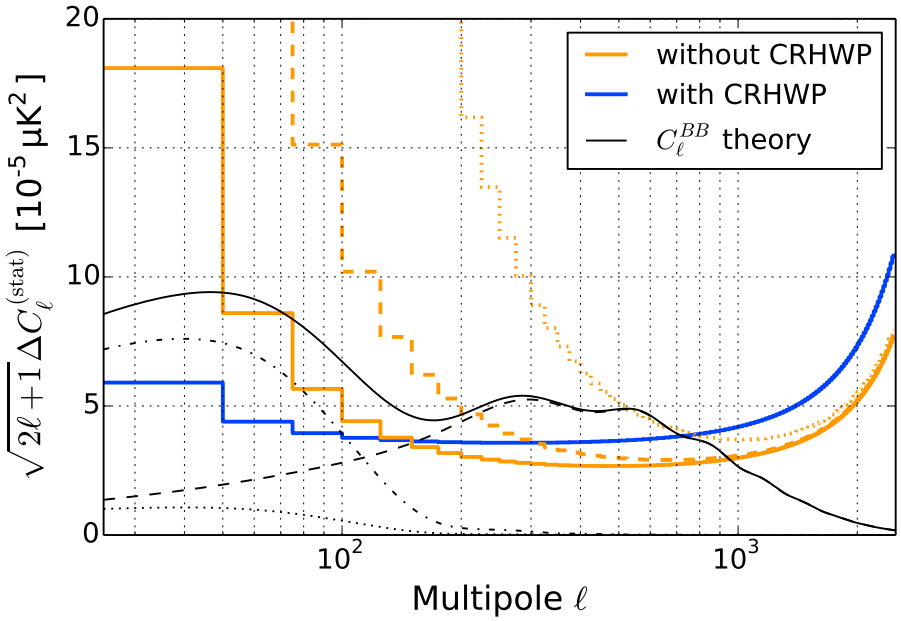

Figure 8.1.1: Comparison of $\Delta C_\ell^{(\mathrm{stat})}$ for the cases with and without the CRHWP. The black dashed line, the black dash-dotted line, and the black dotted line show the expected angular power-spectrum of the lensing B-mode, the primordial B-mode with the tensor-to-scalar ratio $r = 0.07$, and that with $r = 0.01$.

8.2 MULTIPLICATIVE UNCERTAINTIES

As described in section 1.4.3, the multiplicative uncertainties mainly come from the uncertainties in calibrations of responsivity and beam pattern.

The properties of CRHWP related to the responsivity calibration are the transmission, $\mathcal{T}$, and the polarization efficiency, ε. Both of them have a frequency dependence as described in section 5.2, thus the values depend on the spectrum of the source as shown in Eq. (5.2.8). Therefore, use of a calibration source whose spectrum is different from the CMB might cause errors in the responsivity calibration. One solution to this problem is using the CMB temperature and E-mode anisotropies as calibrators.

As discussed in section 7.3, the method to calibrate the beam pattern is the same for observations with and without the CRHWP, and thus there is no difference in the accuracy of the beam calibration for each detector. One benefit coming from the use of the CRHWP might be that we do not have the unnecessary offset due to the differential pointing of the detector pair.

8.3 SYSTEMATIC UNCERTAINTIES

Next, we estimate the systematic bias in the CMB B-mode angular power-spectrum measurements due to the CRHWP. We consider the I→P leakage and the Q↔U mixing, both of which can be implemented as beam imperfections as described in section 5.2.4. We also briefly discuss the aliasing effect, as well as the foregrounds.

8.3.1 *Beam systematics*

The I→P leakage and the Q↔U mixing contaminate the power in the temperature and E-mode anisotropy into the B-mode, and cause the systematic bias. The I→P leakage comes from the non-ideality of the optics on the sky side of the CRHWP (see section 5.2.2), the HWP synchronous beam variation (see section 5.2.4), or even the detector non-linearity (section 5.3.2). The Q↔U mixing mainly comes from the polarization angle calibration error, and the cross polarization of the optics (see Appendix B). Both effects can be treated as the off-diagonal component of the Mueller beam matrix (see O'Dea et al. 2007, as well as Appendix B.2.1). We estimate the impact of the I→P leakage and the Q↔U mixing on the B-mode angular power-spectrum measurement using the analytical formula described in Appendix C.2.

First, we consider the I→P leakage. The I→P leakage beam is shown in Figure 7.3.6 from an observation of Jupiter. Note that the monopole component of the I→P leakage is also measured in section 7.4, and the main origin of the leakage is found to be the detector non-linearity.

We expand the I→P leakage beam in Laguerre Gaussian modes (see Appendix C.1) with a beam size of $\theta_{\mathrm{FWHM}} = \sqrt{8\log 2}\sigma_b = 3.65'$ and an integration radius of $40'$. The results of the expansion coefficients are shown in Figure 8.3.1 and also listed in Table 8.3.1. Note that

Table 8.3.1: Coefficients of Laguerre Gaussian expansion of the I→P leakage beam, $\mathcal{B}^{I\to P^+}(\vec{n})$, estimated from the Jupiter observation in Figure 7.3.6, where $P^+ = Q_{\mathrm{ant}} + iU_{\mathrm{ant}}$. The coefficients are normalized by the coefficient for the main lobe, c^I_{00}, from the intensity beam shown in Figure 7.3.5.

p	l	$\mathrm{Re}(c^{I\to P^+}_{pl})/\lvert c^I_{00}\rvert$	$\mathrm{Im}(c^{I\to P^+}_{pl})/\lvert c^I_{00}\rvert$
0	0	0.53%	0.00%
1	0	0.05%	-0.00%
0	1	-0.04%	0.02%
0	-1	-0.06%	-0.04%
0	2	0.00%	0.03%
0	-2	0.00%	0.00%

these normalized expansion coefficients can be compared to the differential beam parameters used in Shimon et al. 2008, and values from this study are comparable with the performance of ABS (Essinger-Hileman et al. 2016) except the monopole component, $c^{I\to P^+}_{pl}$.

We input the coefficients into the analytic formula (see Appendix C.2) and estimate the systematic bias in the B-mode. We investigate the effect for each Laguerre Gaussian mode, i. e. we set the measured values for specific expansion coefficients, $c^{I\to P^+}_{pl}$, and assume the ideal

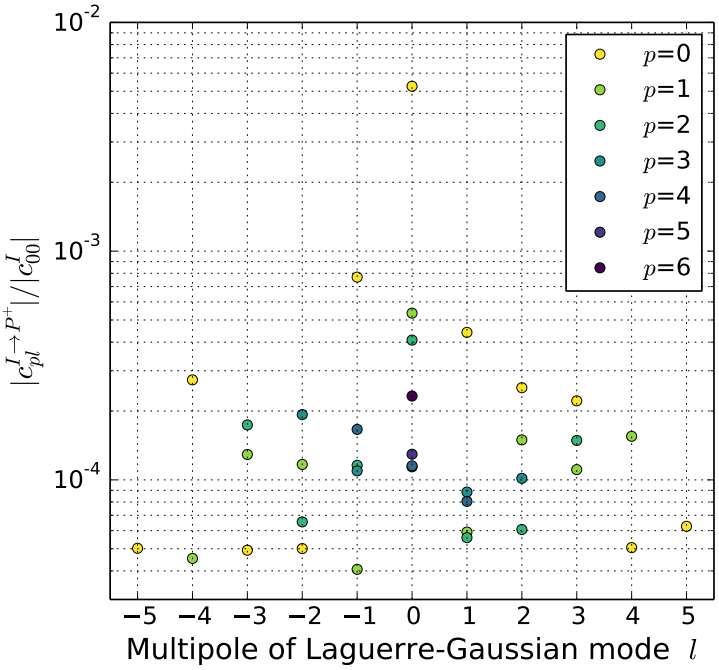

Figure 8.3.1: Amplitude distributions of the coefficients of the Laguerre Gaussian expansion

values for the others. The results for some main components are shown in Figure 8.3.2. The impact from the higher order components is smaller than that from these main components. Here, we can find that the systematic bias due to the monopole component denoted by $l = 0$ has a significant impact especially at the low multipole region, $\ell < 300$, which could be larger than the lensing B-mode signal expected from the ΛCDM model and becomes a critical obstruction for the primordial B-mode measurement. As described in section 7.5.1, however, we can subtract this monopole leakage using the intensity signal. Besides, in practice, we expect additional mitigation thanks to the parallactic angle rotation. If we can mitigate the leakage by an order of magnitude from 0.5% to 0.05%, we can suppress the impact of the monopole I→P leakage to the level smaller than the primordial B-mode signal with a tensor-to-scalar ratio $r = 0.01$. This performance is sufficient for the POLARBEAR experiment.

Next, we estimate the impact from the Q↔U mixing on the B-mode angular power-spectrum measurements. The Q↔U mixing comes from the polarization angle error and the cross-polarization of the instrument (see Appendix B).

The impact of the polarization angle error is the same for observations with and without the CRHWP and is described by Eq. (1.4.12). The polarization angle error mainly comes from the uncertainty in the calibration using the polarized point source, or using the EB correlation (see section 3.3.4). In addition, the error in the detector time constant calibration could cause polarization angle uncertainty for the case with the CRHWP. The uncertainty of the time constant calibration in the POLARBEAR experiment is typically ∼ 0.1 ms for each detector for each calibration observation. It corresponds to a polarization angle uncertainty of 0.14° with a rotation speed of $\omega_{\rm rot}/(2\pi) = 2$ Hz. In practice, however, we have random variation of the time constant error for every observation and can expect an order of magnitude suppression

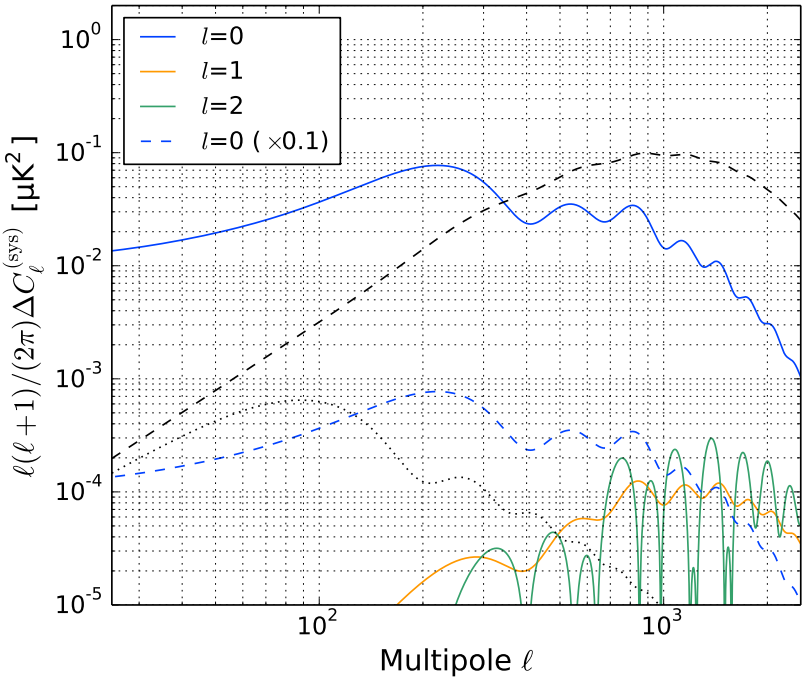

Figure 8.3.2: Systematic bias in the B-mode angular power-spectrum measurement due to the I→P leakage parameterized as Table 8.3.1. The blue, orange, and green lines are the impacts from the monopole, diple, and quadrupole modes, respectively. The blue dashed line shows the contribution of the monopole component with the leakage coefficient smaller by an order of magnitude. The black dashed line and the black dotted line show the expected angular power-spectrum of the lensing B-mode, and the primordial B-mode with the tensor-to-scalar ratio $r = 0.01$.

by averaging hundreds of observations. Therefore, the polarization angle error due to the time constant uncertainty is negligible.

The cross polarization of the instrument can be expressed as the leakage beam from Q polarization to U polarization and its opposite. For the more precise description, we can use the expression with complex values, $P^{\pm} \equiv Q \pm iU$. Then the cross polarization can be decomposed into the two components: one is the imaginary part of the $P^+ \to P^+$ beam, $\mathrm{Im}(\mathcal{B}^{P^+\to P^+})(\vec{n})$, and the other is the $P^+ \to P^-$ beam, $\mathcal{B}^{P^+\to P^-}(\vec{n})$.

Here, we consider the decomposition in the Laguerre Gaussian modes again, and discuss each mode. For the $\mathrm{Im}(\mathcal{B}^{P^+\to P^+})(\vec{n})$ beam, the monopole component is equivalent to the polarization angle error discussed above; thus we assume it is calibrated correctly here. The next prominent structure should be the dipole component. It is expected from physical optics calculations (see Appendix B). The measured Q↔U mixing beam shown in Figure 7.3.9 likely has a dipole structure, whose amplitude is about 4% compared to the main polarization signal shown in Figure 7.3.7. The impact from the dipole $\mathrm{Im}(\mathcal{B}^{P^+\to P^+})(\vec{n})$ beam on the B-mode angular power-spectrum is shown in Figure 8.3.3, where the coefficient of the Laguerre Gauss expansion is set to $|\mathrm{Im}(c_{0,1}^{P^+\to P^+})| = |\mathrm{Im}(c_{0,-1}^{P^+\to P^+}| = 4\%$. Here, we find that the impact depends on the angle of the dipole pattern. The horizontal dipole contaminates the E-mode signal into the B-mode signal, while the vertical dipole contaminates the B-mode signal into the B-mode,

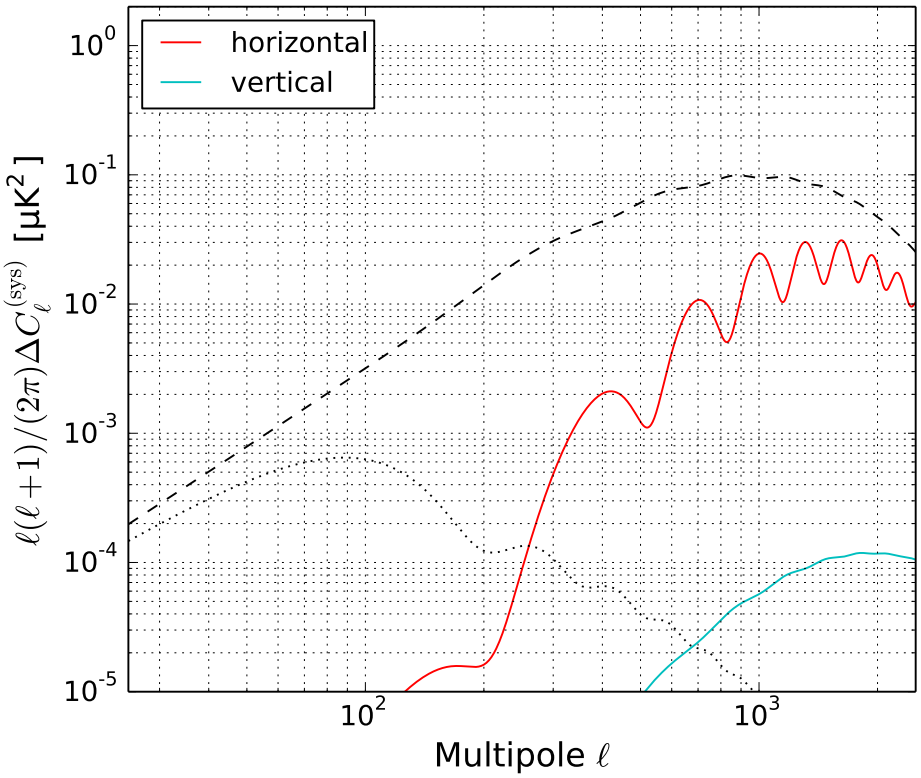

Figure 8.3.3: Systematic bias in the B-mode angular power-spectrum measurements due to dipole $Q \leftrightarrow U$ mixing. The red line and the cyan line show the dependence on the direction of the dipole pattern. The red line corresponds to the horizontal case, and the cyan line corresponds to the vertical case. The amplitudes of the dipole are the same for both cases ($|c_{0,\pm1}^{P^+\to P^+}| = 4\%$). Expectations of lensing B-mode and primordial B-mode with $r = 0.01$ are also shown as the dashed and dotted black lines.

i. e. it distorts the B-mode angular power-spectrum shape. However, the expected impacts are smaller than the lensing B-mode signal for both cases, and moreover we can expect further mitigation from the parallactic angle rotation and cancellation among the detectors. Therefore, the performance is sufficient for the POLARBEAR experiment.

For the $\mathcal{B}^{P^+\to P^-}(\vec{n})$ beam, we could have a monopole component due to the optics on the sky side of the CRHWP as described in section 5.2.2. The $P^+ \to P^-$ leakage coefficient should be comparable with that of the optical I→P leakage due to the primary mirror, which is evaluated in section 7.4 to be less than 0.1%. Figure 8.3.4 shows the impact of the $P^+ \to P^-$ leakage with the leakage coefficient of $c_{0,0}^{P^+\to P^-} = 0.1\%$, which is sufficiently smaller than the searching B-mode signals.

8.3.2 *Aliasing*

Here, we discuss the impact of the aliasing, which is the contamination of signals from different frequencies and a unique problem for the observation using the CRHWP with the demodulation method. Thanks to the modulation of the polarization signal using the CRHWP, the

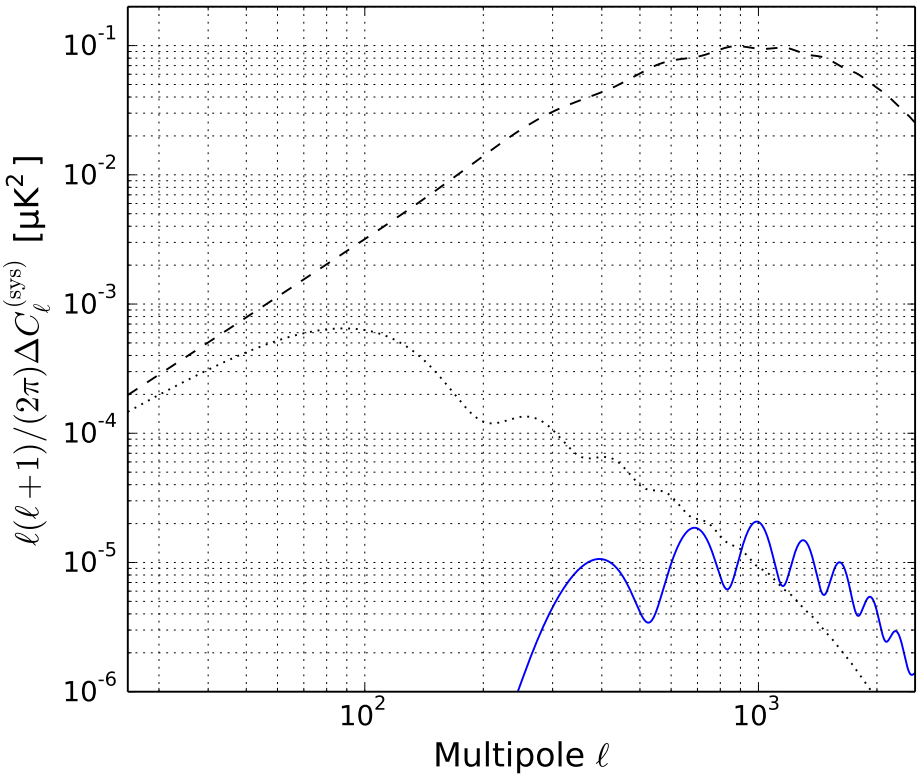

Figure 8.3.4: Systematic bias in the B-mode angular power-spectrum measurement due to the monopole $P^+ \to P^-$ mixing is shown as the blue line. Here, the estimate is calculated with the leakage coefficient $c_{0,0}^{P^+ \to P^-} = 0.1\%$. Expectations of the lensing B-mode and the primordial B-mode with $r = 0.01$ are also shown as the dashed and dotted black lines.

intensity signal and the polarization signal are separated in the frequency domain. The polarization signal is up-converted around the modulation frequency of $\omega_{\mathrm{mod}} = 4\omega_{\mathrm{rot}} = 2\pi \cdot 8\,\mathrm{Hz}$, while the intensity signal stays around 0 Hz. However, intensity signals from small-angular-scale structures appear at high frequencies and contaminates the polarization signal.

The effect is illustrated in Figure 8.3.5 as a contribution to the PSD. Here, the black solid (dashed) curve shows the contribution from the E-mode (B-mode) polarization signal, which has a peak at the modulation frequency of 8 Hz and has sidebands from the small-angular structures. The contribution from the CMB temperature anisotropy signal is shown as the blue solid line, which has a peak at 0 Hz. The sideband of the intensity signal reaches ~ 4 Hz but is sufficiently smaller than the polarization signals above 4 Hz.

Another source of aliasing is the leakage of the intensity signal into the HWPSSs, where the $n = 2$ HWPSS should have the largest contribution. Note that the leakage into the $n = 4$ HWPSS is equivalent to the I→P leakage and already discussed in the previous section. In Figure 8.3.5, the green solid line shows the contributions due to the leakage into $n = 2$ HWPSS, with a leakage coefficient of 1%. The contribution exceeds the B-mode below 6 Hz, but the frequency range corresponds to multipoles of $\ell > 2400$. Thus it only has a limited impact on the primordial B-mode measurement and can be mitigated further by the leakage subtraction as the green dashed line.

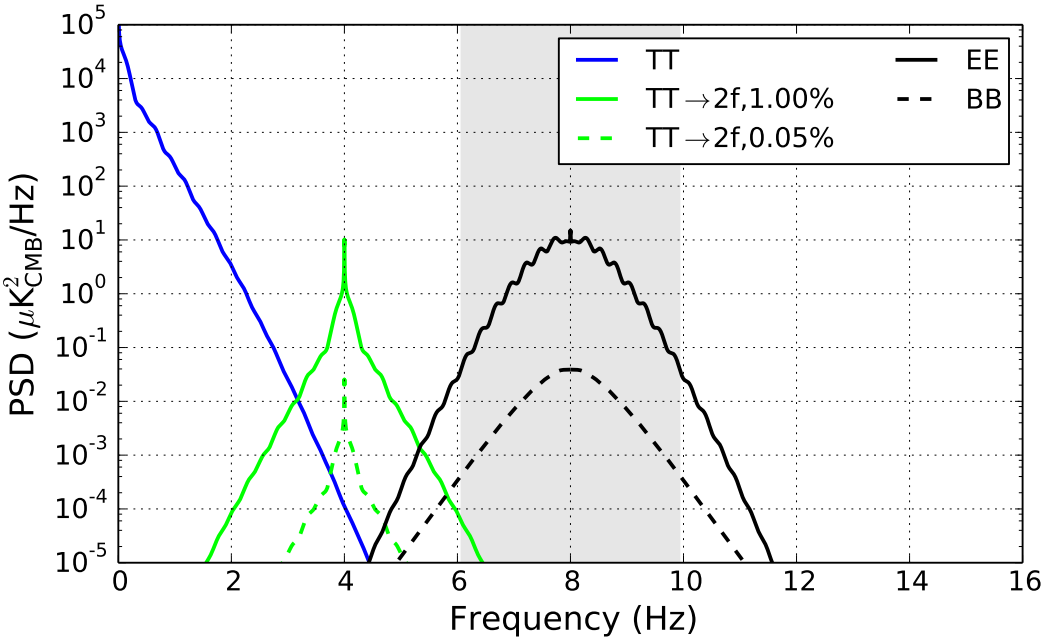

Figure 8.3.5: PSDs from the CMB signal due to aliasing. The scan speed is 0.3°/s. The shaded frequency range shows the science band of polarization signals within $\ell < 2400$.

8.3.3 *Foregrounds*

Finally, we briefly discuss the effect of the CRHWP on the contamination of foregrounds.[1] Since the foregrounds are signals on the sky as well as the CMB, the CRHWP does not help mitigate the contamination of the foregrounds. We thus need to perform foreground removal using observations with multiple frequency bands as explained in section 1.4.3 even with the CRHWP. One potential problem might be the source spectrum dependence of the parameters characterizing the CRHWP, namely the transmission, $\mathcal{T}$, the polarization efficiency, ε, and the I→P leakage coefficients, $\lambda_4^{(opt)}$ (Bryan et al. 2010a).[2] The knowledge of such a frequency dependence of the CRHWP related parameters, as well as the detector bandpass, would be necessary in foreground-removal methods which require both the source spectrum information and the bandpass information. On the other hand, foreground removal methods independent of the source spectrum, would be less affected by the imperfection.

8.4 SUMMARY OF THE IMPACT ON THE B-MODE ANGULAR-POWER SPECTRUM MEASUREMENT

For the statistical uncertainty, $\Delta C_\ell^{(stat)}$, the CRHWP could increase the white noise due to the additional loading from the CRHWP, the decrease of the transmission and the polarization

1 See section 1.4.1.

2 In the case of a stacked achromatic half-wave plate (Matsumura et al. 2009), we also have the source spectrum dependence of the polarization angle, and impact of the effect for foreground removal is investigated in Bao et al. (2012). Note that an idea to mitigate the dependence is also proposed in Matsumura (2014).

efficiency, and the uncertainty of the CRHWP angle. However, the improvement in the 1/f noise performance could be more powerful than the drawback in the white noise, and could improve the sensitivity for the measurement of the primordial B-mode signal.

For the systematic error, $\Delta C_\ell^{(\mathrm{sys})}$, we have investigated the impact of the I→P leakage and the Q↔U mixing, as well as the aliasing effect. The most concerning item is the monopole-type I→P leakage due to the detector non-linearity as described in section 7.4, which could cover the primordial B-mode signal. However, we could remove the leakage using the leakage subtraction method (see section 7.5.1). The sky rotation also helps mitigate the contamination. Therefore, the monopole I→P leakage could be manageable. Contributions from the other items are sufficiently small for the measurement of the primordial B-mode signal at the level of $r \sim 0.01$.

Note that the systematic error due to the Galactic foregrounds is still problematic for observations using the CRHWP as described in chapter 4. Although the CRHWP could change the optical properties, such as the transmission and the I→P leakage, depending on the source spectra, the impact is expected to be small. We could therefore use the same foreground removal method proposed for observations without the CRHWP.

9 FUTURE PROSPECTS

The CRHWP provides the possibility to observe the angular power-spectrum of the CMB anisotropy from large-angular scales to small-angular scales. The practical model constructed in section 5.5, however, predicts potential challenges in future experiments due to the improvement of the sensitivity and the increase of the observing frequency bands. We summarize the challenges in section 9.1.

Finally, in section 9.2, we also discuss the impact of the measurements from large-angular scale to small-angular scales in terms of scientific outcomes, especially for the study of inflation.

9.1 IMPLEMENTATION FOR FUTURE EXPERIMENTS

Future ground-based experiments, such as Simons Array (Stebor et al. 2016), Advanced ACTPol (Henderson et al. 2016), and CMB-S4 (Abazajian et al. 2016) may benefit from using a CRHWP to access low multipoles with a large-aperture telescope.

In this section, we discuss further improvements of CRHWP modules for the full success of such future experiments.

9.1.1 *Half-wave plate*

As described in chapter 4, current B-mode angular power-spectrum measurements are limited by the systematic error due to the galactic foregrounds. We need to subtract the systematic error through a foreground removal method, but the uncertainty in the external data limits the overall sensitivity. To improve the measurement accuracy, future experiments need to observe the frequency band optimal to CMB measurements, as well as other frequencies even though they are not efficient for CMB.

One simple way to observe multiple frequency bands is to prepare one telescope or one focal plane for each frequency band. The approach has been taken in Keck, SPIDER, ACTPol, etc. However, it is possible to observe multiple frequency bands in a single focal plane, if the optical system has sufficient transmission for all the frequency bands. Besides, if the antenna is sensitive to wide-band, and if we can split each frequency band appropriately, we can observe multiple frequency bands in the same detector pixel. Recently, dual-band and tri-band detectors are developed and used for observations.

Then, a HWP for such multiband observations also needs to be adequate for the multiple frequency bands. The most important property is the polarization modulation efficiency. A simple HWP made of a birefringent material is efficient only in a narrow band around the optimal frequency for which the phase delay is exactly π. To improve the modulation efficiency for a wide frequency band, several types of HWPs are proposed Hanany et al. (e.g. 2005), Pisano et al. (2006), Savini et al. (2006), Pisano et al. (2008), Savini et al. (2009), Matsumura et al. (2009), Bryan et al. (2010b), and Moncelsi et al. (2014).

Another important improvement for the HWP is operating it at cryogenic temperatures. An achromatic HWP consists of several HWPs, and also needs multiple layers of ARC. Then, the absorption in the HWP, as well as the loading from the HWP, increases if it is placed at room temperature. To reduce the loading, we need to cool the HWP at cryogenic temperatures such as $\sim 4\,\mathrm{K}$. A rotation mechanism available at cryogenic temperatures has been developed (e.g. Klein et al. 2011).

9.1.2 *Low frequency noise*

Because future experiments will contain thousands of detectors, the all-detector-combined instantaneous sensitivity, $\mathrm{NET}_{\mathrm{array}}$, is expected to improve to $\sim 3\,\mu\mathrm{K}\sqrt{\mathrm{s}}$. On the other hand, most of the $1/f$ noises are correlated among detectors, and thus are not suppressed by averaging among detectors as discussed in section 5.4. It means that controlling the $1/f$ noises at a level below the white noise sensitivity becomes more challenging for future experiments even with the CRHWP. For full success of the large-angular-scale measurements with future experiments, the understanding of all the possible $1/f$ noise sources discussed in section 5.4 is necessary.

Additionally, there is a strong argument for minimizing the leakage coefficients by minimizing the detector non-linearity, as the systematic uncertainty from imperfect knowledge of the leakage coefficients degrades the B-mode power spectrum measurement. As the detector non-linearity arises from resistance variation in the TES, we can reduce the detector non-linearity by operating under a higher loop gain. Furthermore, there are ideas to eliminate the detector non-linearity: operating the SQUID amplifier with a digital active nulling (de Haan et al. 2012) and operating the TES in a resistance-locked loop (van der Kuur et al. 2013).

9.1.3 *Beam systematic*

As shown in section 8.3.1, even with the CRHWP, we could have beam imperfections and resulting systematic uncertainties in the angular power-spectrum measurements of the CMB anisotropy. Again, since future experiments will improve the statistical uncertainty of angular power-spectrum measurements by orders of magnitudes, the beam systematic uncertainty may become a problem. In addition, future experiments will need to use a larger area of the focal plane to place as many detectors as possible. Then, the peripheral detectors could suffer from the effect of aberration, and have larger beam imperfections. In case the beam systematic error becomes greater than the statistical uncertainty, we might need to adopt a dedicated analysis method, e. g. deprojection (BICEP2 Collaboration 2015).

9.2 SCIENTIFIC PROSPECTS

Finally, in this section, we discuss the expected scientific outcomes with the fully statistical performance of future experiments assuming that all the challenges above are solved, i. e. uncertainties of angular power-spectrum measurements are determined by the statistical uncertainties as Eq. (1.4.8).

9.2.1 *Constraint on the tensor-to-scalar ratio, r*

First, we demonstrate the impact of this study from the viewpoint of the constraint on the tensor-to-scalar ratio, r, which is the most important parameter to detect the signal from primordial gravitational waves and to determine the inflation model.

The signature from the tensor-to-scalar ratio, r, only appears in the angular power-spectrum of the CMB B-mode anisotropy. Thus, we estimate the constraint on r from a specific B-mode angular power-spectrum measurement with a statistical uncertainty given by Eq. (1.4.8). Using the Fisher forecast method, the one-sigma limit on $r = 0$ is estimated as

$$\sigma_r = \left[\sum_{\ell=\ell_{min}}^{\ell_{max}} \left(\frac{C_\ell^{BB,prim}(r=1)}{\Delta C_\ell^{BB}} \right)^2 \right]^{-1/2} , \tag{9.2.1}$$

where $C_\ell^{BB,prim}(r=1)$ is the primordial component of the B-mode angular power-spectrum with $r = 1$, and ΔC_ℓ^{BB} is the statistical uncertainty from Eq. (1.4.8), which is determined by the map depth, $w_T^{-1/2}$, the FWHM of the beam, θ_{FWHM}, and the fractional sky area, f_{sky}. ℓ_{min} and ℓ_{max} are the minimum and the maximum multipole that the measurement provides.

Using Eq. (9.2.1), we can calculate the dependence of σ_r on the minimum multipole, ℓ_{min}, as well as the map depth, $w_T^{-1/2}$. The results are shown in Figure 9.2.1.

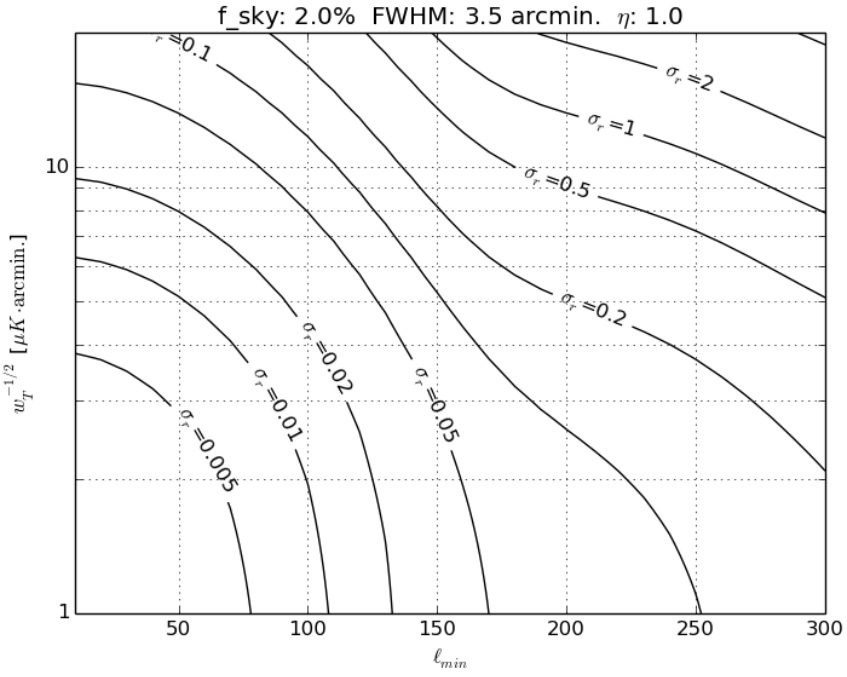

Figure 9.2.1: One-sigma limit on $r = 0$ as a function of both the noise in the CMB map and ℓ_{min}. Here, $f_{sky} = 2\%$, $\theta_{FWHM} = 3.5'$, and $\ell_{max} = 4000$ are used.

Let us discuss the impact of this work using Figure 9.2.1. Here, the vertical axis, the map depth, represents the total statistics, and the lower values corresponds to larger amount of data. As shown in Eq. (1.4.6), the map depth is inversely proportional to square root of the

total observation time as $t_{obs}^{-1/2}$, i.e. , to go down along the vertical axis by a factor of 2, we need an additional observation time three times longer than the observation until that time. The one-sigma limit on r improves as the square of the map depth, i.e. it is proportional to t_{obs}^{-1}, but eventually it hits a limit because of the sample variance.
On the other hand, the horizontal axis, ℓ_{min}, is mainly determined by the low frequency noise ($1/f$ noise) of the instrument. In this study, we have demonstrated that the achievement of $\ell_{min} \lesssim 40$ with a large aperture telescope is very promising. Since the one-sigma limit on r exponentially improves as the ℓ_{min} decreases, the improvement of ℓ_{min} in this work has a significant impact on the measurements of r. For example, let us look at a point ($\ell_{min} = 100$, $w_T^{-1/2} = 8\,\mu K \cdot arcmin$) where $\sigma_r = 0.05$. If we improve ℓ_{min} from 100 to 50, σ_r improves to $\sigma_r = 0.02$. To achieve the same accuracy with $\ell_{min} = 100$, we need to improve the $w_T^{-1/2}$ by a factor of two with three times more observations.

If we achieve a statistical uncertainty sufficiently smaller than the lensing B-mode signal, the constraint on the r hits the limit imposed by the sample variance of the lensing B-mode. The effect can be seen in the Figure 9.2.1 below $w_T^{-1/2} \lesssim 4\,\mu K \cdot arcmin$. One solution to reduce the sample variance is to observe a larger sky region. However, it might be difficult due to the foregrounds, or the location of the experiment. Then, we need to subtract the lensing B-mode using a delensing method.

Using a delensing method, the uncertainty of the angular power-spectrum measurement can be improved as

$$\Delta C_\ell^{BB,delens} = \sqrt{\frac{2}{(2\ell+1)f_{sky}}}(C_\ell^{BB,res} + N_\ell) \quad , \tag{9.2.2}$$

where $C_\ell^{BB,res}$ is the angular power-spectrum of the residual lensing B-mode. Here, we adopt the iterative delensing method (Smith et al. 2012) to estimate the residual, and then perform the Fisher forecast again with the improved angular power-spectrum measurement uncertainty.

Figure 9.2.2 shows the one-sigma limit on r with the delensing method as a function of the FWHM of the beam, θ_{FWHM}, and the map depth, $w_T^{-1/2}$. Here, we can see clear difference in the performance of the delensing depending on the beam size. The delensing with the lower resolution of $\theta_{FWHM} \gtrsim 10'$ is not sufficient and hits a limit due to the sample variance from the residual lensing B-mode. To achieve the measurement at a level of $\sigma_r \lesssim 0.001$, the beam size needs to be smaller than 10 arcmin. The 3.5 arcmin beam of the POLARBEAR experiment satisfies this requirement. Again, we emphasize that achieving the measurement with the minimum multipole of $\ell_{min} \sim 40$ is critical here, too. The CRHWP enables a large aperture telescope with high resolution to observe large-angular scales, which eventually results in the most sensitive measurements of r.

9.2.2 *Constraint on the scalar spectral index, n_s*

A CMB anisotropy measurement over a broad range of scales with a single experiment, like what has been treated in this study, will also give us a better constraint on the scalar spectral index, n_s.

Information on the scalar spectral index can be obtained from the angular power-spectrums of temperature, E-mode, and the cross-correlation between the two, i.e. C_ℓ^{TT}, C_ℓ^{EE}, and C_ℓ^{TE}. If the map depth of a polarization measurement is better than $\sim 10\,\mu K \cdot arcmin$, the uncertainties

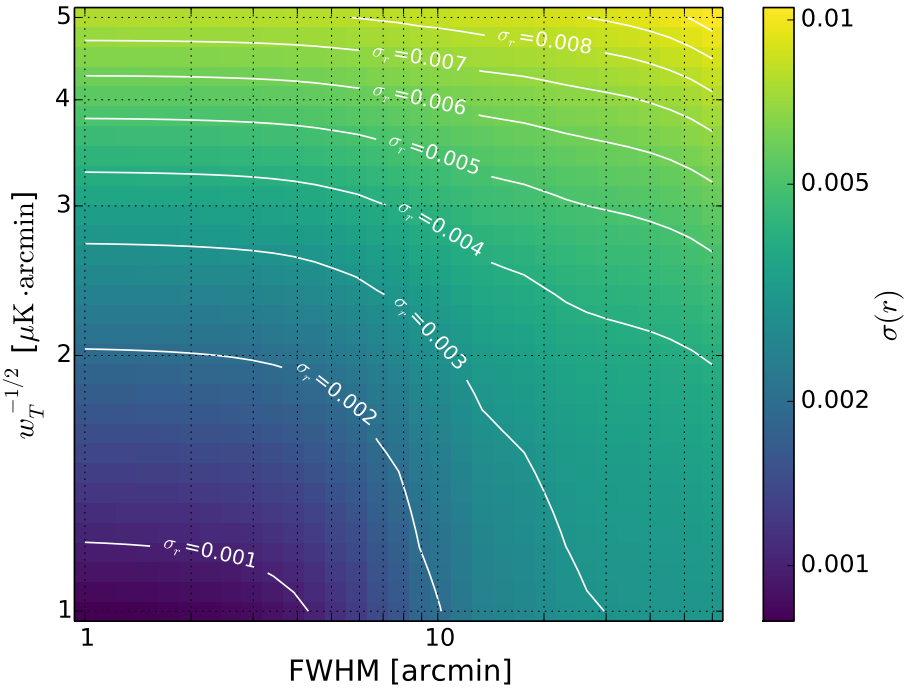

Figure 9.2.2: One-sigma limit on $r = 0$ after delensing as a function of both the noise in the CMB map and the FWHM of the beam. Other parameters are determined as $f_{sky} = 2\%$, $\ell_{min} = 40$, and $\ell_{max} = 4\pi\sqrt{2\ln 2}/\theta_{FWHM}$.

of the angular power-spectrum measurements are limited by the sample variance up to the multipole of ~ 2000. Since we have the more stringent requirement on the map depth with $\lesssim 5\,\mu\text{K}\cdot\text{arcmin}$ to probe the tensor-to-scalar ratio, r, here, we ignore the statistical uncertainties in measurements of C_ℓ^{TT}, C_ℓ^{EE}, and C_ℓ^{TE}, and discuss the uncertainties from the sample variance. Note that observing a large sky area is critical to reduce the sample variance, and we assume the fractional sky area of $f_{sky} = 50\%$ in the following discussion.

Let us consider the constraint on n_s with the sample variance limited measurements of C_ℓ^{TT}, C_ℓ^{EE}, and C_ℓ^{TE}, as described above. We use the Fisher method again. To make the discussion clear, we ignore the correlation with the other cosmological parameters. The one-sigma constraint on n_s can be obtained as

$$\sigma_{n_s} = \left[\sum_{X\in\{TT,EE,TE\}} \sum_{\ell=\ell_{min}}^{\ell_{max}} \left(\frac{\partial C_\ell^X}{\partial n_s} \Big/ \Delta C_\ell^X \right)^2 \right]^{-1/2} , \tag{9.2.3}$$

where $\frac{\partial C_\ell^X}{\partial n_s}$ is the derivative of the angular power-spectrum by n_s, and ΔC_ℓ^X is the uncertainty from the sample variance. The latter is estimated as described in Eq. (1.4.8) as

$$\Delta C_\ell^X = \sqrt{\frac{2}{(2\ell+1)f_{sky}}} |C_\ell^X| \quad ,$$

and the former can be obtained approximately as

$$\frac{\partial C_\ell^X}{\partial n_s} = (\log\ell - \log\ell_*) C_\ell^X \tag{9.2.4}$$

where ℓ_* is an arbitrary pivot multipole. Here, both of them are proportional to the angular power-spectrum, thus their ratio does not depend on the shape of the angular power-spectrum, i. e. the one-sigma limit on n_s can be determined by the multipole range, $[\ell_{min}, \ell_{max}]$, and f_{sky}. The pivot multipole is determined to minimize the bias as

$$\sum_{\ell=\ell_{min}}^{\ell_{max}} \left(\frac{\partial C_\ell^X}{\partial n_s} \Big/ \Delta C_\ell^X \right) = 0 \quad , \tag{9.2.5}$$

which leads to

$$\log \ell_* = \frac{\sum_{\ell=\ell_{min}}^{\ell_{max}} \sqrt{2\ell+1} \log \ell}{\sum_{\ell=\ell_{min}}^{\ell_{max}} \sqrt{2\ell+1}} \quad . \tag{9.2.6}$$

Using Eq. (9.2.3), we calculate the one-sigma limit on n_s for two cases: one of which is a single measurement with a multipole range of $[40, 2000]$, and the other is a combination of two measurements with multipole ranges of $[40, 800]$ and $[800, 2000]$. The results are compared in Table 9.2.1.

Table 9.2.1: Comparison of the one-sigma limit on n_s between the two types of measurements. Here, the fractional sky area $f_{sky} = 50\%$ is assumed.

Multipole range, $[\ell_{min}, \ell_{max}]$	One-sigma limit on n_s, σ_{n_s}
$[40, 800]$	0.0029
$[800, 2000]$	0.0026
$[40, 800]$ and $[800, 2000]$	0.0019
$[40, 2000]$	0.0011

For the latter case, the one-sigma limit is calculated for each of the multipole ranges, and the combined constraint is calculated as $\sigma_{combine} = [\sigma_{low}^{-2} + \sigma_{high}^{-2}]^{-1/2}$, where σ_{low}, σ_{high}, and $\sigma_{combine}$ are the one-sigma limits for the low multipole measurement, the high multipole measurement, and their combination, respectively. Here, we can find that the single measurement which covers the entire multipole range can achieve a sensitivity twice as good as that from the combination of the two measurements covering the same multipole range.

Note that the difference comes from the complete loss of connection between the two multipole ranges. Such an assumption might be too unfavorable for the combination measurements. In practice, we could have an overlap between the two measurements, and connect the measurements matching the overlap region. However, each measurement might have different instrumental systematic error, which may make the connection difficult and may cause a systematic error in the n_s measurement. On the other hand, for the case of the single measurement, we can calibrate the instrumental performances across all the multipole ranges at a time, thus we could minimize the instrumental systematic error on the n_s measurement.

9.2.3 *Constraints on the inflation model*

Finally, we consider the impact of the improvements in the measurements of the tensor-to-scalar ratio, r, and the scalar spectral index, n_s, on the determination of the inflation model.

Inflation is a plausible scenario to solve the horizon problem and the flatness problem as described in section 1.2.2. Currently, however, we have hundreds of models (Martin et al. 2014), which are somewhat different from each other in the origin of the inflaton and in the shape of the inflaton potential. To understand the inflation and the theory describing the physics at the very high-energy scale, we need to determine the actual model from observations of the Universe, especially the primordial perturbations.

The most prominent signal is the amplitude of the scalar-type perturbation, A_s. It has been measured from the CMB temperature anisotropy, and determined as $\ln(10^{10}A_s) = 3.064 \pm 0.023$ (Planck Collaboration 2016c). Under the assumption of the single-field slow-roll, the information gives us a rough estimate of the energy scale of the inflaton potential as $V(\phi)/\epsilon_V^{1/4} \approx (6.55 \pm 0.04) \times 10^{16}\,\mathrm{GeV}$. However, the unknown contribution of the slow-roll parameter, ϵ_V, which represents the slope of the inflaton potential, prevents us from determining the energy scale.

The tensor-to-scalar ratio, r, which is the ratio between the amplitudes of the tensor- and scalar-type perturbations, is directly related to the slow-roll parameter, ϵ_V, as $r \approx 16\epsilon_V$. Thus, the detection and the precise measurement of r determines the energy scale of the inflaton potential as

$$V^{1/4} \approx 1.04 \times 10^{16} \left(\frac{r}{0.01}\right)^{1/4} \mathrm{GeV} \quad . \tag{9.2.7}$$

A one-sigma limit of $\sigma_r = 0.001$ suffices for probing the Grand Unified Theory (GUT) scale precisely.

Another important implication of the tensor-to-scalar ratio, r, or the resulting slow-roll parameter, ϵ_V, is the variation of the inflaton field, $\Delta\phi$, which is approximately $\Delta\phi/M_{\mathrm{pl}} \approx N\sqrt{r/8}$, where $M_{\mathrm{Pl}} = 2.435 \times 10^{18}\,\mathrm{GeV}$ is the reduced Planck mass, and N is the e-folding number of the expansion during the inflation. To solve the horizon problem and the flatness problem, $N \sim 50$ is necessary. Then, if the tensor-to-scalar ratio, r, is sufficiently large, the field variation could exceed the Planck scale. The limit, the so-called Lyth bound (Lyth 1997), can be expressed as

$$r > 0.003 \left(\frac{N}{50}\right)^{-2} \quad . \tag{9.2.8}$$

The one-sigma limit of $\sigma_r = 0.001$ is also sufficient to search the boundary.

In addition, the spectral index of the scalar-type perturbation, n_s, has other information on the inflaton potential as $n_s - 1 = 2\eta_V - 6\epsilon_V$, where η_V is the second slow-roll parameter related to the curvature of the potential. Therefore, the measurements of (r, n_s) determine the slow-roll parameters, (ϵ_V, η_V), and give us the rough shape of the inflaton potential. This information is critical to select the actual inflation model from the hundreds of models with various potential shapes.

Figure 9.2.3 shows the predictions of the (r, n_s) combination from various inflation models in Martin et al. (2014), as well as the one-sigma constraint with $\sigma_r < 0.001$ and $\sigma_{n_s} < 0.001$. The precise measurement of (r, n_s) will enable us to reject most of the inflation models and to select one or a small number of infaltion models. Or, it is also interesting if none of the current models can explain the measured value.

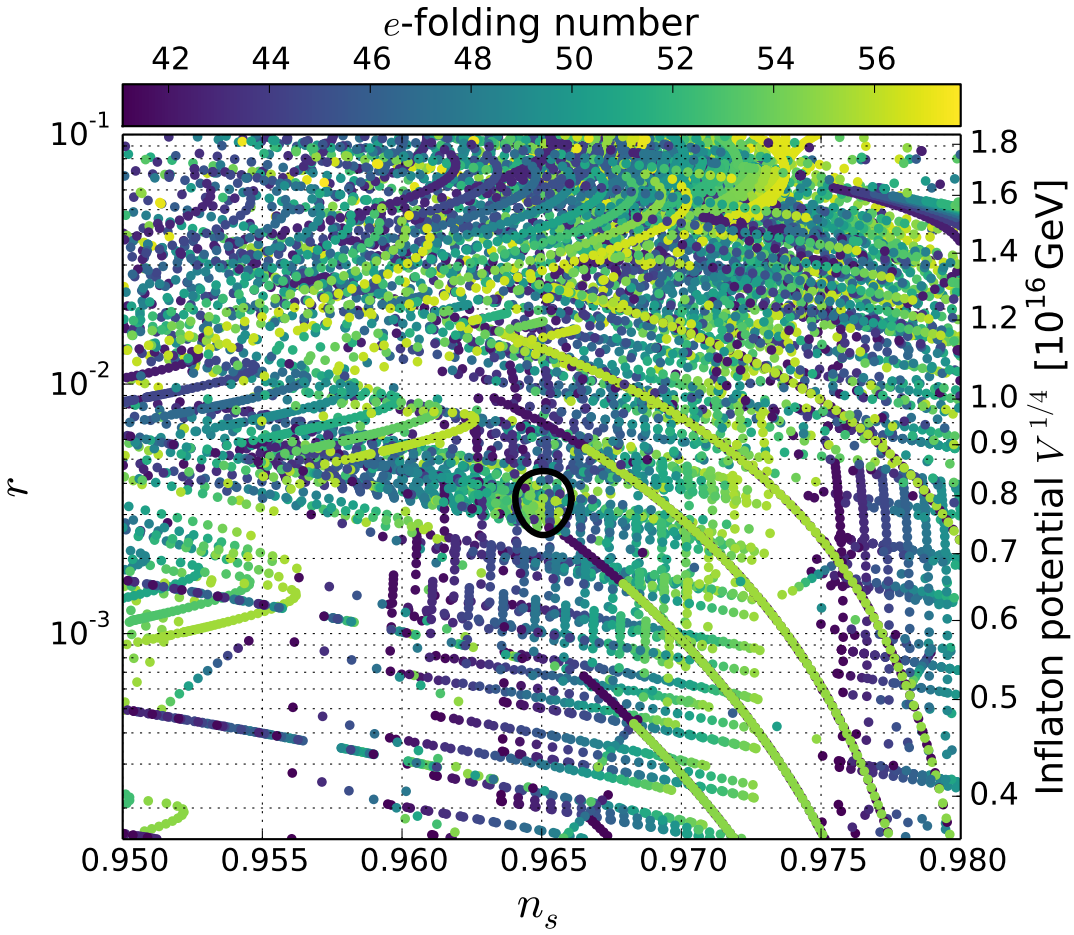

Figure 9.2.3: The inflation models from Martin et al. (2014) as a function of the tensor-to-scalar ratio, r, and the scalar spectral index, n_s. Each point corresponds to a specific inflation model with specific parameters. Gradual variation of the parameters results in a series of points for each category of the inflation models. The color of the points represents the e-folding number of the inflation. The black circle shows the one-sigma constraint with $\sigma_r = 0.001$ and $\sigma_{n_s} = 0.001$ around $(n_s, r) = (0.965, 0.0035)$.

10

SUMMARY

Cosmic inflation is a hypothesis that an accelerating expansion occurred in the very early universe before the hot Big Bang. It is well supported by the precision measurements carried out so far, such as the CMB observations. On the other hand, primordial gravitational waves, which are the most important prediction of the inflation theory, are not yet discovered. The ratio between the fluctuations due to gravitational waves and density perturbations, so-called the tensor-to-scalar ratio r, is directly connected to the energy scale of inflation. Thus it is a clue to physics at the very high energy scale that cannot be accessed in laboratory experiments. The CMB B-mode polarization fluctuation is unique in that it can constrain the value of r. Observations of fluctuation at the angular scale of about 2 degrees is important to this end. The CMB B-mode also arises from the gravitational lensing effect due to the large scale structure of the universe; the typical angular scale is 0.1 degree in this case. If r is less than 0.01, it is necessary to measure the gravitational lensing B-mode precisely and subtract it.

The POLARBEAR experiment, which is a ground-based experiment observing CMB polarization with high-sensitive detectors with a 3.5 arcmin FWHM beam at 150 GHz, started science observations of three $8\,\mathrm{deg}^2$ patches in 2012 June targeting the undetected lensing B-mode signal. Using data from one year observations, we performed three different methods to test the existence of the lensing B-mode signal. In the first method, we directly measured the B-mode angular power-spectrum of the observed CMB polarization anisotropy, and measured nonzero signal with 97.2% confidence. In the second method, we measured the angular power-spectrum of lensing deflection field reconstructed from the measured CMB polarization anisotropy, and reported the first direct evidence of the lensing B-mode signal at 4.2σ (stat. + sys.) significance. In the third method, we measured the cross correlation between the external CIB measurements and the lensing convergence field reconstructed from our CMB polarization measurements, and obtained the evidence at a statistical significance of 4.0σ. Together with first two results, we obtained the first direct evidence for the lensing B-mode with sufficient significance (4.7σ) based on purely CMB polarization information.

However, the sensitivity for large-angular scales was limited by the low frequency noise ($1/f$ noise). To solve the problem, we employed the continuous polarization modulation technique using a CRHWP. We constructed a comprehensive model of the detector signal in observations using the CRHWP including HWPSSs, beam imperfections, detector nonlinearity, and all possible noise sources. We pointed out the possibilities of the $1/f$ noise and instrumental systematics even if we use the CRHWP. We also developed a prototype CRHWP, and evaluated its performance using data from a test observation with the POLARBEAR. Especially, we investigated the I→P leakage carefully, which is the biggest concern for both the low-frequency noise and the instrumental systematic error of B-mode measurements for large-angular scales. We found considerable amount of I→P leakage by $\sim 0.5\%$, which mainly comes from the detector nonlinearity. However, we have also demonstrated that the I→P leakage subtraction method efficiently removes the atmospheric noise contamination to the level of less than 0.1%. and thus measurements with the $1/f$ knee multipole of $\ell_{\mathrm{knee}} \lesssim 40$ are achievable. The performance is sufficient to probe the primordial B-mode. Impacts of other systematic un-

certainties are also investigated and are sufficiently small to observe the primordial B-mode with POLARBEAR.

Employing the continuous polarization modulation technique, future CMB experiments will be able to measure the angular power spectrum of the CMB anisotropy, especially the B-mode, from large-angular scale to small-angular scale with unprecedented statistical sensitivity, as well as minimal contamination of instrumental systematic uncertainty. If there are no systematic errors, future experiments will improve the measurement of the tensor-to-scalar ratio, r, and also the index of scalar tilt n_s, to the level of $\sigma(r = 0) \sim 0.001$ and $\sigma(n_s = 0.96) \sim 0.001$. This enables us to distinguish major inflation models and to obtain insights for the underlying physics at very high-energy scales.

A

NON-LINEARITY OF THE TES BOLOMETER

Here, we describe the non-linearity of the transition-edge sensor (TES) bolometer.

First, we briefly review the basics of the TES bolometer in Appendix A.1. Then, we analyze the non-linearity of the TES bolometer by calculating the second-order perturbation. In Appendix A.3, we also calculate the leakage due to the non-linearity as described in section 5.3.

A.1 BASICS OF THE TES BOLOMETER

The transition-edge sensor (TES) bolometer is high sensitive detector that uses very rapid transition of superconductor material to measure the incoming power (e. g. Irwin et al. 2005). The schematic of the TES is shown in Figure A.1.1.

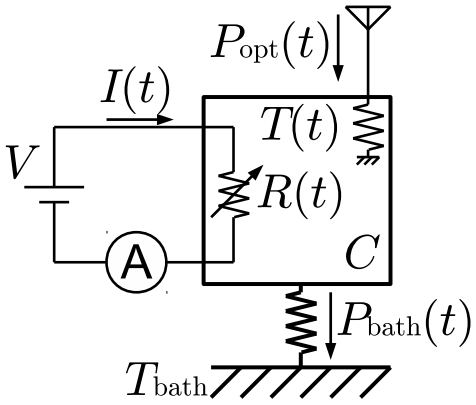

Figure A.1.1: Schematic of the TES. The square represents the island, whose heat capacity and temperature are C and $T(t)$, respectively. The island is weakly connected with the heat bath at the temperature of T_{bath}; thus the steady heat release, $\mathcal{P}_{\mathrm{bath}}(t)$, is there. The island has another port for the heat injection, $\mathcal{P}_{\mathrm{opt}}(t)$, from the antenna. The TES resistance, $R(t)$, made of a superconductor material is placed in the island and biased with the constant voltage, V. We readout the current, $I(t)$, through the bias circuit.

The island of the TES bolometer has two heat injections: one is the optical power, $\mathcal{P}_{\mathrm{opt}}(t)$, from the antenna, and the other is the Joule heat, $\mathcal{P}_{\mathrm{bias}}(t) = I(t)V = \frac{V^2}{R(t)}$, from the TES resistance. They balance with the heat release, $\mathcal{P}_{\mathrm{bath}}(t)$, via the weak link with the heat bath as

$$C\frac{dT(t)}{dt} = \mathcal{P}_{\mathrm{opt}}(t) + \mathcal{P}_{\mathrm{bias}}(t) - \mathcal{P}_{\mathrm{bath}}(t) \quad . \tag{A.1.1}$$

Note that, the constant-voltage bias provides the negative feedback, i. e. the Joule heat, $\mathcal{P}_{\mathrm{bias}}(t) = \frac{V^2}{R(t)}$, decreases when the temperature of the island increases.

The linear perturbation analysis of Eq. (A.1.1) results in the response of the TES bolometer to the optical power as

$$\delta I(\omega) = -\frac{1}{V}\frac{\mathcal{L}}{\mathcal{L}+1}\frac{1}{1+i\omega\tau}\delta\mathcal{P}_{opt}(\omega) \quad , \tag{A.1.2}$$

where $\delta I(\omega)$ and $\delta\mathcal{P}_{opt}(\omega)$ are the perturbation of the bias current and the optical power expressed in the Fourier domain with the frequency, ω. The loop gain, $\mathcal{L}$, and the time constant, τ, are calculated as

$$\mathcal{L} = \frac{\alpha}{1+\beta}\frac{\mathcal{P}_{bias}}{GT} \quad , \tag{A.1.3}$$

$$\tau = \frac{1}{1+\mathcal{L}}\frac{C}{G} \quad , \tag{A.1.4}$$

with $\alpha = \frac{d\ln R(T,I)}{d\ln T}$, $\beta = \frac{d\ln R(T,I)}{d\ln I}$, and $G = \frac{d\mathcal{P}_{bath}(T,T_{bath})}{dT}$. Because of the rapid transition of the superconductor, the TES resistance has the performance of $\alpha \gg 1$, thus $\mathcal{L} \gg 1$. Then, Eq. (A.1.2) becomes independent of the value of the loop gain, which results in the good linearity of the TES bolometer with a large dynamic range.

In practice, however, the non-linearity of the TES bolometer could become problematic if the loop gain is not sufficiently large. Thus, in the following section, we calculate the second order perturbation of Eq. (A.1.1).

A.2 PERTURBATIVE EXPANSION

Here, we calculate the second-order perturbation of Eq. (A.1.1) and obtain the response of the TES bolometer to the optical signal including the first-order non-linear effect. The response would be described as

$$\delta I(\omega) + \delta^2 I(\omega) = -\frac{1}{V}\frac{\mathcal{L}}{\mathcal{L}+1}\frac{1}{1+i\omega\tau}\delta\mathcal{P}_{opt}(\omega) + X(\omega)[\delta\mathcal{P}_{opt} * \delta\mathcal{P}_{opt}](\omega) \quad , \tag{A.2.1}$$

where the left-hand side is the bias current separated into the first- and second-order perturbations, the first term of the right-hand side is the linear response described in Eq. (A.1.1), and the last term comes from the second-order perturbation. Here the $X(\omega)$ is a specific coefficient and the asterisk denotes the convolution in the Fourier domain.

A.2.1 *Definitions of the perturbations*

First, we define the notation of the perturbations as follows:

- The zeroth-order terms are denoted by the overbar.
- The first-order terms are denoted by the single δ.
- The second-order terms are denoted by the δ^2 or expressed as the product of the first-order terms.

Following the notation, all the parameters are expressed as follows:
The electrical parameters:

$$V = \bar{V} = \text{const.} \quad , \tag{A.2.2}$$

$$I(t) = \bar{I} + \delta I(t) + \delta^2 I(t) \quad , \tag{A.2.3}$$

$$R(t) = \bar{R} + \delta R(t) + \delta^2 R(t) \quad . \tag{A.2.4}$$

The temperature of the island:

$$T(t) = \bar{T} + \delta T(t) + \delta^2 T(t) \quad . \tag{A.2.5}$$

The power flows:

$$\mathcal{P}_{opt}(t) = \bar{\mathcal{P}}_{opt} + \delta\mathcal{P}_{opt}(t) \quad , \tag{A.2.6}$$

$$\mathcal{P}_{bath}(t) = \bar{\mathcal{P}}_{bath} + \delta\mathcal{P}_{bath}(t) + \delta^2\mathcal{P}_{bath}(t) \quad , \tag{A.2.7}$$

$$\mathcal{P}_{bias}(t) = \bar{\mathcal{P}}_{bias} + \delta\mathcal{P}_{bias}(t) + \delta^2\mathcal{P}_{bias}(t) \quad , \tag{A.2.8}$$

where we omit the second-order term optical power for simplicity.

A.2.2 *Relation between parameters*

Next, we relate the parameters using the formula that connects them.

A.2.2.1 *The TES resistance in terms of the temperature and the bias current*

The base relation is

$$R(t) = R(T(t), I(t)) \quad . \tag{A.2.9}$$

The relation between the first-order terms is

$$\frac{\delta R(t)}{\bar{R}} = \alpha\frac{\delta T(t)}{\bar{T}} + \beta\frac{\delta I(t)}{\bar{I}} \quad , \tag{A.2.10}$$

where

$$\alpha \equiv \frac{\bar{T}}{\bar{R}}\frac{\partial R}{\partial T} \quad , \qquad \beta \equiv \frac{\bar{I}}{\bar{R}}\frac{\partial R}{\partial I} \quad . \tag{A.2.11}$$

The relation between the second-order terms is

$$\frac{\delta^2 R(t)}{\bar{R}} = \alpha\frac{\delta^2 T(t)}{\bar{T}} + \beta\frac{\delta^2 I(t)}{\bar{I}} + \frac{\alpha^2\alpha_1}{2}\left(\frac{\delta T(t)}{\bar{T}}\right)^2 + \frac{\beta^2\beta_1}{2}\left(\frac{\delta I(t)}{\bar{I}}\right)^2 + \alpha\beta\gamma_1\frac{\delta T(t)}{\bar{T}}\frac{\delta I(t)}{\bar{I}} \quad , \tag{A.2.12}$$

where

$$\alpha_1 = \frac{\bar{R}(\partial^2 R/\partial T^2)}{(\partial R/\partial T)^2} \quad , \tag{A.2.13}$$

$$\beta_1 = \frac{\bar{R}(\partial^2 R/\partial I^2)}{(\partial R/\partial I)^2} \quad , \tag{A.2.14}$$

$$\gamma_1 = \frac{\bar{R}(\partial^2 R/\partial T\partial I)}{(\partial R/\partial T)(\partial R/\partial I)} \quad . \tag{A.2.15}$$

A.2.2.2 *The bias current in terms of the temperature*

The base equation is

$$I(t) = \frac{\bar{V}}{R(t)} \quad . \tag{A.2.16}$$

The relation between the zeroth-order terms is

$$\bar{I} = \frac{\bar{V}}{\bar{R}} \quad . \tag{A.2.17}$$

The relation between the first-order terms is

$$\frac{\delta I(t)}{\bar{I}} = -\frac{\alpha}{1+\beta}\frac{\delta T(t)}{\bar{T}} \quad . \tag{A.2.18}$$

The relation between the second-order terms is

$$\frac{\delta^2 I(t)}{\bar{I}} = -\frac{\alpha}{1+\beta}\left[\frac{\delta^2 T(t)}{\bar{T}} + F\left(\frac{\delta T(t)}{\bar{T}}\right)^2\right] \quad , \tag{A.2.19}$$

where

$$F = -\frac{\alpha}{2}\frac{2-\alpha_1-2\beta\,(\alpha_1-\gamma_1)-\beta^2\,(\alpha_1+\beta_1-2\gamma_1)}{(\beta+1)^2} \quad . \tag{A.2.20}$$

A.2.2.3 *The heat release, $\mathcal{P}_{bath}$, in terms of the temperature, T*

The base equation is

$$\mathcal{P}_{bath}(t) = k\left(T^{n+1}(t) - T_b^{n+1}\right) \quad , \tag{A.2.21}$$

where n is determined by the power law of the thermal conductance depending on the carrier: i. e. $n = 1$ for the electron and $n = 3$ for the phonon.
The relation between the zeroth-order terms is

$$\bar{\mathcal{P}}_{bath} = k\left(\bar{T}^{n+1} - T_b^{n+1}\right) \quad . \tag{A.2.22}$$

The relation between the first-order terms is

$$\delta\mathcal{P}_{bath}(t) = \bar{G}\bar{T}\frac{\delta T(t)}{\bar{T}} \quad , \tag{A.2.23}$$

where

$$\bar{G} = k(n+1)\bar{T}^n \quad . \tag{A.2.24}$$

The relation between the second-order terms is

$$\delta^2\mathcal{P}_{bath}(t) = \bar{G}\bar{T}\frac{\delta^2 T(t)}{\bar{T}} + \frac{nG\bar{T}}{2}\left(\frac{\delta T(t)}{\bar{T}}\right)^2 \quad . \tag{A.2.25}$$

A.2.2.4 *The Joule heat, $\mathcal{P}_{bias}$, in terms of the temperature, T*

The base equation is

$$\mathcal{P}_{bias}(t) = I^2(t)R(t) \quad . \tag{A.2.26}$$

The relation between the zeroth-order terms is

$$\bar{\mathcal{P}}_{bias} = \bar{I}^2\bar{R} = \bar{V}\bar{I} \quad . \tag{A.2.27}$$

The relation between the first-order terms is

$$\delta\mathcal{P}_{\text{bias}} = \bar{I}^2\bar{R}\left(2\frac{\delta I(t)}{\bar{I}} + \frac{\delta R(t)}{\bar{R}}\right) \tag{A.2.28}$$

$$= -\bar{\mathcal{L}}\bar{G}\bar{T}\frac{\delta T(t)}{\bar{T}} \quad , \tag{A.2.29}$$

where

$$\bar{\mathcal{L}} \equiv \frac{\alpha}{1+\beta}\frac{\bar{\mathcal{P}}_{\text{bias}}}{\bar{G}\bar{T}} \quad . \tag{A.2.30}$$

The relation between the second-order terms is

$$\delta^2\mathcal{P}_{\text{bias}} = \bar{I}^2\bar{R}\left[2\frac{\delta^2 I(t)}{\bar{I}} + \frac{\delta^2 R(t)}{\bar{R}} + \left(\frac{\delta^2 I(t)}{\bar{I}}\right)^2 + 2\frac{\delta I(t)}{\bar{I}}\frac{\delta R(t)}{\bar{R}}\right] \tag{A.2.31}$$

$$= -\bar{\mathcal{L}}\bar{G}\bar{T}\left[\frac{\delta^2 T(t)}{\bar{T}} + F\left(\frac{\delta T(t)}{\bar{T}}\right)^2\right] \quad . \tag{A.2.32}$$

A.2.2.5 *Thermal equilibrium*

The base equation is

$$C\frac{dT(t)}{dt} = \mathcal{P}_{\text{bias}}(t) - \mathcal{P}_{\text{bath}}(t) + \mathcal{P}_{\text{opt}}(t) \quad . \tag{A.2.33}$$

The relation between the zeroth-order terms is

$$0 = \bar{\mathcal{P}}_{\text{bias}} - \bar{\mathcal{P}}_{\text{bath}} + \bar{\mathcal{P}}_{\text{opt}} \quad . \tag{A.2.34}$$

The relation between the first-order terms is

$$C\frac{d\delta T(t)}{dt} = \delta\mathcal{P}_{\text{bias}}(t) - \delta\mathcal{P}_{\text{bath}}(t) + \delta\mathcal{P}_{\text{opt}}(t) \quad , \tag{A.2.35}$$

$$C\frac{d\delta T(t)}{dt} + \bar{G}(\bar{\mathcal{L}}+1)\delta T(t) = \delta\mathcal{P}_{\text{opt}}(t) \quad . \tag{A.2.36}$$

The relation between the second-order terms is

$$C\frac{d\delta^2 T(t)}{dt} = \delta^2\mathcal{P}_{\text{bias}}(t) - \delta^2\mathcal{P}_{\text{bath}}(t) \quad , \tag{A.2.37}$$

$$C\frac{d\delta^2 T(t)}{dt} + \bar{G}(\bar{\mathcal{L}}+1)\delta^2 T(t) = -\bar{G}\bar{T}\left[\bar{\mathcal{L}}F + \frac{n}{2}\right]\left(\frac{\delta T(t)}{\bar{T}}\right)^2 \quad . \tag{A.2.38}$$

A.2.3 *Fourier transform*

We Fourier transform the equations with $x(t) = \int x(\omega)e^{i\omega t}d\omega$, where x is a specific parameter, and ω is the frequency.

The Fourier transform of the first-order relation of the thermal equilibrium, Eq. (A.2.36), becomes

$$\bar{G}(\bar{\mathcal{L}} + 1 + i\omega\tau_0)\delta T(\omega) = \delta\mathcal{P}_{\text{opt}}(\omega) \quad , \tag{A.2.39}$$

where

$$\tau_0 \equiv \frac{C}{G} \quad . \tag{A.2.40}$$

Thus, the first-order term of the TES temperature is expressed by the optical power as

$$\frac{\delta T(\omega)}{\bar{T}} = \frac{\delta \mathcal{P}_{\rm opt}(\omega)}{A(\omega)} \quad , \tag{A.2.41}$$

where

$$A(\omega) \equiv \bar{G}\bar{T}(\bar{\mathcal{L}} + 1 + i\omega\tau_0) \quad . \tag{A.2.42}$$

Then, from Eq. (A.2.18), the first-order term of the bias current is expressed as

$$\frac{\delta I(\omega)}{\bar{I}} = -\frac{\alpha}{1+\beta}\frac{\delta \mathcal{P}_{\rm opt}(\omega)}{A(\omega)} \tag{A.2.43}$$

$$= -\frac{\bar{\mathcal{L}}}{\bar{\mathcal{L}} + 1 + i\omega\tau_0}\frac{\delta \mathcal{P}_{\rm opt}(\omega)}{\bar{\mathcal{P}}_{\rm bias}} \quad . \tag{A.2.44}$$

Note that this equation is the same as Eq. (A.1.2).

Next, we Fourier transform the second-order terms. Remember that the multiplication in the real space is the convolution in the Fourier space as

$$\begin{aligned} x^2(t) &= \iint d\omega_1 d\omega_2\, x(\omega_1)x(\omega_2)e^{i(\omega_1+\omega_2)t} \\ &= \int d\omega\, e^{i\omega t}\int d\omega_1\, x(\omega_1)x(\omega-\omega_1) \quad . \end{aligned} \tag{A.2.45}$$

Here, we denote the convolution in the Fourier space as follows:

$$\{x * x\}(\omega) \equiv \int d\omega_1\, x(\omega_1)x(\omega-\omega_1) \quad . \tag{A.2.46}$$

The relation between the second-order terms in the thermal equilibrium, Eq. (A.2.38), is Fourier-transformed as

$$A(\omega)\frac{\delta^2 T(\omega)}{\bar{T}} = B\left\{\frac{\delta T}{\bar{T}} * \frac{\delta T}{\bar{T}}\right\}(\omega) \quad , \tag{A.2.47}$$

where

$$B \equiv -\bar{G}\bar{T}\left[\bar{\mathcal{L}}F + \frac{n}{2}\right] \quad . \tag{A.2.48}$$

Thus, the second-order term of the TES temperature is expressed by the first-order term as

$$\frac{\delta^2 T(\omega)}{\bar{T}} = \frac{B}{A(\omega)}\left\{\frac{\delta T}{\bar{T}} * \frac{\delta T}{\bar{T}}\right\}(\omega) \quad . \tag{A.2.49}$$

From the Fourier transform of Eq. (A.2.19), the second-order term of the bias current is expressed by the optical power as

$$\frac{\delta^2 I(\omega)}{\bar{I}} = -\frac{\alpha}{1+\beta}\left[\frac{\delta^2 T(\omega)}{\bar{T}} + F\left\{\frac{\delta T}{\bar{T}} * \frac{\delta T}{\bar{T}}\right\}(\omega)\right] \tag{A.2.50}$$

$$= -\frac{\alpha}{1+\beta}\left[\frac{B}{A(\omega)} + F\right]\left\{\frac{\delta T}{\bar{T}} * \frac{\delta T}{\bar{T}}\right\}(\omega) \tag{A.2.51}$$

$$= -\frac{\alpha}{1+\beta}\left[\frac{B}{A(\omega)} + F\right]\left\{\frac{\delta \mathcal{P}_{\rm opt}}{A} * \frac{\delta \mathcal{P}_{\rm opt}}{A}\right\}(\omega) \quad . \tag{A.2.52}$$

This equation represents the non-linearity of the TES bolometer.

A.3 LEAKAGE DUE TO THE NON-LINEARITY

If there is a prominent signal at a specific frequency, ω_H, the TES non-linearity couples a signal at a low frequency, ω_L, with the prominent signal, and creates spurious sidebands at $\omega_H \pm \omega_L$. For the case of the observation using the continuously rotating half-wave plate (CRHWP), the prominent signal corresponds to the HWPSS at the modulation frequency, ω_{mod}, and the low frequency signal corresponds to the unmodulated intensity signal. Besides, the spurious signal due to the non-linearity corresponds to the leakage as described in section 5.3.

For the simplified case with the signals at ω_H and ω_L, the optical power becomes

$$\delta\mathcal{P}_{opt}(t) = \frac{C_L}{2}e^{i\omega_L t} + \frac{C_L^*}{2}e^{-i\omega_L t} + \frac{C_H}{2}e^{i\omega_H t} + \frac{C_H^*}{2}e^{-i\omega_H t} \quad , \tag{A.3.1}$$

where $|C_L|$ and $|C_H|$ are the amplitudes of the signals.
From Eq. (A.2.41), the first-order term of the TES temperature is expressed as

$$\frac{\delta T(t)}{\bar{T}} = \frac{C_L}{2A(\omega_L)}e^{i\omega_L t} + \frac{C_L^*}{2A(-\omega_L)}e^{-i\omega_L t} + \frac{C_H}{2A(\omega_H)}e^{i\omega_H t} + \frac{C_H^*}{2A(-\omega_H)}e^{-i\omega_H t} \quad . \tag{A.3.2}$$

The direct calculation of the quadrature of this equation results in

$$\begin{aligned}\left(\frac{\delta T(t)}{\bar{T}}\right)^2 =& \frac{|C_L|^2}{2|A(\omega_L)|^2} + \frac{|C_H|^2}{2|A(\omega_H)|^2} \\ &+ \mathrm{Re}\left[\frac{C_L^2}{2A(\omega_L)^2}e^{2i\omega_L t}\right] \\ &+ \mathrm{Re}\left[\frac{C_H C_L^*}{A(\omega_H)A(-\omega_L)}e^{i(\omega_H-\omega_L)t}\right] \\ &+ \mathrm{Re}\left[\frac{C_H C_L}{A(\omega_H)A(\omega_L)}e^{i(\omega_H+\omega_L)t}\right] \\ &+ \mathrm{Re}\left[\frac{C_H^2}{2A(\omega_H)^2}e^{2i\omega_H t}\right] \quad .\end{aligned} \tag{A.3.3}$$

Hereafter we focus on the signals around the frequency, ω_H. Besides, we set the C_H as the real number. From Eq. (A.2.18) and Eq. (A.2.51), the bias current becomes

$$\begin{aligned}\frac{\delta I(t) + \delta^2 I(t)}{\bar{I}} =& -\frac{\alpha}{1+\beta}\frac{C_H C_L^*}{2A(\omega_H)A(-\omega_L)}\left[\frac{B}{A(\omega_H-\omega_L)} + F\right]e^{i(\omega_H-\omega_L)t} \\ &- \frac{\alpha}{1+\beta}\frac{C_H}{2A(\omega_H)}e^{i\omega_H t} \\ &- \frac{\alpha}{1+\beta}\frac{C_H C_L}{2A(\omega_H)A(\omega_L)}\left[\frac{B}{A(\omega_H+\omega_L)} + F\right]e^{i(\omega_H+\omega_L)t} \\ &+ \cdots\end{aligned} \tag{A.3.4}$$

We emulate the demodulation and the responsivity calibration in the analysis of the real data. The resulting signal is

$$\begin{aligned}&\frac{\delta I(t) + \delta^2 I(t)}{\bar{I}}\left(-\frac{\beta+1}{\alpha}2A(\omega_H)e^{-i\omega_H t}\right) \\ &= C_H + \frac{C_H C_L^*}{A(-\omega_L)}\left[\frac{B}{A(\omega_H-\omega_L)} + F\right]e^{-i\omega_L t} + \frac{C_H C_L}{A(\omega_L)}\left[\frac{B}{A(\omega_H+\omega_L)} + F\right]e^{i\omega_L t} + \cdots \quad ,\end{aligned} \tag{A.3.5}$$

where the terms in the big parentheses represents the demodulation and the responsivity calibration. The first term in the right-hand side is the extracted signal, and the second and third terms correspond to the leakage.

We separate the leakage into the real part and the imaginary part. The real part is obtained as

$$\begin{aligned}&\frac{C_H C_L^*}{2A(-\omega_L)}\left[\frac{B}{A(\omega_H-\omega_L)}+\frac{B}{A(-\omega_H-\omega_L)}+2F\right]e^{-i\omega_L t}\\&+\frac{C_H C_L}{2A(\omega_L)}\left[\frac{B}{A(\omega_H+\omega_L)}+\frac{B}{A(-\omega_H+\omega_L)}+2F\right]e^{i\omega_L t}\quad .\end{aligned}\tag{A.3.6}$$

In the limit of $\omega_L \to 0$, the real part of the leakage becomes

$$\frac{C_H}{A(0)}\left[\frac{B}{A(\omega_H)}+\frac{B}{A(-\omega_H)}+2F\right]\left(\frac{C_L}{2}e^{i\omega_L t}+\frac{C_L^*}{2}e^{-i\omega_L t}\right)\quad .\tag{A.3.7}$$

Thus, the leakage coefficient into the real part is

$$\begin{aligned}\lambda_r &= \frac{C_H}{A(0)}\left[\frac{B}{A(\omega_H)}+\frac{B}{A(-\omega_H)}+2F\right]\\&= -2C_H\frac{1}{2\mathcal{P}_{\rm bias}}\frac{\bar{\mathcal{L}}}{\bar{\mathcal{L}}+1}\frac{\bar{\mathcal{L}}+1+\omega_H^2\tau_0^2}{(\bar{\mathcal{L}}+1)^2+\omega_H^2\tau_0^2}\\&\quad\times\frac{2-\alpha_1-2\beta\,(\alpha_1-\gamma_1)-\beta^2\,(\alpha_1+\beta_1-2\gamma_1)}{1+\beta}+\mathcal{O}\left(\frac{n}{\alpha}\right)\quad .\end{aligned}\tag{A.3.8}$$

The imaginary part of the leakage can also be calculated in the limit of $\omega_L \to 0$ as

$$\frac{C_H}{A(0)}\left[\frac{B}{A(\omega_H)}-\frac{B}{A(-\omega_H)}\right]\left(\frac{C_L}{2}e^{i\omega_L t}+\frac{C_L^*}{2}e^{-i\omega_L t}\right)\quad ,\tag{A.3.9}$$

and the leakage coefficient into the imaginary part becomes

$$\begin{aligned}i\lambda_i &= \frac{C_H}{A(0)}\left[\frac{B}{A(\omega_H)}-\frac{B}{A(-\omega_H)}\right]\\&= -iC_H\omega_H\frac{\tau_0}{\mathcal{P}_{\rm bias}}\frac{\bar{\mathcal{L}}^2}{\bar{\mathcal{L}}+1}\frac{1}{(\bar{\mathcal{L}}+1)^2+\omega_H^2\tau_0^2}\\&\quad\times\frac{2-\alpha_1-2\beta\,(\alpha_1-\gamma_1)-\beta^2\,(\alpha_1+\beta_1-2\gamma_1)}{1+\beta}+\mathcal{O}\left(\frac{n}{\alpha}\right)\quad .\end{aligned}\tag{A.3.10}$$

B

CROSS POLARIZATION

The cross polarization in the optical system is one of the most important properties of the instruments, especially for the polarization measurements of the CMB anisotropy. It could degrade the polarization efficiency and cause the mixing between the E-mode and B-mode.

In this chapter, we describe the increase of the cross polarization due to the HWP placed at the prime focus. First, we explain the problem in Appendix B.1, and then evaluate the effect quantitatively using the physical optics simulation in Appendix B.2.

B.1 CROSS POLARIZATION INCREASE DUE TO THE PRIME FOCUS HWP

First, we introduce the definition of the polarization for the spherical wave. Then, we explain the cross polarization in the off-axis reflector system, as well as the condition to make the optical system equivalent to the on-axis optical system. Finally, we consider the effect of the HWP placed at the prime focus.

B.1.1 *Ludwig's third definition of the polarization*

The polarization of the plane wave propagating toward the z direction can be trivially defined by the bases of the Cartesian coordinate system as

$$\hat{E}(t,z) = E_x(t,z)\hat{e}_x + E_y(t,z)\hat{e}_y \tag{B.1.1}$$

where the $\vec{E}(t,z)$ is the electric field vector, and the $E_x(t,z)$ or $E_y(t,z)$ is the component for each polarization.

For the case of the spherical wave, the definition of the polarization is not trivial as shown in Ludwig (1973). However, the most useful definition for the description of the telescope is the third one as

$$\begin{cases} \hat{e}_{co}(\theta,\phi) \equiv \hat{e}_\theta(\theta,\phi)\cos\phi - \hat{e}_\phi(\theta,\phi)\sin\phi\,, \\ \hat{e}_{cx}(\theta,\phi) \equiv \hat{e}_\theta(\theta,\phi)\sin\phi + \hat{e}_\phi(\theta,\phi)\cos\phi\,. \end{cases} \tag{B.1.2}$$

where the (θ,ϕ) is the direction in the spherical coordinates, and the $\hat{e}_\theta(\theta,\phi)$ and $\hat{e}_\phi(\theta,\phi)$ are the usual bases. The components for the $\hat{e}_{co}$ and $\hat{e}_{cx}$ are called the co-polarization and cross-polarization, respectively.

The reason of the choice becomes clear by considering the on-axis parabolic reflector system, which ideally converts the plane wave into the spherical wave. If we solve the boundary condition for the mirror reflection, we can find that the x- and y-polarization components are perfectly converted into the co- and cross-polarization components, respectively.

B.1.2 *Cross-polarization in the off-axis reflector system*

In practice, the on-axis reflector system has some problems. We need supporting struts to place a receiver at the focus. Besides, the receiver itself blocks the incoming light, which

could cause the diffraction and the resulting sidelobe. On the other hand, the off-axis reflector system can solve such problems. We can place the receiver outside the light path as illustrated in Figure B.1.1.

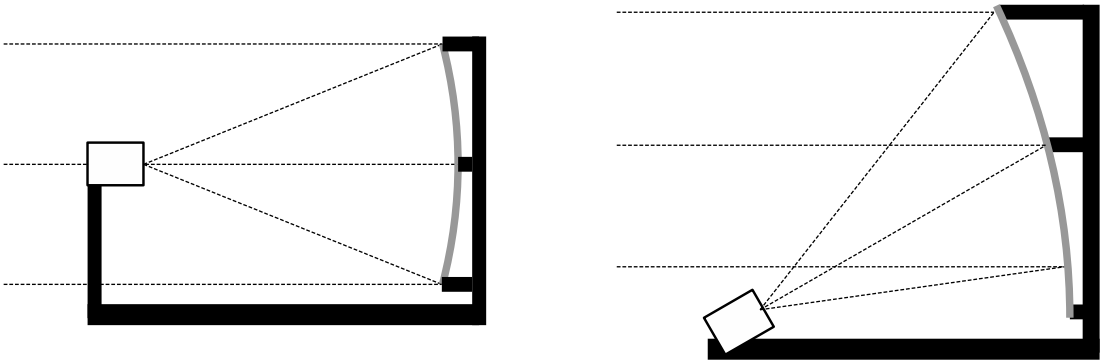

Figure B.1.1: Illustrations of the on-axis and off-axis parabolic systems are shown in the left and right figures, respectively. Here, gray curves represent parabolic reflectors, broken lines represent light path, white boxes represent receivers, and black frames represent the support structure for the reflector and the receiver.

However, the off-axis parabolic system has a mismatch between the axis of the paraboloid and the axis of the receiver. Then, the definitions of the polarization with respect to the two axes become inconsistent with each other as shown in Figure B.1.2. The mismatch in the

Figure B.1.2: Illustrations of the mismatch of the polarization bases. The direction of the basis for each polarization is shown as the line on the sphere. The left figure shows the front view, and the right figure shows the rear view. The solid lines represent the direction of the basis for the co-polarization, and the broken lines represent the direction of the basis for the cross-polarization. The blue lines are the definition with respect to the axis of the paraboloid, and the green lines are that with respect to the axis of the receiver. Here, the offset between the axes is 30°.

definition of the polarization means the imperfect separation of the polarization signal, which results in the degradation in the polarization efficiency.

A solution to the cross-polarization problem of the off-axis parabolic system is the use of the secondary reflector to correct the mismatch of the axes (Tanaka et al. 1975; Mizugutch et al. 1976; Dragone 1978). Figure B.1.3 shows the idea for the case of the Gregorian optics, which is the combination of the paraboloid and the elipsoid. The incoming plane wave converges at

the focus of the paraboloid first, but pass through the focus. After the second reflection, the wave converges again at the other focus of the ellipsoid, and enters the receiver. Here, we consider the image of the paraboloid reflected by the ellipsoid. As shown in Dragone (1978), the image also becomes another paraboloid, which is called the equivalent paraboloid. Therefore, if we match the direction of the receiver with the axis of the equivalent paraboloid, we can construct the optical system equivalent to the on-axis parabolic reflector system and recover the ideal cross-polarization performance. The condition is called the Mizuguch-Dragone condition.

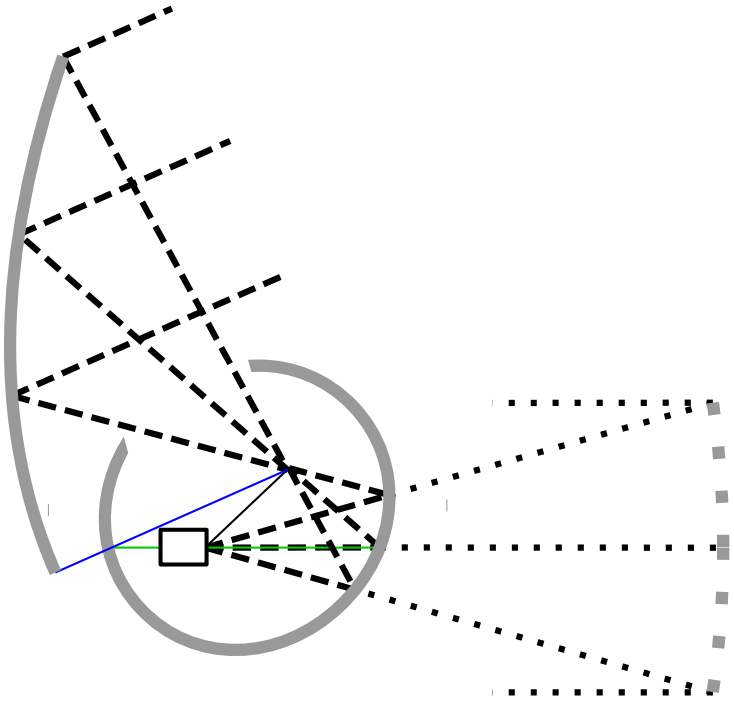

Figure B.1.3: Ilustration of the equivalent paraboloid for the off-axis Gregorian system. The gray curves represent the paraboloid and the ellipsoid, which construct the Gregorian optical system. The white box represents the receiver. The blue, green, and black solid lines are the axes of the paraboloid, ellipsoid, and receiver, respectively. The dotted gray curve represents the equivalent paraboloid, which is the image of the paraboloid with respect to the ellipsoid. The black dashed lines show the actual light paths, and the black dotted lines show the imaginary light path. Note that the axes of the paraboloid and the receiver are crossing on the ellipsoid, which makes the receiver on-axis with respect to the equivalent paraboloid.

B.1.3 *Effect of the HWP at the prime focus*

The improvement of the cross polarization in the optical system satisfying the Mizuguch-Dragone condition can be interpreted as the correction of the polarization angle rotation. The mismatch of the polarization definition is equivalent to the polarization angle rotation. Remember that the mismatch of the polarization definition shown in Figure B.1.2 is dependent on the direction of the ray: i. e. there is no mismatch for the ray on the symmetric plane, but there is for the other rays. The combination of the two reflectors skillfully cancels the angle

rotation for all the rays, which is illustrated in Figure B.1.4, where the difference of the ray is expressed as the position in the aperture.

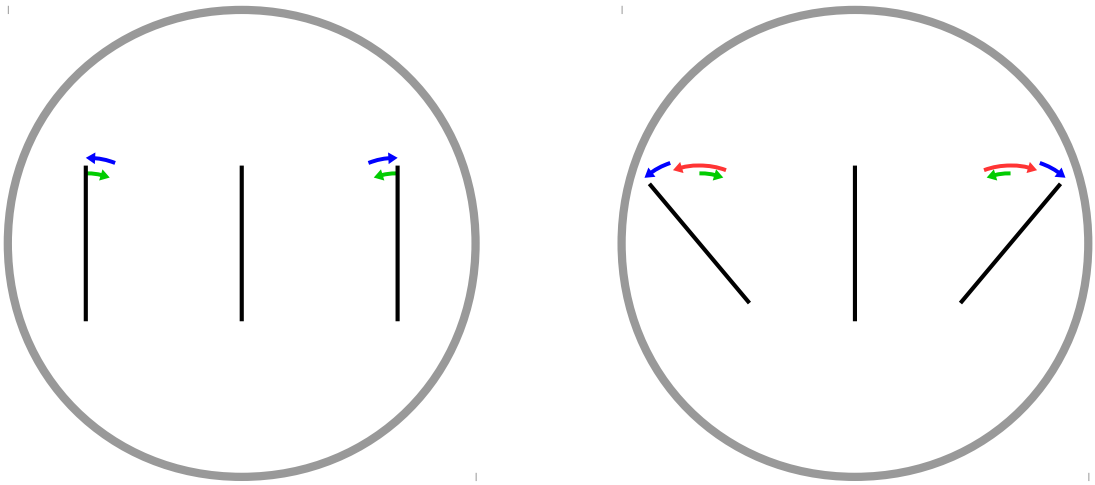

Figure B.1.4: Illustrations of the cross-polarization correction in the optical system satisfying the Mizuguch-Dragone condition (left) and the cross-polarization increase due to the HWP between the reflectors. The gray circle represents the aperture. The black line represents the direction of the polarization for each position in the aperture. The blue, green, and red arrows represent the polarization angle rotation by the primary reflector (the paraboloid), the secondary reflector (the ellipsoid), and the HWP, respectively. Here, the angle of the HWP axis is vertical.

A HWP between the two reflectors, however, breaks the angle cancellation. As described in section 5.1.1, the HWP flips the polarization angle with respect to the HWP axis. The effect is equivalent to flipping the sign of the angle rotation due to the secondary reflector. Thus, the cancellation of the angle rotation breaks as illustrated in the right panel of Figure B.1.4. In this study, the CRHWP is placed at the prime focus. Therefore, the cross-polarization might be significantly degraded due to the mechanism explained here.

Note that we have solutions for this cross polarization problem. One is placing the HWP around the second (Gregorian) focus, where the polarization angle rotation is corrected. Another is placing two HWPs in one location. Flipping the polarization angle twice restore the original sign, thus the cancellation works.

B.2 PHYSICAL OPTICS SIMULATION WITH GRASP

The HWP placed between the mirrors might increase the cross polarization as described in the previous section, section B.1. In this section, we evaluate the effect quantitatively in terms of the Mueller beam matrix using the physical optics simulation.

First, we introduce the Mueller beam matrix. Then, we describe the physical optics simulation, as well as the results.

B.2.1 *Mueller beam matrix*

A detector measures electrical properties on the sky, which are completely expressed by 4 parameters, so called Stokes parameters, I, Q, U and V in the case of incoherent signal. The non-idealities of the telescope, such as the instrumental polarization and the cross-pol, mix these parameters from the sky. Such mixing is expressed by a matrix, so called the Mueller matrix.

Practically, the detector has a finite resolution due to the finite size of the aperture. Therefore, the signals measured by the detector are the convolution of the sky signal with finite kernels, which are often called the beam for simplicity. This argument can be applied not only to the diagonal terms of the Mueller matrix but also off-diagonal terms, which means that all the components of the Mueller matrix have certain beam shapes (O'Dea et al. 2007). We call such a matrix of beam functions as the *Mueller beam matrix*.

We assume that the Mueller beam matrix is constant with respect to the coordinates on the antenna. Therefore, it can be defined as

$$\mathcal{B}^{XY}_{\rm ant}(\vec{x}_{\rm ant})\,, \tag{B.2.1}$$

where $X, Y = \{I, Q, U, V\}$ and $\vec{x}_{\rm ant} = (\Delta AZ, \Delta EL)$. The subscript "ant" on the $\mathcal{B}^{XY}$ means that the coordinate system defines the Q and U. To make following calculation simple, we use complex parameters $P^{\pm} = Q \pm iU$ instead of Q and U. Components of the Mueller matrix for this notation can be obtained as

$$\mathcal{B}^{IP^{\pm}}_{\rm ant} = \mathcal{B}^{IQ}_{\rm ant} \mp i\mathcal{B}^{IU}_{\rm ant} \quad , \tag{B.2.2}$$

$$\mathcal{B}^{P^{\pm}I}_{\rm ant} = \mathcal{B}^{QI}_{\rm ant} \pm i\mathcal{B}^{UI}_{\rm ant} \quad , \tag{B.2.3}$$

$$\mathcal{B}^{P^{+}P^{+}}_{\rm ant} = \mathcal{B}^{QQ}_{\rm ant} + \mathcal{B}^{UU}_{\rm ant} - i(\mathcal{B}^{QU}_{\rm ant} - \mathcal{B}^{UQ}_{\rm ant}) \quad , \tag{B.2.4}$$

$$\mathcal{B}^{P^{-}P^{-}}_{\rm ant} = \mathcal{B}^{QQ}_{\rm ant} + \mathcal{B}^{UU}_{\rm ant} + i(\mathcal{B}^{QU}_{\rm ant} - \mathcal{B}^{UQ}_{\rm ant}) \quad , \tag{B.2.5}$$

$$\mathcal{B}^{P^{+}P^{-}}_{\rm ant} = \mathcal{B}^{QQ}_{\rm ant} - \mathcal{B}^{UU}_{\rm ant} + i(\mathcal{B}^{QU}_{\rm ant} + \mathcal{B}^{UQ}_{\rm ant}) \quad , \tag{B.2.6}$$

$$\mathcal{B}^{P^{-}P^{+}}_{\rm ant} = \mathcal{B}^{QQ}_{\rm ant} - \mathcal{B}^{UU}_{\rm ant} - i(\mathcal{B}^{QU}_{\rm ant} + \mathcal{B}^{UQ}_{\rm ant}) \quad . \tag{B.2.7}$$

B.2.2 *Physical optics simulation with GRASP*

The Mueller beam matrix is obtained using a phisical optics simulator, General Reflector antenna Analysis Software Package (GRASP) (Pontoppidan 2005), with an additional software to emulate the ideal HWP. Besides, we perform the demodulation by averaging Mueller beam matrices for various angles of the HWP.

First, we construct the model of the HTT of the POLARBEAR experiment in GRASP as shown in Figure B.2.1. In GRASP, the electromagnetic fields are injected inversely from a detector in the focal plane, propagated through the optical systems, and projected to the far field. The focal plane is 20 cm in diameter and is placed at the Gregorian focus to focus on the reflective systems and not to include re-imaging lenses which require another plug-in. The optical systems is set to the offset Gregorian system with an 2.5 m diameter aperture. The antenna pattern of the detector is the Gaussian beam which has a 3 db cut-off at 16°. The frequency for the simulation is fixed at 150 GHz.

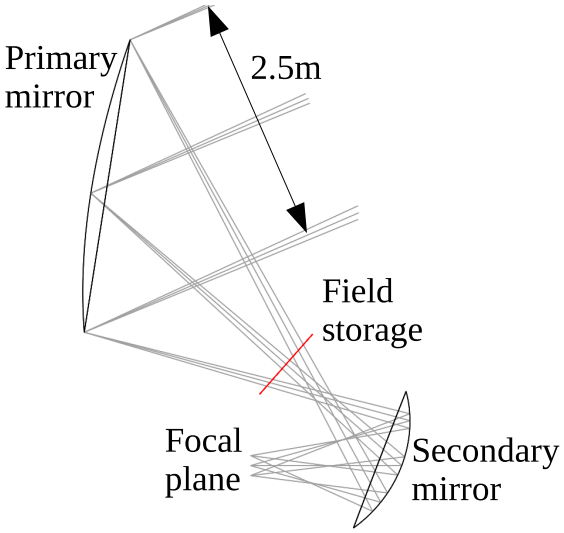

Figure B.2.1: Simulation setup in GRASP. The two mirrors (black lines) form an offset Gregorian optical system with the Mizuguchi-Dragone condition, which is equivalent to an on-axis parabolic mirror with a 2.5 m diameter aperture. The gray lines show rays from detectors on the focal plane with a 20 cm diameter at the Gregorian focus. A red line shows the position of a square field storage with an area of 40 cm × 40 cm to emulate a HWP, which is 50 cm apart from the prime focus.

Emulation of the ideal HWP

GRASP does not support any birefringent materials such as sapphire used for the HWP. Therefore, we developed an external script emulating an ideal HWP. We store the electromagnetic field on the plane where the HWP is placed. The ideal HWP emulator flips the sign of the field. Then we restart the physical optics calculation from the new field.

The output electromagnetic field from the HWP is calculated as follows and illustrated in Figure B.2.2. First, the propagation direction is obtained from the Poynting vector. Next, the electromagnetic fields are separated into an ordinary-wave and an extra-ordinary-wave according to the relation between the HWP's axis and propagation direction. Then, the sign of the electromagnetic fields of the extra-ordinary-wave is fliped. Finally, the ordinary-wave and the extra-ordinary-wave are coadded. This model does not perfectly emulate HWP effects such as refraction. Since the electromagnetic wave at each point on the field storage has to be well approximated by a plane wave, the field storage cannot be placed exactly at the prime focus where waves from various directions converge. Therefore, it is placed 50 cm apart from the prime focus (Figure B.2.1). But this model is enough to know the fundamental effect of the ideal HWP.

Intercepting the electromagnetic wave with the finite area of the field storage (see Figure B.2.3) could introduce a numerical error. To evaluate the error, we run the simulation in which we intercept the electromagnetic wave but restart the calculation without modifying the field. The difference between the simulation and the direct simulation without interception would result in the numerical error. Figure B.2.4 shows the beam profiles and the differences between the two simulations. It suggests that the accuracy is about −20 db level with respect to the original signal.

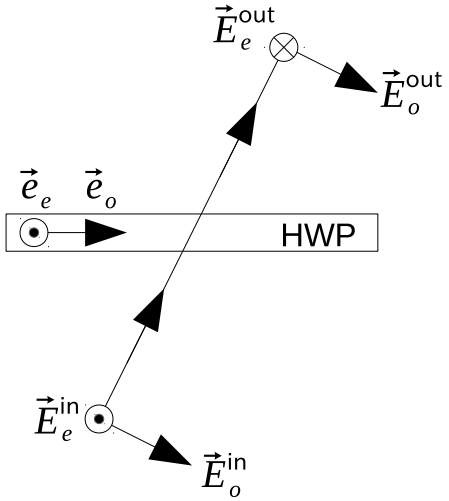

Figure B.2.2: Model of the ideal HWP. The unit vectors $\vec{e}_o$ and $\vec{e}_e$ represent the ordinary-axis and extra-ordinary-axis of the HWP. $\vec{S}$ is the Poynting vector. $\vec{E}_o^{\text{in}}$ is determined to be parpendicular to both $\vec{e}_e$ and $\vec{S}$. $\vec{E}_e^{\text{in}}$ is determined from $\vec{E}_o^{\text{in}}$ and $\vec{S}$. After passing through the HWP, $\vec{E}_o^{\text{out}}$ is the same as $\vec{E}_o^{\text{in}}$, but $\vec{E}_e^{\text{out}}$ has the opposite direction to $\vec{E}_e^{\text{in}}$. The magnetic field is also treated in the same way.

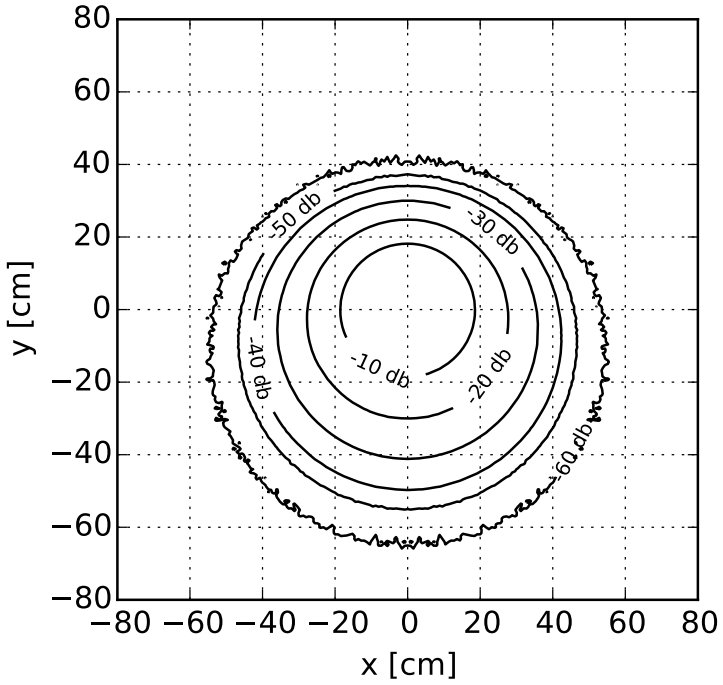

Figure B.2.3: The amplitude distribution of the electromagnetic field from the center pixel on the field storage placed at 50 cm apart from the prime focus. The center area of 80 cm by 80 cm is used for all the other calculations, which covers the electromagnetic field down to −30 db.

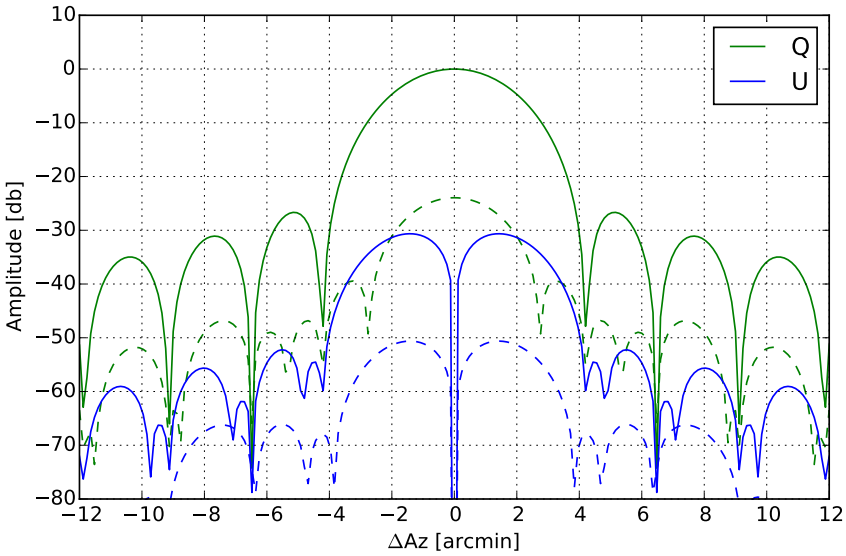

Figure B.2.4: The amplitude profiles for Q and U beams of the center pixel (thick lines) and its difference betweeen the direct simulation and the intercepting simulation (dashed lines).

Calculation of the Mueller matrix

The beam map for each Stokes parameter is obtained from the electric field on the far field using the definition of the Stokes parameters. The beam maps are calculated for 8 HWP angles from 0° to 135° (see Figure B.2.5). The mueller beam matrix is finally obtained by averaging all these maps, $\mathcal{B}_{\rm ant}^{X=\{I,Q,U,V\}}(\vec{x}_{\rm ant}, \theta_{\rm HWP})$ with respect to the HWP angle multiplying certain modulation factors as:

$$\begin{aligned}
\mathcal{B}_{\rm ant}^{IX}(\vec{x}_{\rm ant}) &= \langle \mathcal{B}_{\rm ant}^{X}(\vec{x}_{\rm ant}, \theta_{\rm HWP}) \rangle_{\theta_{\rm HWP}} \,, \\
\mathcal{B}_{\rm ant}^{QX}(\vec{x}_{\rm ant}) &= \langle \mathcal{B}_{\rm ant}^{X}(\vec{x}_{\rm ant}, \theta_{\rm HWP}) 2\cos 4\theta_{\rm HWP} \rangle_{\theta_{\rm HWP}} \,, \\
\mathcal{B}_{\rm ant}^{UX}(\vec{x}_{\rm ant}) &= \langle \mathcal{B}_{\rm ant}^{X}(\vec{x}_{\rm ant}, \theta_{\rm HWP}) 2\sin 4\theta_{\rm HWP} \rangle_{\theta_{\rm HWP}} \,,
\end{aligned} \tag{B.2.8}$$

where brackets represent an average over all HWP angles.

Figure B.2.6 shows the simulated Mueller beam matrix of the center pixel. First, all the diagonal components show similar monopole beam pattern that looks like the Gaussian function, which means that a CRHWP enables a single linear-polarization sensitive detector to reconstruct Stokes parameters Q and U as expected. However, the integral of the beam for polarization is a little smaller than that for I due to the cross-pol leakage. We define a polarization efficiency ε from the ratio as

$$\varepsilon \equiv \frac{\int {\rm Re}(\mathcal{B}_{\rm ant}^{P^+P^+}(\vec{x}_{\rm ant}))\, d\vec{x}_{\rm ant}}{\int \mathcal{B}_{\rm ant}^{II}(\vec{x}_{\rm ant})\, d\vec{x}_{\rm ant}} \quad . \tag{B.2.9}$$

Next, the cross-pol leakage mainly appears as the cross terms between Q and U. The amplitude of about -22 db is 6 times larger than that of the original cross-pol amplitude of -30 db shown in Figure B.2.4 because of the Mizuguchi-Doragone condition breaking. Also, the sign of the beam pattern is flipped each other between $\mathcal{B}_{\rm ant}^{QU}$ and $\mathcal{B}_{\rm ant}^{UQ}$, which means this cross-pol leakage can be expressed as the imaginary part of the $\mathcal{B}_{\rm ant}^{P^+P^+}$. It is reasonable because

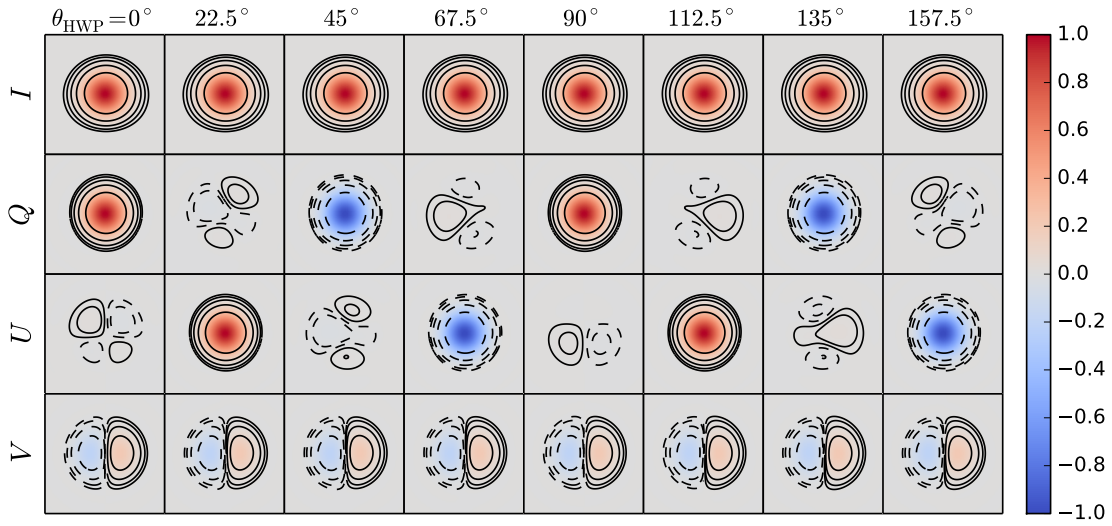

Figure B.2.5: Simulated beam functions of the center pixel for each Stokes parameter as a function of a HWP angle. Each map shows 24 arcmin square region in the antenna coordinate. Unit of the color scale is normalized by the maximum of the I beam. Q and U distributions show clear rotation.

Mizuguchi-Doragone condition breaking causes non-uniformity of the polarization angle rotation but does not break the parity of the rotation. Finally, the cross terms between the intensity and polarization are very small, since the conductivity of the reflectors is assumed to be infinite.

Dependence on the position in the focal plane

The cross-pol beam $\mathcal{B}^{QU}_{ant}$ is calculated for each detector in the different position on the focal plane. Note that the polarization angles for the positions off the symmetry plane of the optics are not trivially defined. This causes monopole-type cross-pol which can be fixed easily by the polarization angle calibration for each detector. Here, the polarization angle of the detector, θ_{det} is determined from the integral of $\mathcal{B}^{P+P+}_{ant}$ as

$$2\theta_{det} = \arg\left(\int \mathcal{B}^{P+P+}_{ant} d^2\vec{x}_{ant}\right) . \tag{B.2.10}$$

Then the Mueller beam matrix is derotated as

$$\begin{aligned} \mathcal{B}'^{XQ}_{ant} &= \mathcal{B}^{XQ}_{ant}\cos 2\theta_{det} - \mathcal{B}^{XU}_{ant}\sin 2\theta_{det} , \\ \mathcal{B}'^{XU}_{ant} &= \mathcal{B}^{XQ}_{ant}\sin 2\theta_{det} + \mathcal{B}^{XU}_{ant}\cos 2\theta_{det} , \end{aligned} \tag{B.2.11}$$

for $X = \{I, Q, U\}$.

Figure B.2.7 shows a distribution of each cross-pol beam $\mathcal{B}^{QU}_{ant}$ normalized by the peak of $\mathcal{B}^{II}_{ant}$. Each beam has a dipole pattern which changes its angle according to the focal plane position.

To reduce the computational cost, the physical optics simulations are done for some representative detectors. The cross-pol beam result is then parametrized to construct the model as a

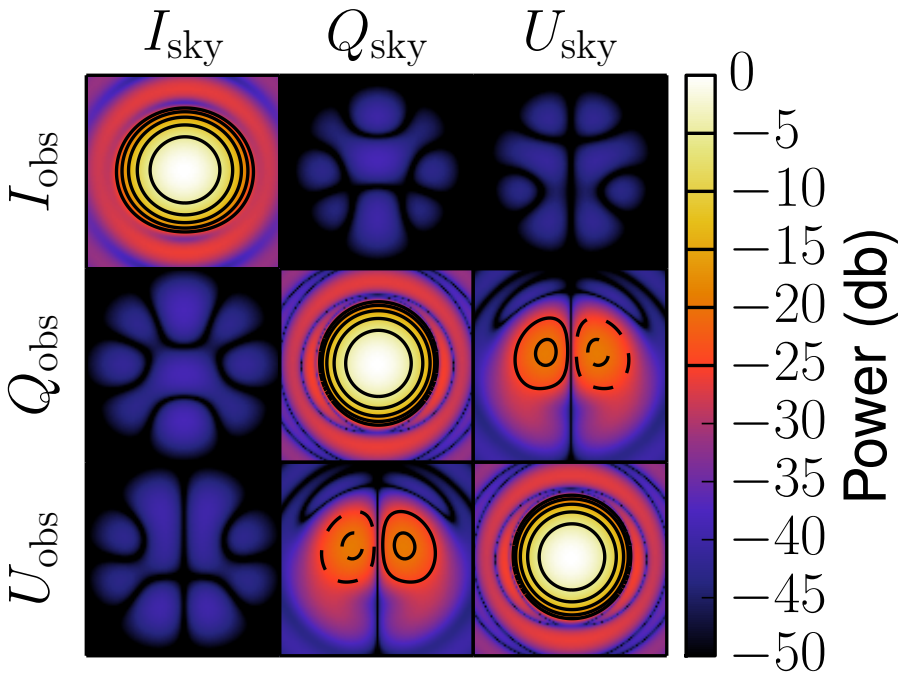

Figure B.2.6: Simulated Mueller beam matrix of the center pixel

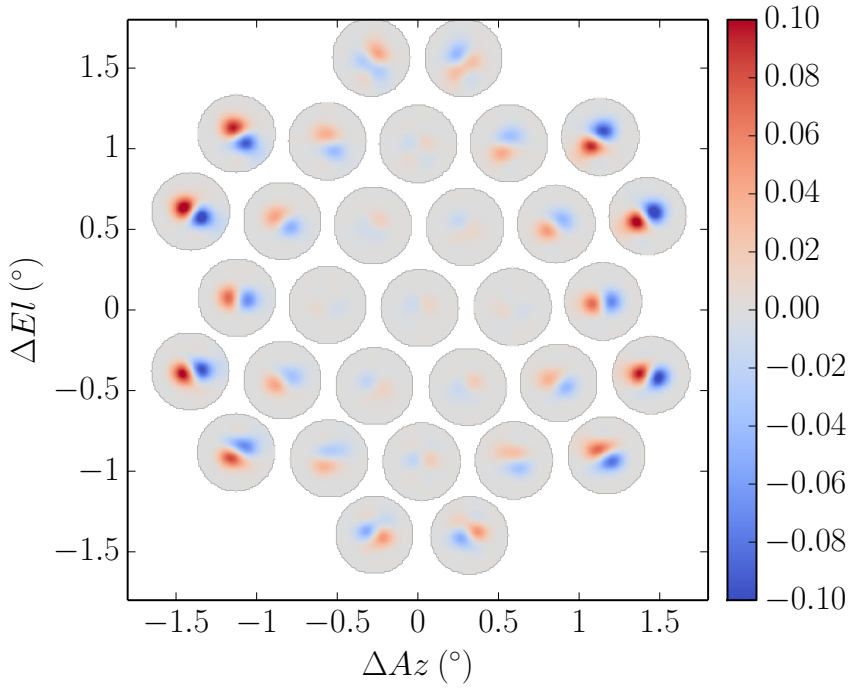

Figure B.2.7: Distribution of P → P beam pattern for each detector

function of the position on the focal plane. The dipole component of the beam is parametrized as

$$A_2 = \frac{\int \mathcal{B}_{ant}^{UQ} e^{i\phi_x} d^2\vec{x}_{ant}}{\int B_{ant}^{II} d^2\vec{x}_{ant}}, \tag{B.2.12}$$

and its distribution is also approximated with polynomial functions as

$$A_2(x,y) = \sum_{n,m} c_{n,m} x^n y^m, \tag{B.2.13}$$

where (x,y) is the position of the detector, $\phi_x = \arg(x+iy)$ and $c_{n,m}$ is a complex coefficient. Figure B.2.8 shows the amplitude and the phase of A_2 distribution model. The other components such as quadrupole are also modeled in the same way.

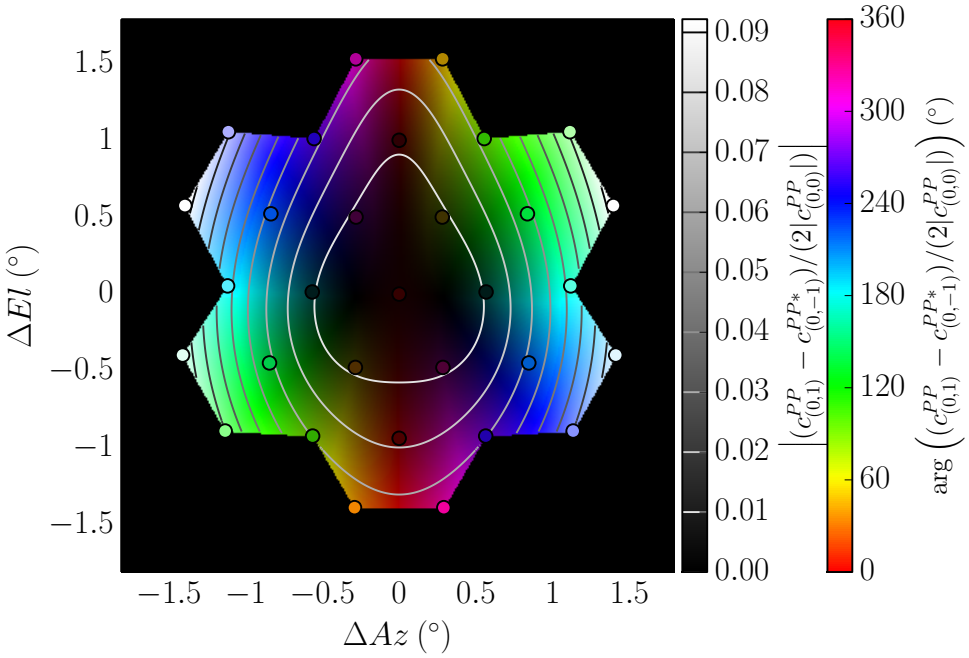

Figure B.2.8: Model of A_2 distribution

C

ANALYTIC FORMULA FOR ESTIMATIONS OF BEAM IMPERFECTIONS

C.1 LAGUERRE GAUSSIAN EXPANSION

It is useful to approximate the beam and to express the beam with some parameters for the systematics uncertainty estimation. Usually, the elliptical Gaussian or Hermite Gaussian are used. However, the elliptical Gaussian cannot express fine structures. Hermite Gaussian can treat such fine structures using higher order modes, but the coefficients of modes depend on the coordinate system.

Here we adopt Laguerre Gaussian functions to approximate beams as presented in O'Dea et al. (2007). The Laguerre Gaussian functions are defined as

$$\nu_{p,l}(r,\phi) = \nu_{p,l}(r) \times \exp(il\phi) \quad , \tag{C.1.1}$$

$$\nu_{p,l}(r) = \frac{1}{\sigma}\sqrt{\frac{p!}{\pi(p+|l|)!}} \exp\left[-\frac{r^2}{2\sigma^2}\right] \left[\frac{r}{\sigma}\right]^{|l|} L_p^{|l|}\left[\left(\frac{r}{\sigma}\right)^2\right] \quad , \tag{C.1.2}$$

where (r,ϕ) are the polar coordinates, σ is the beam size and $L_p^{|l|}$ is the Laguerre function of order (p,l). Since Laguerre gaussian functions form an orthonormal base, we can expand a beam of any shape as

$$\mathcal{B}^{XY}_{ant}(r,\phi_{ant}) = \sum_{p,l} \mathcal{B}^{XY}_{p,l}(r) \exp(il\phi_{ant}) \quad , \tag{C.1.3}$$

$$\mathcal{B}^{XY}_{p,l}(r) = c^{XY}_{p,l}\nu_{p,l}(r) \quad , \tag{C.1.4}$$

where $c^{XY}_{p,l}$ is the expansion coefficient. Laguerre gaussian functions behave well because all the azimuthal dependences are expressed in the last term, $\exp(il\phi)$ and its amplitude is 1. Although $\arg(c^{XY}_{p,l})$ changes depending on the coordinate system, the term $|c^{XY}_{p,l}|$ is constant. The shapes of modes of Laguerre Gaussian functions are displayed in Figure C.1.1.

Their Fourier transforms of Laguerre Gaussian functions are

$$\tilde{\nu}_{p,l}(\ell,\phi) = \tilde{\nu}_{p,l}(\ell) \times \exp(il\phi) \quad , \tag{C.1.5}$$

$$\tilde{\nu}_{p,l}(\ell) = i^{2p-|l|}\sqrt{\frac{p!}{(p+|l|)!}} \exp\left[-\frac{\ell^2\sigma^2}{2}\right] [\ell\sigma]^{|l|} L_p^{|l|}\left[(\ell\sigma)^2\right] \quad , \tag{C.1.6}$$

where ℓ is the multipole in the flat sky approximation. Figure C.1.2 shows $|\tilde{\nu}_{p,l}(\ell)|$.

C.2 ANALYTIC FORMULA OF BEAM SYSTEMATICS

Here, we construct analytic formula to evaluate systematics from the CMB itself due to beam imperfection.

Although the Mueller beam matrix is constant with respect to the antenna coordinate, that on the sky changes due to the sky rotation. The Mueller beam matrix on the sky with the parallactic angele of θ_{pa} is

$$\mathcal{B}^{XY}_{sky}(\vec{x}_{sky}) = \alpha_X(\theta_{pa})\alpha^*_Y(\theta_{pa})\mathcal{B}^{XY}_{ant}(R(\theta_{pa})\cdot\vec{x}_{sky}) \quad , \tag{C.2.1}$$

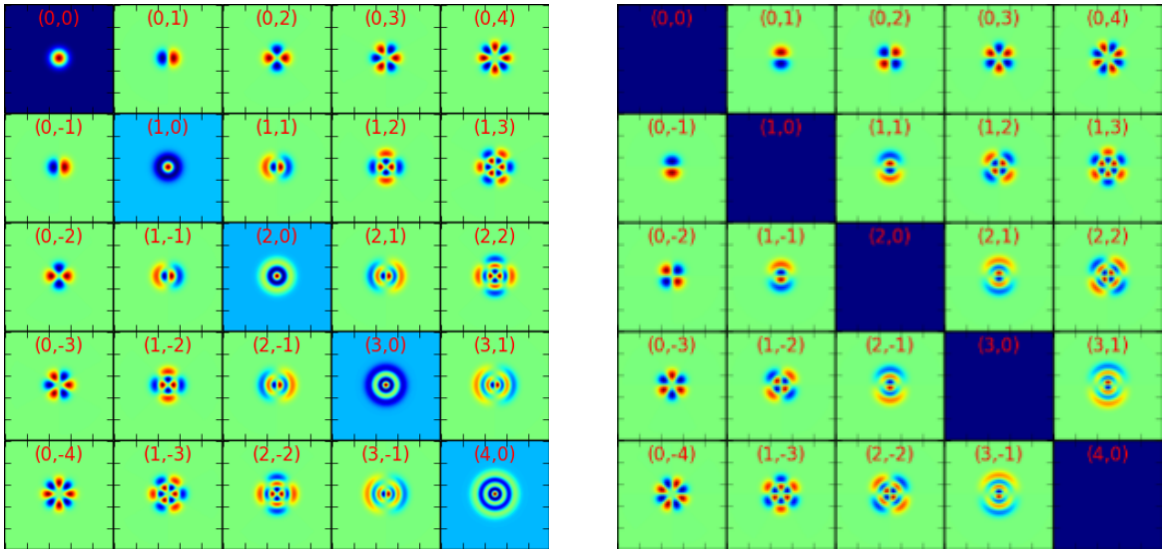

Figure C.1.1: Real part (*left*) and imaginaly part (*right*) of Laguerre Gaussian functions of order (p, l).

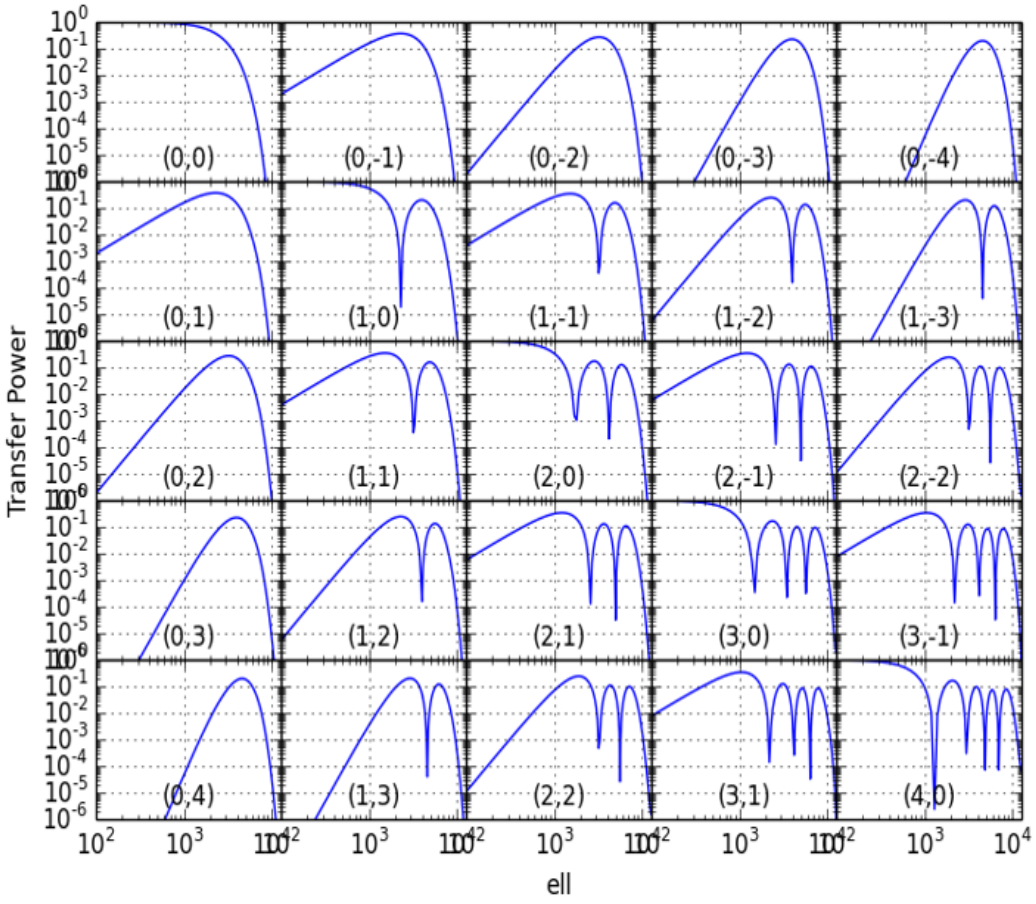

Figure C.1.2: Power spectra of Laguerre Gaussian functions

where $X, Y = \{I, P^+, P^-, V\}$, $\vec{x}_{sky} = (\Delta RA, \Delta DEC)$,

$$R(\theta_{pa}) = \begin{pmatrix} \cos\theta_{pa} & \sin\theta_{pa} \\ -\sin\theta_{pa} & \cos\theta_{pa} \end{pmatrix} \quad , \tag{C.2.2}$$

$$\alpha_X(\theta_{pa}) = \begin{cases} 1 & \text{for} \quad X = \{I, V\} \quad , \\ e^{2i\theta_{pa}} & \text{for} \quad X = P^+ \quad , \\ e^{-2i\theta_{pa}} & \text{for} \quad X = P^- \quad . \end{cases} \tag{C.2.3}$$

Eq. (C.2.1) comes form coordinate dependence of Q and U, and asterisk represents complex conjugate. Using polar coordinates, Eq. (C.2.1) can also be expressed as

$$\mathcal{B}^{XY}_{sky}(r, \phi_{sky}) = \alpha_X(\theta_{pa})\alpha^*_Y(\theta_{pa})\mathcal{B}^{XY}_{ant}(r, \phi_{sky} - \theta_{pa}) \quad . \tag{C.2.4}$$

We observe the same point of the sky many times in many parallactic angles and average them. The observed maps are:

$$T_{obs} = \langle \mathcal{B}^{TT}_{sky} \star T_{sky} \rangle + \langle \mathcal{B}^{TP^+}_{sky} \star P^+_{sky} \rangle + \langle \mathcal{B}^{TP^-}_{sky} \star P^-_{sky} \rangle \quad , \tag{C.2.5}$$

$$P^\pm_{obs} = \langle \mathcal{B}^{P^\pm P^\pm}_{sky} \star P^\pm_{sky} \rangle + \langle \mathcal{B}^{P^\pm T}_{sky} \star T_{sky} \rangle + \langle \mathcal{B}^{P^\pm P^\mp}_{sky} \star P^\mp_{sky} \rangle \quad , \tag{C.2.6}$$

where $\star$ is a convolution operator and the bracket $\langle\rangle$ is average among all observations.

The Fourier transforms of these observed maps are as follows:

$$\begin{aligned} \tilde{T}_{obs}(\ell) = &\sum_{p,l} \left[\tilde{B}^{TT}_{p,l}(\ell) e^{il\phi_l} \tilde{T}_{sky}(\ell) \right] \star \tilde{f}(l) \\ &+ \sum_{p,l} \left[\tilde{B}^{TP^+}_{p,l-2}(\ell) e^{il\phi_l} \tilde{P}^+_{sky}(\ell) \right] \star \tilde{f}(l) \\ &+ \sum_{p,l} \left[\tilde{B}^{TP^-}_{p,l+2}(\ell) e^{il\phi_l} \tilde{P}^-_{sky}(\ell) \right] \star \tilde{f}(l) \quad , \end{aligned} \tag{C.2.7}$$

$$\begin{aligned} \tilde{P}^\pm_{obs}(\ell) = &\sum_{p,l} \left[\tilde{B}^{P^\pm P^\pm}_{p,l}(\ell) e^{il\phi_l} \tilde{P}^\pm_{sky}(\ell) \right] \star \tilde{f}(l) \\ &+ \sum_{p,l} \left[\tilde{B}^{P^\pm P^\mp}_{p,l\pm4}(\ell) e^{il\phi_l} \tilde{P}^\mp_{sky}(\ell) \right] \star \tilde{f}(l) \\ &+ \sum_{p,l} \left[\tilde{B}^{P^\pm P^\mp}_{p,l\pm2}(\ell) e^{il\phi_l} \tilde{T}_{sky}(\ell) \right] \star \tilde{f}(l) \quad , \end{aligned} \tag{C.2.8}$$

where

$$\tilde{B}_{p,l} \equiv c_{p,l} \tilde{\nu}_{p,l}(\ell) \quad , \tag{C.2.9}$$

$$f(l) \equiv \langle e^{-il\theta_{pa}} \rangle \quad , \tag{C.2.10}$$

$$\tilde{P}^\pm(\ell) = \tilde{E}(\ell) \pm i\tilde{B}(\ell) \quad , \tag{C.2.11}$$

and $\tilde{f}(l)$ is Fourier transform of $f(l)$, which is a generalized cross-linking parameter that depends on observation and expresses how we observed the point of the sky in various parallactic angles. Practically $f(l)$ is a function of sky position. In the following calculation, however, we assume uniform observation and set $f(l)$ constant for simplicity.

Power spectra of observed maps are calculated as:

$$\langle \tilde{T}_{obs}(\ell) \tilde{T}^*_{obs}(\ell') \rangle = C^{TT}_{obs}(\ell) \delta(\ell - \ell') \quad , \tag{C.2.12}$$

$$\begin{aligned} \langle \tilde{P}^+_{obs}(\ell) \tilde{P}^{+*}_{obs}(\ell') \rangle &= C^{P^+P^+}_{obs}(\ell) \delta(\ell - \ell') \\ &= \left(C^{EE}_{obs}(\ell) + C^{BB}_{obs}(\ell) \right) \delta(\ell - \ell') \quad , \end{aligned} \tag{C.2.13}$$

$$\begin{aligned} \langle \tilde{P}^+_{obs}(\ell) \tilde{P}^{-*}_{obs}(\ell') \rangle &= C^{P^+P^-}_{obs}(\ell) \delta(\ell - \ell') \\ &= \left(C^{EE}_{obs}(\ell) - C^{BB}_{obs}(\ell) + 2iC^{EB}_{obs}(\ell) \right) \delta(\ell - \ell') \quad , \end{aligned} \tag{C.2.14}$$

$$
\begin{aligned}
C_{\mathrm{obs}}^{TT}(\ell) = \sum_{p,l,q,m} & e^{i(l-m)\phi_\ell} f_l f_m^* \\
& \times \Big[\tilde{\mathcal{B}}_{p,l}^{TT}(\ell) \tilde{\mathcal{B}}_{q,m}^{TT*}(\ell) C_{\mathrm{sky}}^{TT}(\ell) \\
& \quad + \big(\tilde{\mathcal{B}}_{p,l}^{TT}(\ell) \tilde{\mathcal{B}}_{q,m-2}^{TP^+*}(\ell) + \tilde{\mathcal{B}}_{p,l}^{TT}(\ell) \tilde{\mathcal{B}}_{q,m+2}^{TP^-*}(\ell) \\
& \qquad + \tilde{\mathcal{B}}_{p,l-2}^{TP^+}(\ell) \tilde{\mathcal{B}}_{q,m}^{TT*}(\ell) + \tilde{\mathcal{B}}_{p,l+2}^{TP^-}(\ell) \tilde{\mathcal{B}}_{q,m}^{TT*}(\ell) \big) C_{\mathrm{sky}}^{TE}(\ell) \\
& \quad + \big(\tilde{\mathcal{B}}_{p,l-2}^{TP^+}(\ell) \tilde{\mathcal{B}}_{q,m-2}^{TP^+*}(\ell) + \tilde{\mathcal{B}}_{p,l-2}^{TP^+}(\ell) \tilde{\mathcal{B}}_{q,m+2}^{TP^-*}(\ell) \\
& \qquad + \tilde{\mathcal{B}}_{p,l+2}^{TP^-}(\ell) \tilde{\mathcal{B}}_{q,m-2}^{TP^+*}(\ell) + \tilde{\mathcal{B}}_{p,l+2}^{TP^-}(\ell) \tilde{\mathcal{B}}_{q,m+2}^{TP^-*}(\ell) \big) C_{\mathrm{sky}}^{EE}(\ell) \\
& \quad + \big(\tilde{\mathcal{B}}_{p,l-2}^{TP^+}(\ell) \tilde{\mathcal{B}}_{q,m-2}^{TP^+*}(\ell) - \tilde{\mathcal{B}}_{p,l-2}^{TP^+}(\ell) \tilde{\mathcal{B}}_{q,m+2}^{TP^-*}(\ell) \\
& \qquad - \tilde{\mathcal{B}}_{p,l+2}^{TP^-}(\ell) \tilde{\mathcal{B}}_{q,m-2}^{TP^+*}(\ell) + \tilde{\mathcal{B}}_{p,l+2}^{TP^-}(\ell) \tilde{\mathcal{B}}_{q,m+2}^{TP^-*}(\ell) \big) C_{\mathrm{sky}}^{BB}(\ell) \Big] \quad ,
\end{aligned}
\tag{C.2.15}
$$

$$
\begin{aligned}
C_{\mathrm{obs}}^{P^+P^+}(\ell) = \sum_{p,l,q,m} & e^{i(l-m)\phi_\ell} f_l f_m^* \\
& \times \Big[\tilde{\mathcal{B}}_{p,l+2}^{P^+T}(\ell) \tilde{\mathcal{B}}_{q,m+2}^{P^+T*}(\ell) C_{\mathrm{sky}}^{TT}(\ell) \\
& \quad + \big(\tilde{\mathcal{B}}_{p,l+2}^{P^+T}(\ell) \tilde{\mathcal{B}}_{q,m}^{P^+P^+*}(\ell) + \tilde{\mathcal{B}}_{p,l+2}^{P^+T}(\ell) \tilde{\mathcal{B}}_{q,m+4}^{P^+P^-*}(\ell) \\
& \qquad + \tilde{\mathcal{B}}_{p,l}^{P^+P^+}(\ell) \tilde{\mathcal{B}}_{q,m+2}^{P^+T*}(\ell) + \tilde{\mathcal{B}}_{p,l+4}^{P^+P^-}(\ell) \tilde{\mathcal{B}}_{q,m+2}^{P^+T*}(\ell) \big) C_{\mathrm{sky}}^{TE}(\ell) \\
& \quad + \big(\tilde{\mathcal{B}}_{p,l}^{P^+P^+}(\ell) \tilde{\mathcal{B}}_{q,m}^{P^+P^+*}(\ell) + \tilde{\mathcal{B}}_{p,l}^{P^+P^+}(\ell) \tilde{\mathcal{B}}_{q,m+4}^{P^+P^-*}(\ell) \\
& \qquad + \tilde{\mathcal{B}}_{p,l+4}^{P^+P^-}(\ell) \tilde{\mathcal{B}}_{q,m}^{P^+P^+*}(\ell) + \tilde{\mathcal{B}}_{p,l+4}^{P^+P^-}(\ell) \tilde{\mathcal{B}}_{q,m+4}^{P^+P^-*}(\ell) \big) C_{\mathrm{sky}}^{EE}(\ell) \\
& \quad + \big(\tilde{\mathcal{B}}_{p,l}^{P^+P^+}(\ell) \tilde{\mathcal{B}}_{q,m}^{P^+P^+*}(\ell) - \tilde{\mathcal{B}}_{p,l}^{P^+P^+}(\ell) \tilde{\mathcal{B}}_{q,m+4}^{P^+P^-*}(\ell) \\
& \qquad - \tilde{\mathcal{B}}_{p,l+4}^{P^+P^-}(\ell) \tilde{\mathcal{B}}_{q,m}^{P^+P^+*}(\ell) + \tilde{\mathcal{B}}_{p,l+4}^{P^+P^-}(\ell) \tilde{\mathcal{B}}_{q,m+4}^{P^+P^-*}(\ell) \big) C_{\mathrm{sky}}^{BB}(\ell) \Big] \quad ,
\end{aligned}
\tag{C.2.16}
$$

$$
\begin{aligned}
C_{\mathrm{obs}}^{P^+P^-}(\ell) = \sum_{p,l,q,m-4} & e^{i(l-m)\phi_\ell} f_l f_m^* \\
& \times \Big[\tilde{\mathcal{B}}_{p,l+2}^{P^+T}(\ell) \tilde{\mathcal{B}}_{q,m-2}^{P^-T*}(\ell) C_{\mathrm{sky}}^{TT}(\ell) \\
& \quad + \big(\tilde{\mathcal{B}}_{p,l+2}^{P^+T}(\ell) \tilde{\mathcal{B}}_{q,m-4}^{P^-P^+*}(\ell) + \tilde{\mathcal{B}}_{p,l+2}^{P^+T}(\ell) \tilde{\mathcal{B}}_{q,m}^{P^-P^-*}(\ell) \\
& \qquad + \tilde{\mathcal{B}}_{p,l}^{P^+P^+}(\ell) \tilde{\mathcal{B}}_{q,m-2}^{P^-T*}(\ell) + \tilde{\mathcal{B}}_{p,l+4}^{P^+P^-}(\ell) \tilde{\mathcal{B}}_{q,m-2}^{P^-T*}(\ell) \big) C_{\mathrm{sky}}^{TE}(\ell) \\
& \quad + \big(\tilde{\mathcal{B}}_{p,l}^{P^+P^+}(\ell) \tilde{\mathcal{B}}_{q,m-4}^{P^-P^+*}(\ell) + \tilde{\mathcal{B}}_{p,l}^{P^+P^+}(\ell) \tilde{\mathcal{B}}_{q,m}^{P^-P^-*}(\ell) \\
& \qquad + \tilde{\mathcal{B}}_{p,l+4}^{P^+P^-}(\ell) \tilde{\mathcal{B}}_{q,m-4}^{P^-P^+*}(\ell) + \tilde{\mathcal{B}}_{p,l+4}^{P^+P^-}(\ell) \tilde{\mathcal{B}}_{q,m}^{P^-P^-*}(\ell) \big) C_{\mathrm{sky}}^{EE}(\ell) \\
& \quad + \big(\tilde{\mathcal{B}}_{p,l}^{P^+P^+}(\ell) \tilde{\mathcal{B}}_{q,m-4}^{P^-P^+*}(\ell) - \tilde{\mathcal{B}}_{p,l}^{P^+P^+}(\ell) \tilde{\mathcal{B}}_{q,m}^{P^-P^-*}(\ell) \\
& \qquad - \tilde{\mathcal{B}}_{p,l+4}^{P^+P^-}(\ell) \tilde{\mathcal{B}}_{q,m-4}^{P^-P^+*}(\ell) + \tilde{\mathcal{B}}_{p,l+4}^{P^+P^-}(\ell) \tilde{\mathcal{B}}_{q,m}^{P^-P^-*}(\ell) \big) C_{\mathrm{sky}}^{BB}(\ell) \Big] \quad .
\end{aligned}
\tag{C.2.17}
$$

BIBLIOGRAPHY

Abazajian, K. N., et al. 2015. "Neutrino physics from the cosmic microwave background and large scale structure". *Astroparticle Physics* 63 (2015): 66–80. doi:10.1016/j.astropartphys.2014.05.014. arXiv: 1309.5383. (Cit. on p. 31).

Abazajian, K. N., et al. 2016. "CMB-S4 Science Book, First Edition". *ArXiv e-prints* (2016). arXiv: 1610.02743. (Cit. on pp. 47, 121).

Ade, P. A. R., et al. 2009. "Polarization modulators for CMBPol". In *Journal of Physics Conference Series*, 155:012006. Journal of Physics Conference Series. 2009. doi:10.1088/1742-6596/155/1/012006. (Cit. on p. 48).

Ade, P. A. R., et al. 2014a. "Evidence for Gravitational Lensing of the Cosmic Microwave Background Polarization from Cross-Correlation with the Cosmic Infrared Background". *Physical Review Letters* 112, 13 (2014): 131302. doi:10.1103/PhysRevLett.112.131302. arXiv: 1312.6645. (Cit. on p. 45).

Ade, P. A. R., et al. 2014b. "Measurement of the Cosmic Microwave Background Polarization Lensing Power Spectrum with the POLARBEAR Experiment". *Physical Review Letters* 113, 2 (2014): 021301. doi:10.1103/PhysRevLett.113.021301. arXiv: 1312.6646. (Cit. on p. 44).

Arnold, K., et al. 2012. "The bolometric focal plane array of the POLARBEAR CMB experiment". In *Millimeter, Submillimeter, and Far-Infrared Detectors and Instrumentation for Astronomy VI*, 8452:84521D. Proc. SPIE. 2012. doi:10.1117/12.927057. arXiv: 1210.7877 [astro-ph.IM]. (Cit. on p. 93).

Aumont, J., et al. 2010. "Measurement of the Crab nebula polarization at 90 GHz as a calibrator for CMB experiments". A&A 514 (2010): A70. doi:10.1051/0004-6361/200913834. arXiv: 0912.1751. (Cit. on pp. 36, 84, 88).

Bao, C., et al. 2012. "The Impact of the Spectral Response of an Achromatic Half-wave Plate on the Measurement of the Cosmic Microwave Background Polarization". ApJ 747 (2012): 97. doi:10.1088/0004-637X/747/2/97. arXiv: 1112.3057 [astro-ph.IM]. (Cit. on p. 119).

Barkats, D., et al. 2005. "Cosmic Microwave Background Polarimetry Using Correlation Receivers with the PIQUE and CAPMAP Experiments". ApJS 159 (2005): 1–26. doi:10.1086/430208. eprint: astro-ph/0503329. (Cit. on p. 66).

Bennett, C. L., et al. 1996. "Four-Year COBE DMR Cosmic Microwave Background Observations: Maps and Basic Results". ApJ 464 (1996): L1. doi:10.1086/310075. eprint: astro-ph/9601067. (Cit. on pp. 4, 6).

Bennett, C. L., et al. 2013. "Nine-year Wilkinson Microwave Anisotropy Probe (WMAP) Observations: Final Maps and Results". ApJS 208 (2013): 20. doi:10.1088/0067-0049/208/2/20. arXiv: 1212.5225. (Cit. on pp. 36, 39, 42).

BICEP2 and Keck Array Collaborations et al. 2015. "BICEP2/Keck Array V: Measurements of B-mode Polarization at Degree Angular Scales and 150 GHz by the Keck Array". ApJ 811 (2015): 126. doi:10.1088/0004-637X/811/2/126. arXiv: 1502.00643. (Cit. on p. 47).

BICEP2 Collaboration et al. 2014. "Detection of B-Mode Polarization at Degree Angular Scales by BICEP2". *Physical Review Letters* 112, 24 (2014): 241101. doi:10.1103/PhysRevLett.112.241101. arXiv: 1403.3985. (Cit. on p. 47).

BICEP2 Collaboration et al. 2016. "Improved Constraints on Cosmology and Foregrounds from BICEP2 and Keck Array Cosmic Microwave Background Data with Inclusion of 95 GHz Band". *Physical Review Letters* 116, 3 (2016): 031302. doi:10.1103/PhysRevLett.116.031302. arXiv: 1510.09217. (Cit. on pp. 47, 48).

BICEP2 Collaboration et al. 2015. "BICEP2 III: Instrumental Systematics". ApJ 814 (2015): 110. doi:10.1088/0004-637X/814/2/110. arXiv: 1502.00608 [astro-ph.IM]. (Cit. on pp. 23, 122).

BICEP2/Keck Collaboration et al. 2015. "Joint Analysis of BICEP2/Keck Array and Planck Data". *Physical Review Letters* 114, 10 (2015): 101301. doi:10.1103/PhysRevLett.114.101301. arXiv: 1502.00612. (Cit. on p. 47).

Blackman, R. B., and J. W. Tukey. 1958. "The measurement of power spectra from the point of view of communications engineering — Part I". *The Bell System Technical Journal* 37, 1 (1958): 185–282. ISSN: 0005-8580. doi:10.1002/j.1538-7305.1958.tb03874.x. (Cit. on p. 101).

Blas, D., J. Lesgourgues, and T. Tram. 2011. "The Cosmic Linear Anisotropy Solving System (CLASS). Part II: Approximation schemes". J. Cosmology Astropart. Phys. 7 (2011): 034. doi:10.1088/1475-7516/2011/07/034. arXiv: 1104.2933. (Cit. on p. 15).

Boettger, D. 2014. "CMB Polarization Measurements with the POLARBEAR Experiment". PhD thesis, University of California, San Diego. (Cit. on p. 86).

Boggess, N. W., et al. 1992. "The COBE mission - Its design and performance two years after launch". ApJ 397 (1992): 420–429. doi:10.1086/171797. (Cit. on p. 3).

Bryan, S. A., T. E. Montroy, and J. E. Ruhl. 2010a. "Modeling dielectric half-wave plates for cosmic microwave background polarimetry using a Mueller matrix formalism". Appl. Opt. 49 (2010): 6313. doi:10.1364/AO.49.006313. arXiv: 1006.3359 [astro-ph.IM]. (Cit. on pp. 54, 119).

Bryan, S. A., et al. 2010b. "Modeling and characterization of the SPIDER half-wave plate". In *Millimeter, Submillimeter, and Far-Infrared Detectors and Instrumentation for Astronomy V*, vol. 7741, 77412B. Proc. SPIE. 2010. doi:10.1117/12.857837. arXiv: 1006.3874 [astro-ph.IM]. (Cit. on p. 121).

Callen, H. B., and T. A. Welton. 1951. "Irreversibility and Generalized Noise". *Physical Review* 83 (1951): 34–40. doi:10.1103/PhysRev.83.34. (Cit. on p. 54).

Carron, J., A. Lewis, and A. Challinor. 2017. "Internal delensing of Planck CMB temperature and polarization". *ArXiv e-prints* (2017). arXiv: 1701.01712. (Cit. on p. 48).

Cyburt, R. H., et al. 2016. "Big bang nucleosynthesis: Present status". *Reviews of Modern Physics* 88, 1 (2016): 015004. doi:10.1103/RevModPhys.88.015004. arXiv: 1505.01076. (Cit. on p. 2).

Davis, M., et al. 1982. "A survey of galaxy redshifts. II - The large scale space distribution". ApJ 253 (1982): 423–445. doi:10.1086/159646. (Cit. on p. 3).

Davis, M., et al. 1985. "The evolution of large-scale structure in a universe dominated by cold dark matter". ApJ 292 (1985): 371–394. doi:10.1086/163168. (Cit. on p. 4).

de Haan, T., G. Smecher, and M. Dobbs. 2012. "Improved performance of TES bolometers using digital feedback". In *Millimeter, Submillimeter, and Far-Infrared Detectors and Instrumentation for Astronomy VI*, vol. 8452, 84520E. Proc. SPIE. 2012. doi:10.1117/12.925658. arXiv: 1210.4967 [astro-ph.IM]. (Cit. on p. 122).

de Zotti, G., et al. 2005. "Predictions for high-frequency radio surveys of extragalactic sources". A&A 431 (2005): 893–903. doi:10.1051/0004-6361:20042108. eprint: astro-ph/0410709. (Cit. on p. 40).

Delabrouille, J., et al. 2013. "The pre-launch Planck Sky Model: a model of sky emission at submillimetre to centimetre wavelengths". A&A 553 (2013): A96. doi:10.1051/0004-6361/201220019. arXiv: 1207.3675. (Cit. on p. 39).

Desai, P. D., H. M. James, and C. Y. Ho. 1984. "Electrical Resistivity of Aluminum and Manganese". *Journal of Physical and Chemical Reference Data* 13 (1984): 1131–1172. doi:10.1063/1.555725. (Cit. on p. 67).

Dobbs, M. A., et al. 2012. "Frequency multiplexed superconducting quantum interference device readout of large bolometer arrays for cosmic microwave background measurements". *Review of Scientific Instruments* 83, 7 (2012): 073113–073113. doi:10.1063/1.4737629. arXiv: 1112.4215 [astro-ph.IM]. (Cit. on p. 99).

Dragone, C. 1978. "Offset multireflector antennas with perfect pattern symmetry and polarization discrimination". *AT T Technical Journal* 57 (1978): 2663–2684. (Cit. on pp. 28, 140, 141).

Dunkley, J., et al. 2009. "Five-Year Wilkinson Microwave Anisotropy Probe (WMAP) Observations: Bayesian Estimation of Cosmic Microwave Background Polarization Maps". ApJ 701 (2009): 1804–1813. doi:10.1088/0004-637X/701/2/1804. arXiv: 0811.4280. (Cit. on p. 40).

Eales, S., et al. 2010. "The Herschel ATLAS". PASP 122 (2010): 499. doi:10.1086/653086. arXiv: 0910.4279. (Cit. on p. 44).

Einstein, A. 1916. "Die Grundlage der allgemeinen Relativitätstheorie". *Annalen der Physik* 354:769–822. doi:10.1002/andp.19163540702. (Cit. on p. 1).

Essinger-Hileman, T., et al. 2016. "Systematic effects from an ambient-temperature, continuously rotating half-wave plate". *Review of Scientific Instruments* 87, 9 (2016): 094503. doi:10.1063/1.4962023. arXiv: 1601.05901 [astro-ph.IM]. (Cit. on pp. 91, 99, 100, 114).

Fixsen, D. J., and J. C. Mather. 2002. "The Spectral Results of the Far-Infrared Absolute Spectrophotometer Instrument on COBE". ApJ 581 (2002): 817–822. doi:10.1086/344402. (Cit. on p. 3).

Fixsen, D. J., et al. 1996. "The Cosmic Microwave Background Spectrum from the Full COBE FIRAS Data Set". ApJ 473 (1996): 576. doi:10.1086/178173. eprint: astro-ph/9605054. (Cit. on p. 4).

Gamow, G. 1948. "The Evolution of the Universe". Nature 162 (1948): 680–682. doi:10.1038/162680a0. (Cit. on p. 2).

George, E. M., et al. 2015. "A Measurement of Secondary Cosmic Microwave Background Anisotropies from the 2500 Square-degree SPT-SZ Survey". ApJ 799 (2015): 177. doi:10.1088/0004-637X/799/2/177. arXiv: 1408.3161. (Cit. on p. 25).

Hanany, S., and P. Rosenkranz. 2003. "Polarization of the atmosphere as a foreground for cosmic microwave background polarization experiments". New A Rev. 47 (2003): 1159–1165. doi:10.1016/j.newar.2003.09.017. eprint: astro-ph/0307052. (Cit. on p. 60).

Hanany, S., et al. 2005. "Millimeter-wave achromatic half-wave plate". Appl. Opt. 44 (2005): 4666–4670. doi:10.1364/AO.44.004666. eprint: physics/0503122. (Cit. on p. 121).

Henderson, S. W., et al. 2016. "Advanced ACTPol Cryogenic Detector Arrays and Readout". *Journal of Low Temperature Physics* 184 (2016): 772–779. doi:10.1007/s10909-016-1575-z. arXiv: 1510.02809 [astro-ph.IM]. (Cit. on p. 121).

Hivon, E., et al. 2002. "MASTER of the Cosmic Microwave Background Anisotropy Power Spectrum: A Fast Method for Statistical Analysis of Large and Complex Cosmic Microwave Background Data Sets". ApJ 567 (2002): 2–17. doi:10.1086/338126. eprint: astro-ph/0105302. (Cit. on pp. 41–43).

Hu, W. 2000. "Weak lensing of the CMB: A harmonic approach". Phys. Rev. D 62, 4 (2000): 043007. doi:10.1103/PhysRevD.62.043007. eprint: astro-ph/0001303. (Cit. on p. 12).

Hu, W., and T. Okamoto. 2002. "Mass Reconstruction with Cosmic Microwave Background Polarization". ApJ 574 (2002): 566–574. doi:10.1086/341110. eprint: astro-ph/0111606. (Cit. on pp. 25, 43, 44).

Hubble, E. 1929. "A Relation between Distance and Radial Velocity among Extra-Galactic Nebulae". *Proceedings of the National Academy of Science* 15 (1929): 168–173. doi:10.1073/pnas.15.3.168. (Cit. on pp. 2, 3).

Irwin, K. D., and G. C. Hilton. 2005. "Transition-Edge Sensors". In *Cryogenic Particle Detection*, ed. by C. Enss, 99:63–150. Topics in Applied Physics. Berlin, Heidelberg: Springer Berlin Heidelberg, 2005. doi:10.1007/10933596_3. http://dx.doi.org/10.1007/10933596_3. (Cit. on pp. 98, 131).

Irwin, K. D., et al. 1998. "Thermal-response time of superconducting transition-edge microcalorimeters". *Journal of Applied Physics* 83 (1998): 3978–3985. doi:10.1063/1.367153. (Cit. on p. 98).

Johnson, B. R., et al. 2007. "MAXIPOL: Cosmic Microwave Background Polarimetry Using a Rotating Half-Wave Plate". ApJ 665 (2007): 42–54. doi:10.1086/518105. eprint: astro-ph/0611394. (Cit. on pp. 81, 91, 99).

Keating, B. G., M. Shimon, and A. P. S. Yadav. 2013. "Self-calibration of Cosmic Microwave Background Polarization Experiments". ApJ 762 (2013): L23. doi:10.1088/2041-8205/762/2/L23. arXiv: 1211.5734 [astro-ph.CO]. (Cit. on pp. 24, 36).

Keisler, R., et al. 2015. "Measurements of Sub-degree B-mode Polarization in the Cosmic Microwave Background from 100 Square Degrees of SPTpol Data". ApJ 807 (2015): 151. doi:10.1088/0004-637X/807/2/151. arXiv: 1503.02315. (Cit. on p. 47).

Kermish, Z. D. 2012. "The POLARBEAR Experiment: Design and Characterization". PhD thesis, University of California, Berkeley. (Cit. on pp. 29, 98).

Klein, J. R., and A. Roodman. 2005. "Blind Analysis in Nuclear and Particle Physics". *Annual Review of Nuclear and Particle Science* 55 (2005): 141–163. doi:10.1146/annurev.nucl.55.090704.151521. (Cit. on p. 31).

Klein, J., et al. 2011. "A cryogenic half-wave plate polarimeter using a superconducting magnetic bearing". In *Cryogenic Optical Systems and Instruments XIII*, 8150:815004. Proc. SPIE. 2011. doi:10.1117/12.893669. (Cit. on p. 122).

Kozorezov, A., et al. 2011. "Modelling the resistive state in a transition edge sensor". *Applied Physics Letters* 99, 6 (2011): 063503. doi:10.1063/1.3621829. (Cit. on p. 98).

Kusaka, A., et al. 2014. "Modulation of cosmic microwave background polarization with a warm rapidly rotating half-wave plate on the Atacama B-Mode Search instrument". *Review of Scientific Instruments* 85, 2 (2014): 024501. doi:10.1063/1.4862058. (Cit. on p. 81).

La Porta, L., et al. 2008. "The impact of Galactic synchrotron emission on CMB anisotropy measurements. I. Angular power spectrum analysis of total intensity all-sky surveys". A&A 479 (2008): 641–654. doi:10.1051/0004-6361:20078435. arXiv: 0801.0547. (Cit. on p. 40).

Larsen, P., et al. 2016. "Demonstration of Cosmic Microwave Background Delensing Using the Cosmic Infrared Background". *Physical Review Letters* 117, 15 (2016): 151102. doi:10.1103/PhysRevLett.117.151102. arXiv: 1607.05733. (Cit. on p. 48).

Lay, O. P., and N. W. Halverson. 2000. "The Impact of Atmospheric Fluctuations on Degree-Scale Imaging of the Cosmic Microwave Background". ApJ 543 (2000): 787–798. doi:10.1086/317115. eprint: astro-ph/9905369. (Cit. on p. 60).

Louis, T., et al. 2013. "Lensing simulation and power spectrum estimation for high-resolution CMB polarization maps". MNRAS 435 (2013): 2040–2047. doi:10.1093/mnras/stt1421. arXiv: 1306.6692 [astro-ph.CO]. (Cit. on p. 41).

Louis, T., et al. 2016. "The Atacama Cosmology Telescope: Two-Season ACTPol Spectra and Parameters". *ArXiv e-prints* (2016). arXiv: 1610.02360. (Cit. on p. 47).

Ludwig, A. C. 1973. "The definition of cross polarization." *IEEE Transactions on Antennas and Propagation* 21:116–119. doi:10.1109/TAP.1973.1140406. (Cit. on p. 139).

Lyth, D. H. 1997. "What Would We Learn by Detecting a Gravitational Wave Signal in the Cosmic Microwave Background Anisotropy?" *Physical Review Letters* 78 (1997): 1861–1863. doi:10.1103/PhysRevLett.78.1861. eprint: hep-ph/9606387. (Cit. on p. 127).

Manzotti, A., et al. 2017. "CMB Polarization B-mode Delensing with SPTpol and Herschel". *ArXiv e-prints* (2017). arXiv: 1701.04396. (Cit. on p. 48).

Martin, J., C. Ringeval, and V. Vennin. 2014. "Encyclopædia Inflationaris". *Physics of the Dark Universe* 5 (2014): 75–235. doi:10.1016/j.dark.2014.01.003. arXiv: 1303.3787. (Cit. on pp. 8, 127, 128).

Mather, J. C., et al. 1994. "Measurement of the cosmic microwave background spectrum by the COBE FIRAS instrument". ApJ 420 (1994): 439–444. doi:10.1086/173574. (Cit. on p. 3).

Matsumura, T. 2014. "Mitigation of the spectral dependent polarization angle response for achromatic half-wave plate". *ArXiv e-prints* (2014). arXiv: 1404.5795 [astro-ph.IM]. (Cit. on p. 119).

Matsumura, T., et al. 2009. "Performance of three- and five-stack achromatic half-wave plates at millimeter wavelengths". Appl. Opt. 48 (2009): 3614. doi:10.1364/AO.48.003614. arXiv: 0806.1518 [physics.optics]. (Cit. on pp. 119, 121).

Mizugutch, Y., M. Akagawa, and H. Yokoi. 1976. "Offset Dual Reflector Antenna". *ISA Proceedings*: 2–5. (Cit. on pp. 28, 140).

Moncelsi, L., et al. 2014. "Empirical modelling of the BLASTPol achromatic half-wave plate for precision submillimetre polarimetry". MNRAS 437 (2014): 2772–2789. doi:10.1093/mnras/stt2090. arXiv: 1208.4866 [astro-ph.IM]. (Cit. on p. 121).

Naess, S., et al. 2014. "The Atacama Cosmology Telescope: CMB polarization at 200 < l < 9000". J. Cosmology Astropart. Phys. 10 (2014): 007. doi:10.1088/1475-7516/2014/10/007. arXiv: 1405.5524. (Cit. on p. 47).

O'Dea, D., A. Challinor, and B. R. Johnson. 2007. "Systematic errors in cosmic microwave background polarization measurements". MNRAS 376 (2007): 1767–1783. doi:10.1111/j.1365-2966.2007.11558.x. eprint: astro-ph/0610361. (Cit. on pp. 114, 143, 151).

Penzias, A. A., and R. W. Wilson. 1965. "A Measurement of Excess Antenna Temperature at 4080 Mc/s." ApJ 142 (1965): 419–421. doi:10.1086/148307. (Cit. on p. 3).

Perlmutter, S., et al. 1999. "Measurements of Ω and Λ from 42 High-Redshift Supernovae". ApJ 517 (1999): 565–586. doi:10.1086/307221. eprint: astro-ph/9812133. (Cit. on p. 4).

Pietranera, L., et al. 2007. "Observing cosmic microwave background polarization through ice". MNRAS 376 (2007): 645–650. doi:10.1111/j.1365-2966.2007.11464.x. eprint: astro-ph/0611678. (Cit. on p. 60).

Pisano, G., et al. 2006. "Achromatic half-wave plate for submillimeter instruments in cosmic microwave background astronomy: experimental characterization". Appl. Opt. 45 (2006): 6982–6989. doi:10.1364/AO.45.006982. (Cit. on p. 121).

Pisano, G., et al. 2008. "Metal-mesh achromatic half-wave plate for use at submillimeter wavelengths". Appl. Opt. 47 (2008): 6251. doi:10.1364/AO.47.006251. (Cit. on p. 121).

Pisano, G., et al. 2014. "Development of large radii half-wave plates for CMB satellite missions". In *Millimeter, Submillimeter, and Far-Infrared Detectors and Instrumentation for Astronomy VII*, 9153:915317. Proc. SPIE. 2014. doi:10.1117/12.2056380. arXiv: 1409.8516 [astro-ph.IM]. (Cit. on p. 48).

Planck Collaboration et al. 2016a. "Planck 2015 results. I. Overview of products and scientific results". A&A 594 (2016): A1. doi:10.1051/0004-6361/201527101. arXiv: 1502.01582. (Cit. on pp. 5, 19).

Planck Collaboration et al. 2016b. "Planck 2015 results. X. Diffuse component separation: Foreground maps". A&A 594 (2016): A10. doi:10.1051/0004-6361/201525967. arXiv: 1502.01588. (Cit. on p. 24).

Planck Collaboration et al. 2016c. "Planck 2015 results. XIII. Cosmological parameters". A&A 594 (2016): A13. doi:10.1051/0004-6361/201525830. arXiv: 1502.01589. (Cit. on pp. 5, 127).

Planck Collaboration et al. 2016d. "Planck intermediate results. XXX. The angular power spectrum of polarized dust emission at intermediate and high Galactic latitudes". A&A 586 (2016): A133. doi:10.1051/0004-6361/201425034. arXiv: 1409.5738. (Cit. on p. 47).

Pontoppidan, K., ed. 2005. *GRASP Technical Description*. Copenhagen: TICRA, 2005. http://www.ticra.com. (Cit. on p. 143).

QUIET Collaboration et al. 2012. "Second Season QUIET Observations: Measurements of the Cosmic Microwave Background Polarization Power Spectrum at 95 GHz". ApJ 760 (2012): 145. doi:10.1088/0004-637X/760/2/145. arXiv: 1207.5034 [astro-ph.CO]. (Cit. on p. 39).

Rees, M. J. 1968. "Polarization and Spectrum of the Primeval Radiation in an Anisotropic Universe". ApJ 153 (1968): L1. doi:10.1086/180208. (Cit. on p. 11).

Rees, M. J., and D. W. Sciama. 1968. "Large-scale Density Inhomogeneities in the Universe". Nature 217 (1968): 511–516. doi:10.1038/217511a0. (Cit. on p. 3).

Reichardt, C. L., et al. 2012. "A Measurement of Secondary Cosmic Microwave Background Anisotropies with Two Years of South Pole Telescope Observations". ApJ 755 (2012): 70. doi:10.1088/0004-637X/755/1/70. arXiv: 1111.0932 [astro-ph.CO]. (Cit. on p. 40).

Richards, P. L. 1994. "Bolometers for infrared and millimeter waves". *Journal of Applied Physics* 76 (1994): 1–24. doi:10.1063/1.357128. (Cit. on p. 19).

Riess, A. G., et al. 1998. "Observational Evidence from Supernovae for an Accelerating Universe and a Cosmological Constant". AJ 116 (1998): 1009–1038. doi:10.1086/300499. eprint: astro-ph/9805201. (Cit. on p. 4).

Riess, A. G., et al. 2016. "A 2.4% Determination of the Local Value of the Hubble Constant". ApJ 826 (2016): 56. doi:10.3847/0004-637X/826/1/56. arXiv: 1604.01424. (Cit. on p. 2).

Rubin, V. C., W. K. Ford Jr., and N. Thonnard. 1980. "Rotational properties of 21 SC galaxies with a large range of luminosities and radii, from NGC 4605 /R = 4kpc/ to UGC 2885 /R = 122 kpc/". ApJ 238 (1980): 471–487. doi:10.1086/158003. (Cit. on p. 4).

Sadler, E. M., et al. 2006. "The properties of extragalactic radio sources selected at 20GHz". MNRAS 371 (2006): 898–914. doi:10.1111/j.1365-2966.2006.10729.x. eprint: astro-ph/0603437. (Cit. on p. 40).

Savini, G., G. Pisano, and P. A. R. Ade. 2006. "Achromatic half-wave plate for submillimeter instruments in cosmic microwave background astronomy: modeling and simulation". Appl. Opt. 45 (2006): 8907–8915. doi:10.1364/AO.45.008907. (Cit. on p. 121).

Savini, G., et al. 2009. "Recovering the frequency dependent modulation function of the achromatic half-wave plate for POL-2: the SCUBA-2 polarimeter". Appl. Opt. 48 (2009): 2006. doi:10.1364/AO.48.002006. (Cit. on p. 121).

Seiffert, M., et al. 2007. "An upper limit to polarized submillimetre emission in Arp 220". MNRAS 374 (2007): 409–414. doi:10.1111/j.1365-2966.2006.11186.x. eprint: astro-ph/0610485. (Cit. on p. 40).

Shimon, M., et al. 2008. "CMB polarization systematics due to beam asymmetry: Impact on inflationary science". Phys. Rev. D 77, 8 (2008): 083003. doi:10.1103/PhysRevD.77.083003. arXiv: 0709.1513. (Cit. on pp. 24, 114).

Smith, K. M. 2006. "Pure pseudo- C_ℓ estimators for CMB B-modes". New A Rev. 50 (2006): 1025–1029. doi:10.1016/j.newar.2006.09.015. eprint: astro-ph/0608662. (Cit. on pp. 38, 41).

Smith, K. M., et al. 2012. "Delensing CMB polarization with external datasets". J. Cosmology Astropart. Phys. 6 (2012): 014. doi:10.1088/1475-7516/2012/06/014. arXiv: 1010.0048. (Cit. on p. 124).

Song, Y.-S., et al. 2003. "The Far-Infrared Background Correlation with Cosmic Microwave Background Lensing". ApJ 590 (2003): 664–672. doi:10.1086/375188. eprint: astro-ph/0209001. (Cit. on p. 25).

Spergel, D. N., et al. 2003. "First-Year Wilkinson Microwave Anisotropy Probe (WMAP) Observations: Determination of Cosmological Parameters". ApJS 148 (2003): 175–194. doi:10.1086/377226. eprint: astro-ph/0302209. (Cit. on p. 5).

Stebor, N., et al. 2016. "The Simons Array CMB polarization experiment". In *Society of Photo-Optical Instrumentation Engineers (SPIE) Conference Series*, vol. 9914, 99141H. Proc. SPIE. 2016. doi:10.1117/12.2233103. (Cit. on p. 121).

Stokes, G. G. 1852. "Ueber die Veränderung der Brechbarkeit des Lichts". *Annalen der Physik* 163:480–490. doi:10.1002/andp.18521631109. (Cit. on p. 10).

Tanaka, H., and M. Mizusawa. 1975. "Elimination of cross polarization in offset dual-reflector antennas". *Electronics Communications of Japan* 58 (1975): 71–78. (Cit. on pp. 28, 140).

The POLARBEAR Collaboration: P. A. R. Ade et al. 2014. "A Measurement of the Cosmic Microwave Background B-mode Polarization Power Spectrum at Sub-degree Scales with POLARBEAR". ApJ 794 (2014): 171. doi:10.1088/0004-637X/794/2/171. arXiv: 1403.2369. (Cit. on pp. 34–36, 38–40, 43, 67, 71, 82, 103).

Tran, H., et al. 2008. "Comparison of the crossed and the Gregorian Mizuguchi-Dragone for wide-field millimeter-wave astronomy". Appl. Opt. 47 (2008): 103–109. doi:10.1364/AO.47.000103. (Cit. on p. 66).

Ulich, B. L. 1981. "Millimeter wave radio telescopes - Gain and pointing characteristics". *International Journal of Infrared and Millimeter Waves* 2 (1981): 293–310. doi:10.1007/BF01007036. (Cit. on p. 34).

van der Kuur, J., and M. Kiviranta. 2013. "Operation of transition edge sensors in a resistance locked loop". *Applied Physics Letters* 102, 2 (2013): 023505. doi:10.1063/1.4788683. arXiv: 1211.5647 [physics.ins-det]. (Cit. on p. 122).

van der Kuur, J., et al. 2011. "Small-Signal Behavior of a TES Under AC Bias". *IEEE Transactions on Applied Superconductivity* 21 (2011): 281–284. doi:10.1109/TASC.2010.2099092. (Cit. on p. 99).

DECLARATION

Put your declaration here.

Machikaneyama 1 - 1, Toyonaka, Osaka, Japan, June 2017

Satoru Takakura

COLOPHON

This document was typeset using the typographical look-and-feel `classicthesis` developed by André Miede. The style was inspired by Robert Bringhurst's seminal book on typography "*The Elements of Typographic Style*". `classicthesis` is available for both LaTeX and LyX:

https://bitbucket.org/amiede/classicthesis/

Happy users of `classicthesis` usually send a real postcard to the author, a collection of postcards received so far is featured here:

http://postcards.miede.de/

Final Version as of September 14, 2017 (`classicthesis` version 0.1).